

UNIVERSIDADE DE LISBOA
FACULDADE DE CIÊNCIAS



Ciências
ULisboa

**Novel functionalized elongated titanate nanostructures for emergent pollutants
photocatalytic degradation**

“ Documento Definitivo ”

Doutoramento em Química
Especialidade em Química

Beatriz Trindade Martins Vidigal Barrocas

Tese orientada por:
Doutora Olinda Coelho Monteiro

Documento especialmente elaborado para a obtenção do grau de doutor

UNIVERSIDADE DE LISBOA

FACULDADE DE CIÊNCIAS



**Ciências
ULisboa**

**Novel functionalized elongated titanate nanostructures for emergent pollutants
photocatalytic degradation**

Doutoramento em Química

Especialidade em Química

Beatriz Trindade Martins Vidigal Barrocas

Tese orientada por:

Doutora Olinda Coelho Monteiro

Júri:

Presidente:

- Doutora Amélia Pilar Grases dos Santos Silva Rauter,
Professora Catedrática e Presidente do Departamento de Química e Bioquímica
da Faculdade de Ciências da Universidade de Lisboa

Vogais:

- Doutora Magdalena Skompska, Professor
Faculty of Chemistry da University of Warsaw (Polónia);
- Doutor Joaquim Luís Bernardes Martins de Faria, Professor Associado
Faculdade de Engenharia da Universidade do Porto;
- Doutor Tito da Silva Trindade, Professor Catedrático
Departamento de Química da Universidade de Aveiro;
- Doutora Ana Paula Baptista de Carvalho, Professora Auxiliar
Faculdade de Ciências da Universidade de Lisboa;
- Doutora Olinda Coelho Monteiro, Investigadora FCT de Nível Inicial
Faculdade de Ciências da Universidade de Lisboa (orientadora).

Documento especialmente elaborado para a obtenção do grau de doutor

Fundação para a Ciência e a Tecnologia (FCT) no âmbito de uma Bolsa individual de
doutoramento (SFRD/BD/101220/2014)

“Nanotechnology has given us the tools ... to play with the ultimate toy box of nature - atoms and molecules”.

Horst Stormer,
Nobel Prize in Physics, 1998

“I am among those who think that science has great beauty. A scientist in his laboratory is not only a technician: he is also a child placed before natural phenomena which impress him like a fairy tale.”

Marie Curie (Maria Skłodowska-Curie),
Nobel Prize in Physics, 1903
Nobel Prize in Chemistry, 1911

**To my parents and sister,
In memory of my grandparents, Lizette and Daniel**

Acknowledgments

My particular gratitude goes to my supervisor, Doctor Olinda Coelho Monteiro, for guidance, support, precious knowledge transmitted, permanent availability and patience throughout my studies. Her dedication was completely invaluable to the development of this research, and I am sincerely grateful for always believed in me. I also want to thank her for all the opportunities to work abroad, to attend international conferences and training schools around the world.

Significantly warming thank you to Professor Magdalena Skompska, from the University of Warsaw, Poland, for receiving me so warmly in her research group during my internship. I am beholden for her collaboration during my work, scientific discussions, and all the support when I was in Warsaw, and later in Portugal.

I am grateful to Doctor Maria Conceição Oliveira for her collaboration during the LC-HR-ESI/MS measurements and scientific discussions about mass spectroscopy, and all support when I was in the Instituto Superior Técnico (IST). I also want to thank Professor António Silvestre and Doctor Carla Nunes for all the collaborations, support and scientific discussions. I would like to thank all the collaborations, to be possible the Raman and p.z.c. measurements. Thank on top go to Doctor Ana Mourato for the XRD and atomic absorption measurements, helpful discussions and especially due to her friendship, concerns, and advice. I also want to thank Doctor Isabel Tissot for the XRF measurements, constructive discussions, and friendship. I am immensely grateful to all my colleagues at Interfacial Electrochemistry Group (IEG) from CQB/CQE (Centro de Química e Bioquímica/Centro de Química Estrutural) for being a part of my laboratory workdays, for these last years. Thanks also go to Professor Jorge Correia, for the kindness and the precious clarifications provided by extensive experience in electrochemistry. The entire group has been so sympathetic, that I enjoyed every day working with it. To all the people that passed through in these workplaces and became unforgettable. I thank especially Doctor Virgínia Ferreira, for her friendship, kind support, help, and counseling whenever required. I would like to thank my colleagues from the University of Warsaw research group for their assistance on countless occasions. Especially Kamila and Tomasz for all the support, friendship and good moments shared.

To Professor Helena Mendonça and Professor Estrela Melo Jorge for the constant sympathy and motivation, as well as for their pieces of advice.

I heartily thank Frederico Botelho Sampaio for the friendship and critically reading of the entire manuscript.

I would like to thank all my friends, for the support and encouragement. Especially Jorge Diniz for the company in the research lab, friendship, kindness, and the accurate word in the right moments. Daniel Siopa, for all advice and help. To Tia Sisi for all the help, kindness and encouragement. To Pedro Melo, to be like a brother, for his unconditional support (not only but also computer/informatic support), encouragement, friendship and all the pleasant moments shared.

I want to express my gratitude to my sister for her endless friendship, patience, and support. For being my complement and conscience. She was always exceptionally optimistic and believed in my force, which brought out the best of me. Thanks for all the love, smile, laughs and life that we share.

I would like to thank my parents, for the enormous patience, understanding, support, and love expressed in the course of this work, as well as throughout my life.

To Cláudia and Ioana from Departamento de Química e Bioquímica (DQB) secretary, for all the support and kindness. To the DQB 3rd cycle coordination (PhD in Chemistry), Professor Ana Paula Paiva and Doctor Ana Viana, for all the kindness, concerns and advices.

I acknowledge COST Action MP1302 for the financial support for the internship at the University of Warsaw, Poland, by the short-term scientific mission grant (2017). I also thank Fundação para a Ciência e a Tecnologia (FCT) for the financial support with the supplementary training allowance, for the internship at the University of Warsaw, Poland (2018).

I acknowledge FCT for financial support through a PhD grant (SFRH/BD/101220/2014).

Abstract

The primary goal of this work was the preparation of new elongated titanate nanoparticles, like nanotubes (TNT) and nanowires (TNW), with improved ability for pollutants adsorption and photo(electro)catalytic degradation. TNT and TNW were prepared using a hydrothermal approach in alkaline medium, starting from TiO_2 nanoparticles and amorphous precursors, respectively. The TNT/TNW were modified by ion-exchange and doping with metals (Co, Ru, and Fe/Mn), and by sensitization with Ag nanoparticles and ethylenediamine. The catalytic ability of these new materials for the pollutants photodegradation, including phenol, caffeine, theophylline, and dyes, was also investigated. The results showed that all modified TNT/TNW demonstrated excellent photocatalytic activity for the degradation processes studied.

The sensitization process can improve the light absorption on the visible range and the ability for pollutants adsorption and photocatalytic degradation, due to the change imposed on the TNT/TNW surface. The metal modification can impose a light absorption shift to the visible range and/or the introduction of intermediary levels in the forbidden band, reducing the electron-hole (e^-/h^+) recombination.

For the ethylenediamine sensitized samples, it was demonstrated that the N-species improves the photocatalytic activity. The results revealed h^+ was mainly responsible for the hydroxyl radical formation, and the production of nitrogen oxidant species was proposed.

The results for sensitized samples with Ag nanoparticles, Ag-HTNW, revealed the presence of Ag^+ in the interlayers and Ag nanoparticles in the HTNW surface, and the h^+ action with highly oxidant species enhances the photocatalytic performance.

For the cobalt modified powders, depending on the synthesis methodology and Co/Ti ratio, the dopant can replace Na^+ in the interlayers and/or substitute Ti^{4+} in lattice positions or sit in interstitial sites. The structure and optical behavior are dependent on the metal ions either substituting Ti^{4+} or replacing Na^+ .

For RuTNW sample, Ru^{n+} was detected in the crystalline structure replacing Ti^{4+} and in the interlayers replacing Na^+ , and for RuTNT it was only replacing Ti^{4+} . The photocatalytic improvement of these materials was principally to recombination rate reduction, by metal incorporation. The utmost difference between these samples was related to the pollutants' photodegradation mechanism and intermediates formation/degradation.

In this work, the influence of slight metal contaminations on the TNW structural, optical and photocatalytic behavior was also studied. FeMnTNW were obtained due to a reactants' vestigial

contamination. The modification occurred by $\text{Ti}^{4+}/\text{Fe}^{3+}\text{-Mn}^{3+}$ substitution and by Na^+ replacement in the interlayers.

The TNW/TNT immobilization in conductive films to be used in pollutants photo(electro)degradation, was also studied. Ru- and Co-modified TNW/TNT were immobilized on a conductive substrate by drop-casting method followed by 1,8-diaminocarbazole electropolymerization and were remarkably effective catalysts in pollutants photo(electro)degradation. The films' reutilization showed that these are stable and can be used in successive degradation without performance loss.

Keywords

Elongated titanate nanoparticles, metal modification, metal and organic molecules sensitization, emergent pollutants, photo(electro)catalytic degradation.

Resumo

O objetivo do presente trabalho foi a preparação de novas nanopartículas de titanatos alongadas (TNP), tais como nanotubos (TNT) e nanofibras (TNW), para serem utilizadas como adsorventes e foto(electro)catalisadores para a remoção/degradação de poluentes emergentes.

Os poluentes emergentes são substâncias químicas, geralmente não reguladas, sendo os seus efeitos no meio ambiente e na saúde humana a longo prazo ainda desconhecidos. Estes podem ser produtos farmacêuticos, de higiene e cuidado pessoal (PPCPs), tais como antibióticos, analgésicos, antidepressivos, estimulantes, cosméticos, excipientes e parabenos. Como estes poluentes são resistentes a tratamentos convencionais, mesmo em concentrações muito baixas, podem causar sérios riscos para a saúde, devido à elevada toxicidade que apresentam, sendo atualmente a sua eliminação muito problemática. Vários tratamentos têm sido propostos, mas novas soluções, com maior eficiência, são necessárias para uma resolução definitiva deste problema. Neste sentido, nos últimos anos várias investigações têm sido feitas para procurar tratamentos eficazes para degradar estes efluentes e diminuir o seu impacto ambiental. Vários estudos revelam que os processos avançados de oxidação (AOPs) são promissores no tratamento de efluentes, uma vez que são eficazes na degradação de poluentes orgânicos em meio aquoso. Nos AOPs há formação de espécies muito reativas, os radicais hidroxilo ($\cdot\text{OH}$), que têm elevado poder oxidante e podem promover a degradação de vários poluentes de forma rápida e não-seletiva. Existem vários tipos de processos de produção do $\cdot\text{OH}$, sendo os mais promissores os de oxidação fotocatalítica e fotoeletrocatalítica, usando semicondutores nanocristalinos como catalisadores.

Os semicondutores são caracterizados, do ponto de vista eletrónico, por apresentarem uma banda de valência (VB) e uma banda de condução (CB), sendo a região entre as duas bandas o hiato ótico. O processo fotocatalítico dá-se pela irradiação do semicondutor, ocorrendo absorção de fótons com energia igual ou superior à energia do hiato ótico. Formam-se transportadores de carga do tipo elétron-lacuna (e^-/h^+) devido à absorção de energia pelos elétrons da VB que são transferidos para a CB, sendo criada uma lacuna na VB. Os transportadores de carga podem participar diretamente em reações redox à superfície do semicondutor e ainda formar radicais (por exemplo $\cdot\text{OH}$ e $\text{O}_2\cdot^-$) que participam ativamente na degradação dos poluentes orgânicos, quebrando as ligações químicas, até à sua total mineralização. No processo fotoeletrocatalítico, há um aumento da eficiência catalítica devido à diminuição da recombinação de cargas no semicondutor irradiado, quando utilizado como fotoânodo onde se aplica um potencial ou uma corrente constante. Desta forma, cria-se um

gradiente de potencial que facilita o processo de separação de cargas, aumentando assim o tempo de vida do par e^-/h^+ .

Neste contexto, este trabalho propõe a síntese de novos TNT e TNW modificados, para serem utilizados como foto(electro)catalisadores, para a degradação de poluentes. Os TNT e as TNW, foram preparadas através de um processo hidrotérmico em meio alcalino (NaOH 10 M) a 160°C durante 24 horas, partindo de nanopartículas de TiO₂ e de um precursor amorfo, respetivamente. Prepararam-se também amostras HTNW, por troca iónica através de um tratamento ácido da amostra TNW (que contem iões Na⁺ nas intercadas), substituindo os iões Na⁺ por H⁺.

Modificaram-se TNW e TNT por sensibilização com etilenodiamina (EDAmine), obtendo-se as amostras NTNW e NTNT e por sensibilização com nanopartículas de prata, Ag-HTNW. Foram modificadas amostras de TNW com cobalto por dopagem, com diferentes percentagens de substituição, (Co(1%)TNW e Co(5%)TNW) e por troca iónica (TNWCo(5%)). Também foram modificadas amostras com ruténio (1%, nominal), obtendo as amostras RuTNT e RuTNW, e com manganês e ferro, FeMnTNW.

O processo de sensibilização das TNP pode melhorar a absorção de luz no visível, e a capacidade de adsorção e de degradação destes fotocatalisadores, uma vez que provoca uma alteração na superfície das nanopartículas. Por outro lado, a modificação das TNP com metais pode desviar a absorção de luz para a gama do visível e/ou introduzir níveis intermédios na banda proibida, reduzindo assim a recombinação do par e^-/h^+ .

A caracterização estrutural por difração de raios-X de pós revelou que todas as amostras preparadas apresentam uma estrutura cristalina do tipo Na_{2-x}H_xTi₃O₇ ($0 \leq x \leq 2$), não se verificando alterações estruturais após modificação.

A análise por microscopia eletrónica de transmissão revelou uma morfologia homogénea e uniforme, com nanofibras ou nanotubos bem definidos, não se observando alterações significativas nas TNP modificadas. Apenas nas amostras modificadas com nanopartículas de prata (Ag-HTNW) se verificou a presença de nanopartículas na superfície das nanofibras.

Após caracterização e para avaliar a capacidade fotocatalítica das novas amostras de TNP modificadas, foram realizados ensaios de fotoreacção do ácido tereftálico, para analisar a produção de $\cdot\text{OH}$. Os resultados revelaram que estes nanomateriais apresentam elevada atividade fotocatalítica para a produção desta espécie oxidante. Estes novos materiais modificados foram estudados com catalisadores em processos de fotodegradação de poluentes. Os resultados revelaram que todos os TNW e TNT modificados apresentam excelente atividade fotocatalítica para os processos de degradação estudados.

Nas amostras modificadas por sensibilização com EDAmine, NTNW e NTNT, a presença da amina foi confirmada por espectroscopia fotoeletrônica de raios-X (XPS). Verificou-se ainda um desvio para a zona do vermelho da banda de absorção das partículas sensibilizadas, indicando que estas apresentam uma energia do hiato ótico menor. Pelos ensaios de fotodegradação da cafeína, teofilina e do fenol, verificou-se que as amostras após sensibilização apresentam uma maior eficiência em relação às amostras TNT/TNW. A amostra NTNT foi a que apresentou maior atividade catalítica, para todos os poluentes nas condições experimentais utilizadas. Nos ensaios de reutilização a amostra NTNT foi sujeita a quatro ensaios de fotodegradação sucessivos, tendo-se verificado que esta amostra apresenta elevada estabilidade associada a uma alta eficiência catalítica na degradação de soluções de cafeína, teofilina e de fenol.

Na sensibilização com nanopartículas de prata, a presença do metal na amostra Ag-HTNW foi confirmada por XPS e fluorescência de raios-X (μ XRF). A caracterização por espectroscopia de reflectância difusa revelou uma modificação no comportamento ótico da amostra, apresentando uma banda de absorção aos 480 nm devido ao efeito de absorção plasmônica das nanopartículas de Ag, indicando uma melhoria significativa na absorção de luz visível e sugerindo uma possível melhoria no desempenho fotocatalítico da amostra. A atividade fotocatalítica das partículas de Ag-HTNW foi avaliada e os resultados obtidos mostraram que esta foi bastante eficiente na degradação fotocatalítica do fenol usando radiação UV-vis. Os resultados relativos à estabilidade deste fotocatalisador, mostram que é muito estável após 4 degradações sucessivas, revelando-se promissor para ensaios de fotodegradação com radiação UV-visível. Verificou-se, contudo, um aumento na quantidade e no tamanho das nanopartículas de Ag durante estes ensaios. Estes resultados sugerem a possibilidade de simultaneamente se formarem nanopartículas de Ag e de se degradar um poluente, sem diminuição do desempenho fotocatalítico.

Para as TNW modificadas com cobalto, dependendo do método de síntese e da razão entre Co e Ti (Co/Ti), o metal dopante pode substituir os iões Na^+ nas intercamadas, e/ou substituir os iões Ti^{4+} na estrutura cristalina ou ficar nos interstícios. Embora não tenham sido observadas alterações significativas na morfologia das nanofibras devido à introdução do metal, uma alteração no espectro ótico das amostras foi observada, verificando-se uma grande diferença quando os iões cobalto estão a substituir os iões Ti^{4+} ou Na^+ . Nas amostras dopadas foi verificada a presença de iões $\text{Co}^{2+}/\text{Co}^{3+}$ e nas amostras preparadas por troca iónica (amostras intercaladas) a presença de Co^{2+} . Todas as amostras de TNW modificadas com cobalto apresentam uma absorção na gama do visível, e o desvio para o vermelho observado pode ser atribuído à introdução de orbitais $3d$ do cobalto na banda proibida.

Os ensaios da atividade fotocatalítica permitiram concluir que as amostras dopadas são mais eficientes na degradação do fenol e dos corantes amarelo naftol S e verde brilhante do que as amostras intercaladas. Nos ensaios de degradação da mistura destes três poluentes, verificou-se que a amostra Co(1%)TNW apresenta uma elevada e muito promissora eficiência fotocatalítica.

Para a amostra RuTNW, verificou-se por espectroscopia de Raman, XPS e μ XRF a presença de iões Ru^{n+} na estrutura cristalina substituindo o Ti^{4+} e nas intercamadas a substituir os iões Na^+ , no entanto na amostra RuTNT, a substituição foi apenas nos iões Ti^{4+} . A atividade fotocatalítica destes materiais foi estudada na degradação de sulfametazina e de cafeína. Neste estudo, verificou-se uma melhoria do desempenho catalítico dos TNT e TNW após a introdução de rutênio, sendo esta atribuída a uma diminuição da taxa de recombinação do par e^-/h^+ . Concluiu-se também que para as amostras RuTNT e RuTNW, a maior diferença no desempenho fotocatalítico em relação à morfologia, isto é, ter nanotubos ou nanofibras, está principalmente relacionada com o mecanismo de degradação dos poluentes e à formação/degradação dos subprodutos/intermediários da reação.

Neste trabalho foi também possível estudar a influência de contaminações vestigiais por metais, nas características estruturais, óticas e fotocatalíticas das TNW. Devido a uma contaminação vestigial de um reagente com ferro e manganês, foi obtida uma amostra de FeMnTNW. A modificação dos TNW com Fe e Mn, ocorreu por substituição dos iões Ti^{4+} por Fe^{3+} - Mn^{3+} e por incorporação nas intercamadas substituindo os iões Na^+ . A eficiência fotocatalítica desta amostra foi analisada na degradação da cafeína, verificando-se que a presença de Fe/Mn é promissora para a degradação deste poluente. Foi realizado um estudo usando captadores de espécies oxidantes, para analisar quais as espécies intervenientes no processo de degradação da cafeína com a amostra FeMnTNW como catalisador. Pelos resultados obtidos, e tendo em conta a possibilidade de ter $\text{Fe}^{3+/2+}/\text{H}_2\text{O}_2$ no sistema, a combinação dos processos de fotodegradação catalítica e foto-Fenton, com H_2O_2 gerado *via* radical superóxido foi devidamente equacionada. Verificou-se que a degradação da cafeína ocorre *via* radicais $\cdot\text{OH}$ e $\text{O}_2\cdot^-$.

Estudou-se também a imobilização das TNP, pois uma grande limitação nesta área é a utilização de fotocatalisadores em suspensão nos reatores para tratamento de águas residuais. Se por um lado apresentam melhor atividade devido à maior transferência de massa entre os poluentes e o fotocatalisador, por outro lado apresentam como desvantagem a dificuldade em separar o catalisador no final da fotodegradação, sendo necessárias a filtração ou centrifugação da água tratada para recuperar o catalisador. A utilização do semiconductor imobilizado na forma de filme tem como vantagens a facilidade de manuseamento e de recuperação do catalisador. Neste

sentido, neste trabalho preparam-se filmes para imobilizar as TNP em substratos condutores para serem utilizados como foto(electro)catalisadores. Foram preparados filmes condutores híbridos de TNP com poli(1,8-diaminocarbazole). As amostras de TNP modificadas com Ru e com Co foram imobilizadas em substratos condutores pelo método de *drop-casting*. Prepararam-se também filmes híbridos por electropolimerização do monómero 1,8-diaminocarbazole. Estes filmes mostraram-se muito promissores para a degradação foto(electro)catalítica do azul de metileno e da teofilina. A reutilização dos filmes revelou que estes são estáveis e que podem ser utilizados em sucessivos ensaios de degradação sem diminuição do seu desempenho catalítico.

Palavras-chave

Nanopartículas de titanato alongadas, modificação com metais, sensibilização com metais e moléculas orgânicas, poluentes emergentes, degradação foto(electro)catalítica.

Index

Acknowledgements	i
Abstract	iii
Resumo	v
Index of figures	xvii
Index of tables	xxvi
Abbreviations, symbols and constants	xxvii
Chapter 1 – Introduction	1
1.1 - Emerging pollutants	3
1.1.1 – PPCPs	3
1.1.2 – Industrial dyes	7
1.2 - Advanced oxidation processes (AOPs)	9
1.2.1 - Photocatalytic and photoelectrocatalytic methods	10
1.3 - Scavengers	15
1.4 - Hydroxyl radical production	17
1.5 - Semiconductor materials in photocatalysis	18
1.5.1 – Titanium dioxide (TiO ₂)	22
1.5.2 – Elongated titanate nanoparticles (TNP)	22
• Synthesis methodologies	23
• Hydrothermal synthesis	24
• TNP crystalline structure	27
• TNP morphology	30
• Mechanism of formation	31
• TNP modifications and functionalization	33
• TNP applications	35
1.6 - References	39
Chapter 2 – Amine modified elongated titanate nanowires and nanotubes	61
2.1 – Introduction	63
2.2 – Synthesis	65
2.3 – Structural, morphological and optical characterization	65
2.4 – Photocatalytic performance	70
2.4.1 - Photo-induced hydroxyl radical production	70
2.4.2 - Caffeine, theophylline and phenol photocatalytic degradation	73

2.4.3 - Kinetic studies	81
2.4.4 - Reusability and stability studies	83
2.5 – Conclusions	84
2.6 – References	85
Chapter 3 – Titanate nanowires sensitization by silver nanoparticles	91
3.1 – Introduction	93
3.2 – Synthesis	94
3.3 – Structural, morphological and optical characterization	95
3.4 – Photocatalytic performance.....	100
3.4.1 - Photo-induced hydroxyl radical production	100
3.4.2 - Phenol photodegradation	101
3.4.3 - Ag-HTNW photocatalytic reusability and stability	103
3.5 – Conclusions	106
3.6 – References	107
Chapter 4 – Tailoring titanate nanoparticles photocatalytic properties by cobalt incorporation/modification	111
4.1 – Introduction.....	113
4.2 – Synthesis	114
4.3 – Structural, morphological and optical characterization	115
4.4 – Photo-induced hydroxyl radical production	123
4.5 - Adsorption and photocatalytic studies	125
4.5.1 - Phenol, naphthol yellow S and brilliant green adsorption	125
4.5.2 - Phenol photocatalytic degradation	126
4.5.3 - Brilliant green (BG) photocatalytic degradation	127
4.5.4 - Naphthol yellow S (NYS) photocatalytic degradation	128
4.5.5 - Pollutants mixture photodegradation	131
4.5.6 - Kinetic studies	132
4.6 – Conclusions	134
4.7 – References	135
Chapter 5 – Ruthenium modified titanate nanowires for photocatalytic emergent pollutants degradation	141
5.1 – Introduction	143
5.2 – Synthesis	144
5.3 – Structural, morphological and optical characterization	144

5.4 – Photocatalytic performance	150
5.4.1 - Photo-induced hydroxyl radical production	150
5.4.2 - Caffeine photocatalytic degradation	151
5.5 – Photoactivation mechanism study	154
5.6 – Conclusions	156
5.7 – References	157
Chapter 6 – Photocatalytic performance of ruthenium modified titanate nanotubes and nanowires: a comparative study	161
6.1 – Introduction	163
6.2 – Synthesis	164
6.3 – Structural, morphological and optical characterization	164
6.4 – Photocatalytic performance evaluation	172
6.4.1 - Photo-induced hydroxyl radical production	172
6.4.2 - Caffeine and sulfamethazine photocatalytic degradation	173
6.5 – Conclusions	181
6.6 – References	181
Chapter 7 – Influence of iron and manganese vestigial contamination on the properties of titanate nanowires	185
7.1 – Introduction	187
7.2 – Synthesis	190
7.3 – Structural, morphological and optical characterization	191
7.4 – Photocatalytic performance of the prepared samples	196
7.4.1 - Hydroxyl radical production	196
7.4.2 - Photoluminescence characterization	197
7.4.3 - Caffeine photodegradation	198
7.4.4 - Scavengers study	201
7.5 – Photo-activation mechanism proposal	202
7.5.1 - FeMnTNW photocatalytic reusability and stability	204
7.6 – Conclusions	205
7.7 – References	205
Chapter 8 – Immobilization of cobalt and ruthenium modified titanate nanoparticles for photo(electro)catalytic application	213
8.1 – Introduction	215
8.2 – Synthesis	217

8.3 – Immobilization of cobalt and ruthenium modified TNW by drop-casting and electropolymerization - hybrid films preparation	218
8.3.1 – Hybrid films preparation and optimization of the preparation conditions	218
8.3.2 – Cobalt and ruthenium modified ITO/TNW/PDAC films characterization.....	222
8.3.3 – Photocatalytic performance evaluation	224
8.4 – Cobalt and ruthenium modified TNT hybrid films - Influence of the metal position.....	227
8.4.1 – Hybrid films synthesis	227
8.4.2 – Optical and morphological characterization	229
8.4.3 – Electrochemical characterization	229
8.4.4 - Photocatalytic and photoelectrocatalytic pollutants degradation experiments...	236
• Methylene blue (MB) photodegradation	236
• Theophylline photodegradation	240
• Theophylline photo(electro)degradation	242
8.5 – Conclusions	243
8.6 – References	244
Chapter 9 – Final conclusions	249
Chapter 10 – Methods and experimental	253
10.1 - Reagents	255
10.2 – Synthesis	255
10.2.1 - TiO _x amorphous precursor synthesis	255
10.2.2 - Ru-doped precursor	256
10.2.3 - Co-doped precursor synthesis	256
10.2.4 - Titanate nanowires (TNW) synthesis	256
10.2.5 - Protonated titanate nanowires (HTNW) synthesis	256
10.2.6 - Titanium dioxide (TiO ₂) nanoparticles synthesis	257
10.2.7 - Titanate nanotubes (TNT) synthesis	257
10.2.8 - Ag-HTNW synthesis	257
10.2.9 - TNT and TNW modification with amines - ethylenediamine (EDAmine)	258
10.2.10 - Synthesis of ruthenium modified nanoparticles	258
• Ru-TiO ₂ synthesis	258
• RuTNW and RuTNT synthesis	258
10.2.11 - Synthesis of cobalt modified nanoparticles	258
• Co-TiO ₂ synthesis	258

• CoTNT and CoTNW synthesis	258
• TNW/Co and TNT/Co synthesis	259
10.3 - Nanoparticles characterization	259
10.3.1 - X-ray powder diffraction (XRD)	259
• Crystallite size determination	259
10.3.2 - Transmission electron microscopy (TEM)	260
10.3.3 - Energy dispersive X-ray spectroscopy (EDS)	260
10.3.4 - Specific surface area determination (B.E.T. method)	260
10.3.5 - Micro X-ray fluorescence (μ XRF)	260
10.3.6 - Diffuse reflectance spectroscopy (DRS)	260
• Bandgap energy determination	261
10.3.7 - Photoluminescence spectroscopy (PL)	262
10.3.8 - X-ray photoelectron spectroscopy (XPS)	262
• Valence band (VB) determination	263
10.3.9 - Raman spectroscopy	263
10.3.10 - Point of zero charge (p.z.c.)	264
10.4 - Photocatalytic experiments	264
10.4.1 - Fluorescence spectroscopy	265
• Production of hydroxyl radical (\cdot OH)	266
10.4.2 - UV-vis spectrophotometry	266
• Photocatalytic degradation efficiency determination	266
10.4.3 - Gas chromatography-mass spectrometry (GC-MS)	266
10.4.4 - Liquid chromatography high-resolution with electrospray ionization coupled to mass spectrometry (LC-HR-ESI/MS)	267
10.5 - Nanocomposite films preparation, characterization and application in pollutants photo(electro)degradation	267
10.5.1 - Films preparation	267
• Drop-casting films preparation	268
• DAC Electropolymerization	268
10.5.2 - Modified electrodes characterization	269
• Cyclic voltammetry	269
• Optical characterization	269
• Morphology characterization	269
• Photoelectrochemical characterization	269

10.5.3 - Photodegradation experiments	271
10.5.4 - Photo(electro)degradation experiments	272
10.6 - References	272
Chapter 11 - Annexes	275

Index of figures

Figure 1.1 - Schematic representation of diclofenac molecule.	5
Figure 1.2 – Schematic representation of (a) caffeine, (b) theophylline, and (c) phenol molecules.....	7
Figure 1.3 – Schematic representation of advanced oxidation processes (AOPs). (Adapted and based on [41,42,55-59])	9
Figure 1.4 – Schematic representation of the electrochemical cell used by Fujishima and Honda, (adapted from [68]).	11
Figure 1.5 – Schematic representation of a semiconductor when irradiated with $h\nu$ energy.....	12
Figure 1.6 - Terephthalic acid conversion in fluorescent 2-hydroxyterephthalic acid (HTA).....	16
Figure 1.7 - Band structure energy for conductive, semiconductor and insulator materials....	18
Figure 1.8 – Schematic representation of the excitation process in semiconductor materials, from the top of the valence band to the bottom of the conduction band, by photonic absorption, following a direct and an indirect transition process.....	19
Figure 1.9 – Representation of n - and p -type doping in a semiconductor.	21
Figure 1.10 – XRD patterns of the titanate nanostructures prepared at 160°C and different reaction times: 12 h (TNP16012), 24 h (TNP16024), 36 h (TNP16036), 48 h (TNP16048) and 72 h (TNP16072). * $\text{Na}_2\text{Ti}_3\text{O}_7$, JCPDS-ICDD file No. 31-1329; • $\text{H}_2\text{Ti}_3\text{O}_7$, JCPDS-ICDD file No. 41-192, reported by Ylhäinen <i>et al.</i> [196].	26
Figure 1.11 – TEM images of titanate nanostructures prepared at 160°C during (a) 24 h, (b) 36 h, (c) 48 h, and (d) 72 h, reported by Ylhäinen <i>et al.</i> [196].....	26
Figure 1.12 - Crystallographic structures of (a) $\text{Na}_2\text{Ti}_3\text{O}_7$ and (b) $\text{H}_2\text{Ti}_3\text{O}_7$ (adapted from [181]).....	28
Figure 1.13 – HRTEM images of the (a) TNT-pH9, (b) TNT-pH7, and (c) TNT-pH5, reported by Bem <i>et al.</i> [147].....	29
Figure 1.14 – Schematic representation of elongated titanate nanoparticles: (a) multi-wall nanotubes, (b) multiple-wall nanowires, (c) nanorods, (d) rectangular nanofibers, and (e) nanosheets.....	30
Figure 1.15 – Schematic representation of the curl up process of TNT. (a) Exfoliation of the $\text{Na}_2\text{Ti}_3\text{O}_7$ nanosheets; (b) winding a nanosheet in the direction of the TNT main axis [010]; (c) top view of the coiled winding forming a multi-layered TNT. (Adapted from [190]).....	32

Figure 1.16 – Schematic representation of the driving forces for bending titanates nanosheets under alkaline hydrothermal conditions. (a) Asymmetrical chemical environment resulting in different surface tensions; k_1 and k_2 are spring constants on each side of the nanosheet. (b) Imbalance in layer widths resulting in shifting of the layer and bending of nanosheets. (Adapted from [88]).	32
Figure 1.17 – Band structure of $\text{Ag}_2\text{S}(\text{ZnS}/\text{TNP})$ particles and the mechanism of phenol photocatalytic degradation (adapted from [80]).	34
Figure 2.1 - Representation of ethylenediamine (EDAmine) molecule.	64
Figure 2.2 - XRD patterns of the TNW and TNT before and after sensitization with EDAmine.	65
Figure 2.3 - TEM images of the (a) TNW and (b) TNT samples.	66
Figure 2.4 - XPS survey spectrum of the (a) NTNW sample; XPS high resolution spectra of the (b) Ti 2p, (c) O 1s for the NTNW and TNW powders and (d) N 1s for NTNT and NTNW samples.	68
Figure 2.5 - Absorption spectra of the TNW, TNT, NTNW and NTNT samples.	69
Figure 2.6 - HTA concentration variation during 30 min of irradiation of a TA solution (3 mM, 150 mL) using 10 mg of each photocatalyst.	70
Figure 2.7 - Hydroxyl radical production after 15 min of irradiation, with and without O_2 , using 10 mg of each photocatalyst.	71
Figure 2.8 – Schematic representation of the energetic structure proposed for the TNT and hybrid NTNT particles under irradiation.	72
Figure 2.9 – Schematic representation of the (a) theophylline, (b) caffeine and (c) phenol molecules.	73
Figure 2.10 – (a) UV-vis spectra of theophylline solution degradation, using NTNT sample as photocatalyst. (b) Theophylline photocatalytic degradation during 90 min of irradiation using the pristine and hybrid powders as photocatalysts (20 ppm; 0.13 g L^{-1}).	74
Figure 2.11 – Variation of the compounds identified during 75 min of theophylline photocatalytic degradation, using NTNT as catalyst.	76
Figure 2.12 - (a) UV-vis spectra of caffeine solution degradation, using NTNT sample as photocatalyst. (b) Caffeine photocatalytic degradation during 90 min of irradiation using the pristine and hybrid powders as photocatalysts (20 ppm; 0.13 g L^{-1}).	77
Figure 2.13 – (a) Variation of the compounds identified during 90 min of caffeine photocatalytic degradation, using NTNT as catalyst, (b) detail for the lower amount compounds.	79

Figure 2.14 - Phenol photocatalytic degradation during 90 min of irradiation using the pristine and hybrid powders as photocatalysts (20 ppm; 0.13 g L ⁻¹).	80
Figure 2.15 - Kinetics of the photocatalytic degradation reactions of (a) theophylline, (b) caffeine and (c) phenol solutions.	82
Figure 2.16 - Percentage of theophylline, caffeine and phenol removal, during four cycles of photocatalytic degradation using the same NTNT sample as catalyst.	84
Figure 2.17 – Raman spectra of the TNT and NTNT samples before and after being submitted to UV-vis radiation (90 min).	84
Figure 3.1 - XRD patterns of the HTNW before and after sensitization with a 0.5 M AgNO ₃ solution.	95
Figure 3.2 - TEM images of the (a) HTNW, (b) Ag ⁺ HTNW and Ag-HTNW sample prepared during (c) 30 min and (d) 60 min of irradiation.	96
Figure 3.3 – EDS spectrum of the Ag-HTNW sample. (*From copper grids used to support the elongated titanate nanoparticles.)	97
Figure 3.4 - XPS survey spectra of the (a) HTNW and (b) Ag-HTNW samples.....	98
Figure 3.5 - XPS high resolution spectra of the (a) Ti 2 <i>p</i> , (b) O 1 <i>s</i> and (c) Ag 3 <i>d</i> regions, for the HTNW and Ag-HTNW samples.	99
Figure 3.6 - Absorption spectra of the HTNW and Ag-HTNW samples.	100
Figure 3.7 - HTA concentration variation during 30 min of irradiation of a TA solution (3 mM, 150 mL) using 10 mg of each photocatalyst.	101
Figure 3.8 - Phenol photocatalytic degradation of a 20 ppm aqueous solution during 75 min of irradiation using Ag-HTNW and HTNW samples as photocatalysts (0.13 g L ⁻¹).	102
Figure 3.9 - Percentage of a 20 ppm phenol solution removal during four photodegradation cycles, of 60 min each, using the same Ag-HTNW sample as catalyst.	103
Figure 3.10 - XRD patterns of the Ag-HTNW sample before and after four cycles of phenol photodegradation.	103
Figure 3.11 - Representative TEM images of the Ag-HTNW sample after the (a) 1 st , (b) 2 nd , (c) 3 rd and (d) 4 th photocatalytic degradation cycle.	104
Figure 3.12 - Schematic representation of the energetic structure proposed for the Ag-HTNW nanocomposite particles under irradiation.	106
Figure 4.1 – (a) XRD patterns of the TNW, Co(1%)TNW, Co(5%)TNW and TNW/Co(5%) prepared samples; (b) detail of the XRD patterns.	115
Figure 4.2 - TEM image of the (a) TNW, (b) Co(5%)TNW, (c) Co(1%)TNW and (d) TNW/Co(5%) samples.	117

Figure 4.3 - Raman spectra of the TNW, Co(1%)TNW, Co(5%)TNW and TNW/Co(5%) samples.	118
Figure 4.4 – Optical spectra of the TNW, Co(1%)TNW, Co(5%)TNW and TNW/Co(5%) samples.	120
Figure 4.5 – XPS survey spectra of the (a) TNW and (b) Co(5%)TNW samples. XPS high resolution spectra of the (c) Ti 2 <i>p</i> , (d) O 1 <i>s</i> and (e and f) Co 2 <i>p</i> regions.	122
Figure 4.6 – HTA concentration during 20 min of UV-vis irradiation of a TA solution (3 mM, 150 mL) using 10 mg of each photocatalyst.	124
Figure 4.7 – Schematic representation of (a) phenol, (b) naphthol yellow S and (c) brilliant green molecules.	125
Figure 4.8 - Phenol, BG and NYS adsorption ability using pristine TNW, Co(1%)TNW, Co(5%)TNW and TNW/Co(5%) samples as adsorbents.	125
Figure 4.9 – Concentration of phenol during 90 min of irradiation using TNW, Co(1%)TNW, Co(5%)TNW and TNW/Co(5%) samples as photocatalysts.	126
Figure 4.10 – (a) Electronic spectra of a 10 ppm BG solution during 45 min of irradiation using Co(1%)TNW as a photocatalyst and (b) concentration of BG <i>versus</i> irradiation time using the prepared samples as catalysts.	128
Figure 4.11 – (a) Electronic spectra of a 20 ppm NYS solution during 45 min of irradiation using Co(1%)TNW as photocatalyst and (b) concentration of NYS <i>versus</i> irradiation time using the prepared samples as catalysts.	129
Figure 4.12 – Band structure scheme of Co-modified TNW and the mechanism of photo-induced oxidant radical formation.	130
Figure 4.13 – Decrease of the phenol (a), BG (b) and NYS (c) concentration in a pollutant mixture solution, during 150 min of irradiation, using Co(1%)TNW as a catalyst and during photolysis.	131
Figure 4.14 – Kinetics of the photodegradation reaction of phenol and of BG, in single solutions and in a pollutant mixture solution (a and b) <i>via</i> photolysis and (c and d) using Co(1%)TNW as a photocatalyst.	133
Figure 5.1 – (a) XRD patterns of the TNW and RuTNW prepared samples; (b) detail of the XRD patterns.	145
Figure 5.2 - TEM image of the RuTNW sample.	146
Figure 5.3 - Raman spectra of the TNW and RuTNW samples.	146
Figure 5.4 - Raman spectra of the TNW and TNW/Ru samples.	147

Figure 5.5 – (a) XPS survey spectra of the RuTNW sample and high-resolution spectra of the (b) Ti 2 <i>p</i> , (c) O 1 <i>s</i> and (d) Ru 3 <i>p</i> regions of the TNW and RuTNW samples.	148
Figure 5.6 – (a) Absorption spectra and (b) representation of the function $(F_{KM}.hv)^2$ versus hv , for the bandgap energy determination of the TNW and RuTNW prepared samples.	149
Figure 5.7 - (a) XPS high resolution spectra of the O 2 <i>p</i> to Ti 3 <i>d</i> transition, used for valence band determination; (b) Energy-level diagram with E_g , VB and CB positions, for the prepared samples.	150
Figure 5.8 - HTA concentration after 30 min of irradiation of a TA solution (3 mM, 150 mL) using 10 mg of each photocatalyst.	151
Figure 5.9 - Profiles of the photocatalytic degradation of a 20 ppm caffeine aqueous solution during 120 min of irradiation, with the TNW and RuTNW samples acting as catalysts (0.13 g L ⁻¹).....	152
Figure 5.10 - Variation of the intermediate products identified during 120 min of caffeine photodegradation, using RuTNW as a catalyst.	154
Figure 5.11 - Caffeine concentration, after 60 min of visible light irradiation, using the prepared samples as photocatalysts.	155
Figure 5.12 - Photoluminescence spectra of the TNW and RuTNW samples.	155
Figure 5.13 - Charge-transfer mechanism proposal for TNW and RuTNW particles, under irradiation.	156
Figure 6.1 - XRD patterns of the TNT and RuTNT prepared samples.	165
Figure 6.2 - TEM images of the (a) TNT and (b) RuTNT samples.	165
Figure 6.3 - Raman spectra of the TNT and RuTNT prepared samples.	167
Figure 6.4 - (a) XPS survey spectra of the RuTNT sample and high resolution spectra of the (b) Ti 2 <i>p</i> and (c) Ru 3 <i>p</i> regions for the prepared powders.	169
Figure 6.5 – Absorption spectra of the TNT and RuTNT samples. (Inset: energy-level diagram with E_g , VB, and CB positions, for TNT, RuTNT, and TNW, RuTNW [2]).	170
Figure 6.6 – XPS high resolution spectra of the O 2 <i>p</i> to Ti 3 <i>d</i> transition, used for valence band determination.	171
Figure 6.7 – Photoluminescence spectra of RuTNT and TNT prepared powders.	171
Figure 6.8 – HTA concentration during 30 min of irradiation of a TA solution (3 mM, 150 mL) using 10 mg of each photocatalyst.	172
Figure 6.9 – Photocatalytic degradation of a 20 ppm caffeine aqueous solution during 45 min of irradiation using the pristine and modified powders as photocatalysts (0.13 g L ⁻¹).....	174

Figure 6.10 - Variation of the intermediate products identified during 120 min of caffeine photocatalytic degradation, using (a) RuTNT and (b) RuTNW as photocatalysts.	176
Figure 6.11 - Photocatalytic degradation profile of a 10 ppm sulfamethazine aqueous solution during 45 min of irradiation using the prepared powders as photocatalysts (0.13 g L ⁻¹).	177
Figure 6.12 - Variation of the by-products identified during 90 min of sulfamethazine photocatalytic degradation, using (a) RuTNT and (b) RuTNW as catalyst.	179
Figure 6.13 – Sulfamethazine concentration after 45 min of irradiation with visible light, using 20 mg of each photocatalyst.	180
Figure 7.1 – (a) XRD patterns of the TNW and FeMnTNW samples; (b) detail of the XRD patterns.	191
Figure 7.2 - TEM images of the (a) pristine TNW and (b) FeMnTNW prepared samples.	192
Figure 7.3 - XPS survey spectra of the (a) TNW and (b) FeMnTNW samples. High resolution spectra of the (c) Ti 2 <i>p</i> , (d) O 1 <i>s</i> and (e) Fe 2 <i>p</i>	194
Figure 7.4 - Absorption spectra of the TNW and FeMnTNW samples. (Inset: energetic diagram with <i>E_g</i> , VB, and CB positions, for the prepared samples.)	195
Figure 7.5 – XPS high resolution spectra of the O 2 <i>p</i> to Ti 3 <i>d</i> transition, used for valence band determination.	196
Figure 7.6 - HTA concentration after 20 min of irradiation of a TA solution (3 mM, 150 mL) using 20 mg of each sample as photocatalyst.	197
Figure 7.7 - Photoluminescence spectra of the TNW and FeMnTNW prepared samples.	198
Figure 7.8 - Degradation profile of a 20 ppm caffeine solution during 75 min of irradiation using the prepared samples as photocatalyst.	198
Figure 7.9 - Variation of intermediate products identified during 120 min of caffeine photodegradation, by (a) photolysis and (b) FeMnTNW as catalyst.	201
Figure 7.10 - Amount of caffeine degraded after 75 min under UV-vis radiation, in the presence of scavengers, BQ, Ox, and EtOH as radicals' scavengers, and using FeMnTNW as photocatalyst.	202
Figure 7.11 - Mechanism proposal for charge-transfer processes for TNW and FeMnTNW samples, when irradiated with UV-vis light.	204
Figure 7.12 - XRD patterns of the FeMnTNW before and after submitted to four consecutive photocatalytic experiments.	204
Figure 8.1 - Structural representation of (a) 1,8-diaminocarbazole monomer and (b) poly(1,8-diaminocarbazole).	216

Figure 8.2 - Structural representation of (a) methylene blue and (b) theophylline molecules.....	217
Figure 8.3 - Cyclic voltammograms of DAC electropolymerization on ITO/TNW modified electrode 2 mM DAC in 0.1 M LiClO ₄ /ACN; (a) cycles 1 and 2, (b) cycles 1 - 20 at 60 mV s ⁻¹	219
Figure 8.4 - Four successive cyclic voltammograms obtained in the solution of 0.1 M LiClO ₄ /acetonitrile at 60 mV s ⁻¹ , for the ITO (grey lines) and ITO/TNW/PDAC (black lines) films.	220
Figure 8.5 - MB degradation percentage evolution using ITO/PDAC, ITO/TNW/PDAC (2 scans) and ITO/TNW/PDAC (20 scans) films as photocatalysts, under UV-vis _(Xe) irradiation.....	221
Figure 8.6 - Absorption spectra of the (a) ITO/TNW, ITO/CoTNW and ITO/RuTNW and (b) ITO, ITO/PDAC samples.	223
Figure 8.7 - SEM images of the (a) ITO, (b) ITO/PDAC, (c) ITO/TNW, (d) ITO/TNW/PDAC, (e) ITO/CoTNW and (f) ITO/CoTNW/PDAC films.	224
Figure 8.8 - MB photodegradation during 75 min of UV-vis _(Xe) irradiation using ITO/PDAC, ITO/TNW/PDAC, ITO/CoTNW/PDAC and ITO/RuTNW/PDAC films.....	225
Figure 8.9 - MB photodegradation during 120 min of visible _(Xe) irradiation using ITO/PDAC, ITO/TNW, ITO/CoTNW, ITO/RuTNW, ITO/TNW/PDAC, ITO/CoTNW/PDAC and ITO/RuTNW/PDAC samples.	226
Figure 8.10 - Cyclic voltammograms of DAC (2 mM) electropolymerization on ITO and ITO/TNT-Co films in 0.1 M LiClO ₄ /ACN; 2 cycles at 60 mV s ⁻¹	228
Figure 8.11 - SEM image of the (a) ITO/CoTNT and (b) ITO/CoTNT/PDAC films.....	229
Figure 8.12 - Four successive cyclic voltammograms obtained in the solution of 0.1 M LiClO ₄ /acetonitrile, for the (a) ITO/TNT/PDAC, (b) ITO/TNT-Co/PDAC and ITO/CoTNT/PDAC, (c) ITO/TNT-Ru/PDAC and ITO/RuTNT/PDAC samples; 4 cycles at 60 mV s ⁻¹	230
Figure 8.13 - Cyclic voltammograms of the ITO/CoTNT/PDAC sample in 0.1 M Na ₂ SO ₄ aqueous solution in (a) dark during 6 cycles and (b) in dark and under illumination with a xenon lamp (UV-vis _(Xe) radiation).	231
Figure 8.14 - Cyclic voltammograms of the (a) ITO/CoTNT, (b) ITO/TNT-Co, (c) ITO/RuTNT and (d) ITO/TNT-Ru samples in 0.1 M Na ₂ SO ₄ aqueous solution in dark and under illumination with a xenon lamp (UV-vis _(Xe) radiation).	232

Figure 8.15 - Current transients at constant polarization potential of 0.7 V vs. Ag/AgCl in dark and under illumination with a xenon lamp (UV-vis _(Xe) radiation), for the (a) ITO/TNT-Co and ITO/CoTNT and (b) ITO/TNT-Ru and ITO/RuTNT samples.	233
Figure 8.16 - Current transients at constant polarization potential of 0.5 V vs. Ag/AgCl in dark and under illumination with a high-power LED (365 nm), in 0.1 M Na ₂ SO ₄ aqueous solution, for (a) ITO/CoTNT and ITO/TNT-Co and (b) ITO/RuTNT and ITO/TNT-Ru samples.....	235
Figure 8.17 - MB photodegradation during 90 min of visible _(Xe) irradiation using (a) the samples containing cobalt and (b) the samples modified with ruthenium.....	237
Figure 8.18 - Schematic representation of the charge-transfer mechanism proposal for (a) ITO/TNP/PDAC hybrid films and (b) for the pristine and Co- and Ru-containing TNP samples, under irradiation.	239
Figure 8.19 - Percentage of a 10 ppm MB solution removal during four consecutive cycles, of 60 min each, of photocatalytic degradation, using ITO/CoTNT/PDAC and ITO/TNT-Ru/PDAC samples as catalyst, under visible _(Xe) irradiation.	240
Figure 8.20 - Theophylline photodegradation during 90 min of UV-vis _(Xe) irradiation using ITO/PDAC, ITO/TNT/PDAC, ITO/CoTNT/PDAC, ITO/TNT-Co/PDAC, ITO/TNT/PDAC, ITO/RuTNT/PDAC and ITO/TNT-Ru samples.	241
Figure 8.21 - Percentage of a 5 ppm theophylline solution removal during four cycles, of 90 min each, by photocatalytic degradation, using ITO/ CoTNT/PDAC, ITO/TNT-Co/PDAC, ITO/TNT-Ru/PDAC and ITO/TNT-Ru samples as catalyst.	242
Figure 8.22 - Theophylline concentration after 120 min of UV irradiation (LED 365 nm) during photo and photoelectrodegradation using ITO/CoTNT, ITO/TNT-Co, ITO/RuTNT and ITO/TNT-Ru samples as catalysts.	243
Figure 10.1 – Absorption spectra of a TNW sample.	261
Figure 10.2 – Representation of the function $(F_{KM}.hv)^2$ versus hv , for the bandgap energy (of a TNW sample) determination.	262
Figure 10.3 – XPS high-resolution spectra of the O 2 <i>p</i> to Ti 3 <i>d</i> transition, used for valence band determination (of a TNW sample).	263
Figure 10.4 – (a) Representation and (b) photography of the photo-reactor used in the photocatalytic experiments.	265
Figure 10.5 – Schematic representation of TNP deposition methods used.	267
Figure 10.6 - Representation of the cell used for electropolymerization and electrochemical characterization.	268

Figure 10.7 - Representation of the cell used in the photoelectrochemical characterization using a Xe lamp and a LED (365 nm).	270
Figure 10.8 - (a) Schematic representation and (b) photography of the reactor used in the photocatalytic experiments.	271
Figure 10.9 - (a) Schematic representation and (b) photography of the cell used in the photo(electro)catalytic experiments.	272
Figure B.1 – Degradation mechanism used for the intermediate products identification during theophylline removal. (Adapted from [1])	281
Figure B.2 – Degradation mechanism used for the intermediate products identification during caffeine removal. (Adapted from [2])	282
Figure B.3 – Degradation mechanism used for the intermediate products identification during phenol removal. (Adapted from [3])	282
Figure B.4 – Degradation mechanism used for the intermediate products identification during sulfamethazine removal. (Adapted from [4-6])	283

Index of tables

Table 2.1 - Main products identified by LC-HR-ESI/MS for the photocatalytic degradation of theophylline using NTNT as catalyst	75
Table 2.2 - Main fragments and correspondent by-products identified by LC-HR-ESI/MS for the photodegradation of caffeine using NTNT as catalyst	78
Table 2.3 - Main products identified by GC-MS for the phenol photocatalytic degradation process using NTNT as catalyst	81
Table 2.4 - Rate constants for the studied photocatalytic degradations	83
Table 5.1 - Main fragments and correspondent by-products identified by LC-HR-ESI/MS during the caffeine photodegradation using RuTNW as a catalyst	153
Table 6.1 - Raman shifts (cm^{-1}) and tentative assignments of the Raman bands for the prepared samples	167
Table 6.2 - Main fragments and correspondent by-products identified by LC-HR-ESI/MS during caffeine photodegradation using RuTNT and RuTNW samples as catalysts.....	175
Table 6.3 - Main products identified by LC-HR-ESI/MS during the sulfamethazine photodegradation using RuTNT and RuTNW samples as catalysts	178
Table 7.1 - Main fragments identified by LC-HR-ESI/MS and correspondent by-products formed during the photodegradation of caffeine using FeMnTNW as catalyst	200
Table 8.1 – Current peak potentials (<i>vs.</i> Ag/AgCl/Cl ⁻) and respective current densities for the DAC oxidation peak (A) and redox couple (B/B') on ITO, ITO/TNW, ITO/CoTNW and ITO/RuTNW electrodes, evaluated from the voltammograms	220
Table 8.2 – Current peak potentials (<i>vs.</i> Ag/AgCl/Cl ⁻) and respective current densities for the DAC oxidation peak (A) and redox couple (B/B') on ITO and all prepared electrodes, obtained from the respective cyclic voltammograms.....	228
Table A.1 – ICDD-JCPDS file no. 72-0148 (Na ₂ Ti ₃ O ₇).	277
Table A.2 - ICDD-JCPDS file no. 41-0192 (H ₂ Ti ₃ O ₇).	280
Table A.3 - ICDD-JCPDS file no. 04-0783	280

Abbreviations, symbols and constants

Abbreviations

Abs	Absorbance
ACN	Acetonitrile
AOPs	Advanced oxidation processes
ATR	Attenuated total reflectance
B.E.T.	Brunauer, Emmett and Teller method
BG	Brilliant green
CAF	Caffeine
CB	Conduction band
DAC	1,8-diaminocarbazole
DCF	Diclofenac
DRS	Diffuse reflectance spectroscopy
EDAmine	Ethylenediamine
EDS	Energy dispersive X-ray spectroscopy
ESI	Electrospray ionization
F _L	Fermi level
HTA	2-hydroxyterephthalic acid
GC-MS	Gas chromatography – mass spectrometry
ITO	Indium tin oxide
JCPDS-ICDD	Joint committee for powder diffraction standards - international centre for diffraction data
<i>KM</i>	Kubelka-Munk
LC-HR-ESI/MS	Liquid chromatography high-resolution with electrospray ionization coupled to mass spectrometry
MB	Methylene blue
PDAC	Poly(1,8-diaminocarbazole)
PET	Polyethylene terephthalate
PPCPs	Pharmaceutical and personal care products
NHE	Normal hydrogen electrode
NYS	Naphthol yellow S
SEM	Scanning electron microscopy
SMZ	Sulfamethazine

TA	Terephthalic acid
TEM	Transmission electron microscopy
Theo	Theophylline
TNP	Elongated titanate nanoparticles
TNT	Elongated titanate nanotubes
TNW	Elongated titanate nanowires
TOF	Time-of-flight
UV	Ultraviolet
UV-Vis	Ultraviolet – visible spectrophotometry
VB	Valence band
XPS	X-ray photoelectron spectroscopy
XRF	X-ray fluorescence
XRD	X-ray powder diffraction

Symbols and constants

a.u.	Arbitrary units
<i>ca.</i>	Approximately or around - an abbreviation of the Latin expression <i>circa</i>
E°	Standard electrode potential [V or eV]
E_g	Bandgap energy [eV]
e^-	Electron
<i>e.g.</i>	For example - abbreviation of the Latin expression <i>exempli gratia</i>
<i>et al.</i>	And others - abbreviation for the Latin expression <i>et alia</i>
F_{KM}	Kubelka-Munk function
f_{KM}	Function used in the Tauc graphics, which allows to obtain the bandgap energy
h^+	Hole
<i>i.e.</i>	That is - an abbreviation of the Latin expression <i>id est</i>
θ	Diffraction angle [°]
λ	Wavelength [nm]
h	Plank constant [J.s]
ν	Frequency [Hz]
h	Hours
min	Minutes

T	Temperature [°C]
<i>t</i>	Time
vs.	<i>Versus</i>
<i>hkl</i>	Miller indices

Chapter 1
Introduction

Chapter 1 – Introduction

In the past years, the pollution of water systems with pharmaceuticals and personal care products (PPCPs) among other pollutants has become a huge environmental problem. These emergent pollutants are resistant to conventional treatments and even at low concentrations, they may impose toxicity to all biological hierarchy levels. The search for effective and practical treatments to degrade them, and reduce their environmental impact, has attracted the interest of researchers, and innovative solutions are being proposed [1].

1.1 - Emerging pollutants

Emerging pollutants are chemical substances, commonly not regulated, that can be detected in low concentrations, raising particular concern due to their long-term adverse effects on the environment and on human health remaining unknown. These pollutants be defined as compounds of different origin and chemical nature whose presence in the environment, or by consequences of their presence, they have gone mostly unnoticed and due to this remain unregulated [2].

International organizations have proposed some definitions of emerging pollutants, which can illustrate different aspects related to this problem and which can help to understand their dimension and consequences [2]. According to the organization for monitoring emerging environmental substances in Europe (EU NORMAN network), such chemicals can be defined as substances that have been detected in the environment. They are currently not included in routine monitoring programs at the European level and whose fate, behavior, and (eco)toxicological effects are not well understood [2,3]. The emerging pollutants are not included in routine environmental monitoring. However, they may be candidates for future regulation/legislation due to their adverse effects and/or persistency. This regulation will be depending on research works on their (eco)toxicity, potential health effects and public perception and monitoring data regarding their occurrence in the various environmental compartments [3].

1.1.1 – PPCPs

Many thousands of PPCPs, which include pharmaceutical drugs, cosmetics, food supplements and other personal care products, are used worldwide. These products are emerging environmental pollutants due to their inherent ability to induce physiological effects in humans and animals, even at low doses [4]. PPCPs can be, for example, antibiotics, anti-inflammatories,

antiseptics, analgesics, antidepressants, stimulants, cosmetics, excipients, essences, parabens, fragrances, disinfectants, and sunscreens [4]. Unfortunately, after use, these products are disposed in the environment, usually in low doses, without any kind of treatment. Also, a cumulative effect is often observed because standard treatments do not easily degrade them. This widespread and continuous release to the environment has been attracting an increasing concern among the scientific community, media and the public in general [5]. Since most of the PPCPs have polar chemical characteristics, they are not easily adsorbed in the subsoil. These pollutants will reach groundwater aquifers through contaminated surface water, and consequently they will be able to reach potable water systems [6,7]. These non-degraded PPCPs have become one of the biggest problems of contamination of water resources.

The existence of PPCPs in the environment was confirmed for the first time in the 80s [8] and since then, several reports have demonstrated their presence in the effluents of wastewater treatment plants (WWTP), rivers, lakes, groundwater and even in bottled waters [6,9]. Once these pollutants are not easily removed, their potential long-term effects on wildlife and humans it is of great concern. For instance, certain antibiotics can cause irreversible changes in the genomes of microorganisms, creating new resistance to their action. For example, Varela *et al.* [10] reported a vancomycin resistant *Enterococci* (VRE) study, from hospital effluents and urban wastewaters. Vancomycin is an antibiotic used to treat a number of bacterial infections. They demonstrated that hospital effluents could provide VRE to an urban wastewater treatment plant. Once the effluent is received, the multidrug resistance phenotypes, observed in clinical isolate and hospital effluents, can survive to the wastewater treatment, and they will be detected in the final effluent. These multidrug resistance phenotypes contribute to increasing the risk of spread vancomycin multidrug resistance to the environment [10].

For pollutants removal, different methodologies can be used, such as physical, biological and chemical methods. These methods include coagulation, flocculation, sedimentation, filtration or nano-filtration, flotation, activated carbon adsorption, nitrification, biological filters, membrane bioreactors, biological nutrients removal, microbiological degradation, chemical oxidation (*e.g.*, ozonation, ultraviolet and/or hydrogen peroxide advanced oxidation process (AOPs)), membrane filtration, reverse osmosis, chlorination and UV disinfection [11,12]. Biodegradation, photodegradation and other abiotic transformation processes such as hydrolysis, may reduce concentrations of PPCPs in the environment and result in partial loss and mineralization of these compounds [4]. However, for an efficient wastewaters' treatment a combination of different methods, it is frequently required, since the use of a single method, it is rarely satisfactory. For example, the industrial wastewater treatment plan is done using a

combination of biological and chemical treatment methods, in order to comply with the standards for discharge of treated effluents [13].

The biological treatment of municipal wastewater involves the coagulation and removal of non-settleable colloidal solids to reduce the organic content and nutrients such as nitrogen and phosphorus. These are performed using a variety of microorganisms, mainly bacteria (may have 300 species present). The predominant group of bacteria used in this context are heterotrophic. They feed primarily on organic carbon molecules. Inorganic matter is absorbed by autotrophs, such as ammonia-oxidizing bacteria, which oxidize ammonia into nitrite. Heterotrophs often compete with autotrophs, which have lower growth rates and are often more sensitive to process conditions and variations [14]. These processes are usually influenced by pH, temperature, and redox potential [15]. However, on a relative scale, biodegradation can be important, for instance, to naproxen and ibuprofen removal, but only moderately for caffeine. In contrast, for other PPCPs, for instance, diclofenac, ketoprofen, amoxicillin, clarithromycin, triclosan, sotalol, clofibric acid, and carbamazepine, it plays only a relatively minor role [15]. For example, emergent pollutants' removal has been evaluated by reverse osmosis, ozonation and membrane bioreactors. However, these processes are not attractive because none of them show satisfactory results [16]. For example, diclofenac (DCF) was shown to be significantly biodegraded only when the sludge retention times are higher than 8 days, and carbamazepine, which is hardly biodegradable, is only poorly eliminated, independent on hydraulic retention times in WWTP [16]. DCF (illustrated in Figure 1.1) is a well known anti-inflammatory pharmaceutical product frequently detected in wastewaters, effluents and surface waters [14]. This pharmaceutical has been recently included in the list of substances in the EU that requires environmental monitoring in the member states. DCF harmfully affects several environmental species, even if in concentrations lower than $1\mu\text{g L}^{-1}$ [14].

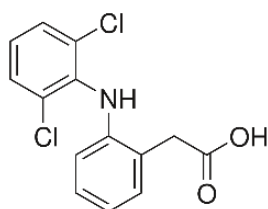


Figure 1.1 - Schematic representation of diclofenac molecule.

Physical-chemical processes, such as coagulation, flocculation and flotation, can be used to agglomerate fine particles and colloids into larger particles for reducing turbidity, natural organic matter and other soluble organic and inorganic pollutants present in the wastewater.

These physical-chemical methods have been reported for the elimination of several pollutants, including DCF, carbamazepine, ibuprofen and naproxen. However, sometimes their total removal from wastewater usually requires posterior treatments [17,18].

For example, using a nitrifying-denitrifying process in a wastewater treatment plant, only 82% and 68% of ibuprofen and naproxen (of an initial concentration of 10 ppb in the effluent) were removed, respectively. Carbamazepine (20 ppb) and diazepam (20 ppb) were removed less than 10%. However more than 300 days were required for the total removal of a 9 compounds mixture from the effluent [19].

The pollutants' photolysis degradation by sunlight action can be an attractive alternative and low-cost methodology; however, it strongly depends on sunlight availability, light intensity and penetration/attenuation by the water depth, PPCPs' absorbance spectra and quantum yield.

Consequently, it is urgent to develop new methodologies that provide high pollutants removal efficiency at a rational cost. Adsorption processes have this potential since PPCPs removal, if ionic, may occur due to electrostatic interactions. Neutral molecules adsorption can occur *via* weak Van der Waals and electron donor-acceptor interactions. For instance, activated carbon [20], and clay complexes [21], have been recently used to remove PPCPs, such as bisphenol A, carbamazepine, naproxen and clofibric acid, from aqueous streams. Nevertheless, adsorption only influences the distribution of substances between aqueous and solid phases and does not eliminate them. Besides, adsorption is dependent on both hydrophobic and electrostatic interactions of pollutants and adsorbent particles [16].

Recently, the use of nanocrystalline semiconductors on the photocatalytic treatment of wastewaters has generated great interest [22]. There are some interesting reports concerning the effective photocatalytic degradation of pharmaceutical products, for instance ibuprofen [23], ketoprofen [24], methyl-paraben [25], carbamazepine, naproxen, and theophylline [26]. Liang *et al.* [26] reported the degradation of carbamazepine, naproxen, and theophylline (15 ppm) using titanate nanobelts, as photocatalysts, achieving the total theophylline and naproxen drugs removal in 90 min under UV-vis irradiation. However, for carbamazepine the photo-assisted removal was not successfully achieved [26]. Nevertheless, in this study, they did not evaluate the formation and degradation of the by-products, a very important parameter in photocatalytic processes, due to the possibility of products formation even more toxic than the initial ones.

Caffeine, theophylline, and phenol are some examples of the PPCPs that have been often found in wastewaters (Figure 1.2).

Caffeine (1,3,7-trimethylxanthine) is a central nervous system stimulant of the methylxanthine class. This is one of the most popular drugs in the world, and it can be found in coffee, tea,

chocolate, soft drinks and pharmaceuticals. Caffeine is a mild stimulant that helps reduce fatigue. It is also thought to enhance the painkilling effect of acetaminophen. This drug can enter the wastewater through human urine or household plumbing as it is present at an average amount of approximately 360 mg L^{-1} in coffee, tea, and soft drinks. Early reports proved the existence of caffeine in sewage effluent, septic tanks, landfill leachates, and the contamination of surface water by wastewater [27]. So, it is reasonable that groundwater can be contaminated by those potential caffeine sources during natural recycling.

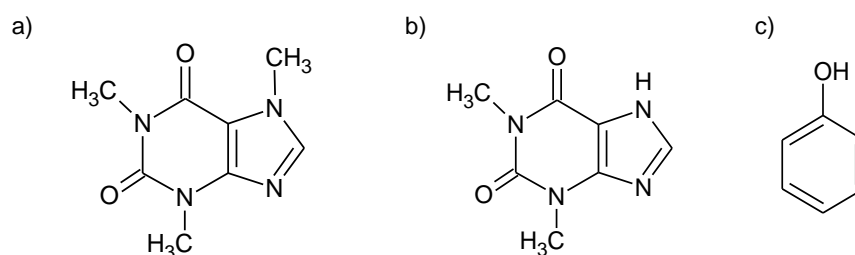


Figure 1.2 – Schematic representation of (a) caffeine, (b) theophylline and (c) phenol molecules.

Theophylline, known as 1,3-dimethylxanthine, it is also a methylxanthine used in therapy for respiratory diseases such as chronic obstructive pulmonary disease and asthma. It was originally used as a bronchodilator and it has been used nowadays to treat airway diseases. More recently it has been shown to have, when at lower concentrations, anti-inflammatory effects in asthma and chronic obstructive pulmonary disease [28]. Theophylline is present in tea and cocoa. It has also been described as a by-product of caffeine photodegradation [29,30].

Phenol is an important aromatic compound often used as a model pollutant in photodegradation catalytic studies due to its relevance as a pollutant itself and also because it is a frequent intermediary product of several other pollutants' degradation processes. It is generally used as a disinfectant, a reactant in chemical analysis, and a raw material of several products, such as herbicides, drugs, paints, cosmetics, artificial resins, pharmaceuticals, organic compounds, fertilizers, pesticides, explosives, industrial dyes and lubricant. It is also the largest used, as an intermediate, in the production of phenolic resins like phenol-formaldehyde ones [31-33].

1.1.2 – Industrial dyes

Dyes become an environmental problem due to the growing use of a wide variety of such compounds in several industries, namely textile, paper, leather, plastics, and cosmetics [1,34,35]. These industries discharge a large number of colored effluents, which are very toxic, and consequently, they can lead to serious ecological problems. Recently it was reported that

more than 700.000 tons of dyes are produced annually, and the chemical class azo represents ~70% of the production due to their high stability, low cost and easy obtainment. Consequently, the final disposal of azo dyes-containing wastewaters has become a serious concern to the environment, considering that only the textile industries release up to 50% of dyes to the aquatic environment through effluents, reaching 10-50 mg L⁻¹ in the aquatic environment [35]. Dyes normally have a synthetic origin and complex aromatic molecular structures, which often make them very stable and difficult to be biodegradable. Most synthetic industrial dyes have an azo bond connected to several aromatic structures. Some, however, are polymeric structures containing metals, for example, chromium, cobalt, nickel, and copper [36,37]. It is also known that wastewaters containing dyes are very difficult to treat since they are molecules resistant to aerobic digestion. This extremely harmful waste not only depreciates the water quality but also elevates their toxicity [38,39]. Dyes generally also exhibit resistance to microbiological attack and temperature, and most of them are not degraded in wastewater treatment plants. These dyes become an integral part of industrial effluents, not only because of the large volume of production but also as a result of their slow biodegradation and discoloration [40,41]. The presence of these colored pollutants in the environment can change the water clarity and appearance and causes considerable non-aesthetic pollution and serious health risk factors, due to their toxicity [1,39]. The impact and toxicity of these pollutants in the environment have been extensively studied. However, the knowledge concerning their carcinogenic, mutagenic, and bactericide properties is still incomplete, owing to the large variety of dyes produced [1,39,42]. Consequently, this is becoming a growing concern for environmentalists and civilians. A sustainable and efficient long-term dye effluent treatment method should be established to reduce or eliminate this problem. Coagulation, flocculation, electrocoagulation, adsorption, ultrasound, membrane filtration, chemical treatment, ozonation, electrochemical destruction, and biological treatment were applied to remove the dyes from wastewater. However, these methods are complicated processes with a high cost and not very efficient. Therefore, researchers have been interested in advanced oxidation processes (AOPs) to dyes removal from the wastewater due to the simplicity and efficiency of this method [43-45]. Since the wastewater composition of the textile industry, it is extremely complex, its treatment is very complicated. Recently, the textile industry conducts on-site wastewater treatment and process water recycling. This wastewater treatment combines biological processes with AOPs [45]. For example, Ray *et al.* recently reported an efficient Indigo carmine dye removal from polluted water using a Ni-modified barium trimolybdate photocatalyst under visible light irradiation [43].

1.2 - Advanced oxidation processes (AOPs)

During the last decade, there has been an increasing interest in the advanced oxidation processes (AOPs) field for the degradation and removal of organic compounds in wastewater. These processes have been proposed as alternative methods for the degradation of pollutants in water, air, and soil [46-50], since they are very effective in the degradation of organic pollutants (in aqueous medium) [41]. Concerning a wastewater treatment plan, the AOPs (Figure 1.3) are extremely effective for the destruction/removal of halogenated hydrocarbons, aromatic compounds, volatile organic compounds, detergents, dyes or pesticides [51,52].

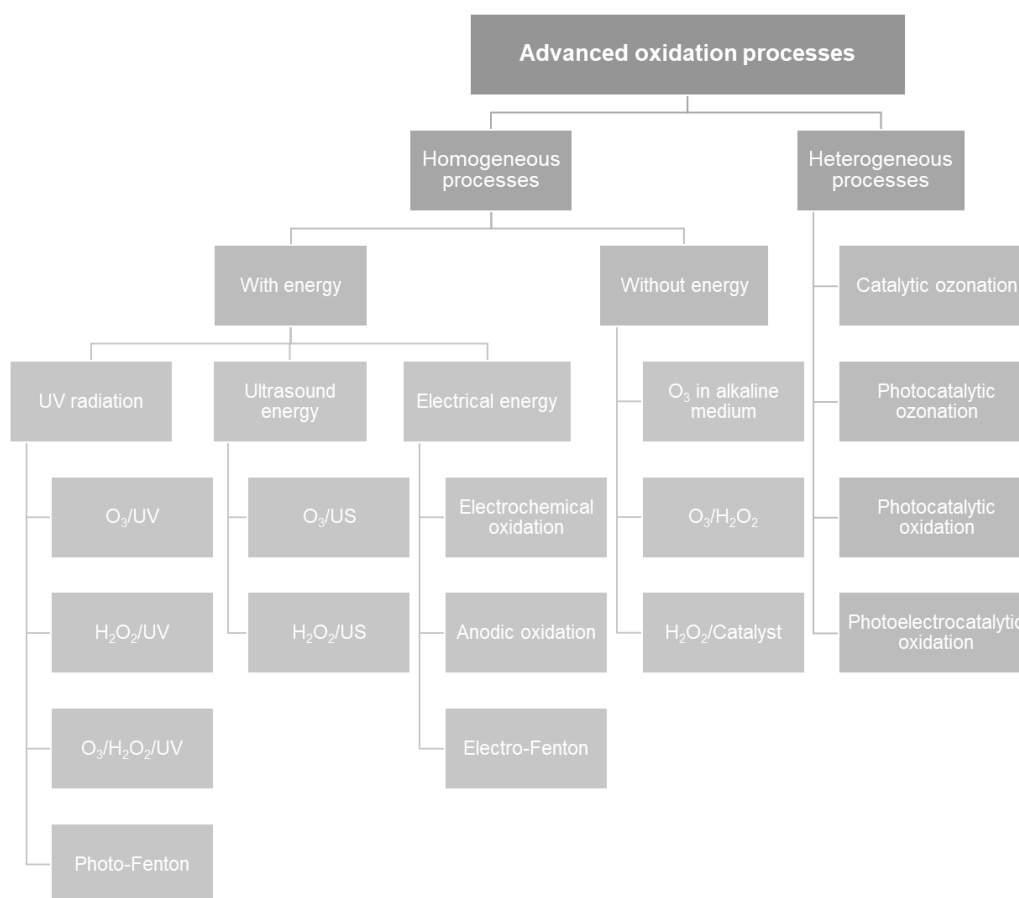


Figure 1.3 – Schematic representation of advanced oxidation processes (AOPs). (Adapted and based on [40,41,54-58])

AOPs (Figure 1.3) are a group of oxidation methods based on the formation of highly reactive species such as hydroxyl radical ($\cdot\text{OH}$) and superoxide radical ($\text{O}_2^{\cdot-}$), which have high oxidizing power, leading to the destruction of organic pollutants [52,53]. These non-selective radicals can readily attack organic molecules by hydroxylation and/or dehydrogenation reactions leading to the pollutants' decomposition. The production of carbon dioxide and water is aimed, or, at least, the conversion to preferably less harmful products [53]. There are several types of $\cdot\text{OH}$ radical

production processes, such as chemical oxidation (ozone, hydrogen peroxide and Fenton reagent), electrochemical, photolysis, photocatalytic, and photoelectrocatalytic oxidation [40,41,54-58].

AOPs have been used in several environmental applications, such as domestic and industrial wastewater treatment, atmospheric pollution reduction, odor control, and soil remediation [59,60].

The AOPs can be classified either as homogeneous or heterogeneous processes, being further divided into photochemical and non-photochemical processes (Figure 1.3). In general, these methods include Fenton reactions, ozonation, photocatalysis, sonolysis, combinations of UV irradiation, and oxidizing chemical agents [60]. Photocatalysis and photoelectrocatalysis have been described as the best and most attractive and promising AOPs for organic pollutants removal.

1.2.1 - Photocatalytic and photoelectrocatalytic methods

Photocatalysis is defined as a change in the rate of a photochemical reaction, by the activation of a photocatalyst (semiconductor) with sunlight or artificial light (ultraviolet or visible radiation). This process allows the degradation of many organic pollutants, with the cleavage of the chemical bonds, until their total mineralization in carbon dioxide and water. Regarding the photocatalytic and photo(electro)catalytic oxidation processes, these methods are very efficient, presenting excellent results in organic compounds degradation, aiming their total mineralization [40,61-66]. They are also very attractive from the economical and eco-friendly point of view, due to, *e.g.*, the possibility of the catalyst reutilization. These methods are based on the use of a catalyst, usually a semiconductor, irradiated with energy equal to or higher than its bandgap energy.

It is known that it is possible to promote the photoelectrolysis of water with an anodic potential [50]. Since this discovery using irradiated titanium dioxide (TiO_2) to produce hydrogen, reported in 1972 by Fujishima and Honda, the photocatalysis has become one of the major topics of interest for scientific researchers [67]. These authors constructed an electrochemical cell (Figure 1.4) in which a TiO_2 electrode was connected with a black platinum electrode through an external load. When the surface of the TiO_2 electrode was irradiated, the current flowed from the platinum electrode to the TiO_2 surface through the external circuit. The direction of the current reveals that the oxidation reaction (oxygen evolution) occurs at the TiO_2 electrode and reduction (hydrogen evolution) at the black platinum electrode [67].

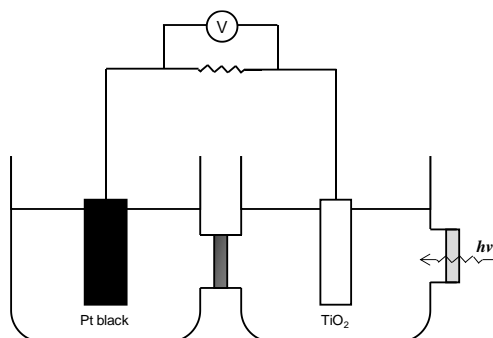
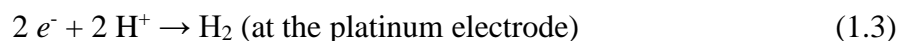


Figure 1.4 – Schematic representation of the electrochemical cell used by Fujishima and Honda, (adapted from [67]).

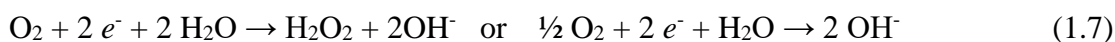
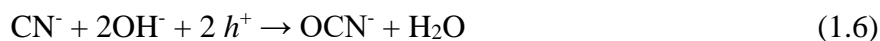
In this system, the authors suggested that water can be decomposed by visible light into oxygen and hydrogen, without the application of any external voltage, according to the following equations [67]:



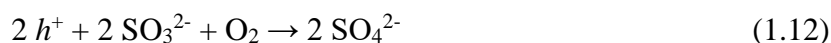
The overall reaction is:



It was also found by Frank and Bard in 1977 [68], that using semiconductor powders (such as TiO_2 , ZnO and CdS) in heterogeneous photocatalytic oxidation processes, it is possible to remove cyanide and sulphite from aqueous solutions. They represented the process of CN^- removal as follows:



and the process of SO_3^{2-} removal as follows:



These works, have promoted the heterogeneous photocatalysis interest in the scientific community, being nowadays one of the most studied technique, in this context. Since then, photocatalysis has been explored to promote organics oxidation, inorganics reduction, disinfection of water containing biological materials and production of electricity and hydrogen [50]. Afterwards, Fujishima reported some photocatalytic applications using TiO_2 , whereby self-cleaning, air cleaning, water purification, antitumor activity and self-sterilizing [69], being nowadays used in water treatment, air purification, destruction of microorganisms, self-cleaning of surfaces and deodorizing effect [63,70,71].

Heterogeneous photocatalysis takes place at the interfacial boundary between two phases (solid/liquid, solid/gas, liquid/gas). Compared to photolysis, the presence of a catalyst typically accelerates the rate of the reaction, increasing the efficiency of the overall process [72].

Photoelectrocatalysis combines, in general, photochemical and electrochemical methods, promoting the interaction of light with electrochemical systems. In the photoelectrocatalytic oxidation, the catalytic process can be improved using the photocatalyst as a photoanode, with a constant potential or current application under UV-vis or visible light irradiation, creating a potential gradient that enhances the e^-/h^+ separation. With these e^-/h^+ separation, there is an increase in the efficiency of the photocatalytic process, since it reduces the charges recombination in the semiconductor, thus increasing the lifetime of the e^-/h^+ pair.

• Photocatalytic process

The photocatalytic process occurs by the irradiation of the semiconductor, as illustrated in Figure 1.5.

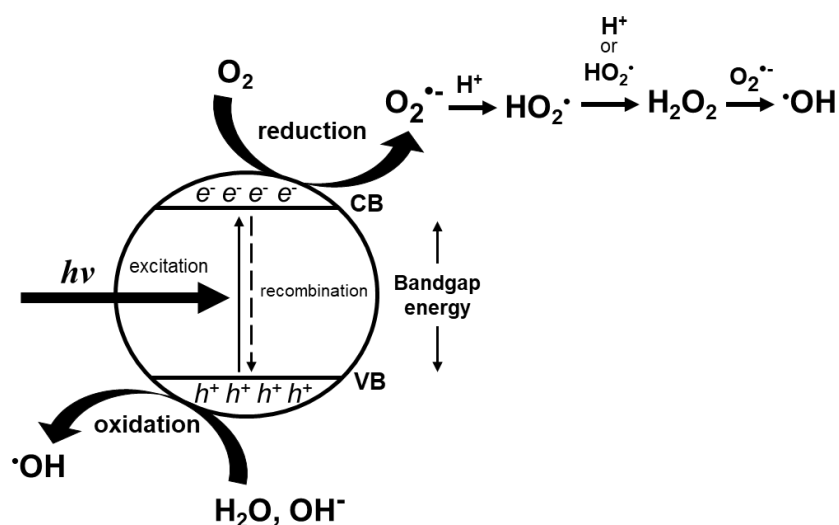


Figure 1.5 – Schematic representation of a semiconductor when irradiated with $h\nu$ energy.

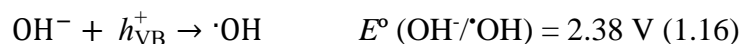
In this process, under irradiation, the semiconductor activation occurs due to the absorption of photons with energy equal to or higher than the bandgap energy ($h\nu \geq E_g$). The bandgap, E_g , is the energy between the semiconductor valence band (VB) and conduction band (CB), (see section 1.5 for further details).

Electron-hole charge carriers (e^-/h^+) are formed due to the energy absorption (as shown in equation 1.13), with the electrons from the top of VB being transferred to the CB (e_{CB}^-), creating holes (h^+) in the VB (h_{VB}^+) [41,72,73]. The e^-/h^+ pairs can participate directly in redox reactions at the semiconductor surface and they can also produce radicals that contribute actively to the organic pollutants' degradation [53].

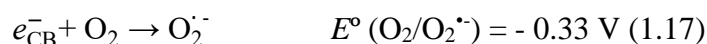


The photo-generated electrons are involved in reduction processes while the holes are consumed in the oxidation process of chemical species at the semiconductor surface.

Considering the pollutants photo-assisted degradation, the organic species can be directly oxidized by the photogenerated h^+ up to their complete mineralization. These holes can also react with adsorbed water molecules (or hydroxyl ions) on the semiconductor surface to form the strong oxidant $\cdot\text{OH}$ radical, as shown in equations (1.14) to (1.16) at the redox potential in V in reference to normal hydrogen electrode (NHE). This radical can be, afterward, involved in the mineralization of the organic pollutants [74-77].

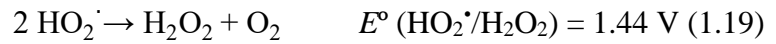
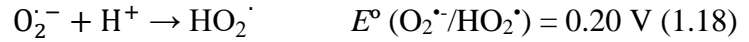


Depending on the CB energy, the photo-transferred electron can react with O_2 producing the superoxide radical $\text{O}_2^{\cdot-}$ as shown in equation (1.17) [1,75,77]:



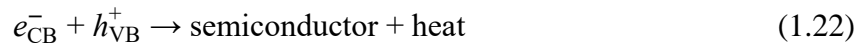
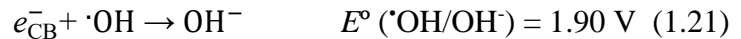
Other reactive species, such as H_2O_2 and hydroperoxyl radical HO_2^{\cdot} , can be produced *via* equations (1.10) and (1.11). Furthermore, additional $\cdot\text{OH}$ radicals' formation may also occur

according to equations (1.10) to (1.12) [74,75]. The production of H₂O₂ from molecular O₂ (E° (O₂/H₂O₂) = 0.695 V vs. NHE) [76,79], can be observed following the equations 1.17 to 1.19, and subsequently the H₂O₂ ⇒ ·OH reduction reaction (E° (H₂O₂/·OH) = 0.38 V vs. NHE) [76,78,79], as represented in equation 1.20.



In the presence of an organic compound, like an emergent pollutant, the ·OH and O₂^{·-} radicals, H₂O₂, and e⁻/h⁺ active species can contribute to their total mineralization [74,80].

Nevertheless, the promoted e⁻ is an unstable specie of an excited state and tends to return to the ground state either with adsorbed ·OH (equation (1.21)) or preeminently by recombination with the unreacted h⁺ (equation 1.22) [75,81-85]:



The reaction in equation (1.22), represents the main drawback for the efficient use of absorbed photons in the classical photocatalysis, *i.e.*, e⁻/h⁺ recombination. To overcome this, several strategies have been studied, such as a combination of more than one semiconductor material, sensitization, doping, and ion-exchange [79,86,87]. A more detailed discussion of these strategies is included in section 1.5. These approaches create alternative paths for the electron decay to the VB, decreasing the recombination rate by prolonging the e⁻/h⁺ lifetime.

• Photoelectrocatalytic process

To improve the reduction of organic pollutants by photocatalysis, the separation of the charge carriers formed in equation (1.13) has been performed using photocatalysts with a high specific area in suspension in the effluent. Unfortunately, the recovery of these materials after treatment can be complex, being necessary sometimes a post-filtration or centrifugation [75,88,89]. Research efforts to solve this problem have been devoted to the immobilization of photocatalysts onto different substrates [75,88,90,91]. For example, TiO₂ or perovskites on glass substrates [88,92], nanoparticles on polymers [93] and BiOCl and TiO₂ nanoparticles on

cotton fibres [94]. The immobilization of photocatalysts on supports can produce a significant reduction of their active specific surface area with the consequent decrease in pollutant removal efficiency. This efficiency can be strongly improved if the photocatalyst can be deposited onto a conductive substrate that will act as the photo-anode in a photoelectrolytic system leading to a photoelectrocatalytic process configuration [46,75,81,82].

Here, a constant potential or current is applied under the anode irradiated, creating a potential gradient that enhances the e^-/h^+ separation. Therefore, there is an increase in the photocatalytic process efficiency, since this reduces the charge recombination in the semiconductor, by increasing the e^-/h^+ pair lifetime [95-100]. In this case, photoinduced electrons are continuously removed from the anode by the external electric circuit. These inhibit the reactions (1.17) to (1.22), and consequently, there is a higher production of holes, as indicated in equation (1.13) and consequently, a higher formation of hydroxyl radicals as shown in equation (1.14).

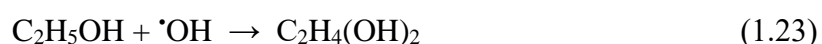
In this way, the combination of photocatalysis and electrocatalysis can promote the organic pollutants' oxidation, increasing its degradation efficiency [41,99,100].

1.3 - Scavengers

Radical scavengers are molecules that can quench specific active species during the degradation processes. Several probes for $\cdot\text{OH}$, $\text{O}_2^{\cdot-}$, H_2O_2 , electrons (e^-) and holes (h^+) have been described in the literature [101-103].

In photo(electro)catalysis it is very important to analyze the active oxidant species involved in the catalytic process. Radical scavengers can be added to the reaction mixture to analyze whether the degradation of the pollutants takes place *via* $\text{O}_2^{\cdot-}$, $\cdot\text{OH}$ radicals or direct electron transfer between the substrate and the positive holes (h^+). Since scavengers are molecules that react readily with the radicals or other oxidizing agents, they are sometimes referred to as antioxidants.

Terephthalic acid (TA), ethanol, isopropanol, methanol, or tertbutanol can be used as hydroxyl radical ($\cdot\text{OH}$) scavengers [79,101,103]. For example, when ethanol is used as $\cdot\text{OH}$ scavenger, it reacts following the equation (1.23):



TA, a well-known hydroxyl radical scavenger, reacts with $\cdot\text{OH}$, forming 2-hydroxyterephthalic acid (HTA), as illustrated in Figure 1.6 [104]. Furthermore, TA is preferably oxidized by hydroxyl radicals and does not react with other radicals, such as $\text{O}_2^{\cdot-}$, HO_2^{\cdot} and H_2O_2 . In this

case, HTA can be detected by fluorescence spectroscopy, since it possesses fluorescent properties.

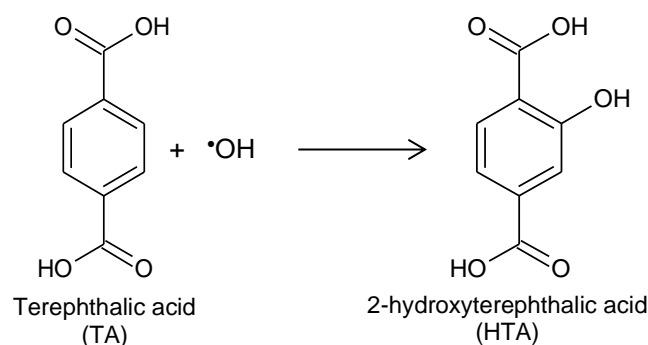
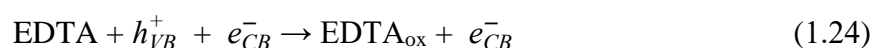


Figure 1.6 - Terephthalic acid conversion in fluorescent 2-hydroxyterephthalic acid (HTA).

Benzoquinone and superoxide dismutase are often used as superoxide radical ($\text{O}_2^{\cdot-}$) scavengers [101,103]. $\text{O}_2^{\cdot-}$ is important in photocatalytic processes, since this radical can react to form singlet oxygen and hydrogen peroxide and the latter producing $\cdot\text{OH}$ [101], as shown above in equations (1.18) to (1.20).

As H_2O_2 scavenger, catalase (*e.g.*, from the bovine liver) can be used. Catalase converts H_2O_2 to water and oxygen, preventing the formation of $\cdot\text{OH}$ [101].

Ethylenediaminetetraacetic acid (EDTA), formic acid, or potassium oxalate can be used as hole scavengers [101,103,105]. In this case, after the semiconductor activation by irradiation, these scavengers trap the h^+ , and the oxidation reactions are no longer possible at the VB (as explained in section 1.5). Therefore, only the e^- already in CB is allowed to react further (equation (1.24)).



Hao *et al.* reported some scavengers' tests for the $\beta\text{-Bi}_2\text{O}_3\text{-NiO/Ni}$ photocatalysts during methyl orange (MO) degradation. It was possible to show that hydroxyl radical and holes species play a major role in the MO oxidation [102]. Kim *et al.* described the photodegradation of rhodamine B (RhB) using BiOCl as a catalyst. Under UV irradiation, $\text{O}_2^{\cdot-}$, h^+ and $\cdot\text{OH}$ species were all of them active for the dye photodegradation. Also interesting is the fact they were able to propose a dye-sensitized photodegradation mechanism, where under visible light irradiation, the active species play roles in the order of $\cdot\text{OH} < \text{O}_2^{\cdot-} \approx h^+$ [103]. This result showed that $\cdot\text{OH}$ and $\text{O}_2^{\cdot-}$ are the most important radicals in the photocatalytic process, being the $\text{O}_2^{\cdot-}$ relevant for increases the $\cdot\text{OH}$ production (equations (1.18) to (1.20)).

Finčur *et al.* showed an alprazolam removal study using ZnO as photocatalyst. They reported that the photocatalysis takes place only *via* hydroxyl radicals [106].

1.4 - Hydroxyl radical production

Since hydroxyl radicals ($\cdot\text{OH}$) are the main responsible for several photo-assisted degradation phenomena, their quantification is very important. Hydroxyl radical demonstrates a very high oxidizing capability ($E^\circ = 2.33$ eV), and it has been responsible for several pollutants' photodegradation processes [79].

Ishibashi *et al.* reported the use of fluorescence techniques for $\cdot\text{OH}$ detection on a photo-illuminated TiO_2 surface using either coumarin or terephthalic acid which readily reacts with $\cdot\text{OH}$ to produce highly fluorescent products [107]. They used TA (in sodium salt) to trap $\cdot\text{OH}$ radicals to produce fluorescent intermediates, namely HTA. The authors also use coumarin (in aqueous media) to trap $\cdot\text{OH}$ radicals. This forms only one monohydroxylated isomer (7-hydroxycoumarin). However, this product has a lower fluorescence than the HTA, being harder to detect. In this study, they reported the TA degradation process at different concentrations and concluded that, for concentrations below 10^{-3} mol dm $^{-3}$, the preferential degradation mechanism is the one shown in Figure 1.6. For higher TA concentrations, competition between the hydroxyl radicals produced and the photogenerated holes at the catalyst surface was observed, so it was concluded that the ideal TA concentration is 10^{-3} mol dm $^{-3}$ [107]. Since 2008, more researchers adopted the TA fluorescence probe method to determine the $\cdot\text{OH}$ radical formation and the semiconductor photocatalytic activity [108-112]. Nowadays, TA is widely used as a probe molecule for quantification of the important $\cdot\text{OH}$ radicals generated from photocatalysts [107,112,113].

This method has been used in radiation chemistry, sonochemistry, and biochemistry for the detection of $\cdot\text{OH}$ generated in water [107]. Ishibashi *et al.* adapted the use of coumarin or terephthalic acid solution to measure $\cdot\text{OH}$ production in TiO_2 photocatalysis. As mentioned, this method relies on the fluorescent signal generated by the hydroxylation of terephthalic acid. Using this technique, the detection of $\cdot\text{OH}$ generated at the water/ TiO_2 interface, it was suggested. In this context, the fluorescence method is rapid, sensitive, specific, and needs only standard instrumentation. Once formed, the fluorescent product is stable and does not affect the normally occurring $\cdot\text{OH}$ reactions [107].

Although TA is an efficient probe for the detection of $\cdot\text{OH}$ radicals, it is also a pollutant by itself. TA is widely used as a raw material to produce polyester fiber, polyethylene terephthalate (PET) bottles, PET films, engineering plastics, and medicines [111]. In 2013, polyester fiber

and PET bottle resin accounted for 93% of global TA demand. TA is toxic and known as an endocrine disruptor. Besides, it may also interfere with the reproductive system and normal embryonic development of animals and humans [111]. Traditional aerobic biological treatment methods are slow and inefficient for TA degradation [111]. Therefore, some authors proposed a photocatalytic degradation mechanism for this compound. The reported intermediate products are aromatic and aliphatic compounds, such as HTA, 4-hydroxybenzoic acid, benzoquinone, benzene and formic, acetic, oxalic, maleic, and fumaric acids [107,111-115]. Although the fact that TA is a toxic pollutant and other probes can be used as $\cdot\text{OH}$ scavengers, TA degradation still one of the best methods for $\cdot\text{OH}$ quantification, during the irradiation of a semiconductor, due to the experimental process facility and their high efficiency and selectivity.

1.5 - Semiconductor materials in photocatalysis

Semiconductor materials are crystalline solids with electrical conductivity between conductors (metals) and insulators, in which the electric charge carrier density can be changed by external means. In a semiconductor, the electrical resistance decreases as temperature increases, which is the opposite behavior in metal. In Figure 1.7 it is shown the energetic band structure for the conductive, semiconductor, and insulator materials.

Semiconductors materials can display a range of useful properties such as current can pass easily, variable resistance, and sensitivity to light or heat [116]. Since their electric properties can be modified by doping or by application of an external electrical field or light, devices containing semiconductors can be used for amplification, switching, and energy conversion [116]. Practical applications of the semiconductors include laser diodes, electronic devices, solar cells, microwave-frequency integrated circuits, and photocatalysis.

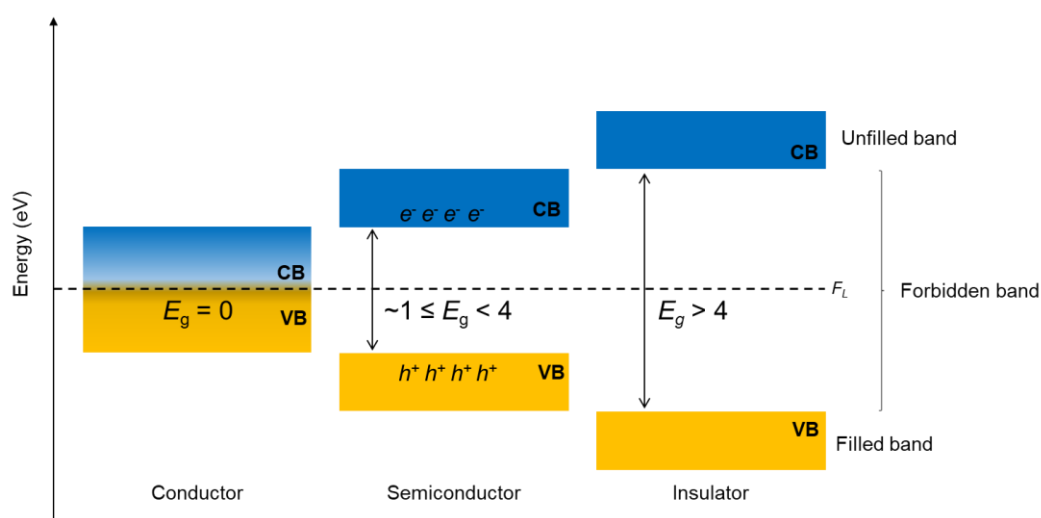


Figure 1.7 - Band structure energy for conductive, semiconductor and insulator materials.

In a solid semiconductor, the band of higher energy filled with electrons is the VB, and the band with the lowest unfilled energy is the CB. The range energies between VB and CB are defined as a forbidden band and delimits in which electrons are not allowed to transit [117]. The range of E_g allows distinguishing conductive materials from semiconductor and insulator materials (Figure 1.7). In conductive materials, the VB overlaps with the CB ($E_g = 0$ eV). Therefore, there is a high density of electrons that contribute to the high electrical conductivity that characterizes these materials. For semiconductor and insulator materials, the $E_g > 0$ eV, with the bandgap energy being substantially higher for isolating materials, typically $E_g > 4$ eV. The semiconductors can be activated either by thermal excitation or by absorption of radiation energy equal or higher than E_g ($E \geq E_g$), giving rise to excited states, as illustrated in Figure 1.7. The band structure of a crystalline semiconductor material can be described by the relationship between energy E and the k -vector (Figure 1.8). Thus, the minimum energy states of the conduction band and the maximum energy of the valence band are characterized by an energy value and a k -vector.

In a direct bandgap semiconductor, the maximum VB and the minimum CB occur for the same k -vector ($\Delta k = 0$). In this case, the transition between two levels is allowed and corresponds to bandgap energy, so the electron of VB is transferred to CB with the same momentum. Therefore, no momentum transfer is required to launch the electron from the VB into the CB [118].

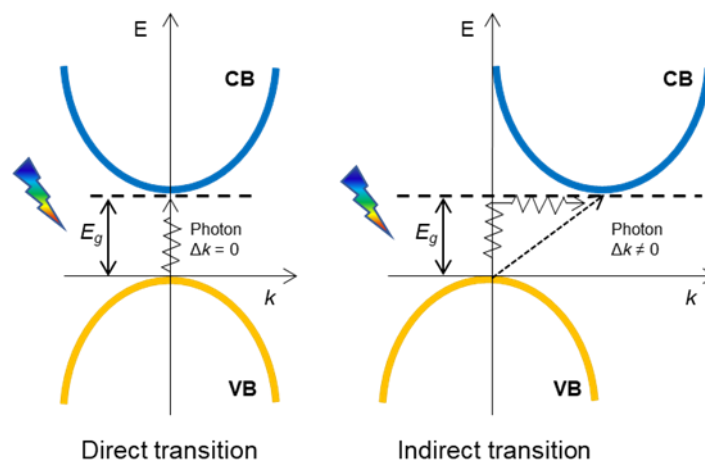


Figure 1.8 – Schematic representation of the excitation process in semiconductor materials, from the top of the valence band to the bottom of the conduction band, by photonic absorption, following a direct and an indirect transition process.

In an indirect bandgap semiconductor, the maximum VB and the minimum CB occur for different k -vector, and thus it is given without conservation of linear momentum since k is changed ($\Delta k \neq 0$). Therefore, a fast electron has to transfer momentum to an electron in VB in

order to excite it into the conduction band. This also implies that the cross-section for interband transitions is lower than in the case of direct semiconductors [118,119].

If semiconductor materials are aimed for photocatalysis, they can be modified by different approaches, including doping, synergetic combination with other semiconductors (formation of composites), or surface sensitization [86,120,121]. This can open the possibility to control the properties of the semiconductors, for instance, by introduction levels in the forbidden zone, which can decrease the e^-/h^+ recombination. This intermediate energy level can also act as either an electron acceptor or a donor, which allows the semiconductor to absorb visible light [120]. For example, wide bandgap semiconductors (such as ZnO and TiO₂) can be photoactivated by visible illumination, after defect engineering or doping. Defect engineering involves the controlled introduction of native defects, such as vacancies or interstitials, while doping implies the controlled incorporation of impurities into the crystal lattice [121]. Doping can be achieved, during semiconductor synthesis using a trace element (*e.g.*, metal) or a chemical doping agent (*e.g.*, non-metal). The dopant will be incorporated into the crystalline structure, to give the material different electrical properties than the pure semiconductor. Doping with metals can introduce extra levels in the forbidden band (as mention above), and doping with non-metal, such as N, F, C, or P, can extend the light absorption of the semiconductor into the visible region [120]. For instance, anion doping could affect the TiO₂ conduction band, which has the contribution of Ti 3*d*, 4*s*, and 4*p* orbitals. In this case, the anion doping usually changes the valence band position and shifts it upward to narrow the bandgap of TiO₂. For example, N is the most suitable doping element as its *p* orbitals could contribute to shifting the VB due to the synergic action with the O 2*p* orbitals, which can narrow the bandgap of TiO₂ by shifting the VB upward [120].

There are two types of intrinsic semiconductor materials, *n*-type and *p*-type. The semiconductor type depends on the position of the Fermi level (F_L). If the F_L is near to the conduction band, it is an *n*-type semiconductor. On the other hand, *p*-type is a semiconductor with the Fermi level close to the valence band. For example, TiO₂ displays *n*-type semiconducting properties due to a tendency for oxygen deficiency which manifests itself in the formation of either oxygen vacancies or titanium interstitials; both are donor-type defects [122]. ZnO is also an *n*-type semiconductor, due to the majority of carriers on this material are electrons. However, NiO is a *p*-type semiconductor once have holes as the majority carriers. For instance, Cu₂O for example is an intrinsic *p*-type semiconductor [123]. However, the type of intrinsic semiconductor materials can be changed by doping, forming extrinsic semiconductors. Semiconductors can be *n*- or *p*-doped (Figure 1.9). *n*-Type semiconductors are

created by doping an intrinsic semiconductor with an electron donor element (n - comes from the negative charge of the electron). Here, the electrons are the majority carriers, and holes are the minority ones. In this case, the Fermi level (F_L) is higher than that of the intrinsic semiconductor and lies closer to the conduction band than the valence band, as depicted in Figure 1.9.

p -Type semiconductors can be formed by doping with an electron acceptor element (p - refers to the positive charge of a hole). In opposition to n -type semiconductors, the p -type has a larger hole concentration, which is the majority charge carriers. For p -type semiconductors, the F_L is below the intrinsic F_L and lies closer to the valence band than the conduction band, as shown in Figure 1.9.

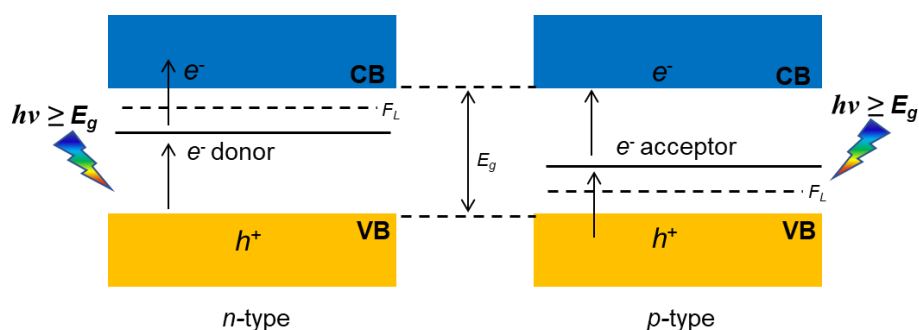


Figure 1.9 – Representation of n - and p -type doping in a semiconductor.

Several semiconductors including TiO_2 , ZnO , CdS , WO_3 , ZrTiO_4 , SnO_2 , CeO_2 and CuO , have been used, for photo(electro)catalysis [124-129].

Recently other semiconductor materials with improved photocatalytic response have been reported, such as carbon nanotubes (CNT) [130], titanate elongated nanoparticles (TNP) [79,87], transition metal sulphides (*i.e.* Bi_2S_3 , ZnS and Ag_2S) [79,131], spinels, perovskites, zeolites or activated carbon [92,132-134]. In addition, the synergetic combination of two or more components, for example in $\text{TiO}_2/\text{Ag}_2\text{CrO}_4$, [135] $\text{ZnO}/\text{Ag}/\text{Ag}_2\text{WO}_4$ or $\text{Fe}_3\text{O}_4/\text{ZnO}/\text{CoWO}_4$ [136,137], it allows the enhancement of photocatalytic properties due to the absorption improvement in the visible range and also the decrease on the charge carriers recombination. For instance, in order to have active photocatalytic materials under visible light, a proficient way to extend the absorbance of TiO_2 to visible light can be the development of heterojunctions of different semiconductors. These semiconductor combinations, such as $\text{Fe}_2\text{O}_3/\text{TiO}_2$, $\text{TiO}_2/\text{SnO}_2$, ZnO/TiO_2 , and WO_3/TiO_2 , have been shown synergetic photocatalytic effects when used for pollutants degradation [138-141].

1.5.1 – Titanium dioxide (TiO₂)

Titanium dioxide (TiO₂) or titania, has become a reference as a photocatalyst, due to its properties: high photocatalytic activity, abundance, low cost, chemical stability, low toxicity, strong oxidizing activity and high reactivity [62,120,142]. This semiconductor may have minor applications other than photocatalysis, such as in photovoltaic cells, sensors, or in cosmetics as white pigment [62,143,144].

TiO₂ can have three different crystalline phases, *brookite*, *rutile*, and *anatase*. *Anatase* structure is considered the most efficient for photocatalytic applications due to its high electron mobility, low dielectric density, and low dielectric constant, high hydroxylation capacity. Also, the VB and CB positions, 2.14 and -1.06 eV, respectively, can promote the formation of reactive oxygen radicals [77,145].

As an *n*-type semiconductor, with a Fermi level closer to the conduction band, the anatase phase of TiO₂ has an $E_g \sim 3.2$ eV. Therefore, it is more efficient in the UV than in the visible range. Nevertheless, TiO₂ presents two important drawbacks for a wide practical application in photo-assisted processes. The high rate of recombination of photogenerated electron-hole pairs within the semiconductor, it is a disadvantage of this material. Its high reported value of E_g is another drawback of TiO₂, due to the low absorption of radiation at wavelength values below 388 nm ($E = 3.2$ eV). This is the main disadvantage of TiO₂ application in solar photocatalysis since the radiation below 400 nm (UV light) represents only $\sim 4\%$ of the sunlight that reaches the Earth's surface. Due to this, one of the main challenges to developing economically attractive photocatalytic materials broadens the photocatalyst response into the visible-light region. Consequently, it is desirable to develop photocatalytic materials that are active under visible light, since this corresponds approximately to all solar spectrum. Therefore, the synthesis of TiO₂-based materials, such as titanate elongated nanoparticles (TNP), with a broader range of light absorption and a lower charge recombination rate, is an important achievement towards the development of successful photoactive materials [146].

1.5.2 – Elongated titanate nanoparticles (TNP)

Stimulated by the discovery of carbon nanotubes, one-dimensional nanostructured materials have become an intense research topic in nanotechnology owing to their unusual properties and a wide variety of potential applications. In contrast with carbon nanotubes, titanate, and titanium oxide nanotubes are readily synthesized using simple chemical methods and low-cost materials [147].

The interest in elongated titanate nanoparticles (TNP) appeared in 1998 after Kasuga *et al.* described an alkaline hydrothermal synthesis methodology to produce these nanoparticles. Kasuga *et al.* reported the synthesis of a new class of materials with a TiO₂-like crystalline structure, mesoporous morphology, and a higher surface area ($\sim 400 \text{ m}^2 \text{ g}^{-1}$) compared to TiO₂ nanoparticles (usually between 20 and 50 $\text{m}^2 \text{ g}^{-1}$) [148,149]. These new materials, TNP, combine the properties and applications of conventional TiO₂ nanoparticles, such as photocatalytic activity, stability, low toxicity, and bandgap energy, with the properties of lamellar titanates such as ion-exchange ability [88,150-152].

• **Synthesis methodologies**

Several methods have been described for elongated tubular nanostructures synthesis, such as sol-gel [153,154], template-assisted [87,151,155], anodic electrochemical oxidation [150,156,157] and hydrothermal treatment [158-162]. However, from those, the popular approaches to titanate elongated nanoparticles production, are the chemical (templating) and electrochemical (*e.g.*, anodization of Ti) synthesis and the alkaline hydrothermal method.

The template-assisted methods make use of the morphological properties of a known and characterized material (template) in order to build materials with a pre-defined morphology by reactive deposition or dissolution. Within this method, a regular and controlled morphology, at both nano- and/or micro-scale, associated with numerous shapes it is possible *via* adjusting the morphology of the template [147]. However, extensive applications of this method may be limited due to the high cost, insufficient characterization of template, and concern over long-term (in)stability of nanotubular products [163-165].

The anodizing approach consists of an electrochemical method for the formation of a layer of oxide on the substrate surface. This method can build highly ordered and crystallized array films of TiO₂-nanotubes immobilized on a titanium foil surface with controllable pore size, good uniformity, and conformability over large areas [166]. So far, many attempts have been successfully devoted to the formation of self-organized and freestanding TiO₂ nanotube arrays [167,168]. The advantage of TiO₂ nanotubes produced by anodization is that they are effectively immobilized on a titanium surface during preparation. As a result, these nanotubes have several possible applications, such as photocatalytic, self-cleaning surfaces or as photoanodes for water splitting, where the efficiency of the photoanodic response depends on the nanotube wall thickness [87].

Several reviews have been published dealing with the details of fabrication, characterization, and applications of nanotubes produced by templating and anodization methods [169-172].

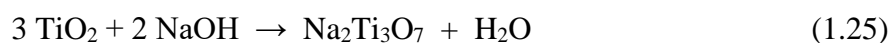
However, the anodizing preparation process suffers from an environmental concern, as the anodization of Ti foil must be processed using highly toxic hydrofluoric acid aqueous solutions [172]. For example, Gong *et al.* reported the preparation of self-organized TiO₂ nanotube arrays by direct anodization of titanium foil in an H₂O–HF electrolyte at room temperature [166]. These nanotubes were oriented in the perpendicular direction to the surface of the electrode, forming a continuous film. The nanotubes were open-end, and while the other end, which was in contact with the electrode, was always closed. For example, TiO₂ nanotubes immobilized on a titanium surface have proven to be promising as photocatalytic and self-cleaning surfaces or as photoanodes for water separation, where the efficiency of the photoanodic response depends on the nanotube wall thickness [87]. In contrast to the templating method using alumina as a template, the TiO₂ nanotubes prepared by anodization are not usually regularly separated from each other. Consequently, there are no well-developed hollows between the nanotubes, having an agglomerate of them in the same direction.

Hydrothermal synthesis is a common method widely used in industry to prepare catalysts. This method has been adapted to produce high yields of elongated titanate nanoparticles with pore and unique nanotubular structures [87,148,172].

• Hydrothermal synthesis

The alkaline hydrothermal synthesis is one of the most widely used for TNP production (such as TNT, TNW, TNF). In 1998 the pioneers Kasuga *et al.*, reported the work of synthesis of TNT using TiO₂ (*anatase* phase) as precursor at 110°C for 20 h in aqueous NaOH solution (10 mol dm⁻³). They proposed that titanate nanotubes were grown by the connection between the two ends of Ti–OH forming sheets. This implied that the ultimate nanotubes were seamless, and the acidic washing procedure played an important role in the formation of nanotubes [173], concluding that the nanotubes were formed during the process of washing the treated with HCl aqueous solution [148]. However, Du *et al.* observed, as later reported, the existence of titanate nanotubes even before the acidic washing treatment [173,174].

The nanotubes prepared by Kasuga *et al.* method, had a surface area of ~ 400 m² g⁻¹ and an average diameter of 8 nm [148]. The authors suggested that the formation of TNT was achieved by the slow dissolution of TiO₂ nanoparticles in a concentrated solution of NaOH, according to equation 1.25.



With the introduction of the alkaline hydrothermal synthesis of titanate nanotubes by Kasuga *et al.* [148], many efforts have been made to adapt this approach to technological processes, allowing an easy and cheap scale-up of industrial production.

Experimentally, the hydrothermal method requires the use of an autoclave with chemically resistant vessels, in order to withstand such a concentrated alkaline solution at temperatures range of 100 – 200°C. This method has the advantage of a single-stage process. In addition, low hydrothermal temperatures are required to achieve the complete conversion of the precursor into elongated titanate nanoparticles (TNP).

TiO₂ *anatase* or *rutile* phases, amorphous TiO_x, and even Ti metal can be used as a titanium source [87]. However, it has been reported that the morphology of the resultant elongated tubular nanoparticles (TNP) is strongly affected by the Ti precursor used. This is not the only parameter that can control the morphology; the TNP formation can also be influenced by the concentration of the alkaline solution, the hydrothermal time and the post-treatment processes (acid treatment) [175]. For example, the ultrasonic treatment of the TiO₂ precursor or an improvement in the fluid flow and mass transport during alkaline hydrothermal treatment, it can modify the length of the TNP. The improvement of the dynamics of nanotube growth, in the axial direction it is a direct consequence of the dissolved titanium (IV) species higher availability. On the other hand, it has been reported that the mean diameter of the nanotubes can be controlled by the synthesis temperature [147].

The influence of the reaction time in the TNT morphology was recently studied by Hfayedh *et al.* [175]. The TNT were prepared using as precursor TiO₂ *rutile* nanoparticles in NaOH (10 mol dm⁻³) at 150°C, and the reaction time was 12, 24, 48, 72, 96, and 120 h. The authors conclude that the obtained nanotubes exhibited a major number of layers and major external diameter, which vary from 3 to 5 and from 7 to 11 nm, respectively, when reaction time increase from 12 to 120 h. Deformations appeared at long reaction times (96 h and 120 h). For 120 h of reaction, a deformation of some nanotubes occurred, and nanoribbons were formed, obtaining a mixture of nanotubes and nanoribbons [175].

Identically, Ylhäinen *et al.* [195] reported, for the first time, the TNP preparation using an amorphous precursor instead of crystalline TiO₂ as starting material, using temperatures ranging from 130 to 220°C, varying the reaction time between 12 and 72 h. This new and swift hydrothermal chemical route to prepare TNP, uses a commercial solution of TiCl₃ as titanium source to prepare an amorphous precursor, circumventing the use of hazardous chemical compounds. The authors reported that for the samples prepared using $t < 12$ h no crystalline

material was obtained. On the other hand, no changes on the XRD patterns of samples prepared for 36, 48, and 72 h were obtained, as shown in Figure 1.10.

However, these samples have a distinct structural feature compared to those prepared for 12 and 24 h: by increasing the reaction time from 24 to 36 h and above, the diffraction peaks are well defined and new peaks (at $2\theta \sim 35 - 24^\circ$) are detected (Figure 1.10).

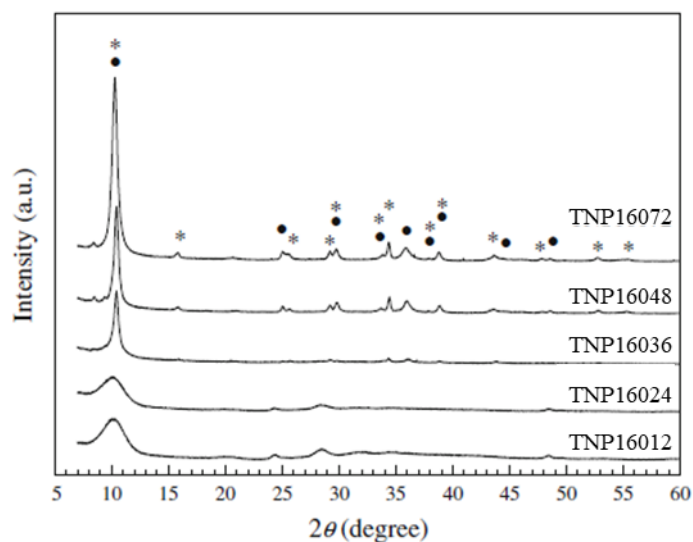


Figure 1.10 – XRD patterns of the titanate nanostructures prepared at 160°C and different reaction times: 12 h (TNP16012), 24 h (TNP16024), 36 h (TNP16036), 48 h (TNP16048) and 72 h (TNP16072). * $\text{Na}_2\text{Ti}_3\text{O}_7$, JCPDS-ICDD file No. 31-1329; • $\text{H}_2\text{Ti}_3\text{O}_7$, JCPDS-ICDD file No. 41-192, reported by Ylhäinen *et al.* [195].

The authors concluded that the reaction time has a strong influence on the TNP morphology, as can be seen in Figure 1.11.

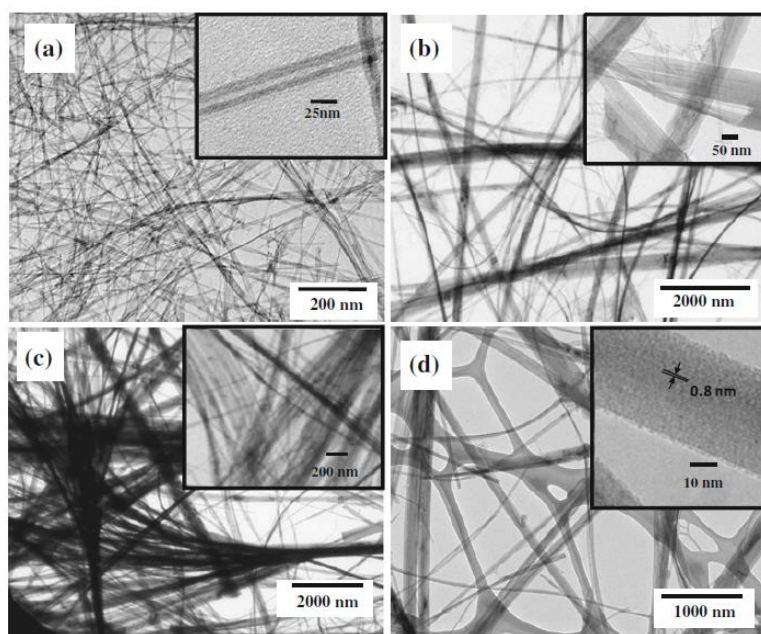


Figure 1.11 – TEM images of titanate nanostructures prepared at 160°C during (a) 24 h, (b) 36 h, (c) 48 h, and (d) 72 h, reported by Ylhäinen *et al.* [195].

For a reaction temperature of 160°C, the sample synthesized with $t = 24$ h is very homogeneous and consists of thin tubular nanoparticles, while the sample prepared at $t = 36$ h shows a mixture of nano- and micro-scale particles. Broomstick-like large bundles characterize the sample prepared at $t = 48$ h. Increasing further the reaction time up to 72 h, the broomstick-like large bundles lead to TNP, yet with a larger diameter than the samples prepared at $t = 24$ h. For reaction temperatures varying from 130 to 160°C, no significant differences were observed in the length/diameter aspect ratio of the samples, all of them with very similar morphology. However, samples prepared at 200 and 220°C for 24 h, larger diameters, in the range 75-100 nm were obtained. They conclude that the best experimental conditions to prepare very homogeneous titanate nanotubular structures with a high length/diameter aspect ratio were at 160°C and 24 h [195].

The TNP preparation process presented in this work, resulted from a procedure developed and previously optimized [176]. Unlike the alkaline hydrothermal synthesis reported by Kasuga *et al.* [148], whose TNP are synthesized from TiO₂ nanoparticles, the synthesis used during this work innovates by the elimination of the TiO₂ requirement to obtain titanate nanowires (TNW). It is well known that the use of distinct commercial sources of TiO₂ powders, or of those synthesized in distinct research laboratories often leads to nanostructures with different microstructural characteristics, making the reproducibility of the TNP synthesis process highly dependent on the TiO₂ starting material and far from being well established [195].

During this work, two different ways were proposed starting with an amorphous precursor to obtain TNW and starting to TiO₂ nanoparticles to obtain titanate nanotubes (TNT). All procedure details are described in Chapter 9. This synthesis methodology is an efficient, low cost and easily scalable technique for TNP production therefore it can be very attractive for industrial applications.

• TNP crystalline structure

It has been observed that the chemical composition of TNP strongly depends on the experimental conditions used during synthesis. In order to explain the atomic organization of TNP, some crystalline structures for these materials have been presented and discussed in the literature such as lepidocrocite Na_xTi_{2-x/4}□_{x/4}O₄ or H_xTi_{2-x/4}□_{x/4}O₄, with □ : vacancy in the crystalline lattice, Na₂Ti₃O₇, H₂Ti₃O₇, Na_{2-x}H_xTi₃O₇, H₂Ti₄O₉(H₂O) or H₂Ti₂O₄(OH)₂/Na₂Ti₂O₄(OH)₂/Na_{2-x}H_xTi₂O₅(H₂O) [151,152,177].

The most accepted by the scientific community, for alkaline hydrothermal synthesis processes, is Na_{2-x}H_xTi₃O₇ ($0 \leq x \leq 2$) chemical structure of TNP [146,151,152,178,179]. Figure 1.12

shows a schematic representation of the crystallographic structure of TNP ($\text{Na}_2\text{Ti}_3\text{O}_7$ and $\text{H}_2\text{Ti}_3\text{O}_7$). The Na^+/H^+ concentration can be adjusted after synthesis by Na^+/H^+ ion-exchange processes by treatment of the nanoparticles with a dilute acidic solution. In this way, it is possible to explain the general formula: $\text{Na}_{2-x}\text{H}_x\text{Ti}_3\text{O}_7$ with $0 \leq x \leq 2$, where x depending strongly on the TNP washing conditions (or acid treatment).

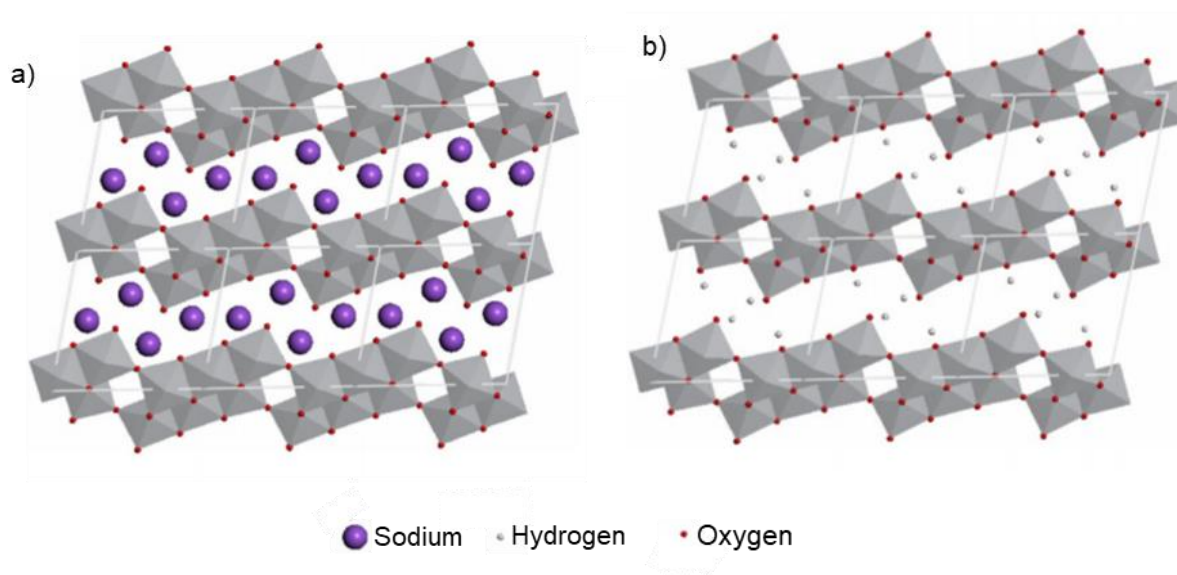
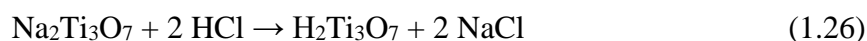


Figure 1.12 - Crystallographic structures of (a) $\text{Na}_2\text{Ti}_3\text{O}_7$ and (b) $\text{H}_2\text{Ti}_3\text{O}_7$ (adapted from [180]).

The $\text{Na}_2\text{Ti}_3\text{O}_7$ conversion to $\text{H}_2\text{Ti}_3\text{O}_7$, which is a related structure, requires an ion exchange process. When $\text{Na}_2\text{Ti}_3\text{O}_7$ is immersed, for example, in diluted hydrochloric acid or nitric acid solution, the Na^+ ions in the titanate matrix are replaced by H_3O^+ or H^+ ions to form $\text{H}_2\text{Ti}_3\text{O}_7$, as shown in equation (1.26) [181].



Through the hydrothermal treatment, shown in reaction (1.25), some of the Ti–O–Ti bonds of the TiO_2 precursor break and a six-coordinated monomer $[\text{Ti}(\text{OH})_6]_2$ is formed and saturated. This monomer is unstable, and it combines oxolation or ololation to form nuclei when they grow. They become thermodynamically stable, and their size exceeds the critical nuclei size [182]. During the growing process, thin nanosheets can be formed and integrated into layer unit cells. The growth of these nanosheets is isotropic, being the growth along the b -axis the fastest, which leads to the formation of 1D $\text{Na}_2\text{Ti}_3\text{O}_7$ nanoparticles. The crystal structure of $\text{Na}_2\text{Ti}_3\text{O}_7$ is monoclinic with layers of $(\text{Ti}_3\text{O}_7)^{2-}$ (or $[\text{TiO}_6]$) octahedral sites with shared edges and vertices, and with Na^+ cations located between the $[\text{TiO}_6]$ layers (Figure 1.12). The high mobility of

these Na^+ ions intercalated is one factor responsible for the high efficiency in ion exchange processes of these materials since they can easily be replaced by other cationic species, including proton (H^+) [180,183]. For example, Bem *et al.* [146] reported the sodium/proton replacement on the titanate nanoparticles prepared using an amorphous precursor (the same used by Ylhäinen *et al.* [196]). They reported that the pH influence in interlayers distance. After an ion-exchange acidic treatment, the interlayer distance in the crystalline structure due to the $\text{Na}^+ \rightarrow \text{H}^+$ replacement changed. They analyzed the TNT preparation at pH 5, 7, and 9. A decrease in the dimensions was observed with the pH decrease, as shown in Figure 1.13. Furthermore, the TNT-pH5 sample (Figure 1.13.(c)) has the lowest interlayers distance due to a complete sodium replacement [146].

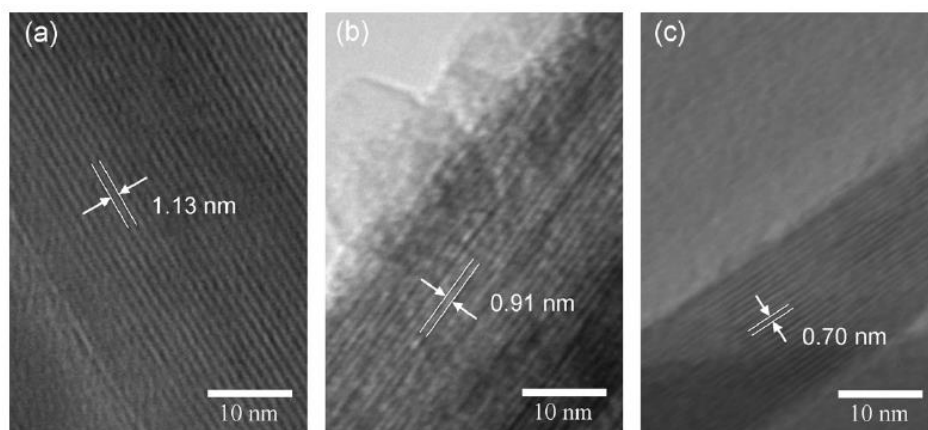


Figure 1.13 – HRTEM images of the (a) TNT-pH9, (b) TNT-pH7, and (c) TNT-pH5, reported by Bem *et al.* [146].

A different optical behavior was observed depending on the Na^+/H^+ samples' content. Marques *et al.* [184] reported the intercalation of Ce^{4+} and Ce^{3+} within the titanate nanotubes layers by the ion-exchange method. Santos *et al.* [185] showed several metals intercalation (Ce^{4+} , La^{3+} , Co^{2+} and Cu^{2+}) in the titanate nanotubes, by Na^+ replacement. The authors used these new materials as catalysts in Knoevenagel condensation. The results showed that the Ce-containing TNT had a catalytic performance for $\alpha\beta$ -unsaturated esters production 5–7 times higher than pure TNT, even after five times of repeated uses, due to the accessibility of both Ce^{4+} species in the interlayers region and CeO_2 nanoparticles distributed on the external walls of this sample [185].

The intercalation of larger species, for instance, organic entities, is possible but is dependent on the ion-exchange ability of the TNP and on the organic molecules size and protonation equilibrium constants. Ferreira *et al.* [186] reported the cationic dyes sensitization of elongated titanate nanoparticles. In this work the intercalation of thionine, methylene blue, crystal violet,

and rhodamine 6G in the TNP materials was studied. The sample with the highest sodium content (NaTNP) was the best dyes up taking material. However, for the protonated titanates (HTNP), only the thionine molecules were incorporated, due to the reduced dimension of the HTNP interlayers [186].

• **TNP morphology**

TNP have been reported in the literature as cylindrically shaped nanotubes with a hollow cavity along its length, and also as nanofibers (TNF), nanowires (TNW), nanorods and nanosheets as illustrated in Figure 1.14 [147].

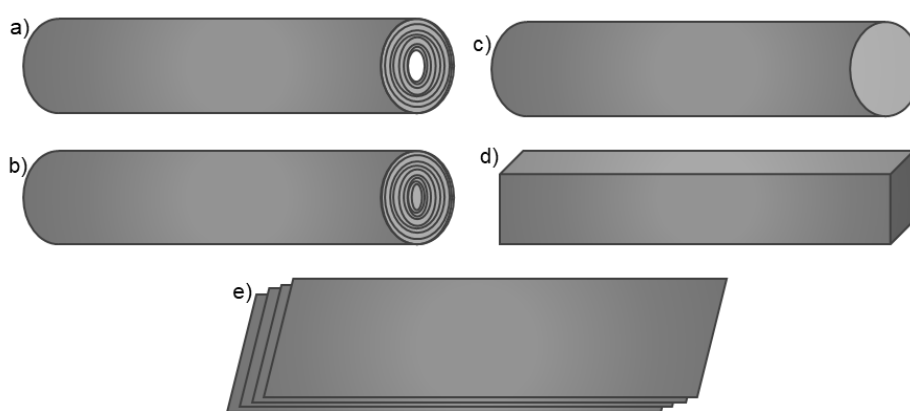


Figure 1.14 – Schematic representation of elongated titanate nanoparticles: (a) multi-wall nanotubes, (b) multiple-wall nanowires, (c) nanorods, (d) rectangular nanofibers and (e) nanosheets.

Titanate nanotubes (TNT) are long cylinders with a central hollow cavity (Figure 1.14(a)). They are always multi-layered walls (the number of layers can change between 2 to 10) and usually straight with a relatively constant diameter. Structurally, nanotubes can be scrolled, “onion” or concentric in type. Occasionally, in a single nanotube, different numbers of layers can be observed in the two walls [147]. This is usually produced by folding nanosheets (Figure 1.14(e)), and there are two types of nanosheets: single-layer nanosheets, which are isolated (100) planes of titanates, or multilayer nanosheets, which are several conjugated (100) planes of titanates. Both types are very thin and could be found in planar or curved shapes, with < 10 nm of thickness and > 100 nm of height and width. Nanosheets are frequently observed in the initial stage of the nanotubes’ preparation or as small impurities in the final product, when obtained through an alkaline hydrothermal process [147].

Nanowires and nanorods are long solid cylinders with a circular base (Figure 1.14(b) and (c)). Usually, nanowires are longer than nanorods. TNW have layered structure (multi-layered

morphology) without a center cavity. Nanorods morphology does not have an internal layered structure.

Nanofibers (Figure 1.14(d)) are long parallel-piped titanates, have length typically in the range of 10 - 100 nm, and tend to have good crystallinity. These are usually produced during alkaline hydrothermal reactions at high temperatures and can be found in straight, as well as curved forms [147].

• **Mechanism of formation**

The mechanism of TNP formation has already been studied by many researchers including Peng *et al.* [187]. A possible formation mechanism in which TiO_2 reacts with NaOH to form $(\text{Ti}_3\text{O}_7)^{2-}$, as an intermediate product, it has been reported.

In general, the process of transformation of TiO_2 precursor to elongated titanate nanoparticles can be considered to take place in several phases. Firstly, partial dissolution of TiO_2 precursor accompanied by epoxial growth of layered nanosheets of sodium trititanates occurs, and after exfoliation of the nanosheets is observed. The crystallization of dissolved titanates to obtain nanosheets result from mechanical tensions, which will induce the curving and wrapping nanosheets to nanotubes, and after that, a growth of nanotubes along the length occurs [87,147]. The single intermediate layer and multi-layered titanates nanosheets have a key role during the precursor transformation under alkaline conditions. These nanosheets can scroll or fold into a nanotubular morphology [147]. There is a strong consensus that this intermediate product has a two-dimensional plate morphology, resulting from the stacking of a reduced number of lamellae, nanosheets. The continued nanosheets' growth tends to curl up on themselves, leading to the formation of nanotubes (Figure 1.15) [188,189]. It has been suggested that the hydrogen deficiency on the surface of $(\text{Ti}_3\text{O}_7)^{2-}$ nanosheets cause asymmetry of charges resulting in oxidation state variations or cation deficiency. This provides the driving force (surface tension) for the separation of the $(\text{Ti}_3\text{O}_7)^{2-}$ nanosheets and therefore resulting in folded layers for the elongated morphology of the TNP.

The number of layers on TNP depends on the Coulomb energy, which it is induced by the negatively charged $(\text{Ti}_3\text{O}_7)^{2-}$ layers. Charges equilibrium is achieved due to Na^+ ions are between the TNP layers due to the strongly alkaline medium used. Coupling energy results from the contribution of an uneven distribution between the two sides of the $(\text{Ti}_3\text{O}_7)^{2-}$ sheet and the usual elastic deformation energy of the folded crystalline sheet [190].

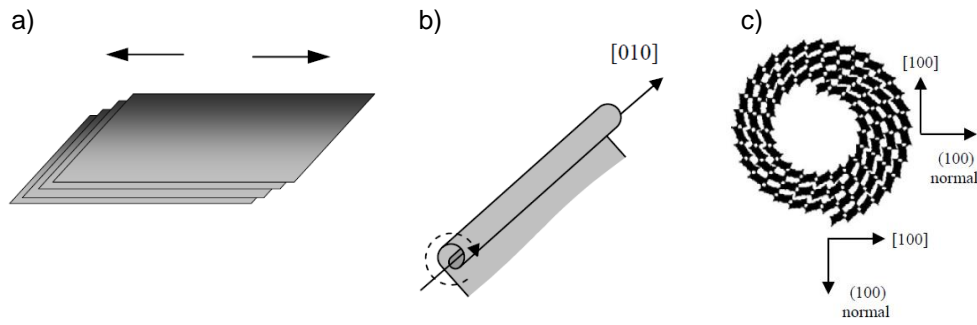


Figure 1.15 – Schematic representation of the curl up process of TNT. (a) Exfoliation of the $\text{Na}_2\text{Ti}_3\text{O}_7$ nanosheets; (b) winding a nanosheet in the direction of the TNT main axis [010]; (c) top view of the coiled winding forming a multi-layered TNT. (Adapted from [189])

Zhang *et al.* reported that single surface layers in an asymmetrical chemical environment, due to the imbalance of H^+ or Na^+ ion concentration on two different sides of a nanosheet, gives rise to excess surface energy, results in bending, as illustrated in Figure 1.16(a) [147,191]. When both sides have a symmetrical chemical environment, both spring constants have similar values (Figure 1.16(a)), and as a result, all tensions are compensated, and the plane is straight [87]. When the trititanate nanosheets have a proton-distribution asymmetry, both sides have different free surface energy values (spring constants), and, in order to compensate imbalance in surface tensions, the plane bends towards the surface with a higher spring constant value. During the folding process, strain energy arises and prevents work against bending [87,147].

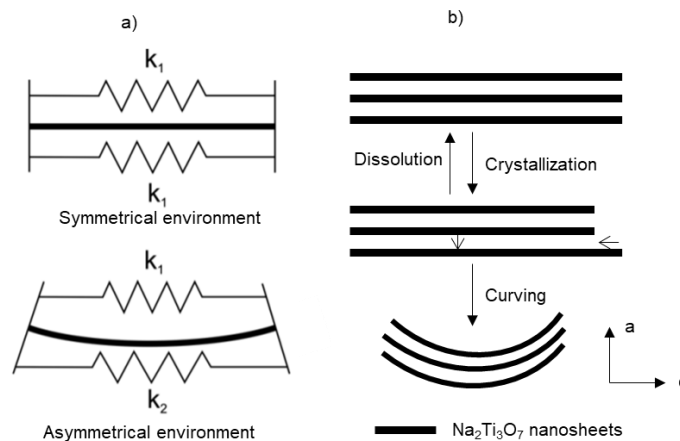


Figure 1.16 – Schematic representation of the driving forces for bending titanates nanosheets under alkaline hydrothermal conditions. (a) Asymmetrical chemical environment resulting in different surface tensions; k_1 and k_2 are spring constants on each side of the nanosheet. (b) Imbalance in layer widths resulting in shifting of the layer and bending of nanosheets. (Adapted from [87])

The bending multi-layered nanosheets can also occur by the mechanical tensions that arise during the process of dissolution/crystallization of nanosheets (Figure 1.16(b)). During spontaneous crystallization and rapid growth of the layers, a variation in the width of the different layers can occur. The unbalance in the width of the layer may create a tendency for

the layers to move within the multi-walled nanosheet to decrease excess surface energy. This can result in the bending of multi-layered nanosheets (Figure 1.16(b)). During the simultaneous shift of the layer and fold of the nanosheet, the surface energy gain is enough to compensate for the mechanical tensions that arise in the material during the curving and wrapping into nanotubes. The kinetic rate of curving the nanotubes might control the diameter of the nanotubes produced, which can be adjusted by changing the synthesis conditions [87,147].

It is interesting to note that the *axis* of nanotubes (vector [010]) does not always coincide with the axis of nanowires (vector [001]). This provides an insight into the growth mechanism of titanate nanotubes. The fact that nanowires crystallize, preferably along the crystallographic *c*-axis, suggests that the rate of dissolution/crystallization along this axis is maximized. Under certain conditions, an imbalance in nanosheet width it is expected along the *c*-axis (Figure 1.16 (b)). Thus, the bending of nanosheets will occur around the *b*-axis. When the curved nanosheet closes the loop, the direction of the fastest growth will disappear, and there will be only two directions for nanotube growth, namely, the radial direction (*a*-axis) and the axial direction (*b*-axis). Kukovecz *et al.* reported that the nanoloops provide seeds for further growth of nanotubes with the preferable direction of growth being the *b*-axis. If the nanosheet rollup to tubes of conical shape occurs, then further growth will result in the formation of closed-end elongated nanoparticles, being formed the nanowires [87,147,192].

• TNP modification and functionalization

Despite their relatively high charge recombination rate (however, smaller than the TiO₂) and wide bandgap (~ 3.3 eV), the TNP's ion-exchange ability makes them potential materials for photocatalytic and solar energy cells' applications [82,193-196]. However, the limited radiation absorption capacity in the visible region represents one of their limitations; if solar-based applications are intended. In order to shift the TNP band absorption to the visible, many studies have been performed with the purpose of photosensitizing these materials. Under this context, several methods have been reported, namely metal and non-metal doping [197,198], co-doping, ion-exchange, and surface sensitization with organic molecules or other semiconductor nanoparticles [199]. These methodologies have been used to improve the photochemical performances of TNP, mainly by shift the absorption into the visible range and/or promote the reduction of the charge recombination rate.

Surface sensitization with metal/non-metal is an outstanding technique to renew TNP electronic properties and improve the photocatalytic efficiency. Metal dopants play an important role in the separation of electron-hole pairs during light irradiation by decreasing the e^-/h^+

recombination rate, due to the introduction of new intermediate levels in the forbidden zone. These dopants can also shift the optical absorption to the visible range, due to the electron trap mechanism, surface plasmon resonance effect, incorporation of new energy levels and generation of gap states by interaction with VB states [200].

The synergetic combination of two or more semiconductors, with improved and/or innovated photocatalytic properties, it has been one of the most popular methods for accomplishing the modification of the TNP. For example, zinc sulfide (ZnS) is a direct semiconductor that shows interesting properties, especially in the nanometer range, and it has been used in applications on several technological fields, including photocatalysis [201]. Studies have revealed that ZnS nanoparticles are good photocatalysts due to the rapid generation of electron-hole pairs by photoexcitation and highly negative reduction potentials of excited electrons [202,203]. Naudin *et al.* reported a new ZnS/TNP composite materials with high photocatalytic activity for organic pollutants removal. In this case, the authors concluded that this improvement is due to a decrease in the recombination rate of the photogenerated charge carriers due to the ZnS presence in the TNP surface [86].

The combination of TNP with active photosensitizers in the visible range should increase the optical absorption of the nanocomposite material. For example, the synergetic combination of Ag₂S, ZnS and TNP was recently reported [79]. The Ag₂S(ZnS/TNP) nanocomposite has a high photocatalytic activity for phenol and their by-products photodegradation (Figure 1.17).

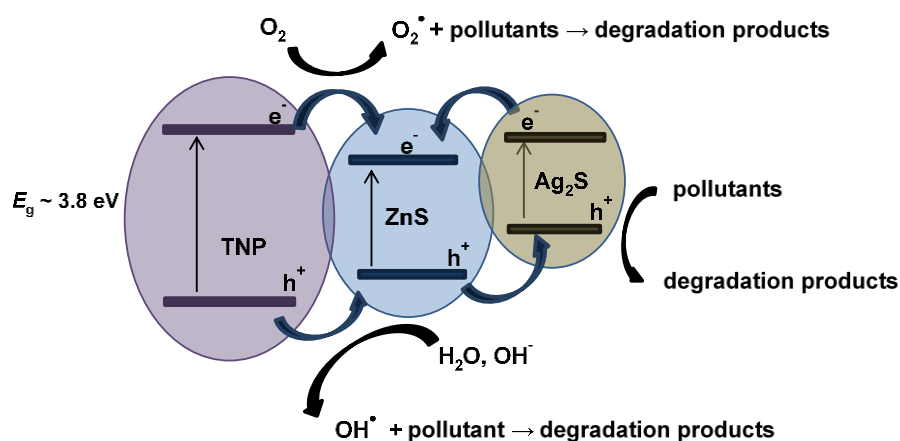


Figure 1.17 – Band structure of Ag₂S(ZnS/TNP) particles and the mechanism of phenol photocatalytic degradation (adapted from [79]).

Due to the relative energetic positions of TNP, ZnS, and Ag₂S valence bands (Figure 1.17), the holes generated in TNP and ZnS particles react with OH^- or H_2O oxidizing them to OH^\bullet radicals. On the other hand, the h^+ transferred to the VB of Ag₂S, acts as holes scavenger,

promoting carrier separation. In this system, the Ag_2S surface act as catalytic sites for phenol oxidation too. Simultaneously, some of the e^- from Ag_2S and TNP conduction bands were transferred to ZnS , enhancing the separation of electrons and holes and reducing the recombination rate [79], as illustrated in Figure 1.17.

• TNP applications

Nowadays, elongated titanate nanoparticles applications has stimulated the interest of many researchers. Many research studies for the TNP applications have been reported in several areas, such as chemistry, physics, biology and medicine.

In recent years, few studies have been published focus on nanostructured elongated titanate and TiO_2 -based materials [87,124,150,159,204]. These materials, depending on the synthesis conditions and/or post-treatment modifications, can have various types of applications. For example, the TNP synthesized by the hydrothermal method has a high surface area and ion-exchange ability, which make these materials very suitable to act as substrate/carrier for different compounds, including pollutants [146]. Their high stability, high surface area, and low cost make them very attractive for photocatalysis [205].

As mentioned above, the TNP ion-exchange ability offers an opportunity for further modification of TNP with other ions to improve their characteristics, such as the adsorption and catalytic activity. The TNP are attractive in several fields, including organic molecules immobilization and adsorption [147,186] and photocatalysis [195], once the hollow TNP tubular structure improves the organic molecules contact and also the photo-produced carriers' motion which prevents charge recombination during photocatalysis. Previous works have demonstrated that pristine, metal doped and sensitized TNP possess adsorbent/photocatalytic affinities for several organic pollutants [152]. Related to the layered structure of the TNP, significant attention has been given in the field of photon-mediated water decomposition, fuel cell electrolytes, adsorbent, lithium ion batteries (LIBs) and wettability control [189]. These titanate elongated nanoparticles can also be used in electrochemistry, solar cells, hydrogen storage, biomedicine [87,150,159,204], sensors [206], photo(electro)catalysis [142,207,208], photovoltaic generation, dye-sensitized solar cells (DSSC) and direct alcohol fuel cells (DAFCs) [151,209-211]. For these applications, the control of TNP dimensions and properties is essential for the achievement of enhanced performance.

Very recently, Abbas *et al.* [212] reported a review of advances in the use of TiO_2 -based nanotubes powder in different applications. The authors reported that these materials have several applications in different areas, biological (*e.g.*, antibacterial, sensing and drug delivery),

environmental (sensing and pollutants degradation), energy storage (supercapacitor), and energy conversion (solar-cells and water splitting).

Mor *et al.*, reported the preparation of transparent titanium oxide nanotube-array thin films, by anodization method, for application as sensors [206]. These optically transparent nanotube-array films can serve as excellent hydrogen sensors, exhibiting a four-order magnitude drop in resistance with exposure to 1000 ppm hydrogen at room temperature, and negligible sensitivity to other reducing gases like methane, carbon monoxide, and ammonia. The sensors are mechanically and electrically stable with operation air or oil, over a tested temperature range of 25°C to 250°C. The authors showed that these transparent films could also be actively used in photovoltaic and anti-reflection coating applications [206].

Mydin *et al.* [213], reported TiO₂-nanotubes arrays for biomedical implants and nanomedicine applications. These materials provide a promising approach for advanced biomedical and nanomedicine implant applications. The TiO₂-nanotubes arrays have gained considerable interest as biomedical implant materials and nanomedicine applications (such as nanotherapeutics, nano diagnostics, and nano biosensors). In bio-implants studies, the properties of these nanostructures could modulate diverse cellular processes, such as cell adhesion, migration, proliferation, and differentiation. Furthermore, this material structure provides larger surface areas and energy to regulate positive cellular interactions toward mechanosensitivity activities.

Recently, M. Nair *et al.* [214] reported the application of titania nanotubes for orthopedic bone implants. These materials were prepared by electrochemical anodization, and their influence on osteoblast cells and staphylococcus aureus and the corrosion resistance of TNT were analyzed. They showed that the TNT has a good interaction of osteoblasts or their lineage cells with the implant surface, and the bacterial interaction study and biofilm formation on the implant was successfully obtained. The authors reported that TNT has drastically improved the properties of orthopedic implants. Another work with titanium dioxide nanotubes for biomedical applications was recently reported by Mansoorianfar *et al.* [215]. The authors showed modification of TiO₂-nanotubes with vancomycin (an antibiotic) immersing and electrophoretic to adsorb the antibiotic on the surface and inside the nanotubes. The vancomycin-modified nanotubes, anodized at 60-75 V, have signified strong antibacterial behaviors against *S. aureus* bacteria. The authors concluded that this anodization potential might be considered as an optimum voltage in point of drug loading/releasing, antibacterial activity, and cell/protein attachment studies [215]. This work can be seen from two points of view, one is the removal of an antibiotic by adsorption on nanotubes (producing drug-modified

nanotubes), and the second is the utilization of these drug-modified nanotubes with antibacterial properties in bone implants.

Dong *et al.* [216], reported novel Pt nanoclusters/titanium dioxide nanotubes composites (nano-Pt/TiO₂-nanotubes) for hydrazine oxidation. The nano-Pt/TiO₂-nanotubes showed excellent electrocatalytic activity for hydrazine oxidation, and this may be attributed to the good dispersion of Pt nanoclusters as well as the unique properties of TiO₂-nanotubes supports. They reported that the mechanism of hydrazine electrochemical oxidation on nano-Pt/TiO₂-nanotubes implies that TiO₂-nanotubes are the promising supporting materials for noble metals catalysts with high activity.

Recently, the preparation of modified TiO₂ nanostructures modified with Rh₃O₂ and Rh⁰ nanoparticles to be used as a photocatalyst in H₂ production it has been reported by Camposeco *et al.* [217]. In this reported work, Rh on TiO₂ nanostructured photocatalysts were obtained by the sol-gel (nanoparticles) and hydrothermal (nanotubes) methods and tested in the water-splitting reaction for hydrogen production using a sacrificial agent (ethanol) in aqueous solution. The authors showed that the Rh/TiO₂ nanotubes have higher photocatalytic activity for hydrogen production than the Rh/TiO₂ nanoparticles. The photocatalytic improvement obtained with the Rh modified TiO₂ nanotubes was supported by the combination of charge separators represented by Rh⁺³ species that can act as electron/hole traps. The synergistic effect between the Rh⁺³ species and electrons transferred from ethanol to different nanostructured TiO₂ species improved the H₂ production remarkably.

Mejía-Centeno *et al.* reported the NO selective catalytic reduction (SCR) with NH₃ using trititanic nanotubes (H₂Ti₃O₇) modified with V₂O₅, V₂O₅-WO₃ and Al₂O₃ as catalysts [218]. The authors showed that the V₂O₅/H₂Ti₃O₇, V₂O₅-WO₃/H₂Ti₃O₇, and Al₂O₃/H₂Ti₃O₇ catalysts have high activity and selectivity for the NO reduction with NH₃, and a catalytic enhancement was observed by adding WO₃ and Al₂O₃ to the H₂Ti₃O₇. The V₂O₅-WO₃/H₂Ti₃O₇ catalyst reached 96% of NO conversion at 400°C, whereas, at 480°C, 98% of NO conversion is reported for Al₂O₃/H₂Ti₃O₇ catalyst. Furthermore, the high NO conversion (97%) was obtained at low temperatures (240°C) with the V₂O₅/H₂Ti₃O₇.

He *et al.* [219] reported the preparation of Pt modified Na₂Ti₃O₇ nanowires, for methanol and ethanol electrooxidation. The authors compare the Pt/Na₂Ti₃O₇ catalyst with other common Pt based catalyst; Pt supported on carbon black (Pt/C). The Na₂Ti₃O₇ nanowires were used as support for Pt nanoparticles distribution. Due to the good ion-exchange properties of Na₂Ti₃O₇ nanowires, the Pt nanoparticles of about 8 to 10 nm in diameter are evenly distributed on the surface of Na₂Ti₃O₇ nanowires. The Pt/Na₂Ti₃O₇ electrocatalyst displays better catalytic

activity and higher catalytic steady current for the methanol and ethanol electrooxidation in both acidic and alkaline media than Pt/C electrocatalyst at the same loading of Pt as a result of more effective Pt catalyst sites. The current density enhancement for the Pt/Na₂Ti₃O₇ electrocatalyst is more obvious under alkaline conditions than acidic conditions. These findings suggest promising applications of the Pt/Na₂Ti₃O₇ electrocatalyst in direct alcohol fuel cells (DAFCs) [219].

Grandcolas *et al.* [220] reported the antibacterial activity of silver oxide nanoparticles loaded on titanate nanotubes (AgO-TNT) and also the combination with photocatalysis. Decontamination under either dark conditions or visible light irradiation showed excellent antibacterial activity. The enhanced antibacterial activity was observed in visible irradiation. They showed that TNT are good support for silver nanoparticles and their related effects on disinfection. Silver oxide nanoparticles enhance the photocatalytic activity of TNT in the visible range by absorbing visible radiation and minimizing electron-hole recombination during photoexcitation.

Li *et al.* reported the application of hydrogen titanate nanowires modified by lithium ion intercalation in high-performance rechargeable lithium-ion batteries and high-power electrochemical supercapacitors. The authors conclude that this electrode can work smoothly at various charge/discharge current densities and even at very high discharge current density; hence, they have an excellent high rate cycling stability [221].

Recently, Monteiro *et al.* reported a CO₂ conversion to propylene carbonate catalyzed by ionic liquid (IL) containing organosilane groups supported on titanate nanotubes/nanowires [222]. They showed that TNT and TNW materials have good catalytic activity after CO₂ cycloaddition to propylene oxide. IL-TNT and IL-TNW exhibited high catalytic performance (turnover frequency of 46 and 49 h⁻¹, respectively) and 100% selectivity in propylene carbonate (propylene/catalyst molar ratio = 580, 4.0 MPa of CO₂, 383.15 K, 6 h) [222].

Previous works have demonstrated that undoped, metal-doped and semiconductor sensitized elongated titanate nanoparticles have high photocatalytic activity and adsorption capacity for various organic pollutants [86,152,195]. For example, TNF modified with Bi₂S₃ and ZnS have shown to be promising as adsorbents and photocatalysts of organic pollutants [131], and Vitamin-B12 sensitized TNW efficient in dyes degradation [223]. Another recent work has shown that TNF co-modified with Ag₂S and ZnS was very efficient in the degradation of phenol and its by-products [79].

In conclusion, several emergent pollutants' removal methodologies have already been proposed, but the definitive answer to solve this pollution issue is far from being found.

The main goal of this PhD work was the preparation of new elongated titanate nanoparticles, using a hydrothermal approach, to be used as catalysts in the degradation of emergent pollutants. This research project proposed the synthesis of TNT and TNW modified by surface sensitization and metal doping and/or ion-exchange processes, in order to change the intrinsic properties of TNP, mainly physical/chemical adsorption and photo(electro)catalytic. Therefore, new modified materials with improved affinity/ability and enhanced adsorption and photo(electro)catalytic properties for pollutants' removal/degradation were expected to be obtained. Experimentally, pollutants' removal was achieved by a synergetic combination of selective adsorption and photo(electro)catalytic degradation processes, using the synthesized modified TNP as adsorbents and also as photocatalysts. Caffeine, theophylline, sulfamethazine, phenol and organic dyes are examples of the model pollutants used. These new elongated titanate nanoparticles were modified by sensitization with organic molecules/groups, such as ethylenediamine (Chapter 2) and silver nanoparticles (Chapter 3), and also modified by metal ion-exchange or doped and co-doped with metals (such as Co, Ru and Fe/Mn), Chapters 4-7. Furthermore, another goal of this research was the TNP immobilization in films to be used in photo(electro)degradation, and for the fast recovery and reuse of the catalyst (Chapter 8). This part of the work was performed at the University of Warsaw in Poland under Professor Doctor Magdalena Skompska supervision during a three-month internship.

1.6 - References

- 1 - C.A. Martinez-Huitle, E. Brillas, Decontamination of wastewaters containing synthetic organic dyes by electrochemical methods: A general review, *Appl. Catal.*, B 87 (2009) 105-145.
- 2 - F.G. Calvo-Flores, J. Isac-Garcia, J.A. Dobado, *Emerging pollutants: Origin, structure, and properties*, John Wiley & Sons, 2017.
- 3 - Network of reference laboratories, research centres and related organisations for monitoring of emerging environmental substances (NORMAN). Accessed August 2019. (<https://www.norman-network.net>)
- 4 - A.J. Ebele, M.A.E. Abdallah, S. Harrad, Pharmaceuticals and personal care products (PPCPs) in the freshwater aquatic environment, *Emerg. Contam.* 3 (2017) 1-16.

- 5 - D. Zhang, R.M. Gersberg, W.J. Ng, S.K. Tan, Removal of pharmaceuticals and personal care products in aquatic plant-based systems: A review, *Environ. Pollut.* 184 (2014) 620-639.
- 6 - A.R.M. Silva, F.C.M. Portugal, J.M.F. Nogueira, Advances in stir bar sorptive extraction for the determination of acidic pharmaceuticals in environmental water matrices: Comparison between polyurethane and polydimethylsiloxane polymeric phases, *J. Chromatogr. A* 1209 (2008) 10-16.
- 7 - V. Koutsouba, T. Heberer, B. Fuhrmann, K. Schmidt-Baumler, D. Tsipi, A. Hiskia, Determination of polar pharmaceuticals in sewage water of Greece by gas chromatography-mass spectrometry, *Chemosphere* 51 (2003) 69-75.
- 8 - C.G. Daughton, T.A. Ternes, Pharmaceuticals and personal care products in the environment: agents of subtle change?, *Environ. Health Perspect.* 107 (1999) 907-938.
- 9 - D. Bendz, N.A. Paxéus, T.R. Ginn, F.J. Loge, Occurrence and fate of pharmaceutically active compounds in the environment, a case study: Høje River in Sweden, *J. Hazard. Mater.* 122 (2005) 195-204.
- 10 - A.R. Varela, G. Ferro, J. Vredenburg, M. Yanik, L. Vieira, L. Rizzo, C. Lameiras, C.M. Manaia, Vancomycin resistant enterococci: From the hospital effluent to the urban wastewater treatment plant, *Sci. Total Environ.* 450-451 (2013) 155-161.
- 11 - K. Ikehata, Hazardous agents in wastewater: Public health impacts and treatment options for safe disposal and reuse - Wastewater reuse and management. S.K. Sharma, R. Sanghi (Eds.), Springer Netherlands, 2013.
- 12 - A. Gogoi, P. Mazumder, V.K. Tyagi, G.G.T. Chaminda, A.K. An, M. Kumar, Occurrence and fate of emerging contaminants in water environment: A review, *Groundw. Sustain. Dev.* 6 (2018) 169-180.
- 13 - G. Tchobanoglous, F.L. Burton, H.D. Stensel, Advanced wastewater treatment - Wastewater engineering: Treatment and reuse (4th ed.), Metcalf & Eddy Inc. (Eds.), McGraw-Hill: New York, 2004.
- 14 - N. Vieno, M. Sillanpää, Fate of diclofenac in municipal wastewater treatment plant - A review, *Environment Int.* 69 (2014) 28-39.

- 15 - Y. Li, G. Zhu, W.J. Ng, S.K. Tan, A review on removing pharmaceutical contaminants from wastewater by constructed wetlands: Design, performance and mechanism, *Sci. Total Environ.* 468-469 (2014) 908-932.
- 16 - K. Fent, A.A. Weston, D. Caminada, Ecotoxicology of human pharmaceuticals, *Aquat. Toxicol.* 76 (2006) 122-159.
- 17 - M. Carballa, F. Omil, J.M. Lema, M. Llompart, C. Garcia-Jares, I. Rodriguez, M. Gómez, T. Ternes, Behavior of pharmaceuticals, cosmetics and hormones in a sewage treatment plant, *Water Res.* 38 (2004) 2918-2926.
- 18 - C.Y. Teh, P.M. Budiman, K.P.Y. Shak, T.Y. Wu, Recent advancement of coagulation–flocculation and its application in wastewater treatment, *Ind. Eng. Chem. Res.* 55 (2016) 4363-4389.
- 19 - S. Suárez, M. Ramil, F. Omil, J.m. Lema, Removal of pharmaceutically active compounds in nitrifying–denitrifying plants, *Water Sci. Technol.* 52 (2005) 9-14.
- 20 - Y. Wang, G.Y. Rao and J.Y. Hu, Adsorption of EDCs/PPCPs from drinking water by submicron-sized powdered activated carbon, *Water Sci. Tech-W. Sup.* 11 (2011) 711-718.
- 21 - Z. Hasan, J. Jeon, S.H. Jhung, Adsorptive removal of naproxen and clofibric acid from water using metal-organic frameworks, *J. Hazard. Mater.* 209 (2012) 151-157.
- 22 - M. Kaneko, I. Okura (Eds.), *Photocatalysis: Science and technology, biological and medical physics series*, Springer, Berlin, 2010.
- 23 - F. Méndez-Arriaga, M.I. Maldonado, J. Gimenez, S. Esplugas, S. Malato, Abatement of ibuprofen by solar photocatalysis process: Enhancement and scale up, *Catal. Today* 144 (2009) 112-116.
- 24 - C. Martínez, S. Vilarino, M.I. Fernández, J. Faria, M. Canle, J.A. Santaballa, Mechanism of degradation of ketoprofen by heterogeneous photocatalysis in aqueous solution, *Appl. Catal. B* 142 (2013) 633-646.
- 25 - Y. Lin, C. Ferronato, N. Deng, F. Wu, J. Chovelon, Photocatalytic degradation of methylparaben by TiO₂: Multivariable experimental design and mechanism, *Appl. Catal. B* 88 (2009) 32-41.

- 26 - R. Liang, A. Hu, W. Li, Y.N. Zhou, Enhanced degradation of persistent pharmaceuticals found in wastewater treatment effluents using TiO₂ nanobelt photocatalysts, *J. Nanopart. Res.* 15 (2013) 1990-2003.
- 27 - Q. Sui, X. Cao, S. Lu, W. Zhao, Z. Qiu, Gang Yu, Occurrence, sources and fate of pharmaceuticals and personal care products in the groundwater: A review, *Emerg. Contam.* 1 (2015) 14-24.
- 28 - P.J. Barnes, Theophylline, *Am. J. Respir. Crit. Care Med.* 188 (2013) 901-906.
- 29 - R. Franco, A. Oñatibia-Astibia, E. Martínez-Pinilla, Health benefits of methylxanthines in cacao and chocolate, *Nutrients* 5 (2013) 4159-4173.
- 30 - M. Hakil, S. Denis, G. Viniegra-González, C. Augur, Degradation and product analysis of caffeine and related dimethylxanthines by filamentous fungi, *Enzyme Microb. Technol.* 22 (1998) 355-359.
- 31 - H. Fiege, H.W. Voges, T. Hamamoto, S. Umemura, T. Iwata, H. Miki, Y. Fujita, H.J. Buysch, D. Garbe, W. Paulus, Phenol derivatives. In: *Ullmann's Encyclopedia of Industrial Chemistry* (6 th ed.), Wiley-VCH: Weinheim, Germany, 2012.
- 32 - M. Weber, M. Weber, Phenols. In: *Phenolic Resins: A Century of Progress*, Pilato, L. (Ed.), Springer-Verlag: Berlin Heidelberg; Chapter 2, 9-23, 2010.
- 33 - S. Mohammadi, A. Kargari, H. Sanaeepur, K. Abbassian, A. Najafi, E. Mofarrah, Phenol removal from industrial wastewaters: a short review, *Desalin. Water Treat.* 53 (2015) 22215-2234.
- 34 - R. Malik, D.S. Ramteke, S.R.Wate, Adsorption of malachite green on groundnut shell waste based powdered activated carbon, *Waste Manage.* 27 (2007) 1129-1138.
- 35 - F.R. Abe, A.L. Machado, A.M.V.M. Soares, D.P. de Oliveira, J.L.T. Pestana, Life history and behavior effects of synthetic and natural dyes on *Daphnia magna*, *Chemosphere* 236 (2019) 124390(1)-124390(8).
- 36 - N. Hidalgo, G. Mangiameli, T. Manzano, G.G. Zhadan, J.F. Kennedy, V.L. Shnyrov, M.G. Roig, Oxidation and removal of industrial textile dyes by a novel peroxidase extracted from post-harvest Lentil (*Lens culinaris* L.) stubble, *Biotechnol. Bioprocess Eng.* 16 (2011) 821-829.

- 37 - R.B. Chavan, Metal-complex dyes, Handbook of Textile and Industrial Dyeing - Principles, Processes and Types of Dyes, Woodhead Publishing Series in Textiles 1 (2011) 515-561
- 38 - G.Z. Kyzas, A decolorization technique with spent “Greek coffee” grounds as zero-cost adsorbents for industrial textile wastewaters, Materials 5 (2012) 2069-2087.
- 39 - S. Sharma, S. Basu, Highly reusable visible light active hierarchical porous WO_3/SiO_2 monolith in centimeter length scale for enhanced photocatalytic degradation of toxic pollutant, Sep. Purif. Technol. 231 (2020) 115916(1)-115916(10).
- 40 - J.F. Luan, M. Li, K. Ma, Y.M. Li, Z.G. Zou, Photocatalytic activity of novel Y_2InSbO_7 and Y_2GdSbO_7 nanocatalysts for degradation of environmental pollutant rhodamine B under visible light irradiation, Chem. Eng. J. 167 (2011) 162-171.
- 41 - M.A. Rauf, S.S. Ashraf, Fundamental principles and application of heterogeneous photocatalytic degradation of dyes in solution, Chem. Eng. J. 151 (2009) 10-18.
- 42 - S.M.A.G. Ulson de Souza, E. Forgiarini, A.A. Ulson de Souza, Toxicity of textile dyes and their degradation by the enzyme horseradish peroxidase (HRP), J. Hazard. Mater. 147 (2007) 1073-1078.
- 43 - S.K. Raya, D. Dhakal, S.W. Lee, Visible light driven $\text{Ni-BaMo}_3\text{O}_{10}$ photocatalyst for Indigo Carmine degradation: Mechanism and pathways, Mater. Sci. Semicond. Process. 105 (2020) 104697(1)-104697(9).
- 44 - V. Katheresan, J. Kannedo, S.Y. Lau, Efficiency of various recent wastewater dye removal methods: A review, J. Environ. Chem. Eng. 6 (2018) 4676-4697.
- 45 - K. Paździor, L. Bilińska, S. Ledakowicz, A review of the existing and emerging technologies in the combination of AOPs and biological processes in industrial textile wastewater treatment, Chem. Eng. J. 376 (2019) 120597(1)-120597(25).
- 46 - R. Daghrir, P. Drogui, D. Robert, Photoelectrocatalytic technologies for environmental applications, J. Photoch. Photobio. A: Chem. 238 (2012) 41-52.
- 47 - R. Andreozzi, V. Caprio, A. Insola, R. Marotta, Advanced oxidation processes (AOP) for water purification and recovery, Catal. Today 53 (1999) 51-59.

- 48 - P. Pichat, J. Disdier, C. Hoang-Van, D. Mas, G. Goutailler, C. Gaysse, Purification/deodorization of indoor air and gaseous effluents by TiO₂ photocatalysis, *Catal. Today* 63 (2000) 363-369.
- 49 - R.D. Villa, A.G. Trovo, R.F.P. Nogueira, Soil remediation using a coupled process: soil washing with surfactant followed by photo-Fenton oxidation, *J. Hazard. Mater.* 174 (2010) 770-775.
- 50 - G.G. Bessegato, T.T. Guaraldo, M.V.B. Zanoni, Enhancement of photoelectrocatalysis efficiency by using nanostructured electrodes, *Modern electrochemical methods in nano, Surface and Corrosion Science*, Chapter 10 (2014) 271-319.
- 51 - C. Comninellis, A. Kapalka, S. Malato, S.A. Parsons, I. Poulios, D. Mantzavinos, Advanced oxidation processes for water treatment: advances and trends for R & D, *J. Chem. Technol. Biotechnol.* 83 (2008) 769-776.
- 52 - J.M. Poyatos, M.M. Muñio, M.C. Almecija, J.C. Torres, E. Hontoria, F. Osorio, Advanced oxidation processes for wastewater treatment: state of the art, *Water Air Soil Pollut.* 205 (2010) 187-204.
- 53 - S. Das, P.V. Kamat, S. Padmaja, V. Au, S.A. Madison, Free radical induced oxidation of the azo dye Acid Yellow 9, *J. Chem. Soc. Perkin Trans. 2* (1999) 1219-1224.
- 54 - P. Saritha, C. Aparna, V. Himabindu, Y. Anjaneyulu, Comparison of various advanced oxidation processes for the degradation of 4-chloro-2 nitrophenol, *J. Hazard. Mater.* 149 (2007) 609-614.
- 55 - E. Neyens, J. Baeyens, A review of classic Fenton's peroxidation as an advanced oxidation technique. *J. Hazard. Mater.* 98 (2003) 33-50.
- 56 - D. Rajkumar, K. Palanivelu, Electrochemical treatment of industrial wastewater, *J. Hazard. Mater.* 113 (2004) 123-129.
- 57 - G. Waldner, M. Pourmodjib, R. Bauer, M. Neumann-Spallart, Photoelectrocatalytic degradation of 4-chlorophenol and oxalic acid on titanium dioxide electrodes, *Chemosphere* 50 (2003) 989-998.

58 - X. Zhao, Qu, J. H.; Liu, H. J.; Qiang, Z. M.; Liu, R. P.; Hu, C. Z., Photoelectrochemical degradation of anti-inflammatory pharmaceuticals at Bi₂MoO₆-boron-doped diamond hybrid electrode under visible light irradiation, *Appl. Catal. B* 91 (2009) 539-545.

59 - S. Parsons, *Advanced Oxidation Processes for Water and Wastewater Treatment*, IWA publishing, London, UK, 2004.

60 - M. Cheng, G. Zeng, D. Huang, C. Lai, P. Xu, C. Zhang, Y. Liu, Hydroxyl radicals based advanced oxidation processes (AOPs) for remediation of soils contaminated with organic compounds: A review, *Chem. Eng. J.* 284 (2016) 582-598.

61 - M. Antoniadou, D.I. Kondarides, D. Labou, S. Neophytides, P. Lianos, An efficient photoelectrochemical cell functioning in the presence of organic wastes, *Sol. Energy Mater. Sol. Cells* 94 (2010) 592-597.

62 - A. Mills, S. LeHunte, An overview of semiconductor photocatalysis, *J. Photochem. Photobiol. A* 108 (1997) 1-35.

63 - A. Fujishima, X. Zhang, D.A. Tryk, Heterogeneous photocatalysis: From water photolysis to applications in environmental cleanup, *Int. J. Hydrogen Energy* 32 (2007) 2664-2672.

64 - J.M. Herrmann, Heterogeneous photocatalysis: fundamentals and applications to the removal of various types of aqueous pollutants, *Catal. Today* 53 (1999) 115-129.

65 - D. Bahnemann, Photocatalytic water treatment: solar energy applications, *Sol. Energy* 77 (2004) 445-459.

J. Zhao, X.D. Yang, Photocatalytic oxidation for indoor air purification: a literature review, *Build. Environ.* 38 (2003) 645-654.

66 - A. Franco, M.C. Neves, M. Carrott, M.H. Mendonca, M.I. Pereira, O.C. Monteiro, Photocatalytic decolorization of methylene blue in the presence of TiO₂/ZnS nanocomposites. *J. Hazard. Mater.* 161 (2009) 545-550.

67 - A. Fujishima, K. Honda, Electrochemical photolysis of water at a semiconductor electrode, *Nature* 238 (1972) 37-38.

68 - S.N. Frank, A.J. Bard, Heterogeneous photocatalytic oxidation of cyanide and sulfite in aqueous solutions at semiconductor powders, *J. Phys. Chem. A* 81 (1977) 1484-1488.

- 69 - A. Fujishima, T.N. Rao, D.A. Tryk, Titanium dioxide photocatalysis, *J. Photoch. Photobio. C* 1 (2000) 1-21.
- 70 - A. Fujishima, X.T. Zhang, Titanium dioxide photocatalysis: present situation and future approaches, *C. R. Chim.* 9 (2006) 750-760.
- 71 - K. Hashimoto, H. Irie, A. Fujishima, TiO₂ photocatalysis: A historical overview and future prospects, *Jpn. J. Appl. Phys.* 44 (2005) 8269-8285.
- 72 - M.A. Fox, M.T. Dulay, Heterogeneous photocatalysis. *Chem. Rev.* 93 (1993) 341-57.
- 73 - R. Pelton, X.L. Geng, M. Brook, Photocatalytic paper from colloidal TiO₂ - fact or fantasy, *Adv. Colloid Interface Sci.* 127 (2006) 43-53.
- 74 - N.M. Mahmoodi, M. Arami, N.Y. Limaee, N.S. Tabrizi, Kinetics of heterogeneous photocatalytic degradation of reactive dyes in an immobilized TiO₂ photocatalytic reactor, *J. Colloid Interface Sci.* 295 (2006) 159-164.
- 75 - S. Garcia-Segura, E. Brillas, Applied photoelectrocatalysis on the degradation of organic pollutants in wastewaters, *J. Photochem. Photobiol. C Photochem. Rev.* 31 (2017) 1-35.
- 76 - A. Akhundi, A. Habibi-Yangjeh, Novel g-C₃N₄/Ag₂SO₄ nanocomposites: Fast microwave-assisted preparation and enhanced photocatalytic performance towards degradation of organic pollutants under visible light, *J. Colloid Interface Sci.* 482 (2016) 165-174.
- 77 - P. Pichat, *Photocatalysis and water purification: From fundamentals to recent applications*, Wiley-VCH, 2013.
- 78 - Y. Nosaka, A. Nosaka, Understanding hydroxyl radical ([•]OH) generation processes in photocatalysis, *ACS Energy Lett.* 1 (2016) 356-359.
- 79 - B. Barrocas, T.J. Entradas, C.D. Nunes, O.C. Monteiro, Titanate nanofibers sensitized with ZnS and Ag₂S nanoparticles as novel photocatalysts for phenol removal, *Appl. Catal. B* 218 (2017) 709-720.
- 80 - X. Cheng, Q. Cheng, X. Deng, P. Wang, H. Liu, A facile and novel strategy to synthesize reduced TiO₂ nanotubes photoelectrode for photoelectrocatalytic degradation of diclofenac, *Chemosphere* 144 (2016) 888-894.

- 81 - X. Meng, Z. Zhang, X. Li, Synergetic photoelectrocatalytic reactors for environmental remediation: a review, *J. Photochem. Photobiol. C Photochem. Rev.* 24 (2015) 83-101.
- 82 - G.G. Bessegato, T.T. Guaraldo, J. Ferreira de Brito, M.F. Brugnera, M.V.B. Zanoni, Achievements and trends in photoelectrocatalysis: from environmental to energy applications, *Electrocatalysis* 6 (2015) 415-441.
- 83 - C. Acar, I. Dincer, C. Zamfirescu, A review on selected heterogeneous photocatalysts for hydrogen production, *Int. J. Energy Res.* 38 (2014) 1903-1920.
- 84 - M. Ahmed, I. Dincer, A review on photoelectrochemical hydrogen production systems: Challenges and future directions, *Int. J. Hydrogen Energy* 44 (2019) 2474-2507.
- 85 - H. Yang, P. Wang, D. Wang, Y. Zhu, K. Xie, X. Zhao, J. Yang, X. Wang, New understanding on photocatalytic mechanism of nitrogen-doped graphene quantum dots-decorated BiVO₄ nanojunction photocatalysts, *ACS Omega* 2 (2017) 3766-3773.
- 86 - G. Naudin, T. Entradas, B. Barrocas, O.C. Monteiro, Titanate nanorods modified with nanocrystalline ZnS particles and their photocatalytic activity on pollutant removal, *J. Mater. Sci. Technol.* 32 (2016) 1122-1128.
- 87 - D.V. Bavykin, J.M. Friedrich, F.C. Walsh, Protonated titanates and TiO₂ nanostructured materials: Synthesis, properties, and applications, *Adv. Mater.* 18 (2006) 2807-2824.
- 88 - B. Barrocas, O.C. Monteiro, M.E. Melo Jorge, S. Sérgio, Photocatalytic activity and reusability study of nanocrystalline TiO₂ films prepared by sputtering technique, *Appl. Surf. Sci.* 264 (2013) 111-116.
- 89 - M.A. Sousa, C. Gonçalves, V.J.P. Vilar, R.A.R. Boaventura, M.F. Alpendurada, Suspended TiO₂-assisted photocatalytic degradation of emerging contaminants in a municipal WWTP effluent using a solar pilot plant with CPCS, *Chem. Eng. J.* 198-199 (2012) 301-309.
- 90 - S. Garcia-Segura, S. Dosta, J.M. Guilemany, E. Brillas, Solar photoelectrocatalytic degradation of Acid Orange 7 azo dye using a highly stable TiO₂ photoanode synthesized by atmospheric plasma spray, *Appl. Catal. B* 132–133 (2013) 142-150.
- 91 - D. Cao, Y. Wang, X. Zhao, Combination of photocatalytic and electrochemical degradation of organic pollutants from water, *Curr. Opin. Green Sustain. Chem.* 6 (2017) 78-84.

- 92 - B. Barrocas, S. Sérgio, A. Rovisco, M.E. Melo Jorge, Visible-light photocatalysis in $\text{Ca}_{0.6}\text{Ho}_{0.4}\text{MnO}_3$ films deposited by RF-magnetron sputtering using nanosized powder compacted target, *J. Phys. Chem. C* 118 (2014) 590-597.
- 93 - V.C. Ferreira, A.I. Melato, A.F. Silva, L.M. Abrantes, Attachment of noble metal nanoparticles to conducting polymers containing sulphur - preparation conditions for enhanced electrocatalytic activity, *Electrochim. Acta* 56 (2011) 3567-3574.
- 94 - V.C. Ferreira, A.J. Goddard, O.C. Monteiro, *In situ* synthesis and modification of cotton fibers with bismuthoxychloride and titanium dioxide nanoparticles for photocatalytic applications, *J. Photoch. Photobio. A* 357 (2018) 201-212.
- 95 - L. Pinhedo, R. Pelegrini, R. Bertazzoli, A.J. Motheo, Photoelectrochemical degradation of humic acid on a $(\text{TiO}_2)_{0.7}(\text{RuO}_2)_{0.3}$ dimensionally stable anode. *Appl. Catal. B* 57 (2005) 75-81.
- 96 - M.V.B. Zanoni, J.J. Sene, H. Selcuk, M.A. Anderson, Photoelectrocatalytic production of active chlorine on nanocrystalline titanium dioxide thin-film electrodes, *Environ. Sci. Technol.* 38 (2004) 3203-3208.
- 97 - Z. Xu, X.J. Li, J. Li, L.P. Wu, Q.Y. Zeng, Z.Y. Zhou, Effect of CoOOH loading on the photoelectrocatalytic performance of WO_3 nanorod array film, *Appl. Surf. Sci.* 284 (2013) 285-290.
- 98 - L. Xing, J.B. Jia, Y.Z. Wang, S.J. Dong, Lanthanide-doped TiO_2 nanoparticles modified electrode for photoelectrocatalytic degradation of dye, *Environ. Prog. Sustain. Energy* 32 (2013) 302-306.
- 99 - M.E. Osugi, G.A. Umbuzeiro, M.A. Anderson, M.V.B. Zanoni, Degradation of metallophthalocyanine dye by combined processes of electrochemistry and photoelectrochemistry, *Electrochim. Acta* 50 (2005) 5261-5269.
- 100 - M.E. Osugi, G.A. Umbuzeiro, F.J.V. De Castro, M.V.B. Zanoni, Photoelectrocatalytic oxidation of remazol turquoise blue and toxicological assessment of its oxidation products, *J. Hazard. Mater.* 137 (2006) 871-877.
- 101 - M. Pelaez, P. Falaras, V. Likodimos, K. O'Shea, A.A. Cruz, P.S.M. Dunlop, J. Anthony Byrne, Dionysios D. Dionysiou, Use of selected scavengers for the determination of NF- TiO_2

reactive oxygen species during the degradation of microcystin-LR under visible light irradiation, *J. Mol. Catal. A Chem.* 425 (2016) 183-189.

102 - Y. Hao, F. Li, S. Wang, M. Chai, R. Liu, X. Wang, One-step combustion synthesis of β - Bi_2O_3 -NiO/Ni composites and their visible light photocatalytic performance, *Mater. Sci. Eng. B* 186 (2014) 41-47.

103 - W.J. Kim, D. Pradhan, B.-K. Min, Y. Sohn, Adsorption/photocatalytic activity and fundamental natures of BiOCl and $\text{BiOCl}_x\text{I}_{1-x}$ prepared in water and ethylene glycol environments, and Ag and Au-doping effects, *Appl. Catal. B* 147 (2014) 711-725.

104 - K. Ishibashi, A. Fujishima, T. Watanabe, K. Hashimoto, Detection of active oxidative species in TiO_2 photocatalysis using the fluorescence technique, *Electrochem. Commun.* 2 (2000) 207-210.

105 - E.S. Da Silva, N.M.M. Moura, M.G.P.M.S. Neves, A. Coutinho, M. Prieto, C.G. Silva, J.L. Faria, Novel hybrids of graphitic carbon nitride sensitized with *free-base meso-tetrakis(carboxyphenyl) porphyrins* for efficient visible light photocatalytic hydrogen production, *Appl. Catal., B.* 221 (2018) 56-69.

106 - N.L. Finčur, J.B. Krstić, F.S. Šibul, D.V. Šojić, V.N. Despotović, N.D. Banić, J.R. Agbaba, B.F. Abramović, Removal of alprazolam from aqueous solutions by heterogeneous photocatalysis: Influencing factors, intermediates, and products, *Chem. Eng. J.* 307 (2017) 1105-1115.

107 - K. Ishibashi, A. Fujishima, T. Watanabe, K. Hashimoto, Detection of active oxidative species in TiO_2 photocatalysis using the fluorescence technique, *Electrochem. Commun.* 2 (2000) 207-210.

108 - W.J. Ong, L.L. Tan, S.P. Chai, S.T. Yong, Graphene oxide as a structure-directing agent for the two-dimensional interface engineering of sandwich-like graphene-g-C₃N₄ hybrid nanostructures with enhanced visible-light photoreduction of CO_2 to methane, *Chem. Commun.* 51 (2015) 858-861.

109 - W.J. Wang, X.Q. Chen, G. Liu, Z.R. Shen, D.H. Xia, P.K. Wong, J.C. Yu, Monoclinic dibismuth tetraoxide: a new visible-light-driven photocatalyst for environmental remediation, *Appl. Catal. B.* 176 (2015) 444-453.

110 - J. Zhang, Y. Nosaka, Photocatalytic oxidation mechanism of methanol and the other reactants in irradiated TiO₂ aqueous suspension investigated by OH radical detection, *Appl. Catal. B* 166 (2015) 32-36.

111 - X.H. Lin, S.N. Lee, W. Zhang, S.F.Y. Li, Photocatalytic degradation of terephthalic acid on sulfated titania particles and identification of fluorescent intermediates, *J. Hazard. Mater.* 303 (2016) 64-75.

112 - K. Bubacz, E. Kusiak-Nejman, B. Tryba, A.W. Morawski, Investigation of OH radicals formation on the surface of TiO₂/N photocatalyst at the presence of terephthalic acid solution. Estimation of optimal conditions, *J. Photochem. Photobiol. A-Chem.* 261 (2013) 7-11.

113 - K. Ishibashi, A. Fujishima, T. Watanabe, K. Hashimoto, Quantum yields of active oxidative species formed on TiO₂ photocatalyst, *J. Photochem. Photobiol. A-Chem.* 134 (2000) 139-142.

114 - R. Thiruvengkatachari, T.O. Kwon, J.C. Jun, S. Balaji, M. Matheswaran, I.S. Moon, Application of several advanced oxidation processes for the destruction of terephthalic acid (TPA), *J. Hazard. Mater.* 142 (2007) 308-314.

115 - A. Shafaei, M. Nikazar, M. Arami, Photocatalytic degradation of terephthalic acid using titania and zinc oxide photocatalysts: Comparative study, *Desalination* 252 (2010) 8-16.

116 - M.A. Rahman, A review on semiconductors including applications and temperature effects in semiconductors, *Am. Sci. Res. J. Eng., Technol., Sci.* 7 (2014) 50-70.

117 - H.L. Tan, F.F. Abdi, Y.H. Ng, Heterogeneous photocatalysts: an overview of classic and modern approaches for optical, electronic, and charge dynamics evaluation, *Chem. Soc. Rev.* 48 (2019) 1255-1271.

118 - L. Smart, E. Moore, *Solid state chemistry - An introduction*, 2nd Ed., Chapman & Hall, London, 1996.

119 - J.P. Bird, *Encyclopedia of materials: Science and technology*, Semiconductors: An introduction, Elsevier, 2002.

120 - Y. Ma, X. Wang, Y. Jia, X. Chen, H. Han, C. Li, Titanium dioxide-based nanomaterials for photocatalytic fuel generations, *Chem. Rev.* 114 (2014) 9987-10043.

- 121 - A.B. Djurišić, Y.H. Leung, A.M.C. Ng, Strategies for improving the efficiency of semiconductor metal oxide photocatalysis, *Mater. Horiz.* 1 (2014) 400-410.
- 122 - M.K. Nowotny, P. Bogdanoff, T. Dittrich, S. Fiechter, A. Fujishima, H. Tributsch, Observations of p-type semiconductivity in titanium dioxide at room temperature, *Mater. Lett.* 64 (2010) 928-930.
- 123 - P.A. Korzhavyi, B. Johansson, Literature review on the properties of cuprous oxide Cu_2O and the process of copper oxidation, Svensk Kärnbränslehantering AB, Stockholm, 2011.
- 124 - C.L. Wong, Y.N. Tan, A.R. Mohamed, A review on the formation of titania nanotube photocatalysts by hydrothermal treatment, *J. Environ. Manage.* 92 (2011) 1669-1680.
- 125 - V.E. Nawin, S. Noriaki, C. Tawatchai, K. Takeyuki, T. Wiwut, A step towards length control of titanate nanotubes using hydrothermal reaction with sonication pretreatment. *Nanotechnol* 19 (2008) 1-6.
- 126 - D.S. Seo, J.K. Lee, H. Kim, Preparation of nanotubes-shaped TiO_2 powder. *J. Cryst. Growth* 229 (2001) 428-432.
- 127 - M.H. Seo, M. Yuasa, T. Kida, J.S. Huh, K. Shimano, N. Yamazoe, Gas sensing characteristics and porosity control of nanostructured films composed of TiO_2 nanotubes. *Sens. Actuators, B.* 137 (2009) 513-520.
- 128 - L. Gnanasekaran, R. Hemamalini, R. Saravanan, K. Ravichandran, F. Gracia, S. Agarwal, V.K. Gupta, Synthesis and characterization of metal oxides (CeO_2 , CuO , NiO , Mn_3O_4 , SnO_2 and ZnO) nanoparticles as photo catalysts for degradation of textile dyes, *J. Photoch. Photobio. B* 173 (2017) 43-49.
- 129 - S. Zhao, J. Li, L. Wang, X. Wang, Degradation of rhodamine B and safranin-T by $\text{MoO}_3:\text{CeO}_2$ nanofibers and air using a continuous mode, *Clean: Soil, Air, Water* 38 (2010) 268-274.
- 130 - Y.H. Yin, Z.P. Wu, M. Zhao, G. Wu, Y.S. Li, Z.X. Guo, W.J. Yu, L.S. Tang, Preparation of highly dispersed WO_3 nanoparticles on carbon nanotubes and application as visible photocatalyst, *J. Nanosci. Nanotechnol.* 19 (2019) 4771-4777.

- 131 - T.J. Entradas, J.F. Cabrita, B. Barrocas, M.R. Nunes, A.J. Silvestre, O.C. Monteiro, Synthesis of titanate nanofibers co-sensitized with ZnS and Bi₂S₃ nanocrystallites and their application on pollutants removal, *Mater. Res. Bull.* 72 (2015) 20-28.
- 132 - A.A.A. Alves, G.L.O. Ruiz, T.C.M. Nonato, L.C. Müller, M.L. Sens, Performance of the fixed-bed of granular activated carbon for the removal of pesticides from water supply, *Journal Environ. Technol.* 40 (2019) 1977-1987.
- 133 - Z. Li, A. Gómez-Avilés, L. Sellaouic, J. Bedia, A. Bonilla-Petriciolet, C. Belver, Adsorption of ibuprofen on organo-sepiolite and on zeolite/sepiolite heterostructure: Synthesis, characterization and statistical physics modelling, *Chem. Eng. J.* 371 (2019) 868-875.
- 134 - F. Soleimani, M. Salehi, A. Alizadeh, Comparison of visible light photocatalytic degradation of different pollutants by (Zn, Mg)_xCu_{1-x}Bi₂O₄ nanoparticles, *Ceram. Int.* 45 (2019) 8926-8939.
- 135 - S. Feizpoor, A. Habibi-Yangjeh, S. Vadivel, Novel TiO₂/Ag₂CrO₄ nanocomposites: Efficient visible-light-driven photocatalysts with n-n heterojunctions, *J. Photochem. Photobiol. A Chem.* 341 (2017) 57-68.
- 136 - R.E. Adam, M. Pirhashemi, S. Elhag, X. Liu, A. Habibi-Yangjeh, M. Willandera, O. Nur, ZnO/Ag/Ag₂WO₄ photo-electrodes with plasmonic behavior for enhanced photoelectrochemical water oxidation, *RSC Adv.* 9 (2019) 8271-8279.
- 137 - M. Shekofteh-Gohari, A. Habibi-Yangjeh, Fe₃O₄/ZnO/CoWO₄ nanocomposites: Novel magnetically separable visible-light-driven photocatalysts with enhanced activity in degradation of different dye pollutants, *Ceram. Int.* 43 (2017) 3063-3071.
- 138 - C.F. Lin, C. H. Wu, Z.N. Onn, Degradation of 4-chlorophenol in TiO₂, WO₃, SnO₂, TiO₂/WO₃ and TiO₂/SnO₂ systems, *J. Hazard. Mater.* 154 (2008) 1033-1039.
- 139 - G. Marci, V. Augugliaro, M.J. López-Munoz, C. Martín, L. Palmisano, V. Rives, M. Schiavello, R.J. Tilleyand, A.M. Venezia, Preparation characterization and photocatalytic activity of polycrystalline ZnO/TiO₂ Systems 2. Surface, bulk characterization, and 4-nitrophenol photodegradation in liquid–solid regime, *J. Phys. Chem. B* 105 (2001) 1033-1040.
- 140 - V. Keller, P. Bernhardt, F. Garin, Photocatalytic oxidation of butyl acetate in vapor phase on TiO₂, Pt/TiO₂ and WO₃/TiO₂ catalysts, *J. Catal.* 215 (2003) 129-138.

- 141 - O. Akhavan, R. Azimirad, Photocatalytic property of Fe₂O₃ nanograin chains coated by TiO₂ nanolayer in visible light irradiation, *Appl. Catal.*, A 369 (2009) 77-82.
- 142 - M. Grätzel, Photoelectrochemical Cells, *Nature*, 414 (2001) 338-344.
- 143 - T.L. Thompson, J.T. Yates, Surface science studies of the photoactivation of TiO₂ - New photochemical processes, *Chem. Rev.* 106 (2006) 4428-4453.
- 144 - U. Diebold, The surface science of titanium dioxide, *Surf. Sci. Rep.* 48 (2003) 53-229.
- 145 - G. Mital, T. Manoj, A review of TiO₂ nanoparticles, *Chinese Sci. Bull.* 56 (2011) 1639-1657.
- 146 - V. Bem, M.C. Neves, M.R. Nunes, A.J. Silvestre, O.C. Monteiro; Influence of the sodium/proton replacement on the structural, morphological and photocatalytic properties of titanate nanotubes, *J. Photochem. Photobiol.*, A 232 (2012) 50-56.
- 147 - D.V. Bavykin, F.C. Walsh, Titanate and titania nanotubes: synthesis, properties and applications, RSC Publishing, Cambridge, UK, 2010.
- 148 - T. Kasuga, M. Hiramatsu, A. Hoson, T. Sekino, K. Niihara, Titania nanotubes prepared by chemical processing. *Adv. Mater.* 11 (1999) 1307-1311.
- 149 - T. Kasuga, M. Hiramatsu, A. Hoson, T. Sekino, K. Niihara, Formation of Titanium Oxide Nanotube, *Langmuir* 14 (1998) 3160-3163.
- 150 - D.V. Bavykin, F.C. Walsh, Elongated Titanate Nanostructures and Their Applications. *Eur. J. Inorg. Chem.* 2009 (2009) 977-997.
- 151 - H.-H. Ou, S.-L. Lo, Review of titania nanotubes synthesized via the hydrothermal treatment: Fabrication, modification, and application, *Sep. Purif. Technol.* 58 (2007) 179-191.
- 152 - V.C. Ferreira, M.R. Nunes, A.J. Silvestre, O.C. Monteiro, Synthesis and properties of Co-doped titanate nanotubes and their optical sensitization with methylene blue, *Mater. Chem. Phys.* 142 (2013) 355-362.
- 153 - J.C. Colmenares, M.A. Aramendía, A. Marinas, J.M. Marinas, F.J. Urbano, Synthesis, characterization and photocatalytic activity of different metal-doped titania systems. *Appl. Catal. A Gen.* 306 (2006) 120-127.

- 154 - J.M. Macak, H. Tsuchiya, A. Ghicov, K. Yasuda, R. Hahn, S. Bauer, P. Schmuki, TiO₂ nanotubes: Self-organized electrochemical formation, properties and applications, *Curr. Opin. Solid St. M.* 11 (2007) 3-18.
- 155 - K. Nakata, A. Fujishima, TiO₂ Photocatalysis: Design and Applications. *J. Photochem. Photobiol. C Photochem. Rev.* 13 (2012) 169-189.
- 156 - R. Liu, W.-D. Yang, L.-S. Qiang, J.-F. Wu, Fabrication of TiO₂ nanotube arrays by electrochemical anodization in an NH₄F/H₃PO₄ electrolyte, *Thin Solid Films* 519 (2011) 6459-6466.
- 157 - X. Yu, Y. Li, W. Wlodarski, S. Kandasamy, K. Kalantar-Zadeh, Fabrication of nanostructured TiO₂ by anodization: A comparison between electrolytes and substrates, *Sensor Actuat. B Chem.* 130 (2008) 25-31.
- 158 - A. Zaleska, Doped-TiO₂: A Review, *Recent Patents on Engineering* 2 (2008) 157-164.
- 159 - H. Ou, S. Lo, Review of titania nanotubes synthesized via the hydrothermal treatment: fabrication, modification, and application. *Sep. Purif. Technol.* 58 (2007) 179-191.
- 160 - T. Brunatova, D. Popelkova, W. Wan, P. Oleynikov, S. Danis, X. Zou, R. Kuzel, Study of titanate nanotubes by X-ray and electron diffraction and electron microscopy, *Mater. Charact.* 87 (2014) 166-171.
- 161 - S. Chatterjee, K. Bhattacharyya, P. Ayyub, A. K. Tyagi, Photocatalytic Properties of One-Dimensional Nanostructured Titanates. *J. Phys. Chem. C* 114 (2010) 9424-9430.
- 162 - Z-Y. Yuan, B-L. Su, Titanium oxide nanotubes, nanofibers and nanowires, *Colloid. Surface A* 241 (2004) 173-183.
- 163 - S. Kobayashi, K. Hanabusa, N. Hamasaki, M. Kimura, H. Shirai, S. Shinkai, Preparation of TiO₂ Hollow-Fibers Using Supramolecular Assemblies, *Chem. Mater.* 12 (2000) 1523-1525.
- 164 - J.H. Jung, H. Kobayashi, K.J.C. van Bommel, S. Shinkai, T. Shimizu, Creation of novel helical ribbon and double-layered nanotube TiO₂ structures using an organogel template *Chem. Mater.* 14 (2002) 1445-1447.

- 165 - T. Peng, A. Hasegawa, J. Qiu, K. Hirao, Fabrication of titania tubules with high surface area and well-developed mesostructural walls by surfactant-mediated templating method, *Chem. Mater.* 15 (2003) 2011-2016.
- 166 - D. Gong, C.A. Grimes, O.K. Varghese, W. Hu, R.S. Singh, Z. Chen, E.C. Dickey, Titanium oxide nanotube arrays prepared by anodic oxidation, *J. Mater. Res.* 16 (2001) 3331-3334.
- 167 - S.P. Albu, A. Ghicov, J.M. Macak, R. Hahn, P. Schmuki, Self-organized, free-standing TiO₂ nanotube membrane for flow-through photocatalytic applications, *Nano Lett.* 7 (2007) 1286-1289.
- 168 - J. Wang, Z. Lin, Freestanding TiO₂ nanotube arrays with ultrahigh aspect ratio via electrochemical anodization, *Chem. Mater.* 20 (2008) 1257-1261.
- 169 - K. Shankar, J.I. Basham, N.K. Allam, O.K. Varghese, G.K. Mor, X. Feng, M. Paulose, J.A. Seabold, K.-S. Choi, C.A. Grimes, Recent advances in the use of TiO₂ nanotube and nanowire arrays for oxidative photoelectrochemistry, *J. Phys. Chem. C* 113 (2009) 6327-6359.
- 170 - P. Roy, S. Berger, P. Schmuki, TiO₂ nanotubes: synthesis and applications, *Angew. Chem. Int. Ed.* 50 (2011) 2904-2939.
- 171 - J. Yan, F. Zhou, TiO₂ nanotubes: Structure optimization for solar cells, *J. Mater. Chem.* 21 (2011) 9406-9418.
- 172 - N. Liua, X. Chen, J. Zhang, J.W. Schwank, A review on TiO₂-based nanotubes synthesized via hydrothermal method: Formation mechanism, structure modification, and photocatalytic applications, *Catal. Today* 225 (2014) 34-51.
- 173 - B.D. Yao, Y.F. Chan, X.Y. Zhang, W.F. Zhang, Z.Y. Yang, N. Wang, Formation mechanism of TiO₂ nanotubes, *Appl. Phys. Lett.* 82 (2003) 281-283.
- 174 - G.H. Du, Q. Chen, R.C. Che, Z.Y. Yuan, L.-M. Peng, Preparation and structure analysis of titanium oxide nanotubes, *Appl. Phys. Lett.* 79 (2001) 3702-3704.
- 175 - N. Hfayedh, W. Saidi, M. Haouari, C. Autret-Lambert, S. Roger, A. Megriche, M.E. Maaoui, HRTEM study of the variation of TNTs morphology synthesized via hydrothermal method at different reaction times, *Curr. Appl. Phys.* 16 (2016) 1308-1314.

- 176 - M.R. Nunes, O.C. Monteiro, A.L. Castro, D.A. Vasconcelos, A.J. Silvestre, A New Chemical Route to Synthesise TM-Doped (TM = Co, Fe) TiO₂ Nanoparticles, *Eur. J. Inorg. Chem.* 2008 (2008) 961-965.
- 177 - T. Gao, H. Fjellvåg, P. Norby, Raman Scattering Properties of a Protonic Titanate H_xTi_{2-x/4□x/4}O₄.H₂O (□, Vacancy; x=0.7) with Lepidocrocite-Type Layered Structure. *J. Phys. Chem. B* 112 (2008) 9400-9405.
- 178 - Y.M. Wang, H. Liu, Preparation and Characterizations of Na₂Ti₃O₇, H₂Ti₃O₇ and TiO₂ Nanobelts. *Adv. Mater. Res.* 306-307 (2011) 1233-1237.
- 179 - D.V. Bavykin, F.C. Walsh, Kinetics of alkali metal ion exchange into nanotubular and nanofibrous titanates, *J. Phys. Chem. C* 111 (2007) 14644-14651.
- 180 - S. Zhang, Q. Chen, L.-M. Peng, Structure and formation of H₂Ti₃O₇ nanotubes in an alkali environment, *Physical review B* 71 (2005) 014104(1)-014104(11).
- 181 - M.Á.L. Zavala, S.A.L. Morales, M. Ávila-Santos, Synthesis of stable TiO₂ nanotubes: effect of hydrothermal treatment, acid washing and annealing temperature, *Heliyon* 3 (2017) e00456:1-18.
- 182 - C.J. Brinker, G.W. Scherer, *Sol-Gel Science. The physics and chemistry of sol-gel processing*, Academic Press Inc., San California, USA, 1990.
- 183 - L.G. Devi, R. Kavitha, A Review on non metal ion doped titania for the photocatalytic degradation of organic pollutants under UV/solar light: role of photogenerated charge carrier dynamics in enhancing the activity. *Appl. Catal. B* 140-141 (2013) 559-587.
- 184 - T.M.F. Marques, O.P. Ferreira, J.A.P. da Costa, Kazunori Fujisawa, M. Terrones, B.C. Viana, Study of the growth of CeO₂ nanoparticles onto titanate nanotubes, *J. Phys. Chem. Solids* 87 (2015) 213-220.
- 185 - N.M. Santos, J.M. Rocha, J.M.E. Matos, O.P. Ferreira, J.M. Filho, B.C. Viana, A.C. Oliveira, Metal cations intercalated titanate nanotubes as catalysts for, unsaturated esters production, *Appl. Catal. A Gen.* 454 (2013) 74-80.
- 186 - V.C. Ferreira, O.C. Monteiro, New hybrid titanate elongated nanostructures through organic dye molecules sensitization, *J. Nanopart. Res.* 15 (2013) 1923-1938.

- 187 - S. Zhang, L.M. Peng, Q. Chen, G. Du, G. Dawson, W. Zhou, Formation Mechanism of $\text{H}_2\text{Ti}_3\text{O}_7$ nanotubes. *Phys. Rev. Lett.* 91 (2003) 256103(1)-256103(4).
- 188 - N. Liu, X. Chen, J. Zhang, J.W. Schwank, A Review on TiO_2 -Based Nanotubes Synthesized via Hydrothermal Method: Formation Mechanism, Structure Modification, and Photocatalytic Applications. *Catal. Today* 225 (2014) 34-51.
- 189 - Y. Zhang, Z. Jiang, J. Huang, L.Y. Lim, W. Li, J. Deng, D. Gong, Y. Tang, Y. Lai, Z. Chen, Titanate and titania nanostructured materials for environmental and energy applications: a review, *RSC Adv.* 5 (2015) 79479-79510.
- 190 - T. Kijima, *Inorganic and metallic nanotubular materials: Recent technologies and applications*, Springer, 2010.
- 191 - S. Zhang, L.-M. Peng, Q. Chen, G. H. Du, G. Dawson, W. Z. Zhou, Formation Mechanism of $\text{H}_2\text{Ti}_3\text{O}_7$ Nanotubes, *Phys. Rev. Lett.* 91 (2003) 256103(1)-256103(4).
- 192 - A. Kukovecz, M. Hodos, E. Horvath, G. Radnoczi, Z. Konya, I. Kiricsi, Oriented Crystal Growth Model Explains the Formation of Titania Nanotubes, *J. Phys. Chem. B* 109 (2005) 17781-17783.
- 193 - H.-H. Ou, C.-H. Liao, Y.-H. Liou, J.-H. Hong, S.-L. Lo, Photocatalytic oxidation of aqueous ammonia over microwave-induced titanate nanotubes, *Environ. Sci. Technol.* 42 (2008) 4507-4512.
- 194 - X.D. Li, D.W. Zhang, Z. Sun, Y.W. Chen, S.M. Huang, Metal-free indoline-dye-sensitized TiO_2 nanotube solar cells, *Microelectron. J.* 40 (2009) 108-114.
- 195 - E.K. Ylhäinen, M.R. Nunes, A.J. Silvestre, O.C. Monteiro, Synthesis of titanate nanostructures using amorphous precursor material and their adsorption/photocatalytic properties, *J. Mater. Sci.* 47 (2012) 4305-4312.
- 196 - Z.Y. Wang, W.P. Mao, H.F. Chen, F.A. Zhang, X.P. Fan, G.D. Qian, Copper(II) phthalocyanine tetrasulfonate sensitized nanocrystalline titania photocatalyst Synthesis in situ and photocatalysis under visible light, *Catal. Commun.* 7 (2006) 518-522.
- 197 - S. So, K. Lee, P. Schmuki, Ru-doped TiO_2 nanotubes: improved performance in dye-sensitized solar cells, *Phys. Status Solidi RRL* 6 (2012) 169-171.

- 198 - J. Choi, H. Park, M.R. Hoffmann, Effects of single metal-ion doping on the visible-light photoreactivity of TiO₂, *J. Phys. Chem. C* 114 (2010) 783-792.
- 199 - X. Li, L. Liu, S.-Z. Kang, J. Mu, G. Li, Titanate nanotubes co-sensitized with cadmium sulfide nanoparticles and porphyrin zinc, *Catal. Commun.* 17 (2012) 136-139.
- 200 - V. Kumaravel, S. Mathew, J. Bartlett, S.C. Pillai, Photocatalytic hydrogen production using metal doped TiO₂: A review of recent advances, *Appl. Catal. B* 244 (2019) 1021-1064.
- 201 - D. Chen, F. Huang, G. Ren, D. Li, M. Zheng, Y. Wang, Z. Lin, ZnS nano-architectures: photocatalysis, deactivation and regeneration, *Nanoscale* 2 (2010) 2062-2064.
- 202 - P. Dhatshanamurthi, B. Subash, A. Senthilraja, V. Kuzhalosai, B. Krishnakumar, M. Shanthi, Synthesis and characterization of ZnS–TiO₂ photocatalyst and its excellent sun light driven catalytic activity, *J. Nanosci. Nanotechnol.* 14 (2014) 4930-4939.
- 203 - X.J. Xu, L. Hu, N. Gao, S. Liu, S. Wageh, A. Al-Ghamdi, A. Alshahrie, X.S. Fang, Controlled growth from ZnS nanoparticles to ZnS–CdS nanoparticle hybrids with enhanced photoactivity, *Adv. Funct. Mater.* 25 (2015) 445-454.
- 204 - W. Zhou, H. Liu, R.I. Boughton, G. Du, J. Lin, J. Wang, D. Liu, One-dimensional single-crystalline Ti–O based nanostructures: properties, synthesis, modifications and applications, *J. Mater. Chem.* 20 (2010) 5993-6008.
- 205 - S.M. Gupta, M. Tripathi, A Review of TiO₂ Nanoparticles, *Chinese Sci. Bull.* 56 (2011) 1639-1657.
- 206 - G.K. Mor, O.K. Varghese, M. Paulose, K.G. Ong, C.A. Grimes, Fabrication of hydrogen sensors with transparent titanium oxide nanotube-array thin films as sensing elements, *Thin Solid Films* 496 (2006) 42-48.
- 207 - L.-C. Chen, Y.-C. Ho, W.-S. Guo, C.-M. Huang, T.-C. Pan, Enhanced visible light-induced photoelectrocatalytic degradation of phenol by carbon nanotube-doped TiO₂ electrodes, *Electrochim. Acta* 54 (2009) 3884-3891.
- 208 - P.A. Kolinko, D.V. Kozlov, A.V. Vorontsov, S.V. Preis, Photocatalytic oxidation of 1,1-dimethyl hydrazine vapours on TiO₂: FTIR *in situ* studies, *Catal. Today* 122 (2007) 178-185.

- 209 - G.K. Mor, O.K. Varghese, M. Paulose, K. Shankar, C.A. Grimes, A review on highly ordered, vertically oriented TiO₂ nanotube arrays: Fabrication, material properties, and solar energy applications, *Sol. Energ. Mater. Sol. Cell.* 90 (2006) 2011-2075.
- 210 - C.A. Grimes, G.K. Mor, *TiO₂ Nanotube Arrays: Synthesis, Properties and Applications*, 1a ed., Springer: New York, 2009.
- 211 - D. Wang, B. Yu, F. Zhou, C. Wang, W. Liu, Synthesis and characterization of anatase TiO₂ nanotubes and their use in dye-sensitized solar cells, *Mater. Chem. Phys.* 113 (2009) 602-606.
- 212 - W.A. Abbas, I.H. Abdullah, B.A. Ali, N. Ahmed, A.M. Mohamed, M.Y. Rezk, N. Ismail, M.A. Mohamed, N.K. Allam, Recent advances in the use of TiO₂ nanotube powder in biological, environmental, and energy applications, *Nanoscale Adv.* 1 (2019) 2801-2816.
- 213 - R.B.S.M.N. Mydin, R. Hazan, M.F. FaridWajidi, S. Sreekantan, Titanium dioxide - material for a sustainable environment, Chapter 23 - Titanium dioxide nanotube arrays for biomedical implant materials and nanomedicine applications, IntechOpen publisher, UK, 2017.
- 214 - M. Nair, E. Elizabeth, Applications of titania nanotubes in bone biology, *J. Nanosci. Nanotechnol.* 15 (2015) 939-955.
- 215 - M. Mansoorianfar, A. Khataee, Z. Riahi, K. Shahin, M. Asadnia, A. Razmjou, A.H. Najafabadi, C. Mei, Y. Orooji, D. Li, Scalable fabrication of tunable titanium nanotubes via sonoelectrochemical process for biomedical applications, *Ultrason. Sonochem.* (2019) 104783. (In Press, Journal Pre-proof - DOI:10.1016/j.ultsonch.2019.104783)
- 216 - B. Dong, B. He, Y. Chai, C. Liu, Novel Pt nanoclusters/titanium dioxide nanotubes composites for hydrazine oxidation, *Mater. Chem. Phys.* 120 (2010) 404-408.
- 217 - R. Camposeco, S. Castillo, V. Rodriguez-Gonzalez, M. Hinojosa-Reyes, I. Mejía-Centeno, Tailored TiO₂ nanostructures for supporting Rh₃O₂ and Rh⁰ nanoparticles: Enhanced photocatalytic H₂ production, *J. Photoch. Photobio. A* 356 (2018) 92-101.
- 218 - I. Mejía-Centeno, S. Castillo, R. Camposeco, J. Marín, L.A. García, G.A. Fuentes, Activity and selectivity of V₂O₅/H₂Ti₃O₇, V₂O₅-WO₃/H₂Ti₃O₇ and Al₂O₃/H₂Ti₃O₇ model catalysts during the SCR-NO with NH₃, *Chem. Eng. J.* 264 (2015) 873-885.

219 - X. He, C. Hu, H. Liu, Fabrication of 3D Pt catalysts via support of Na₂Ti₃O₇ nanowires for methanol and ethanol electrooxidation, *Catal. Commun.* 12 (2010) 100-104.

220 - M. Grandcolas, J. Ye, N. Hanagata, Combination of photocatalytic and antibacterial effects of silver oxide loaded on titania nanotubes, *Mater. Lett.* 65 (2011) 236-239.

221 - J. Li, Z. Tang, Z. Zhang, Layered hydrogen titanate nanowires with novel lithium intercalation properties, *Chem. Mater.* 17 (2005) 5848-5855.

222 - W.F. Monteiro, M.O. Vieira, A.S. Aquino, M.O. Souza, J. Lima, S. Einloft, R. Ligabue, CO₂ conversion to propylene carbonate catalyzed by ionic liquid containing organosilane groups supported on titanate nanotubes/nanowires, *Appl. Catal. A Gen.* 544 (2017) 46-54.

223 - T.A. Silva, J. Diniz, L. Paixão, B. Vieira, B. Barrocas, C.D. Nunes, O.C. Monteiro, Novel titanate nanotubes-cyanocobalamin materials: Synthesis and enhanced photocatalytic properties for pollutants removal, *Solid State Sci.* 63 (2017) 30-41.

Chapter 2

Amine modified titanate nanowires and nanotubes

The presented work was subject of the scientific publication:

B. Barrocas, M.C. Neves, M. Conceição Oliveira, O.C. Monteiro, Enhanced photocatalytic degradation of psychoactive substances using amine modified elongated titanate nanostructures, *Environmental Science: Nano* 5 (2018) 350-361.

Chapter 2 – Amine modified titanate nanowires and nanotubes

2.1 - Introduction

The properties of the elongated titanate nanoparticles can be changed by sensitization with other semiconductors, metallic nanoparticles or organic molecules. The combination of organic-inorganic host lattices, *e.g.* elongated titanates, with organic entities, not only through intercalation/ion exchange but also by grafting and sol-gel procedures, it has been seen as a promising synthesis methodology to produce new organic-inorganic hybrid materials with multifunctional performances [1]. Several works have been published related to this issue, including co-sensitization with zinc porphyrin and CdS [2], or vitamin B12 hybridization [3]. Also, the incorporation of nitrogen species, by doping or adsorption, it has been seen as a promising approach to modify the optical and catalytic properties of TiO₂-based materials, including titanate layered nanoparticles [4]. The use of small molecules containing nitrogen, like amines, it is described as a route to modifying the surface adsorption properties and also for doping TiO₂-based materials [5-7]. There are many discussions about the mechanism of interaction of ionic surfactants with metal oxide nanoparticles, with some models suggesting the presence of electrostatic interactions, covalent bonding, and the formation of bilayers and micelles. However, it is well-known that amines can be adsorbed on the titania surface at Lewis acid sites, *via* hydrogen bonds or electrostatic interactions [8,9].

Anion doping (*e.g.* I, N, C, F) is commonly employed to increase the photocatalytic activity of a semiconductor under visible light. In most of the recently reported studies, N was used as a non-metal dopant to improve the water-splitting efficiency of TiO₂. The bandgap energy of TiO₂ is narrowed, after N modification, through the generation of gap states by the interaction of N 2*p* and O 2*p* states. The mixing up of orbitals uplifts the valence band (VB) level of TiO₂ while the conduction band (CB) remains unaffected. Consequently, the photo-reduction ability of TiO₂ is unchanged; however, its oxidation capability is decreased [10]. N-doping is an ideal candidate to tailor the properties of the semiconductors, because nitrogen can be easily introduced in the TiO₂ structure, due to its comparable atomic size with oxygen, its low ionization energy, and high stability [11-13]. Di Valentin *et al.* [14] employed density functional theory (DFT) to demonstrate interstitial nitrogen as π character NO within *anatase* TiO₂. It was also found that there is no significant shift in the TiO₂ CB or VB. The anti-bonding π^* NO orbitals between the TiO₂ VB and CB can improve the visible light absorption by acting as a stepping stone for excited *e*⁻ between conduction and valence bands [13]. The N-TiO₂ can be synthesized using various nitrogen-containing chemicals (*e.g.* urea, ethylamine, NH₃ or

gaseous nitrogen) at high temperatures or inductively coupled plasma containing a wide range of nitrogen precursors, and the nitrogen atoms are predominantly on the TiO₂ surface [13]. Many results describe nitrogen doping as a substitutional element on the oxygen lattice sites or at interstitial sites [13]. There is some conflict in the literature concerning the preferred N sites, substitutional or interstitial, which induce the highest photocatalytic action [13]. Independently of the origin of visible light absorption in substitutional or interstitial nitrogen discrete energy states, the low photocatalytic efficiency is mainly attributed to the limited photo-excitation of electrons in such narrow states, the very low mobility of the corresponding photo-generated holes and the concomitant increase of the recombination rate due to the creation of oxygen vacancies by doping [13].

For the modification of semiconductors with amine groups, several organic molecules can be used, such as ethylenediamine (EDAmine), diethylenetriamine and (3-aminopropyl) trimethoxysilane [15-18]. These molecules containing nitrogen, carbon, hydrogen, and oxygen, can change the surface adsorption properties and/or doping the TiO₂-based materials [19-22]. Li *et al.*, reported a N-doped TiO₂ photocatalyst prepared by a sol-gel method using ethylenediamine (Figure 2.1) as a nitrogen source. The obtained results demonstrated an improvement in the hydrogen production rate and for methyl orange photodegradation performance when compared with TiO₂ [23]. Several other investigations have also shown that the N doping can efficiently improve the photocatalytic activity of TiO₂ [24,25].

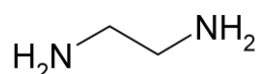


Figure 2.1 - Representation of ethylenediamine (EDAmine) molecule.

Based on the mentioned above, in this research, the modification of elongated titanate nanoparticles (TNT and TNW) by sensitization of the surface with organic species, such as amine groups, using ethylenediamine (EDAmine) [9] was proposed. These new hybrid materials with adsorption and photocatalytic improved properties were prepared to be used as catalysts in emergent pollutants photodegradation.

In this study, caffeine, theophylline, and phenol were used as model pollutants, for photodegradation under UV-vis and visible irradiation.

2.2 - Synthesis

Titanate nanotubes (TNT) and titanate nanowires (TNW) were prepared using a hydrothermal approach in alkaline medium, starting from TiO₂ nanoparticles and amorphous precursors, respectively. These nanostructures were then modified with ethylenediamine (EDAmine), in acetone at reflux temperature, to produce NTNT and NTNW modified samples. A detailed description of the experimental procedure is presented in Chapter 10 (Methods and experimental).

2.3 – Structural, morphological and optical characterization

The identification and structural characterization of the prepared samples were performed using X-ray powder diffraction (XRD). The obtained diffractograms for the pristine, TNW and TNT, and EDAmine modified samples, NTNT and NTNW, are presented in Figure 2.2.

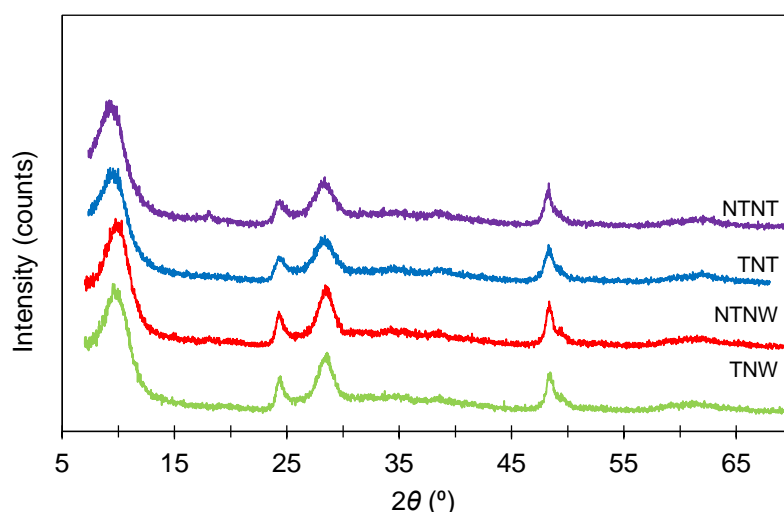


Figure 2.2 - XRD patterns of the TNW and TNT before and after sensitization with EDAmine.

The hydrothermal treatment of the amorphous precursor and TiO₂ nanoparticles in alkaline aqueous media at 160°C for 24 hours results in the production of two crystalline solids, TNW and TNT, respectively. For both samples, the XRD patterns are in agreement with the existence of a crystalline layered structure, type Na_{2-x}H_xTi₃O₇ (0 ≤ x ≤ 2) [26,27], with the diffraction peak at 2θ ~10° being characteristic of the interlayer distance between the TiO₆ sheets and the 24°, 28° and 48° peaks typical of tri-titanate 1D nanomaterials [28]. Comparing the TNT and TNW samples, it is perceptible a slight shift, for higher 2θ values, of the peak at 2θ ~10° for the TNW sample. Identical behavior has been described for titanate elongated powders with different Na⁺ contents [27]. These Na⁺ ions are localized between the TiO₆

layers and can be easily replaced by H^+ , or other cationic species, due to the high ion exchange ability of the layered titanate materials [29]. In this case, the difference observed on the 2θ values, for the TNT and TNW materials, 9.38° and 9.92° , respectively, can be attributed to Na^+H^+ partial replacement due to the difficulty of controlling this parameter during the H_2O washing process. This fact was confirmed by X-ray photoelectron spectroscopy (XPS) analysis, after which values of 14.16 and 9.48% were found for sodium contents in TNT and TNW samples, respectively. However, it must be said that this parameter didn't influence the results once the samples used for amine sensitization (TNT and TNW) were the same as those used for the characterization process.

After the EDAmine modification process, no shifts on the 10° or other peaks were observed (Figure 2.2) suggesting that no amine molecules were incorporated in the interlayers, replacing the Na^+ ions.

Due to the small dimensions expected for these powders, their morphology was analyzed by transmission electronic microscopy (TEM). The TEM images for the TNW and TNT samples are depicted in Figure 2.3.

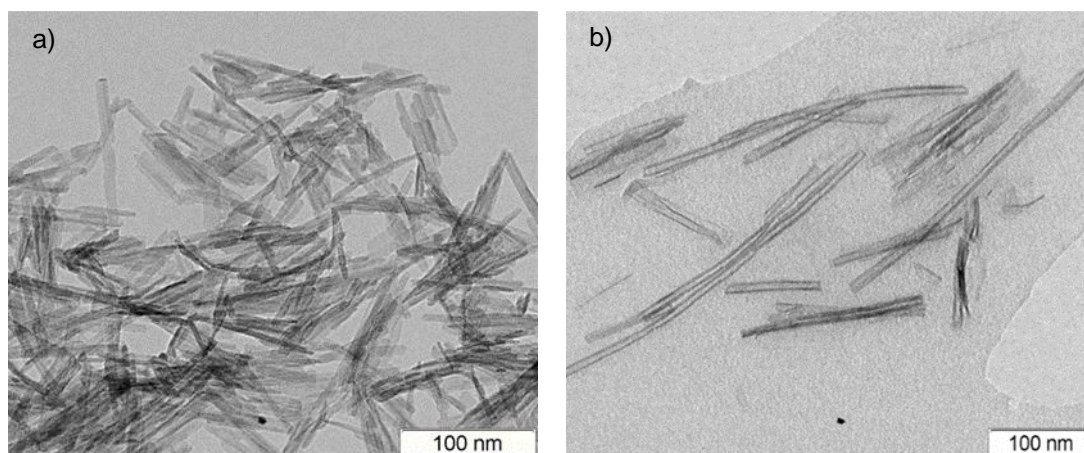


Figure 2.3 - TEM images of the (a) TNW and (b) TNT samples.

Images of both samples show very thin and elongated particles (Figure 2.3). However, a well-defined nanotubular morphology was observed for TNT sample in contrast with the not well-defined nanowires observed for the TNW sample. These samples (TNT and TNW) were prepared using the same experimental conditions (time, temperature and solvent) but distinct precursors; TNT was produced using nanocrystalline TiO_2 as the starting material while an amorphous precursor was used for the TNW synthesis. These results are in accordance with a previously reported work [30], but in disagreement with other reports, indicating that precise

control over the experimental conditions, mainly temperature and time, are essential to tailor the morphology of titanate nanotubes, nanowires or nanobelts [31,32].

The dimensions of the TNW and TNT particles were estimated by direct images measurements and diameter values of 4.5 ± 1.4 nm and 6.5 ± 2.6 nm were found, respectively. No morphological differences between the samples before and after EDAmine sensitization were observed (results not shown). Energy dispersive X-ray spectroscopy (EDS) analyses were performed in all the samples confirming Ti and Na existence. The presence of N, from the amine, was not observed due to equipment limitations. However, the existence of this element was, confirmed later by XPS, as discussed below.

Since the surface area is an important parameter to evaluate the catalytic performance of materials, the samples were characterized by N₂ adsorption-desorption measurements and the B.E.T. surface area of the samples was also calculated. TNT sample presents a surface area of 164.94 m² g⁻¹ and a slight decrease in this value, for 158.29 m² g⁻¹ was observed for the NTNNT sample. A 20% decrease was observed in the surface area of the TNW sample due to the EDAmine incorporation, from 233.66 m² g⁻¹ to 185.91 m² g⁻¹ respectively. These results are following previous reports describing different amino-functionalization of metal oxide particles [33] and can be seen as an possible effect of the increasing weight of the sample after modification.

The electronic structure of pristine (TNW and TNT) and modified samples (NTNW and NTNNT) was analyzed by XPS. As an example, the survey spectrum of NTNNT is shown in Figure 2.4. The Ti $2p_{3/2}$ and Ti $2p_{1/2}$ peaks, for TNW sample, appears at 458.641 and 464.441 eV, respectively. After EDAmine sensitization, and for sample NTNNT, a very small shifts to 458.717 and 464.517 eV were observed for those peaks, respectively. This increase of Ti $2p$ binding energy indicates an increase in the electro-positivity of the titanium ions on the catalyst surface [34]. No signals in the 456.2 – 457.4 eV range are visible, indicating no Ti³⁺ in the structure [35,36]. The Ti $2p$ peaks doublet splitting energies for these two samples is 5.8 eV, which also indicates the existence of titanium only as Ti⁴⁺ [37,38].

The main peak in the O $1s$ core-spectrum corresponds to lattice oxygen and the peak at ~ 530.241 eV it has a contribution of the sodium Auger peak (Na KLL). In both O $1s$ spectra, but more perceptible for NTNNT sample, a smaller peak at higher binding energy (around 532 eV) is observed. This peak can be attributed to surface hydroxyl groups, indicating the possible presence of chemisorbed water molecules.

From reported works, [39-41] typical binding energies of less than 397.5 eV are assigned to TiN species mostly with substitutional N, whilst N $1s$ peaks at binding energies above 400 eV

indicate that N is in the chemical adsorption state, like NO or NO₂, which can be formed due to surface oxidation. These latter species are reported as to be responsible for visible-light sensitization [42]. The N 1s binding energy, for NTNW and NTNT samples, it is visible at 400.225 eV and 400.117 eV, respectively (Figure 2.4(d)), confirming the existence of N-containing species on the TNT and TNW surface. In the C 1s spectrum, a strong peak at 285.217 eV can be assigned to the C–C bonds. However, the presence of carbon from most likely sample contamination doesn't allow any definitive conclusion to be made about the existence of amine on the surface. The XPS results obtained for TNT and NTNT samples are in agreement with the ones above discussed for TNW/NTNW.

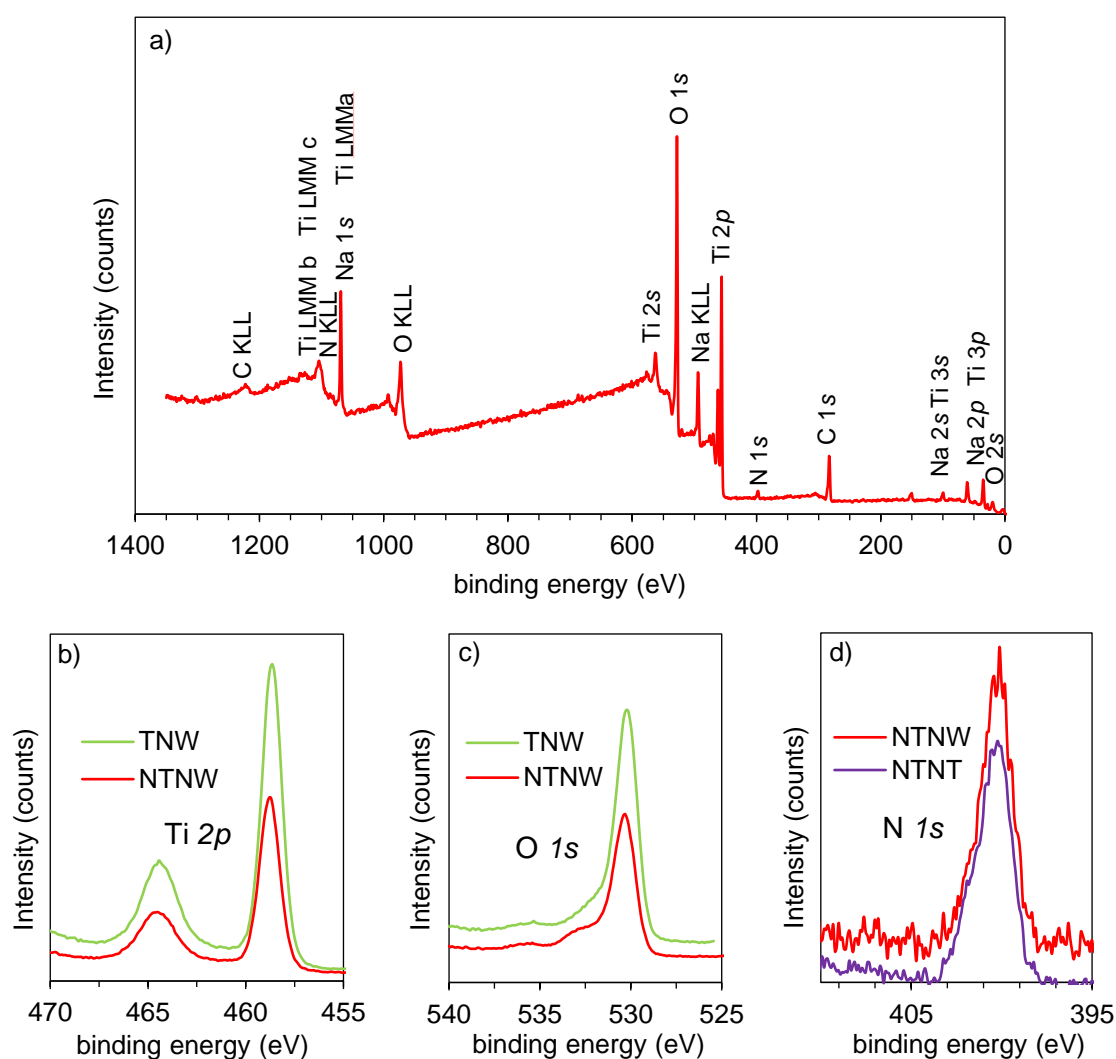


Figure 2.4 - XPS survey spectrum of the (a) NTNW sample; XPS high resolution spectra of the (b) Ti 2p, (c) O 1s for the NTNW and TNW powders and (d) N 1s for NTNT and NTNW samples.

Once the thickness of the particles is inferior to the XPS radiation penetration, and the sensitizing molecules are expected to be predominantly at the surface, the quantification of the

nitrogen in the prepared samples was performed. The ethylenediamine molecule (Figure 2.1) contains atoms, carbon, and hydrogen, which are not likely to be quantified by XPS. However, considering only Ti, Na, O and N for quantification, (underestimated) values of 2.8 and 3.1 at% were found for N contents in the NTNT and NTNW samples, respectively. These values are very similar, indicating that similar amounts of amine were immobilized in the surface of TNT and TNW particles. It was also interesting that the Na/Ti ratios obtained for NTNT and NTNW samples are similar, which are 0.533 and 0.540, respectively.

The prepared samples were optically characterized by diffuse reflectance spectroscopy (DRS) and the reflectance data were subsequently converted through the Kubelka–Munk function, as shown in Figure 2.5 (Chapter 10, for details).

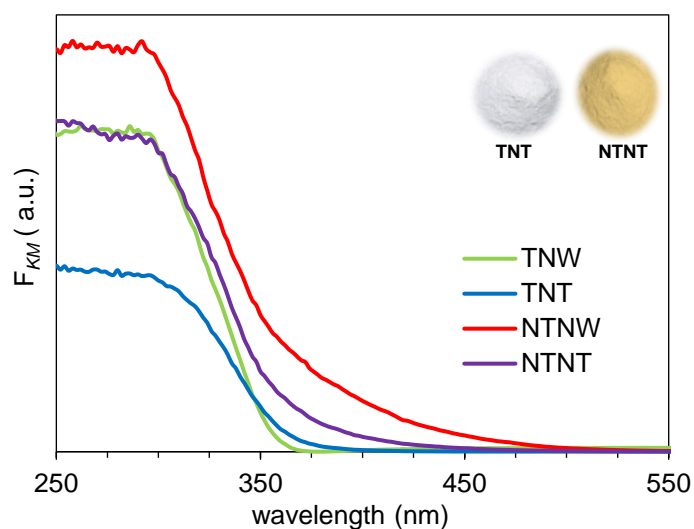


Figure 2.5 - Absorption spectra of the TNW, TNT, NTNW and NTNT samples.

The strong optical absorption edge near 400 nm observed for all the samples is characteristic of elongated titanate nanoparticles and it is due to the charge transfer mechanism of the O $2p$ orbital of the valence band to the Ti $3d t_{2g}$ orbital of the conduction band [26]. The optical absorption spectra of the TNT and TNW samples are similar but the band edge of the TNT is slightly shifted to the visible range. After EDAmine modification, both spectra are red shifted and an increase in the absorption intensity was observed. No other features were visualized resulting from the amine treatment. The bandgap energy (E_g) of the samples was calculated from the Kubelka–Munk (KM) spectra shown in Figure 2.5, by plotting the function $f_{KM} = (F_{KM} \cdot hv)^{0.5}$ versus hv . The values obtained were 3.35 and 2.88 eV for TNW and NTNW and 3.21, 3.09 eV for the TNT and NTNT samples, respectively.

The point of zero charge (p.z.c.) of the prepared samples was evaluated due to its relevance in heterogeneous processes, like photocatalysis. The p.z.c. is the value at which a solid submerged

in an electrolyte exhibits zero net electrical charge on the surface. Furthermore, p.z.c. determination is important to predict the charge on the surface of the nanoparticles during the photodegradation process. Since the photocatalysis occurs on the surface of the nanoparticles, the photocatalyst performance is highly influenced by the solution pH, the pollutant type and the surface ability to adsorb the pollutant. For pH values lower than p.z.c. the nanoparticles are carried with a positive charge (attracting anions), whereas, higher pH values promote the formation of negative charge on the surface of the nanoparticles (attracting cations/repelling anions).

The pH at which the surface carries no net charge was 2.4 and 2.8 for the TNT and TNW samples, respectively. The lower p.z.c. value obtained for the TNT agrees with the existence of enhanced ion-exchange ability due to the existence of more Na^+ ions in this sample's structure. This result also agrees with the one obtained during quantification by XPS. After EDAmine ($\text{pK}_{\text{a}1} = 7.6$) sensitization, positive shifts in the p.z.c. were observed for the NTNT and NTNW samples to around 2.8 and 2.9, respectively. These upward shifts indicate that the surfaces have been modified with the positively charged amino groups [43].

2.4 - Photocatalytic performance

2.4.1 - Photo-induced hydroxyl radical production

The hydroxyl radical ($\cdot\text{OH}$) photocatalytic formation was monitored during terephthalic acid (TA) degradation. Figure 2.6 shows the HTA amount produced from TA suspensions, during 30 min of irradiation.

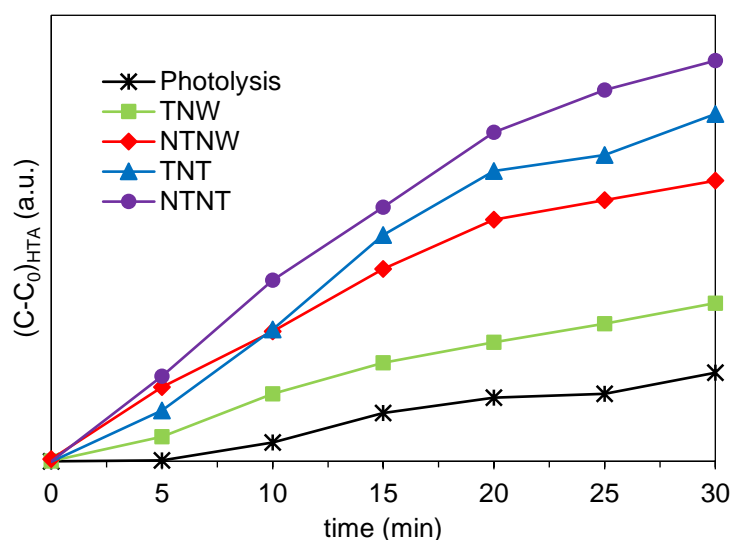


Figure 2.6 - HTA concentration variation during 30 min of irradiation of a TA solution (3 mM, 150 mL) using 10 mg of each photocatalyst.

As can be seen in Figure 2.6, all the samples showed catalytic activity, with the NTNT as the best catalyst for the photo-induction production of $\cdot\text{OH}$. Considering the TA photolysis as a reference, an increase of 350% in the $\cdot\text{OH}$ production was achieved using the NTNT photocatalyst and increases of 290 and 220% were attained for the use of TNT and NTNW samples, respectively. Using the pristine TNW sample, an increase of 80% in this radical production was observed. These results cannot be attributed only to surface area differences since NTNT sample presents the lowest surface area, but they allow the conclusion that the amine sensitization leads to an enhancement of the catalytic performance of the samples for this reaction. This suggests an active role of the surface amine groups in this process and permits anticipation of the best results for the amine modified samples especially in photocatalytic applications where $\cdot\text{OH}$ plays a crucial role.

However, to better clarify this point, TA photodegradation experiments without O_2 were performed (Figure 2.7). Generally, in this process, O_2 can have two main functions: as an electron scavenger and as an oxidant of fluorescent to non-fluorescent intermediates or final products [44].

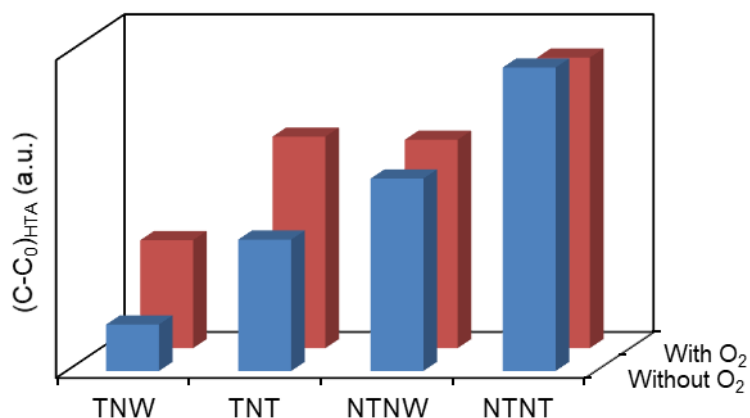


Figure 2.7 - Hydroxyl radical production after 15 min of irradiation, with and without O_2 , using 10 mg of each photocatalyst.

As expected for pristine samples, and after 15 min of irradiation, it is perceptible that the $\cdot\text{OH}$ production decreases in the absence of O_2 (Figure 2.7). O_2 is a natural e^- scavenger and without its presence, the production of the superoxide doesn't take place. Therefore, the photogenerated charge carrier recombination will increase. Consequently, the production of hydroxyl radical *via* superoxide route ($\text{O}_2 \rightarrow \text{O}_2^{\cdot-} \rightarrow \cdot\text{OH}$) and *via* H_2O and OH^- oxidation will decrease. This is also valid for the noncatalyzed process: when no catalyst was used, the decrease in HTA production due to the absence of O_2 in the system was 53% for the evaluation period.

For the amine modified samples, the O₂ presence/absence had almost no influence on their catalytic performances, with deviations of ~4 and 7% in the $\cdot\text{OH}$ production, for TNT and NTNW, respectively. These results strongly support the hypothesis that $\cdot\text{OH}$ production, in the amine modified samples, is mainly based on the hole trapping by adsorbed water molecules and hydroxyl groups (H₂O and OH⁻) and not *via* superoxide route. This also agrees with the results previously reported for nitrogen doped layered titanates [45]. On the other hand, these results also suggest no significant variation in the charge recombination rate in the absence of O₂, indicating that a new scavenger for the electrons should be present. This new scavenger must be correlated to the amine entities present on the catalyst surface.

Based on the above discussion and supported in literature [46-48], a mechanism for the charge-transfer processes in the TNT/TNW and NTNT/NTNW nanoparticles, after being activated by UV-vis radiation is proposed in Figure 2.8.

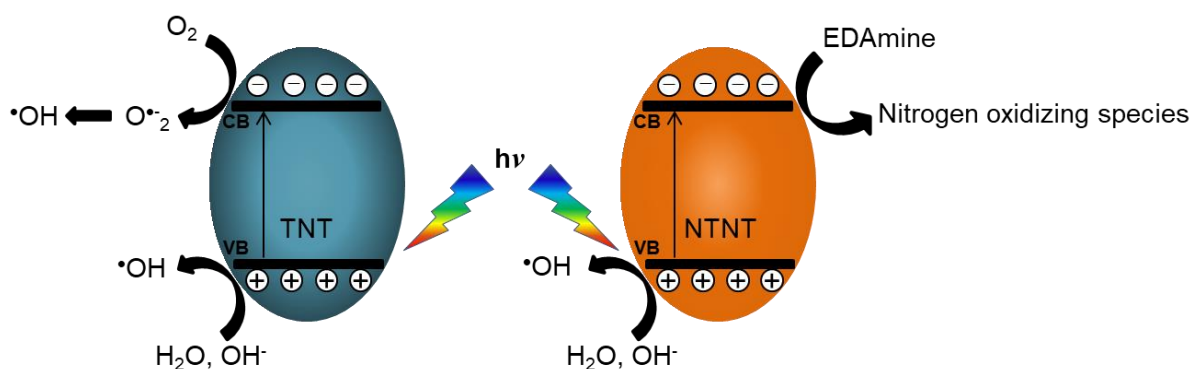


Figure 2.8 – Schematic representation of the energetic structure proposed for the TNT and hybrid NTNT particles under irradiation.

After irradiation of a TNT (or TNW) particle with energy higher than its bandgap, electrons (e^-) and holes (h^+) are generated in the conduction (CB) and valence band (VB) of the semiconductor, respectively. The photogenerated holes will react with OH⁻ and/or H₂O oxidizing them to $\cdot\text{OH}$ radicals. Simultaneously, the formation of O₂^{·-} species arises from the reduction of adsorbed oxygen. The extension of this process will determine the decrease in the recombination rate. The synergistic action of photogenerated h^+ and other highly oxidizing species, including O₂^{·-} and $\cdot\text{OH}$ radicals, will be responsible for the pollutants' photodegradation. If no O₂ is present during this process, no O₂^{·-} species will be formed and the photogenerated charge carrier recombination will be enhanced. Therefore, much fewer holes will be available to oxidize OH⁻/H₂O for $\cdot\text{OH}$ production. Consequently, no photocatalytic effect will be noticed, and the pollutant degradation will only be due to the photolysis effect.

For the NTNT and NTNW hybrid nanoparticles, some differences in this mechanism can be pointed out: slightly less energetic requirements to activate the catalyst since these particles possess lower bandgap energy when compared to the pristine samples. Nevertheless, the obtained results using visible light radiation (results presented below) indicate that this should not be the main reason justifying the better photocatalytic performance of these samples. For the N-modified samples, the obtained results in the presence and absence of O₂ are similar, suggesting that species other than O₂ will act as e⁻ scavengers. The amine entities on the surface should have an active role in this process by acting as scavengers themselves for the electrons injected in the CB. Thus, it will delay the electron-hole recombination and therefore the photocatalytic process efficiency will be enhanced. Under these circumstances, the formation of nitrogen oxidizing species, which will also promote the pollutant degradation, it cannot be completely ruled out.

2.4.2 - Caffeine, theophylline, and phenol photocatalytic degradation

As mentioned in Chapter 1, caffeine, theophylline and phenol (Figure 2.9) are some examples of emergent pollutants that have been often found in wastewaters. Caffeine and theophylline are present in energy drinks, tea, coffee, and pharmaceuticals, and phenol is widely used in the chemical industry and is also a by-product of many other pollutants. For these reasons, these three compounds were chosen as model contaminants to further evaluate the photocatalytic performance of the prepared samples, under UV-vis and visible radiation. The adsorption characteristics of the pollutant/catalyst system are expected to be important since photo-oxidation reactions usually occur at the catalyst surface. Therefore, the ability of the samples to adsorb these three pollutants was previously investigated for 60 min, under dark conditions.

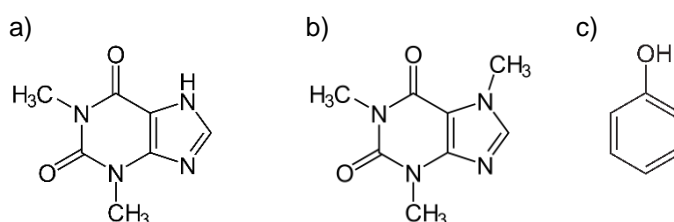


Figure 2.9 – Schematic representation of the (a) theophylline, (b) caffeine and (c) phenol molecules.

• Theophylline photodegradation

The photocatalytic efficiency of the pristine and modified TNT and TNW samples on a theophylline solution (20 ppm) degradation was evaluated during 90 min of UV-vis irradiation (Figure 2.10). Figure 2.10(a) depicts the theophylline spectra during irradiation, in the presence

of the NTNT sample as a catalyst. Theophylline concentration decreases during irradiation time, using all the prepared samples as catalysts, which were analyzed by LC-HR-ESI/MS. The obtained results are shown in Figure 2.10(b).

As can be seen in Figure 2.10(a), the theophylline removal is easily confirmed by the decrease gradually of the 272 nm peak during irradiation time.

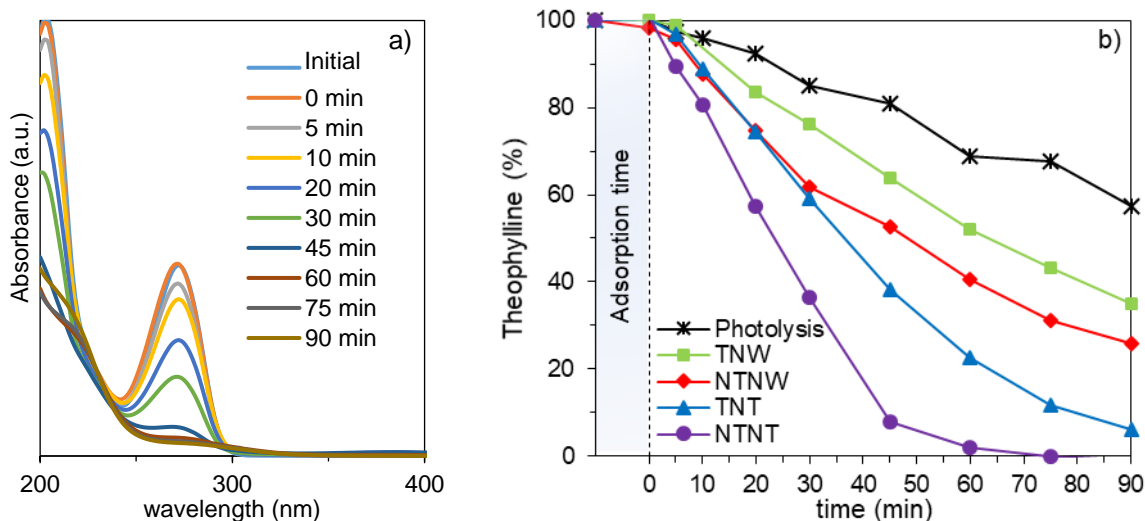
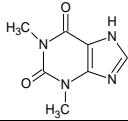
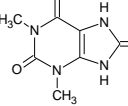
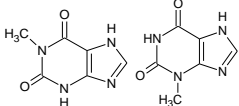
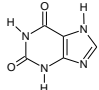
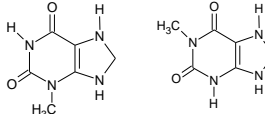
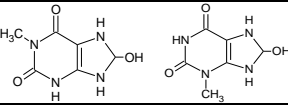
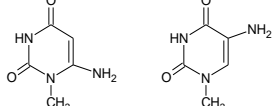
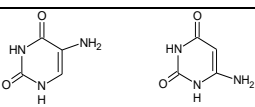
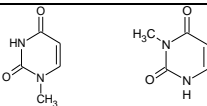
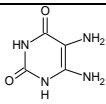


Figure 2.10 – (a) UV-vis spectra of theophylline solution degradation, using NTNT sample as photocatalyst. (b) Theophylline photocatalytic degradation during 90 min of irradiation using the pristine and hybrid powders as photocatalysts (20 ppm; 0.13 g L⁻¹).

After 60 min in the dark (Figure 2.10(b)), no substantial adsorption of theophylline was observed, independent of the sample used. Under irradiation, all the powders demonstrated photocatalytic activity for theophylline degradation. After 60 min of irradiation, the best sample for this pollutant removal was NTNT with a 98.0% decrease in its concentration. The second best photocatalyst, for the same period, was the unmodified TNT with 77.5% of theophylline removal. For this sample, 45 min more was needed to achieve 98.0% of degradation. During this irradiated process, and considering the two TNW based samples, the modified NTNW was the one presenting the highest photocatalytic activity. This result corroborates the positive influence of the amine sensitization on the production of better photocatalysts for processes based on the $\cdot\text{OH}$ radical oxidizing action.

The identification of the by-products produced during theophylline photodegradation using NTNT as catalyst was carried out by LC-HR-ESI/MS. The results are presented in Table 2.1 and agree with a degradation mechanism reported in the literature [49] and shown in Annex B – Figure B.1.

Table 2.1 - Main products identified by LC-HR-ESI/MS for the photocatalytic degradation of theophylline using NTNT as catalyst

Compound	Product	Mol. wt.	Elemental composition	m/z	structure
---	Theophylline	180.16	C ₇ H ₈ N ₄ O ₂	181.0727	
Theo-1	1,3-Dimethyluric acid	196.16	C ₇ H ₈ N ₄ O ₃	197.0675	
Theo-2	1/3-Methylxanthine	166.14	C ₆ H ₆ N ₄ O ₂	167.0565	
Theo-3	Xanthine	152.11	C ₅ H ₄ N ₄ O ₂	153.0410	
Theo-4	1/3-Methyltetrahydro-1H-purine-2,6-dione	168.15	C ₆ H ₈ N ₄ O ₂	169.0720	
Theo-5	8-Hydroxy-1/3-methyl-3,7,8,9-tetrahydro-1H-purine-2,6-dione	184.15	C ₆ H ₈ N ₄ O ₃	185.0669	
Theo-6	5/6-Amino derivative of 1/3-methylpyrimidine-2,4(1H,3H)-dione	141.13	C ₅ H ₇ N ₃ O ₂	142.0611	
Theo-7	5/6-Aminopyrimidine-2,4(1H,3H)-dione	127.10	C ₄ H ₅ N ₃ O ₂	128.0454	
Theo-8	1/3-Methylpyrimidine-2,4(1H,3H)-dione	126.11	C ₅ H ₆ N ₂ O ₂	127.0502	
Theo-9	5,6-Diaminopyrimidine-2,4(1H,3H)-dione	142.12	C ₄ H ₆ N ₄ O ₂	143.0563	

The profile of such intermediates with the irradiation time was also studied and the results are in Figure 2.11 where a sequential degradation process can be visualized.

In the first minutes after turning on the irradiation, high production of compounds **Theo-1** and **Theo-8** was detected and after 10 min other products start to be formed, namely **Theo-7** and **Theo-6**. Although after 75 min no theophylline was detected in solution, the presence of products **Theo-1** and **Theo-8** is still high, indicating that more time is required to complete the degradation of these by-products.

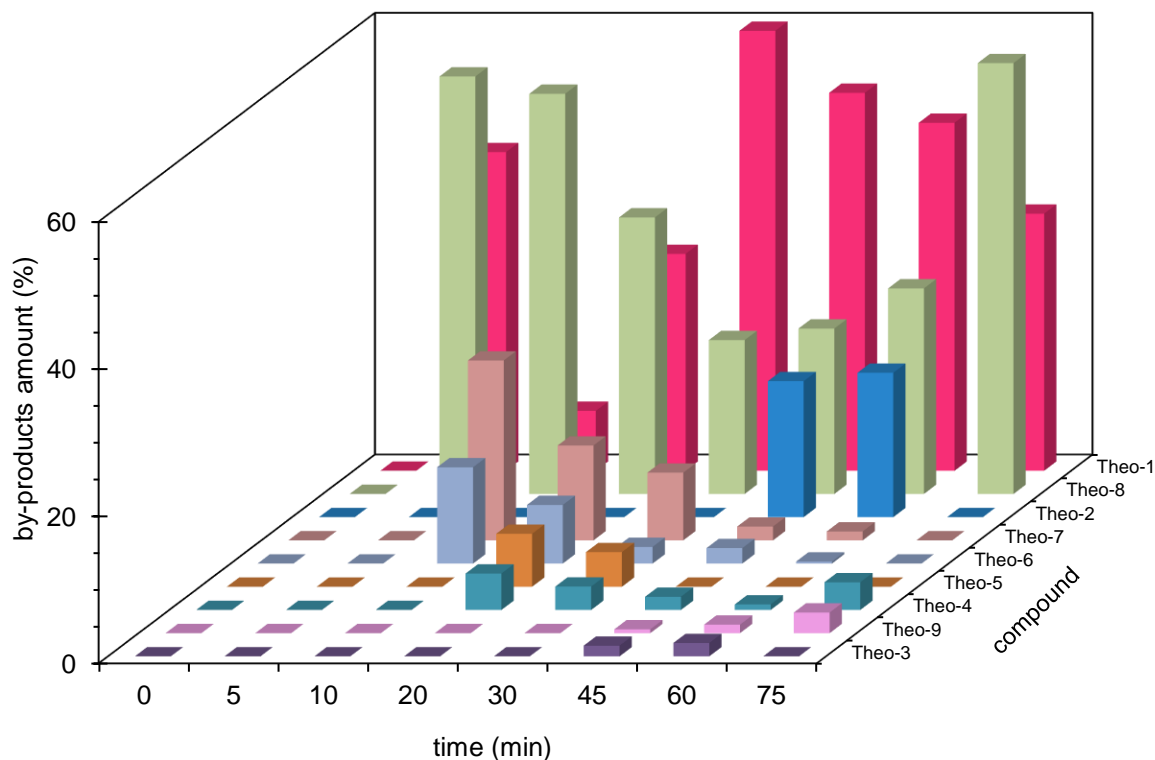


Figure 2.11 – Variation of the compounds identified during 75 min of theophylline photocatalytic degradation, using NTNT as catalyst.

• Caffeine photodegradation

The catalytic efficiency of the samples on caffeine (20 ppm solution) photo-assisted removal was evaluated during 90 min of UV-vis irradiation. The obtained degradation results are presented in Figure 2.12. The UV-vis spectra obtained during irradiation time using NTNT sample as catalyst were also depicted in Figure 2.12(a), and it is possible to confirm the caffeine degradation due to the decrease of the characteristic peak, at 272 nm, with the irradiation time. As can be seen in Figure 2.12(b), for this pollutant and as observed for theophylline, no substantial caffeine was adsorbed independent on the sample used. However, all the samples showed photocatalytic activity for this degradation process, but the samples modified with EDamine (NTNT and NTNW) demonstrated better catalytic performances than the pristine ones.

The best photocatalytic performance was obtained using the NTNT sample with 80% caffeine degradation over 90 min of irradiation. For the two pristine samples (TNT and TNW), the best photocatalytic activity was achieved using the nanotubes (TNT). After 90 min without catalyst (photolysis), only 20% of the initial caffeine was removed from the solution.

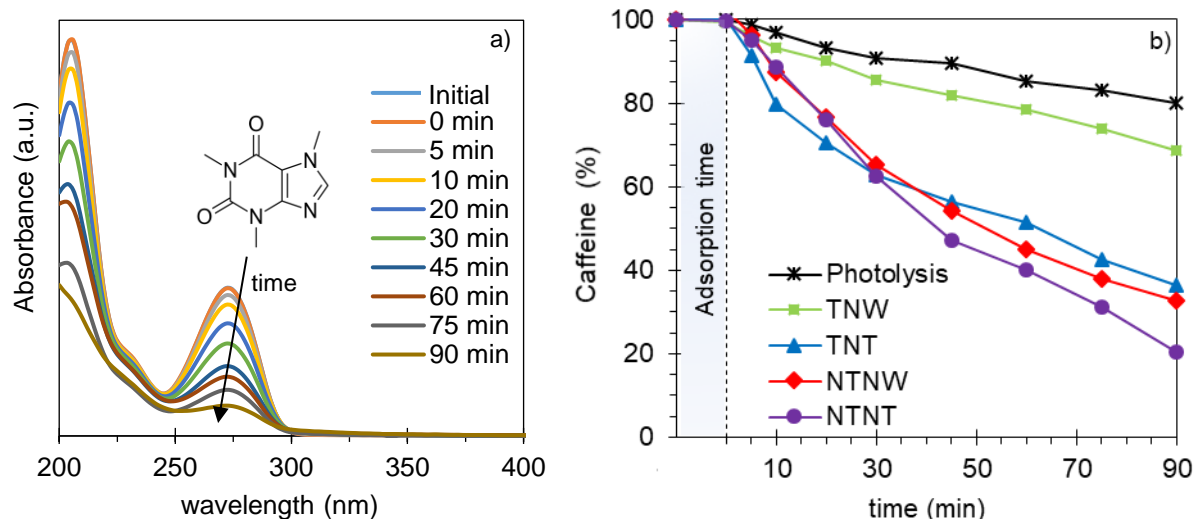


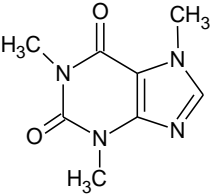
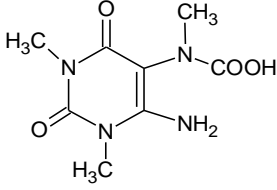
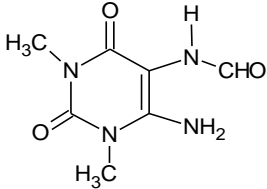
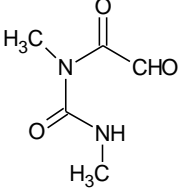
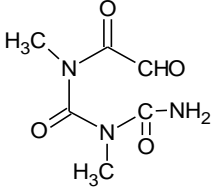
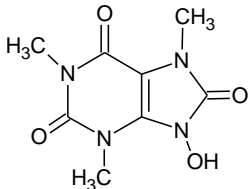
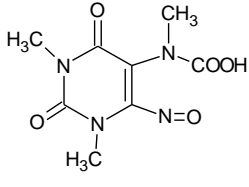
Figure 2.12 - (a) UV-vis spectra of caffeine solution degradation, using NTNT sample as photocatalyst. (b) Caffeine photocatalytic degradation during 90 min of irradiation using the pristine and hybrid powders as photocatalysts (20 ppm; 0.13 g L⁻¹).

It is interesting to compare the results obtained for the two methylxanthine compounds, theophylline, and caffeine (Figure 2.9): the chemical structures of these compounds are very similar, but caffeine possesses more methyl groups instead of protons and this seems to be the reason why, under identical experimental conditions, the theophylline degrades faster than caffeine.

As for theophylline, the evaluation of the by-products formed during caffeine photodegradation was performed by LC-HR-ESI/MS and the identified compounds are shown in Table 2.2. These results are in agreement with a degradation mechanism proposed by others in literature [50,51] and shown in Annex B – Figure B.2.

The profile of the by-products with irradiation time was also studied and the results are in Figure 2.13. It is visible that the caffeine degradation starts with its conversion to compound **CAF-1** and after 5 min of irradiation the formation of compound **CAF-4** begins. The amount of this product increases during the 90 min of irradiation, contrasting with the fast decrease observed for compound **CAF-1**. Together with product **CAF-4**, the profiles of the by-products detected in lower quantities (Figure 2.13(b)) also suggest that caffeine degrades first to product **CAF-4** and afterward this it degrades to the other compounds detected. Also, as in theophylline study, a longer irradiation period will be necessary to complete the degradation of all the secondary products.

Table 2.2 - Main fragments and correspondent by-products identified by LC-HR-ESI/MS for the photodegradation of caffeine using NTNT as catalyst

Compound	Formula	Experimental mass (m/z)	Mol.wt.	Structure
Caffeine	$C_8H_{11}N_4O_2$	195.0876	194	
CAF-1	$C_8H_{12}N_4O_4Na$	251.0751	228	
	$C_7H_{10}N_3O_3$	184.0713		
	$C_5H_7N_2O_2$	127.0499		
CAF-2	$C_7H_{11}N_4O_3$	199.0824	198	
	$C_5H_8N_3O_2$	142.0609		
CAF-3	$C_5H_8N_2O_3Na$	167.0426	144	
CAF-4	$C_6H_9N_3O_4Na$	210.0485	187	
	$C_6H_8N_3O_3$	170.0560		
CAF-5	$C_8H_{11}N_4O_4$	227.0774	226	
CAF-6	$C_8H_{10}N_4O_5Na$	265.0547	242	
	$C_8H_9N_4O_4$	225.0620		

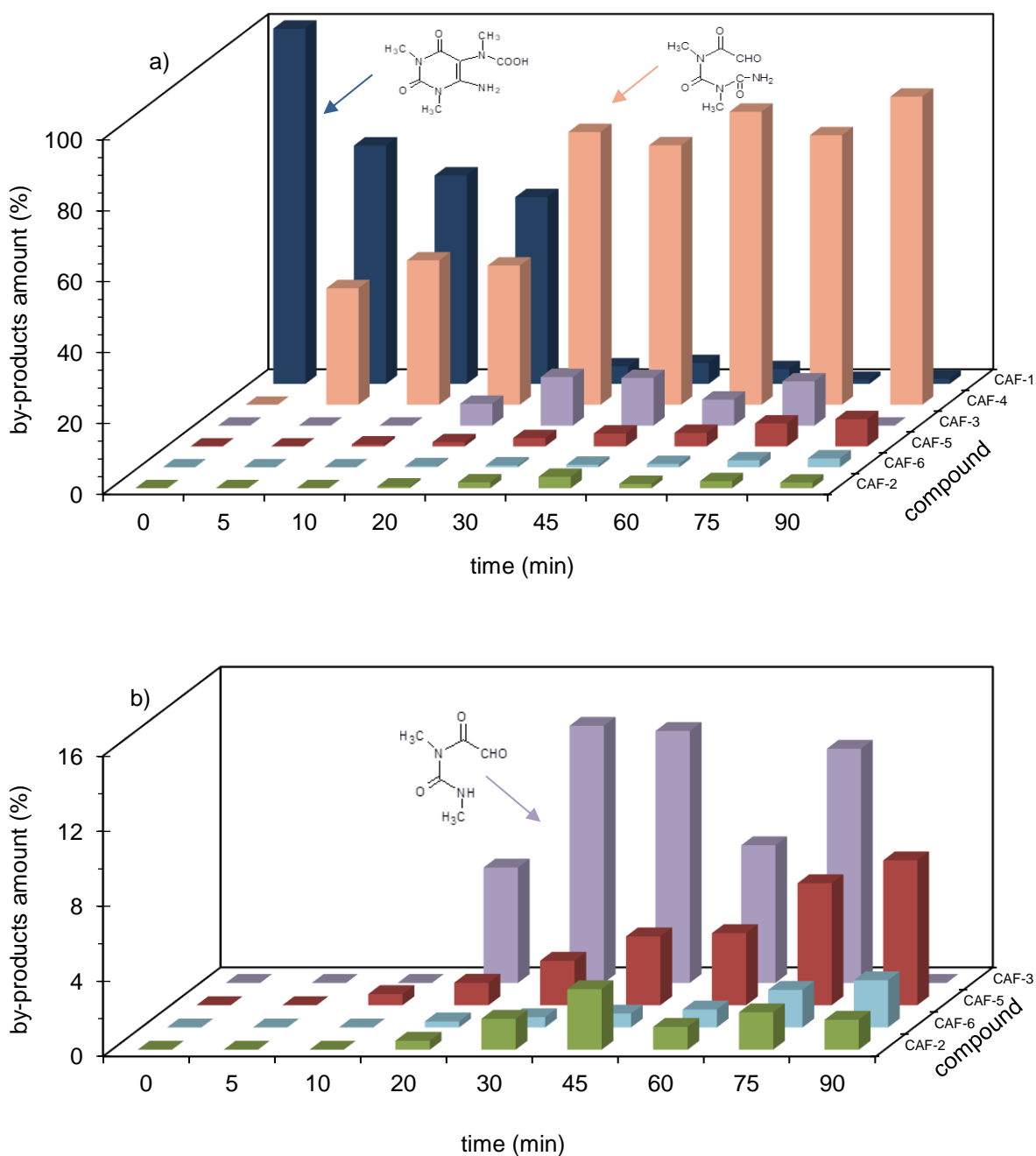


Figure 2.13 – (a) Variation of the compounds identified during 90 min of caffeine photocatalytic degradation, using NTNT as catalyst, (b) detail for the lower amount compounds.

• Phenol photodegradation

The photocatalytic activity of the prepared samples for phenol degradation was also analyzed. The phenol absorption spectrum is characterized by one main band at $\lambda = 270$ nm. During the phenol photodegradation, the intensity of this band sometimes increases and/or broadens due to the simultaneous absorption of phenol and/or several degradation by-products [52,53]. To avoid incorrect conclusions about this process, GC-MS was chosen to quantify the phenol photodegradation process. Figure 2.14 shows the phenol concentration profiles during 90 min

of irradiation for all the prepared samples tested as photocatalysts. As can be seen in Figure 2.14, after a dark period, ~10% of the initial phenol was adsorbed by both pristine samples (TNT and TNW), and ~20% was adsorbed by the EDAmine modified ones. This agrees with the p.z.c of the samples and the pK_a of phenol ($pK_a = 10.0$).

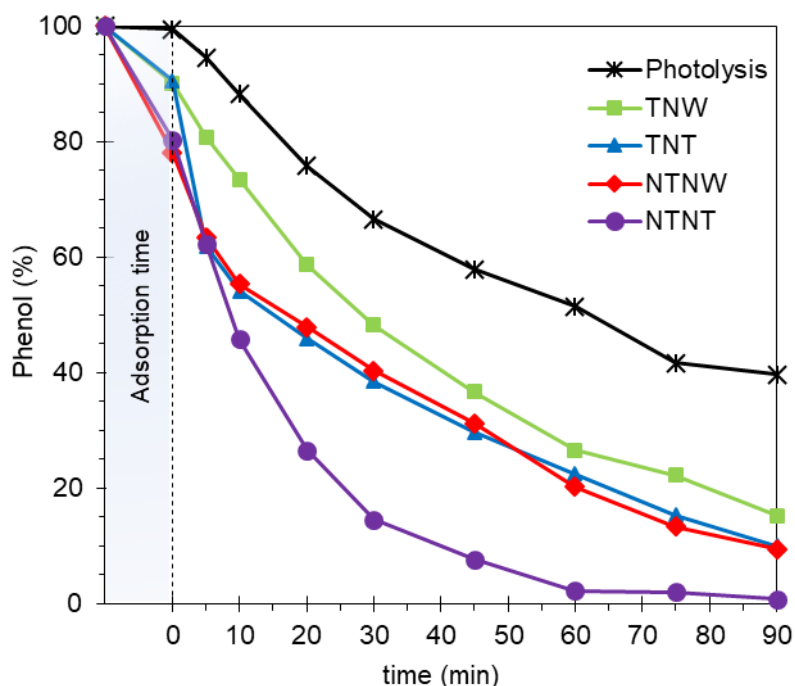
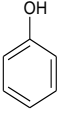
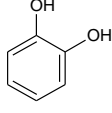
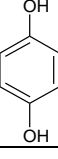
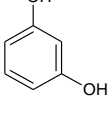


Figure 2.14 - Phenol photocatalytic degradation during 90 min of irradiation using the pristine and hybrid powders as photocatalysts (20 ppm; 0.13 g L⁻¹).

It is possible to see that all the samples are catalytic for phenol degradation. Using the NTNT sample as a photocatalyst, a decrease of 97.8% on the phenol in solution was achieved within 60 min of irradiation. To complete the phenol removal, 30 min more was required. Without any catalyst (photolysis), it decreases by 48.6% and 60.3% in phenol concentration, after 60 and 90 min, respectively. The TNT and NTNW photocatalytic performances were very similar with nearly 90% pollutant removal attained after 90 min of irradiation. These results confirm that the $\cdot\text{OH}$ radical is one of the most active oxidizing species in charge of phenol photodegradation [54].

During phenol photodegradation, the identification of the formed by-products was monitored by GC-MS. The existence of hydroquinone, catechol, and resorcinol, in very low percentages, was confirmed (Table 2.3), being these results in agreement with a degradation mechanism reported work [55] and shown in Annex B – Figure B.3.

Table 2.3 - Main products identified by GC-MS for the phenol photocatalytic degradation process using NTNT as catalyst

Product	Mol. wt.	Elemental composition	Structure
Phenol	94	C ₆ H ₆ O	
Catechol	110	C ₆ H ₆ O ₂	
Hydroquinone	110	C ₆ H ₆ O ₂	
Resorcinol	110	C ₆ H ₆ O ₂	

The photocatalytic degradation of theophylline, caffeine, and phenol, using the TNT and NTNT catalysts was also tested under visible radiation; over 90 min for theophylline and phenol and 120 min for caffeine. As expected, the photocatalytic degradation rate of all the pollutants was significantly lower compared to the performances obtained using UV-vis radiation. However, as for the UV-vis radiation experiments, the best photocatalytic results were obtained using the NTNT sample. These results seem in agreement with the slight shift observed in the NTNT bandgap energy, in the visible range. However, this increase in energy absorption, due to the presence of the amine entities on the TNT surface, cannot justify, by itself, the enhanced photocatalytic performance of these materials, which should be validated by the essential role of the amine groups in the decrease of the electron-hole recombination rate, as discussed in Section 2.4.1.

2.4.3 – Kinetic studies

The kinetics of the caffeine, theophylline, and phenol photodegradation were evaluated through the application of a first-order kinetics model, characterized by an exponential decrease in pollutant concentration with time. In this case, the plot of $\ln(C)$ versus t , where C is the concentration at time t , is a straight line, whose slope is $-k$, which is the reaction rate constant. The profiles of the TNT and NTNT catalyzed processes are presented in Figure 2.15, and the results obtained for all the samples are presented in Table 2.4.

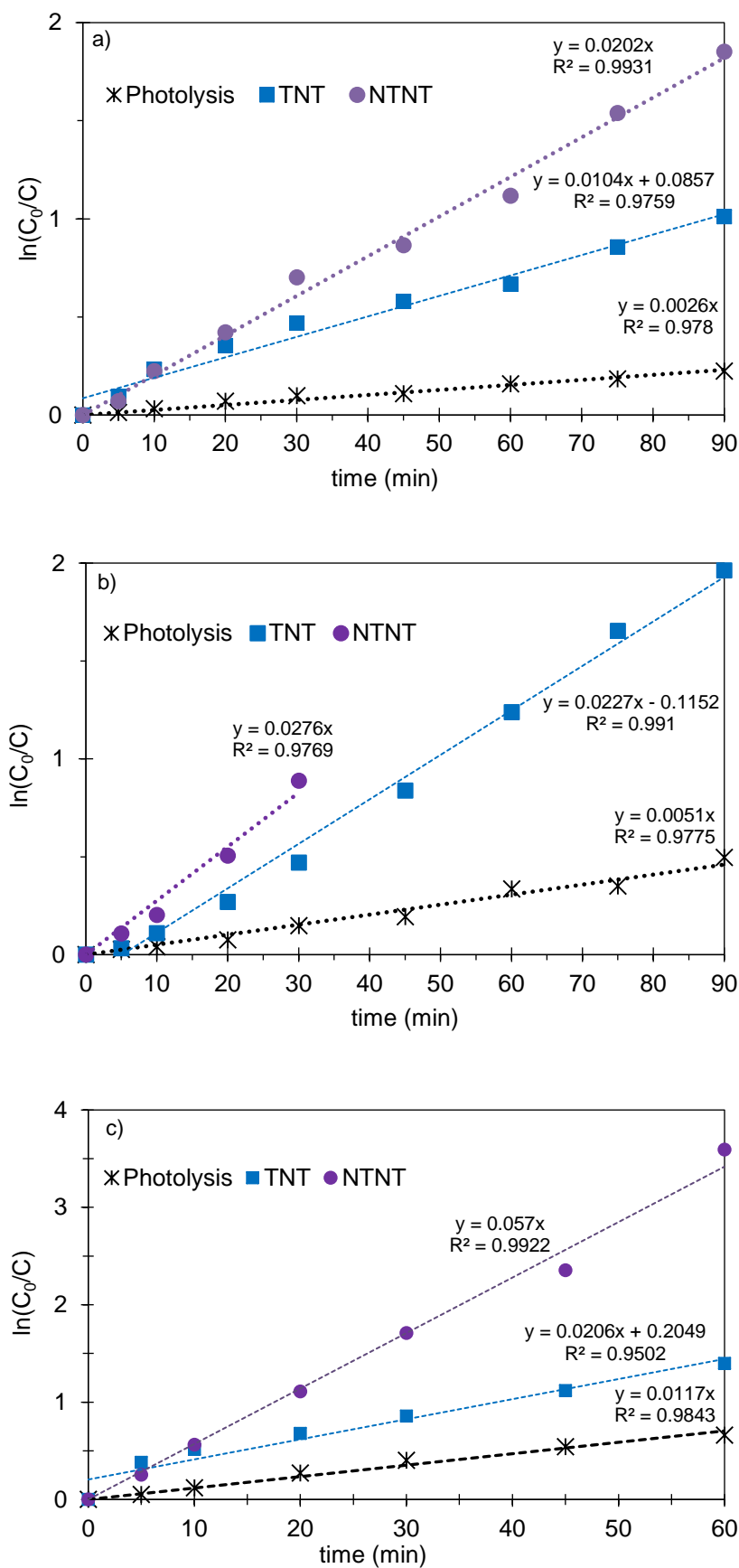


Figure 2.15 - Kinetics of the photocatalytic degradation reactions of (a) theophylline, (b) caffeine and (c) phenol solutions.

Considering the caffeine degradation, the k obtained for the photolysis and the TNT and NTNT catalyzed processes were 0.0026, 0.0104 and 0.0202 min^{-1} , respectively. These results confirm a faster caffeine photodegradation for the catalyzed runs when compared with the photolysis (0.0026 min^{-1}) or the ones obtained using the TNW and NTNW particles (0.0041 and 0.0133 min^{-1} , respectively). Interestingly, the process with the best photocatalytic results (using NTNT) is almost 10 times faster than photolysis. After amine sensitization, increases of 1.7 and 3.2 times in the constant value were observed for TNT and TNW samples, respectively, demonstrating its relevance for the caffeine photodegradation process success.

The analysis of theophylline photodegradation kinetics indicates that the faster process is the one catalyzed by NTNT with a k value of 0.0276 min^{-1} . Once again, the values obtained for k indicate that the photocatalytic degradation of theophylline is faster than that of caffeine, independent on the catalyst used. In the presence of the best photocatalyst, NTNT, phenol was the pollutant easier to be degraded, presenting in these circumstances a k of 0.0570 min^{-1} .

Table 2.4 - Rate constants for the studied photocatalytic degradations

Sample	Surface area ($\text{m}^2 \text{g}^{-1}$)	Rate constant ^a (min^{-1})		
		Caffeine	Theophylline	Phenol
TNT	164.94	0.0104	0.0227	0.0206
NTNT	158.29	0.0202	0.0276	0.0570
TNW	233.66	0.0041	0.0103	0.0204
NTNW	185.91	0.0133	0.0127	0.0222
Photolysis	-	0.0026	0.0051	0.0117

^a With correlation coefficients higher than 0.9770.

2.4.4 – Reusability and stability studies

The reusability of the best photocatalyst (NTNT sample) was tested for the three pollutants removal during 4 runs of 75 min each. Due to the inferior photocatalytic results obtained for caffeine, a period of 120 min was chosen in this case. Figure 2.16 shows the photodegradation results obtained for these 4 runs, indicating that NTNT sample is stable without significant loss of catalytic activity. These results indicate that during these 4 cycles, no signals of surface poisoning and no release from the surface to the solution of the amine groups were observed, attesting the high stability of this sample when used as photocatalysts under UV-vis radiation. Only for caffeine, a slight decrease in catalytic performance was observed for the 4th cycle.

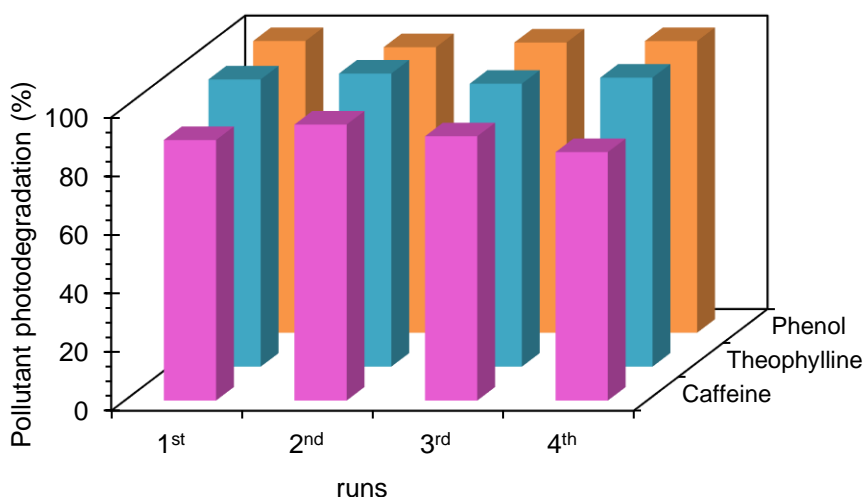


Figure 2.16 - Percentage of theophylline, caffeine and phenol removal, during four cycles of photocatalytic degradation using the same NTNT sample as catalyst.

Raman spectroscopy was used to confirm the stability of the TNT/NTNT samples before and after being submitted to UV-vis radiation (Figure 2.17).

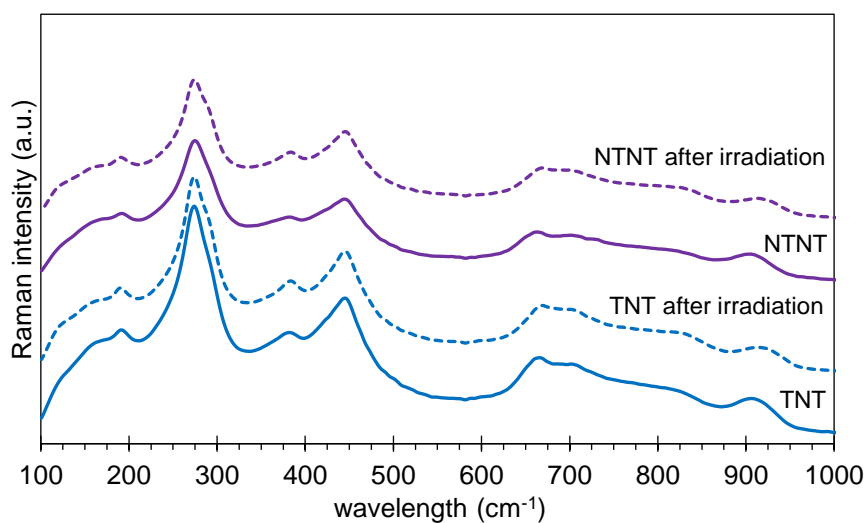


Figure 2.17 – Raman spectra of the TNT and NTNT samples before and after being submitted to UV-vis radiation (90 min).

The obtained results for the as-prepared sample are in agreement with the literature [46,56] and the ones obtained after irradiation indicate that no perceptible changes or rearrangements in the microstructure occurred for all the analyzed samples.

2.5 - Conclusions

The obtained results indicate that TNT/TNW and NTNT/NTNW are promising materials, with high stability, to be further investigated as photocatalysts for the organic pollutants removal.

For both sensitized materials, experiments performed in the absence of O₂ indicate no changes in hydroxyl radical production, thus confirming that holes are the main responsible for the formation of this radical. The photocatalytic performance of the sensitized materials for the degradation of the psychoactive substances, caffeine and theophylline, and for phenol removal was evaluated. The best results were obtained using NTNT, achieving 60% photodegradation efficiency for caffeine and 98% for phenol and theophylline (20 ppm solutions), respectively, within 60 min under UV-vis radiation. However, an issue that must be carefully examined before proceeding with a scale-up methodology is the toxicity of the by-products produced during the photocatalytic degradation of the pollutants. The production of more toxic products than the initial pollutants must be avoided.

2.6 - References

- 1 - M. Neouze, U. Schubert, Surface modification and functionalization of metal and metal oxide nanoparticles by organic ligands, *Monatsh. Chem.* 139 (2008) 183-195.
- 2 - X. Li, L. Liu, S.Z. Kang, J. Mu, G. Li, Titanate nanotubes co-sensitized with cadmium sulfide nanoparticles and porphyrin zinc, *Catal. Commun.* 17 (2012) 136-139.
- 3 - T.A. Silva, J. Diniz, L. Paixão, B. Vieira, B. Barrocas, C.D. Nunes, O.C. Monteiro, Novel titanate nanotubes-cyanocobalamin materials: Synthesis and enhanced photocatalytic properties for pollutants removal, *Solid State Sci.* 63 (2017) 30-41.
- 4 - G. Liu, L. Wang, C. Sun, X. Yan, X. Wang, Z. Chen, S.C. Smith, H. Cheng, G.Q. Lu, Band-to-band visible-light photon excitation and photoactivity induced by homogeneous nitrogen doping in layered titanates, *Chem. Mater.* 21 (2009) 1266-1274.
- 5 - N.M. Nursam, X. Wang, J.Z.Y. Tan, R.A. Caruso, Probing the Effects of templating on the UV and visible light photocatalytic activity of porous nitrogen-modified titania monoliths for dye removal, *ACS Appl. Mater. Interfaces* 8 (2016) 17194-17204.
- 6 - N. Bao, J. Niu, Y. Li, G. Wu, X. Yu, Low-temperature hydrothermal synthesis of N-doped TiO₂ from small-molecule amine systems and their photocatalytic activity, *Environ. Technol.* 34 (2013) 2939-2949.

- 7 - X. Fu, H. Yang, H. Sun, G. Lu, J. Wu, The multiple roles of ethylenediamine modification at TiO₂/activated carbon in determining adsorption and visible-light-driven photoreduction of aqueous Cr(VI), *J. Alloy. Compd.* 662 (2016) 165-172.
- 8 - M. Raza, A. Bachinger, N. Zahn, G. Kickelbick, Interaction and UV-stability of various organic capping agents on the surface of anatase nanoparticles, *Materials* 7 (2014) 2890-2912.
- 9 - B. Barrocas, M.C. Neves, M.C. Oliveira, O.C. Monteiro, Enhanced photocatalytic degradation of psychoactive substances using amine-modified elongated titanate nanostructures, *Environ. Sci.: Nano* 5 (2018) 350-361.
- 10 - V. Kumaravel, S. Mathew, J. Bartlett, S.C. Pillai, Photocatalytic hydrogen production using metal-doped TiO₂: A review of recent advances, *Appl. Catal. B* 244 (2019) 1021-1064.
- 11 - J. Wang, D.N. Tafen, J.P. Lewis, Z.L. Hong, A. Manivannan, M. Zhi, M. Li, N. Wu, Origin of photocatalytic activity of nitrogen-doped TiO₂ nanobelts, *J. Am. Chem. Soc.* 131 (2009) 12290-12297.
- 12 - J.G. Mahy, V. Cerfontaine, D. Poelman, F. Devred, E.M. Gaigneaux, B. Heinrichs, S.D. Lambert, Highly Efficient Low-Temperature N-Doped TiO₂ Catalysts for Visible Light Photocatalytic Applications, *Materials* 11 (2018) 584(1)-584(20).
- 13 - M. Pelaez, N.T. Nolan, S.C. Pillai, M.K. Seery, P. Falaras, A.G. Kontos, P.S.M. Dunlop, J.W.J. Hamilton, J.A. Byrne, K. O'Shea, M.H. Entezari, D.D. Dionysiou, A review on the visible light active titanium dioxide photocatalysts for environmental applications, *Appl. Catal. B* 125 (2012) 331-349.
- 14 - C. Di Valentin, E. Finazzi, G. Pacchioni, A. Selloni, S. Livraghi, M.C. Paganini, E. Giamello, *Chemical Physics* 339 (2007) 44-56.
- 15 - J. Lv, J. Liu, J. Zhang, K. Dai, C. Liang, Z. Wang, G. Zhu, Construction of organic-inorganic cadmium sulfide/diethylenetriamine hybrids for efficient photocatalytic hydrogen production, *J. Colloid Interf. Sci.* 512 (2018) 77-85.
- 16 - Zhen Li, Yang Yang, Kai Dai, Jinfeng Zhang, Luhua Lu, Construction of defective Mo₁₅S₁₉/CdS-diethylenetriamine heterostructure photocatalyst for highly active and stable

noble-metal-free photocatalytic hydrogen production, *Applied Surface Science* 469 (2019) 505-513.

17 - S. Photong, V. Boonamnuayvitaya, Enhancement of formaldehyde degradation by amine functionalized silica/titania films, *J. Environ. Sci.* 21 (2009) 1741-1746.

18 - S. Photong, V. Boonamnuayvitaya, Synthesis of APTMS-functionalized SiO₂/TiO₂ transparent film using peroxy titanate acid refluxed solution for formaldehyde removal, *Water Air Soil Pollut.* 210 (2010) 453-461.

19 - Y. Ma, X. Wang, Y. Jia, X. Chen, H. Han, C. Li, Titanium dioxide-based nanomaterials for photocatalytic fuel generations, *Chem. Rev.* 114 (2014) 9987-10043.

20 - N.M. Nursam, X. Wang, J.Z.Y. Tan, R.A. Caruso, Probing the Effects of templating on the UV and visible light photocatalytic activity of porous nitrogen-modified titania monoliths for dye removal, *ACS Appl. Mater. Interfaces* 8 (2016) 17194-17204.

21 - N. Bao, J. Niu, Y. Li, G. Wu, X. Yu, Low-temperature hydrothermal synthesis of N-doped TiO₂ from small-molecule amine systems and their photocatalytic activity, *Environ. Technol.* 34 (2013) 2939-2949.

22 - X. Fu, H. Yang, H. Sun, G. Lu, J. Wu, The multiple roles of ethylenediamine modification at TiO₂/activated carbon in determining adsorption and visible-light-driven photoreduction of aqueous Cr(VI), *J. Alloy. Compd.* 662 (2016) 165-172.

23 - H. Li, Y. B. Hao, H. Q. Lu, L. P. Liang, Y. Y. Wang, J. H. Qiu, X. C. Shi, Y. Wang, J. F. Yao, A systematic study on visible-light N-doped TiO₂ photocatalyst obtained from ethylenediamine by sol-gel method, *Appl. Surf. Sci.* 344 (2015) 112-118.

24 - M. Sun, Y. Fang, S. Sun, Y. Wang, Surface co-modification of TiO₂ with N doping and Ag loading for enhanced visible-light photoactivity, *RSC Adv.* 6 (2016) 12272-12279.

25 - Z. Jiang, L. Kong, F.S. Alenazey, Y. Qian, L. France, T. Xiao P.P. Edwards, Enhanced visible-light-driven photocatalytic activity of mesoporous TiO_{2-x}N_x derived from the ethylenediamine-based complex, *Nanoscale* 5 (2013) 5396-5402.

- 26 - F.C. Bavkin, Titanate and Titania Nanotubes: Synthesis, Properties and Applications. RSC Nanoscience & Nanotechnology Series, RSC Publishing, Cambridge, 2010.
- 27 - V. Bem, M.C. Neves, M.R. Nunes, A.J. Silvestre, O.C. Monteiro, Influence of the sodium/proton replacement on the structural, morphological and photocatalytic properties of titanate nanotubes, *J. Photochem. Photobiol. A* 232 (2012) 50-56.
- 28 - E.K. Ylhäinen, M.R. Nunes, A.J. Silvestre, O.C. Monteiro, Synthesis of titanate nanostructures using amorphous precursor material and their adsorption/photocatalytic properties, *J. Mater. Sci.* 47 (2012) 4305-4312.
- 29 - V.C. Ferreira, O.C. Monteiro, New hybrid titanate elongated nanostructures through organic dye molecules sensitization, *J. Nanopart. Res.* 15 (2013) 1923-1938.
- 30 - Z. Yuan, B. Su, Titanium oxide nanotubes, nanofibers and nanowires, *Colloids and Surfaces A: Physicochem, Colloids Surf. A* 24 (2004) 173-183.
- 31 - D. Wu, J. Liu, X. Zhao, A. Li, Y. Chen, N. Ming, Sequence of events for the formation of titanate nanotubes, nanofibers, nanowires, and nanobelts, *Chem. Mater.* 18 (2006) 547-553.
- 32 - R. Ma, K. Fukuda, T. Sasaki, M. Osada, Y. Bando, Structural features of titanate nanotubes/nanobelts revealed by Raman, X-ray absorption fine structure and electron diffraction characterizations, *J. Phys. Chem. B* 109 (2005) 6210-6214.
- 33 - M. Sakeye, J. Smått, Comparison of different amino-functionalization procedures on a selection of metal oxide microparticles: degree of modification and hydrolytic stability, *Langmuir* 28 (2012) 16941-16950.
- 34 - Z. Han, Z. Du, Y. Zhang, L. Zhao, X. Cong, Degradation effect of super acid modified Fe₂O₃-TiO₂-N on acrylic acid under visible light, *J. Inorg. Mater.* 29 (2014) 1110-1114.
- 35 - P. Finetti, F. Sedona, G.A. Rizzi, U. Mick, F. Sutara, M.Svec, V. Matolin, K. Schierbaum, G. Granozzi, Core and valence band photoemission spectroscopy of well-ordered ultrathin TiO_x films on Pt(111), *J. Phys. Chem. C* 111 (2007) 869-876.
- 36 - A.A. Rempel, E.A. Kozlova, T.I. Gorbunova, S.V. Cherepanova, E.Yu. Gerasimov, N.S. Kozhevnikova, A.A. Valeeva, E. Yu. Korovin, V.V. Kaichev, Yu. A. Shchipunov, Synthesis

and solar light catalytic properties of titania–cadmium sulfide hybrid nanostructures, *Catal. Commun.* 68 (2015) 61-66.

37 - T T. Pham, B. Lee, Feasibility of silver doped TiO₂/Glass fiber photocatalyst under visible irradiation as an indoor air germicide, *Int. J. Environ. Res. Public Health* 11 (2014) 3271-3288.

38 - X. Chen, S.S. Mao, Titanium dioxide nanomaterials: synthesis, properties, modifications, and applications, *Chem. Rev.* 107 (2007) 2891-2959.

39 - J. Ananpattarachai, P. Kajitvichyanukul, S. Seraphin, Visible light absorption ability and photocatalytic oxidation activity of various interstitial N-doped TiO₂ prepared from different nitrogen dopants, *J. Hazard. Mater.* 168 (2009) 253-261.

40 - F. Peng, L. Cai, H. Yu, H. Wang, J. Yang, Synthesis and characterization of substitutional and interstitial nitrogen-doped titanium dioxides with visible light photocatalytic activity, *J. Solid State Chem.* 181 (2008) 130-136.

41 - K. Lee, A. Mazare, P. Schmuki, One-dimensional titanium dioxide nanomaterials: nanotubes, *Chem. Rev.* 114 (2014) 9385-9454.

42 - R. Asahi, T. Morikawa, Nitrogen complex species and its chemical nature in TiO₂ for visible-light sensitized photocatalysis, *Chem. Phys.* 339 (2007) 57-63.

43 - A. Justo, O. González, C. Sans, S. Esplugas, BAC filtration to mitigate micropollutants and EfOM content in reclamation reverse osmosis brines, *Chem. Eng. J.* 279 (2015) 589-596.

44 - X.H. Lin, S.N. Lee, W. Zhang, S.F.Y. Li, Photocatalytic degradation of terephthalic acid on sulfated titania particles and identification of fluorescent intermediates, *J. Hazard. Mater.* 303 (2016) 64-75.

45 - G. Liu, L. Wang, C. Sun, X. Yan, X. Wang, Z. Chen, S.C. Smith, H. Chen, G.Q. Lu, Band-to-band visible-light photon excitation and photoactivity induced by homogeneous nitrogen doping in layered titanates, *Chem. Mater.* 21 (2009) 1266-1274.

46 - B. Barrocas, A.J. Silvestre, A.G. Rolo, O.C. Monteiro, The effect of ionic Co presence on the structural, optical and photocatalytic properties of modified cobalt–titanate nanotubes, *Phys. Chem. Chem. Phys.* 18 (2016) 18081-18093.

- 47 - S. Nagarajan, N.C. Skillen, F. Fin, G. Zang, C. Randorn, L.A. Lawton, J.T.S. Irvine, P.K.J. Robertson, Comparative assessment of visible light and UV active photocatalysts by hydroxyl radical quantification, *J. Photochem. Photobiol. A* 334 (2017) 13-19.
- 48 - M. Hakil, S. Denis, G. Viniegra-González, C. Augur, Degradation and product analysis of caffeine and related dimethylxanthines by filamentous fungi, *Enzyme Microb. Technol.* 22 (1998) 355-359.
- 49 - M.M. Sunil Paul, U.K. Aravind, G. Pramod, A. Saha, C.T. Aravindakumar, Hydroxyl radical induced oxidation of theophylline in water: a kinetic and mechanistic study, *Org. Biomol. Chem.* 12 (2014) 5611-5620.
- 50 - R. Rosal, A. Rodríguez, J.A. Perdigón-Melón, A. Petre, E. García-Calvo, M.J. Gómez, A. Agüera, A.R. Fernández-Alba, Degradation of caffeine and identification of the transformation products generated by ozonation, *Chemosphere* 74 (2009) 825-831.
- 51 - F. Qi, W. Chu, Bingbing Xu, Catalytic degradation of caffeine in aqueous solutions by cobalt-MCM41 activation of peroxymonosulfate, *Appl. Catal. B* 134-135 (2013) 324-332.
- 52 - T.A. Silva, J. Diniz, L. Paixão, B. Vieira, B. Barrocas, C.D. Nunes, O.C. Monteiro, Novel titanate nanotubes-cyanocobalamin materials: Synthesis and enhanced photocatalytic properties for pollutants removal, *Solid State Sci.* 63 (2017) 30-41.
- 53 - M.C. Neves, J.M.F. Nogueira, T. Trindade, M.H. Mendonça, M.I. Pereira, O.C. Monteiro, Photosensitization of TiO₂ by Ag₂S and its catalytic activity on phenol photodegradation, *J. Photochem. Photobiol. A* 204 (2009) 168-173.
- 54 - E. Grabowska, J. Reszczynska, A. Zaleska, Mechanism of phenol photodegradation in the presence of pure and modified-TiO₂: A review, *Water Res.* 46 (2012) 5453-5471.
- 55 - T.T.T. Dang, S.T.T. Le, D. Channei, W. Khanitchaidecha, A. Nakaruk, Photodegradation mechanisms of phenol in the photocatalytic process, *Res. Chem. Intermediat.* 42 (2016) 5961-5974.
- 56 - V. Bellat, R. Chassagnon, O. Heintz, L. Saviot, D. Vandroux and N. Millot, A multi-step mechanism and integrity of titanate nanoribbons, *Dalton Trans.* 44 (2015) 1150-1160.

Chapter 3

Titanate nanowires sensitization by silver nanoparticles

This work was subject of the publication:

B. Barrocas, C.D. Nunes, M.L. Carvalho, O.C. Monteiro, Titanate nanotubes sensitized with silver nanoparticles: Synthesis, characterization and *in-situ* pollutants photodegradation, Applied Surface Science, 385 (2016) 18-27.

Chapter 3 – Titanate nanowires sensitization by silver nanoparticles

3.1 - Introduction

The properties of the elongated titanate nanoparticles (TNP) can also be modified by sensibilization with metallic nanoparticles. The production of hybrid plasmonic photocatalysts using titanate nanostructures can be seen as an interesting alternative to bring the semiconductor absorption edge into the visible region and to reduce the photogenerated charges recombination rate [1]. In this context, the incorporation of metallic nanoparticles has been used to modified metal oxides materials since they can act as electron traps delaying electron-hole recombination and therefore increasing the photocatalytic activity. Additionally, the use of nanoparticles exhibiting surface plasmon resonance on the surface also generates an additional, and positive, increase in light absorption efficiency by the local electric field amplification and scattering processes [2].

Studies on noble metal nanoparticles (NPs) have increased extensively due to their unique properties, which make them attractive in a wide range of applications such as optical, bio-labeling, antibacterial and (photo)catalytic applications. For instance, the modification with Ag nanoparticles leads to an increase in the photocatalytic performance and stability of ZnO films, avoiding the semiconductor photo corrosion under UV radiation [3]. Various methods have been reported to synthesize silver nanoparticles on TiO₂ supports by reducing Ag⁺ to the metallic form, including heat-induced reduction, reducing agents, photo-reduction, ionic liquids, citrate reduction, silver mirror reaction, polyol process seed-mediated growth and light (UV or gamma-ray) mediated synthesis [4-8]. However, these methods are not straightforward as they use reducing agents or templates and require either high temperature or long reaction time. Thus, new loading strategies of noble nanoparticles on TiO₂-based materials are required. The biosynthesis of extracellular AgNPs with the cell filtrate of *Penicillium sp.* under light radiation has been reported [9]. Nevertheless, it was found that the reaction time, particle size, dispersity, and stability of the synthesized AgNPs were dependent on the cell filtrate's pH [9]. Metallic Ag nanoparticles were successfully prepared using a direct *in situ* electrochemical method before being supported on TiO₂ for photocatalytic applications [10]. Bacterial growth inhibition was accomplished using TiO₂-Ag nanocomposites, making titania an appropriate matrix for silver as antibacterial agent [11]. Several works about the synthesis and photocatalytic performance of nanocrystalline Ag-TiO₂ and related materials have been reported, but a complete knowledge about the effective role of the metallic nanoparticles in these photoactivated processes are still missing.

TNP can be modified with noble metals by doping, on the crystalline structure, or can be sensitized with metallic nanoparticles, on their surface. Through these modifications positive effects are expected, on its photocatalytic activity, once they can:

- (i) enhance the electron-hole separation by acting as electron traps;
- (ii) extend the light absorption into the visible range and enhance surface electron excitation by plasmon resonances excited by visible radiation;
- (iii) modify the surface properties of the photocatalyst.

This work is in line with this concern and intends to contribute to better understand the influence of the presence of metallic Ag nanoparticles in the photocatalytic activity of titanate nanotubular materials. To achieve this goal, the synthesis and photocatalytic performance of elongated titanate nanowires (TNW) modified with crystalline Ag nanoparticles is described. For this study, the sodium and protonated titanate nanowires, NaTNW and HTNW, respectively, were used. Nevertheless, protonated titanate nanowires presented better results, thereby only these samples were considered in this study. This process is based on an ion-exchanged and photo-reduction step-by-step process: after hydrothermal synthesis, the HTNW particles were first treated with an Ag^+ aqueous solution to promote the metal ion immobilization; the formation of the metallic nanoparticles, over the HTNW surface, was afterward attained by UV-vis light irradiation. Considering the photocatalytic properties of the pristine HTNW, the evaluation of the Ag nanoparticles' incorporation effect on the photocatalytic performance of this sample was evaluated through phenol degradation. Phenol was chosen as a model molecule for this study due to its relevance as a pollutant by itself and also as a by-product in several pollutants photodegradation processes.

3.2 – Synthesis

A detailed description of the experimental procedure followed is shown in Chapter 10.

The HTNW amorphous precursor was prepared based on a published procedure [12]. The obtained solid was first hydrothermally treated in alkaline solution (NaOH, 10 M) at 160°C for 24 hours, producing sodium titanate nanostructures, type $\text{Na}_2\text{Ti}_3\text{O}_7$ (NaTNW sample) [13]. Afterward, an acidic treatment was performed, to exchange the Na^+ ions for H^+ , to obtain the protonated titanate nanowires, HTNW ($\text{H}_2\text{Ti}_3\text{O}_7$). After that, the HTNW was modified using an Ag^+ ion exchange process, and the Ag^+HTNW sample was obtained. The formation of metallic silver nanoparticles was attained by UV-vis irradiation of the white solid aqueous suspension with a mercury lamp, to produce Ag-HTNW samples. Previously to the conversion of the

immobilized Ag^+ into Ag^0 , the Ag^+HTNW sample was washed several times with water to eliminate the Ag^+ excess. The photo-reduction of the immobilized Ag^+ ions was attained for 60 min. To better control the process, a sample was taken, and analyzed, after 30 min of irradiation.

3.3 – Structural, morphological and optical characterization

The identification and structural characterization of the prepared samples were performed by X-ray powder diffraction (XRD). Analyzes of the Ag-HTNW samples were performed for different irradiation periods (0, 30 and 60 min), and the XRD patterns are shown in Figure 3.1.

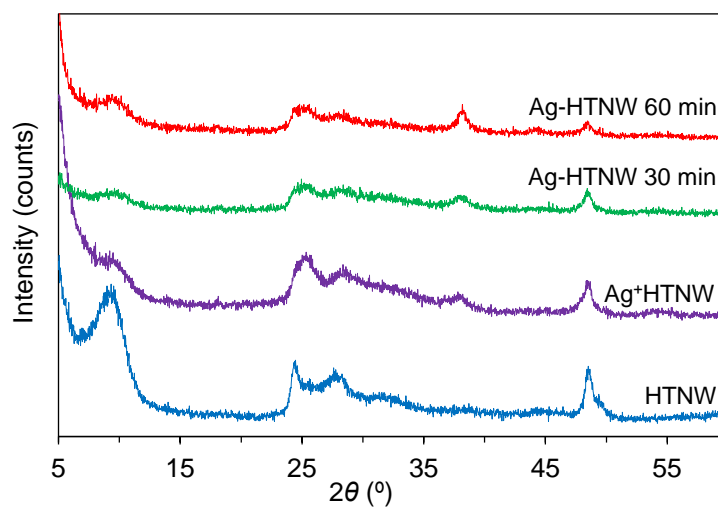


Figure 3.1 - XRD patterns of the HTNW before and after sensitization with a 0.5 M AgNO_3 solution.

The XRD patterns of the prepared samples are in agreement with the existence of a $\text{Na}_{2-x}\text{H}_x\text{Ti}_3\text{O}_7$ ($0 \leq x \leq 2$) titanate layered structure [14], being the diffraction peak identified at $2\theta \sim 10^\circ$ related to the interlayer distance between TiO_6 sheets and the peaks at 24° , 28° and 48° , characteristics of tri-titanate 1D nanomaterials [14].

After the silver ion exchange process, the Ag^+HTNW sample, a clear decrease in the 10° peak intensity was observed (Figure 3.1) suggesting that some Ag^+ ions could be preferentially incorporated between the TiO_6 layers, by replacing the H^+ entities. No crystalline impurities containing Ag, such as Ag_2O , were observed in the XRD pattern of this sample.

After being submitted to 60 min of irradiation, no drastic changes in the typical crystalline structure of the HTNW were observed. However, the Ag-HTNW diffraction pattern shows additional peaks at 2θ values of 38° and 44° , which were attributed to the (111) and (200) crystal planes of metallic silver (JCPDS file no. 004-0783), respectively [15].

A gradual increase in the intensity and definition of Ag^0 peaks is perceptible with the UV irradiation time increase, for the samples prepared using 30 and 60 min. Simultaneously, the 10° peak intensity, related to the HTNW structure, also increases with the irradiated time. These results seem to suggest that the Ag^+ ions immobilized in the interlayers during the ion-exchange process, migrate in the opposite direction during irradiation: from the interior of the interlayers for the exterior surface of the nanostructures, to originate, by reduction, the Ag^0 nanoparticles. These results are in agreement with published works related to long-term silver release and effective antibacterial action of Ag-HTNW [16]. No other Ag crystalline phases were identified. The amount of silver incorporated was quantified by micro X-ray fluorescence (μXRF) and a value of 8.97% was obtained for the Ag/Ti ratio. The morphology of the powders was analyzed by transmission electron microscopy (TEM), and the obtained images are shown in Figure 3.2.

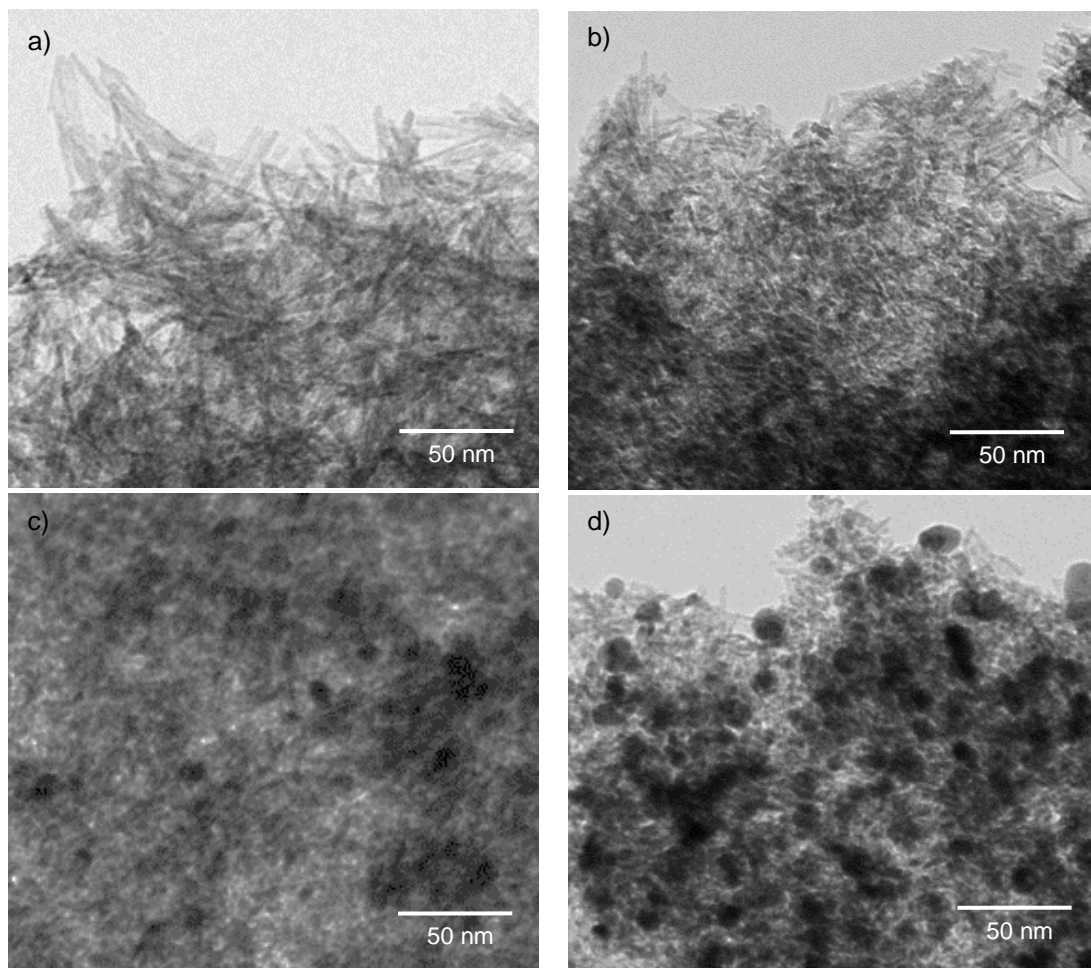


Figure 3.2 - TEM images of the (a) HTNW, (b) Ag^+HTNW and Ag-HTNW sample prepared during (c) 30 min and (d) 60 min of irradiation.

An image of the HTNW sample before Ag^+ sensitization shows the existence of a uniform sample composed of very long and thin elongated nanoparticles (Figure 3.2(a)). As expected, no morphological differences were observed between the Ag^+ HTNW and HTNW samples, Figure 3.2(a) and Figure 3.2(b), respectively. Extremely small particles spread over the HTNW surface can be highlighted in the TEM images of the Ag-HTNW after 30 and 60 min of irradiation (Figure 3.2(c) and (d)). For this last sample, irradiated during 60 min (Ag-HTNW), Ag spheroidal nanoparticles, with an average diameter of 15 nm can be seen in contrast to the titanate elongated nanowires (Figure 3.2(d)).

For the modified samples, the presence of Ag in addition to Ti and O elements was analyzed by energy-dispersive X-ray spectroscopy (EDS). As an example, the EDS spectrum for the Ag-HTNW sample is shown in Figure 3.3, confirming the presence of Ag, Ti and O elements. EDS analyzes were also performed for the HTNW and Ag^+ HTNW samples, being in accordance with the obtained for the Ag-HTNW sample.

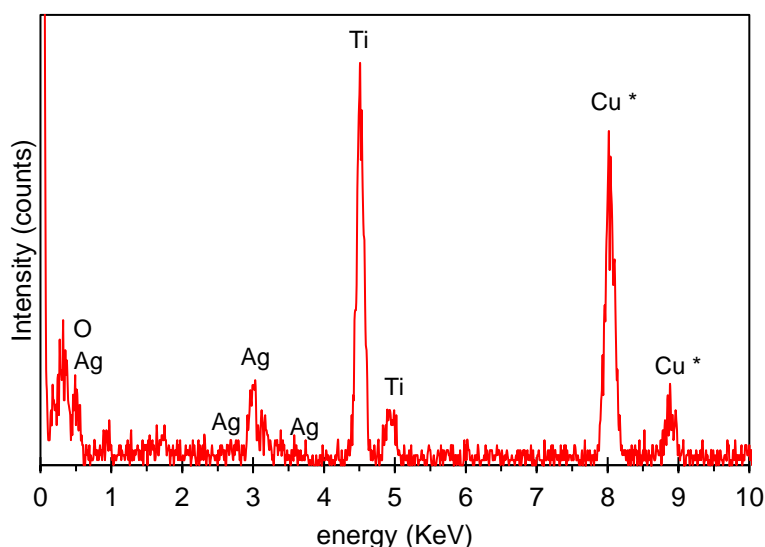


Figure 3.3 – EDS spectrum of the Ag-HTNW sample. (*From copper grids used to support the elongated titanate nanoparticles.)

Due to the importance of the surface area on catalytic studies, the samples were characterized by N_2 adsorption-desorption at -196°C . B.E.T. surface areas were calculated and values of 346.22 and 257.31 $\text{m}^2 \text{g}^{-1}$ were obtained for the HTNW and Ag-HTNW samples respectively. This decrease in the surface area is following previous works related with Ag/ TiO_2 -nanotubes produced by a microwave-assisted approach [17]. The 25% decrease observed in the surface area of the sample containing Ag (Ag-HTNW) can be due to the penetration of Ag ions in the interlayers and consequent blocking this surface area access. This is in agreement with the XRD results observed, namely the substantial decrease of the $2\theta \sim 10^\circ$ peak intensity.

The electronic structure of the Ag-HTNW sample was analyzed by X-ray photoelectron spectroscopy (XPS) and the survey spectra of the HTNW and Ag-HTNW are shown in Figure 3.4. In addition to the Ti 2*p* and O 1*s* photoelectron peaks, typical of the HTNW, the Ag-HTNW' spectrum shows an Ag 3*d* doublet peak. No Na 1*s* peak was detected, confirming the complete Na⁺ to H⁺ replacement during the acidic treatment.

For the HTNW sample, the Ti 2*p*_{3/2} and 2*p*_{1/2} peaks appear at 459.535 and 465.425 eV, respectively. A slight shift due to the Ag incorporation (Ag-HTNW sample) was observed for these peaks, 459.125 and 464.825 eV, respectively. As expected, no signals in the 456.2 – 457.4 eV range are perceptible, indicating no Ti³⁺ in these samples [18,19].

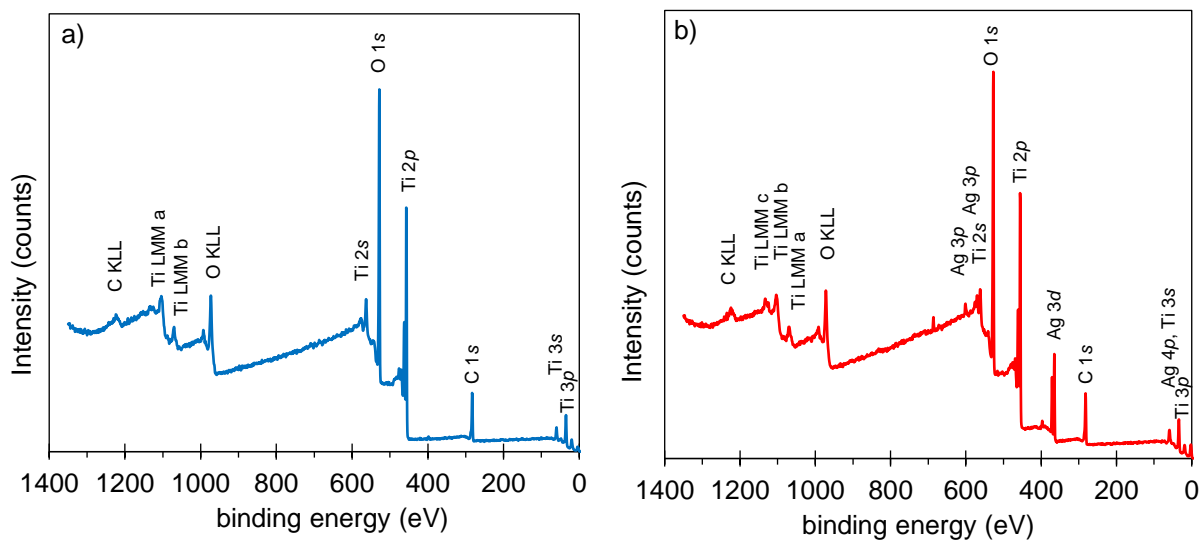


Figure 3.4 - XPS survey spectra of the (a) HTNW and (b) Ag-HTNW samples.

Figure 3.5 (a and b) shows the higher resolution spectra of Ti 2*p* and O 1*s* for HTNW and Ag-HTNW samples.

The doublet splitting energies of the Ti 2*p* peaks, for the HTNW and Ag-HTNW samples, are 5.9 and 5.8 eV, respectively, which also agrees with the presence of titanium only as Ti⁴⁺ in both samples [20,21]. The main peak in the O 1*s* core-spectrum (Figure 3.5(b)) at ~534 eV corresponds to lattice oxygen and has a contribution of the sodium Auger peak (Na KLL).

For the Ag-HTNW sample, negative shifts of 0.4 and 0.3 eV were observed for the Ti 2*p* and O 1*s* peaks, respectively (Figure 3.5(a and b)). These shifts can be due to the presence of Ag that could contribute to the titanium ion radius expansion, resulting in electron movement far from the titanium nuclei; therefore, the peaks of Ti 2*p* will shift into lower binding energies [22].

A high-resolution spectrum of the Ag 3d region is shown in Figure 3.5(c). The binding energies for Ag 3d_{5/2} and Ag 3d_{3/2} are 368.4 and 374.5 eV, respectively. These energies should be attributed to Ag⁰ nanoparticles. However, the undoubted assignment of the spectral features can be difficult once published values for metallic silver's binding energies are not in total agreement, revealing some dispersion [23-25].

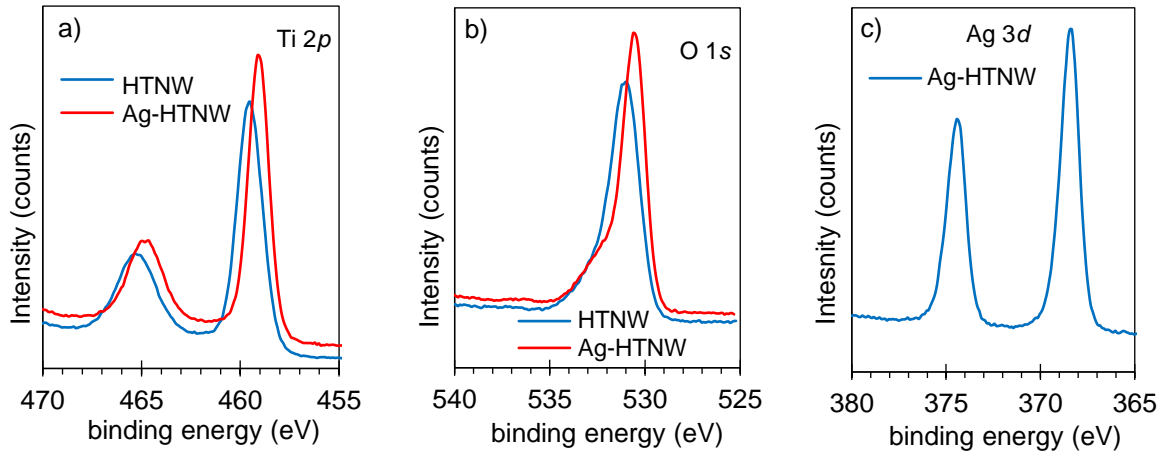


Figure 3.5 - XPS high resolution spectra of the (a) Ti 2p, (b) O 1s and (c) Ag 3d regions, for the HTNW and Ag-HTNW samples.

To elucidate this point and considering that small binding energy shifts, concerning the metal peaks, can happen in silver compounds, *e.g.* oxides, the Auger parameter was evaluated. The Auger parameter usually allows to distinguish between Ag⁰ and other oxidized Ag species; being 2 eV higher for Ag⁰ than for the corresponding oxides [26].

$$\text{Auger parameter (AP)} = \text{Ag } E_B(3d_5) + \text{Ag } E_K(M_4N_{45}N_{45}) \quad (3.1)$$

In this particular material, Ag-HTNW, the AP determination, for the identification of the Ag oxidation state, it had some imprecision due to the Ag M₄N₄₅N₄₅ and Ti LMM peaks overlapping. Although AP values between 725.8 and 724.7 eV were obtained, allowing to conclude that the Ag oxidation state is in the frontier between the metallic and oxidized state. This unexpected result can be justified by the Ag nanoparticles reduced dimensions once it is known, from literature, that XPS core levels can be influenced by metallic nanoparticles size, shifting to higher binding energies for small Ag nanoparticles [27,28].

The optical characterization of the prepared samples was performed by measuring their diffuse reflectance spectra and subsequent conversion of the reflectance data through the Kubelka–Munk function [29]. The bandgap energy (E_g) of the HTNW and Ag-HTNW samples, was

evaluated from the Kubelka–Munk (KM) data (Chapter 10). The optical spectra obtained for HTNW and Ag-HTNW samples are shown in Figure 3.6.

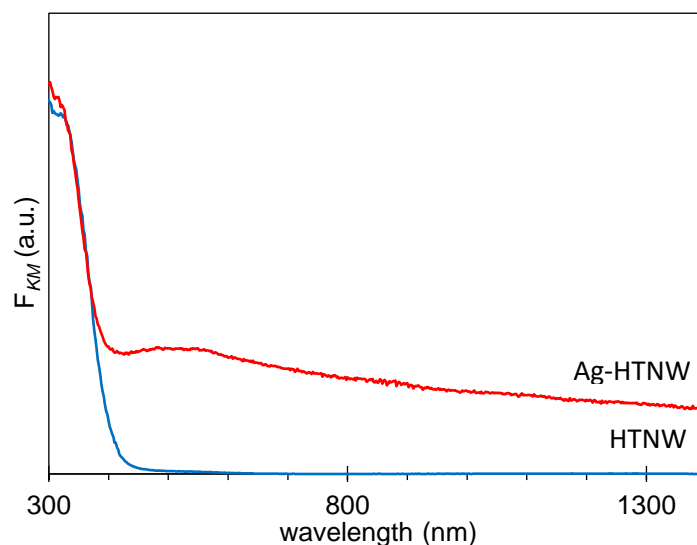


Figure 3.6 - Absorption spectra of the HTNW and Ag-HTNW samples.

Figure 3.6 indicates that the sample optical behavior was modified by the Ag nanoparticles' presence. The optical absorption below 400 nm is due to the charge transfer mechanism of O $2p$ orbital of the valence band to the Ti $3d t_{2g}$ orbital of the conduction band [30]. The new absorption band centered at 480 nm is due to the plasmonic absorption effect of the Ag nanoparticles indicating a significant improvement in the visible light absorption and suggesting a possible photocatalytic performance enhancement for Ag-HTNW. No shift in the absorption band edge of the pristine HTNW was observed, indicating no changes in the HTNW intrinsic energetic structure.

3.4 – Photocatalytic performance

3.4.1 - Photo-induced hydroxyl radical production

The hydroxyl radical ($\cdot\text{OH}$) demonstrates a very high oxidizing capability and has been responsible for several pollutants' degradation processes [31]. Due to this, and to evaluate the catalytic ability of the Ag-HTNW sample, the photocatalytic production of this oxidant specie, was monitored. Experimentally, the generation and quantification of $\cdot\text{OH}$ radicals can be evaluated by the detection of the hydroxylated reaction intermediates formed. A detailed description of the experimental procedure followed is shown in Chapter 10.

As described in Chapter 1 (Section 1.3), the $\cdot\text{OH}$ radical can convert terephthalic acid (TA) into 2-hydroxyterephthalic acid (HTA) which has fluorescent properties. Figure 3.7 shows the

amount of the HTA molecule produced during 30 min of TA/HTNW and TA/Ag-HTNW suspensions irradiation analyzed by fluorescence spectroscopy.

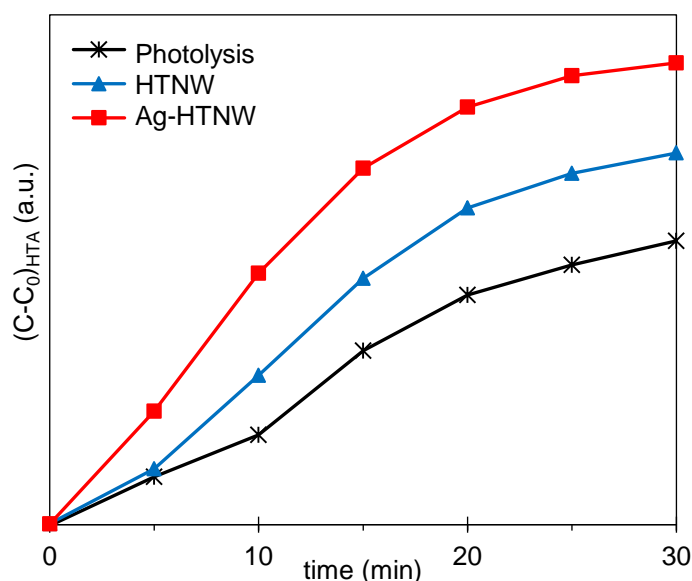


Figure 3.7 - HTA concentration variation during 30 min of irradiation of a TA solution (3 mM, 150 mL) using 10 mg of each photocatalyst.

As can be observed in Figure 3.7, both samples have demonstrated catalytic activity for this reaction, being the Ag-HTNW the best sample for the catalytic photo-induced hydroxyl radical production. This suggests an active and direct role of the metallic Ag nanocrystallites in the hydroxyl radical production and allows to anticipate good results for Ag-HTNW photocatalytic applications, where this radical plays an active role.

3.4.2 - Phenol photodegradation

Phenol was chosen as a model contaminant to further evaluate the photocatalytic performance of the Ag-HTNW under UV-vis light irradiation. A detailed description of the experimental procedure is described in Chapter 10. Briefly, a 20 ppm phenol solution was irradiated for 75 min in the presence of the catalyst. During this period samples were withdrawn and analyzed by GC-MS, and the results are shown in Figure 3.8.

Generally, the photo-oxidation reaction occurs at the catalyst surface, therefore the adsorption characteristics of the catalyst/pollutant system are expected to be a key factor in the photocatalytic process evaluation. The ability of the Ag-HTNW to adsorb phenol was investigated in dark conditions for 60 min. After this period, 16.3% and 23.6% of the initial phenol have been removed from the solution, being adsorbed in the Ag-HTNW and HTNW surfaces, respectively. The difference between the surface areas of both samples (25%) cannot

justify by itself the lower adsorption ability observed for the Ag-HTNW sample (less 33% than the pristine HTNW). Distinct phenol's abilities to be adsorbed by the HTNW and Ag surface must be in charge of this behavior.

Figure 3.8 shows the decrease of the 20 ppm phenol solution concentration over 75 min of irradiation, in the presence of HTNW and Ag-HTNW samples as catalysts. Both samples demonstrated photocatalytic activity for this degradation process. The sample with the best photocatalytic performance was the Ag-HTNW: after 30 min of irradiation, 99.0% of phenol degradation was attained. Using the pristine HTNW sample, a period of 75 min was required to achieve identical degradation results. At this time (75 min) and with no catalyst (photolysis), 19.1% of the initial phenol remains in solution.

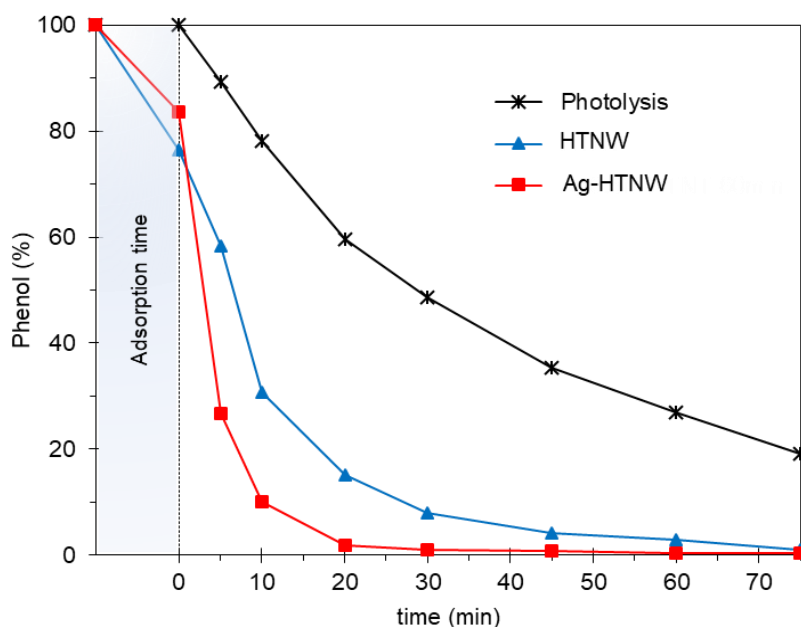


Figure 3.8 - Phenol photocatalytic degradation of a 20 ppm aqueous solution during 75 min of irradiation using Ag-HTNW and HTNW samples as photocatalysts (0.13 g L⁻¹).

The kinetic of the phenol photodegradation reaction was studied, under the experimental conditions used. A first-order kinetic model, characterized by an exponential decrease in the pollutant concentration with time, was applied. The plot of $\ln(C)$ versus t , where C is the concentration at time t , was a straight line, whose slope is $-k$, the reaction rate constant. The values of k obtained for the phenol photolysis and the degradation catalyzed by HTNW and Ag-HTNW samples, were 0.0175, 0.0549 and 0.1857 min⁻¹, respectively. These results confirm a faster photodegradation process for the Ag-HTNW catalyzed process when compared with the phenol photolysis or with the one catalyzed by the HTNW pristine sample. These results indicate that the presence of crystalline Ag nanoparticles over the HTNW surface contributes to the HTNW photocatalytic performance enhancement.

3.4.3 - Ag-HTNW photocatalytic reusability and stability

The (photo)chemical stability of a material is an important parameter that must be analyzed to better evaluate its catalytic ability. In this work, to test the photocatalyst recycling possibility, the Ag-HTNW sample was used for 4 successive phenol degradation runs, 60 min each. The obtained results are depicted in Figure 3.9. Ag-HTNW sample presents an excellent catalytic performance associated with excellent stability since only 1.0% of the initial phenol remains in solution after the fourth reuse cycle. In the first degradation trial, 99.5% of the initial phenol was degraded, 98.4% and 98.6% after the second and third cycles, respectively.

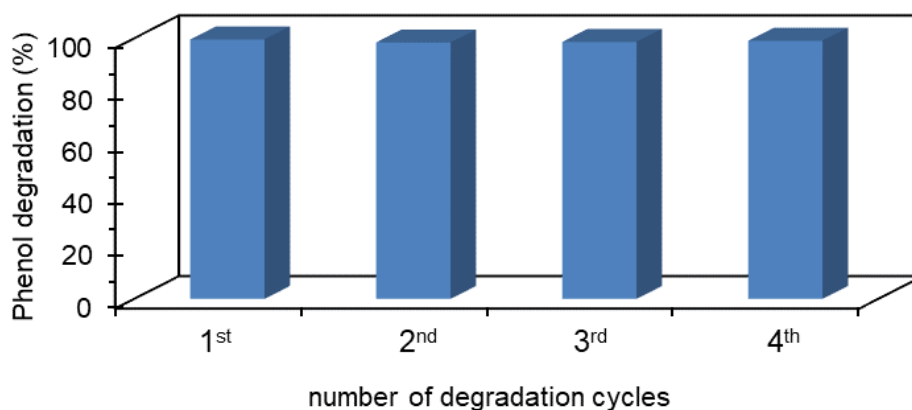


Figure 3.9 - Percentage of a 20 ppm phenol solution removal during four photodegradation cycles, of 60 min each, using the same Ag-HTNW sample as catalyst.

To better evaluate the catalyst stability, after the successive photodegradation experiments, the Ag-HTNW sample was analyzed by XRD and TEM. Figure 3.10 shows the XRD patterns of the Ag-HTNW before and after the fourth irradiation cycle.

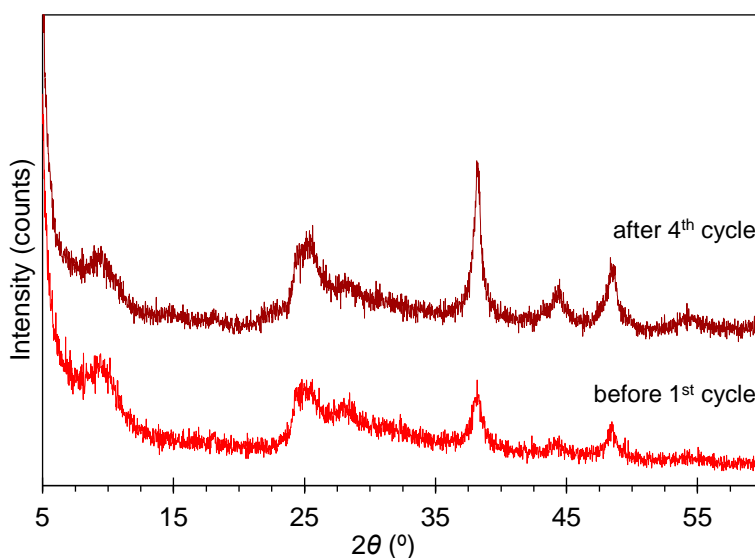


Figure 3.10 - XRD patterns of the Ag-HTNW sample before and after four cycles of phenol photodegradation.

No significant changes were observed between the two powders indicating that this catalyst is photo-stable. After four cycles of photocatalysis, a slight increase on the metallic silver peaks intensity, mainly the peak at 38.18° was observed. No changes in the HTNW characteristic peaks were detected. This phenomenon suggests an increase in the sample crystallinity with the irradiation time and has been described for several materials, being attributed to a photo-irradiation activation process [32].

To go further at this point, after each cycle, the catalyst was analyzed by TEM (Figure 3.11).

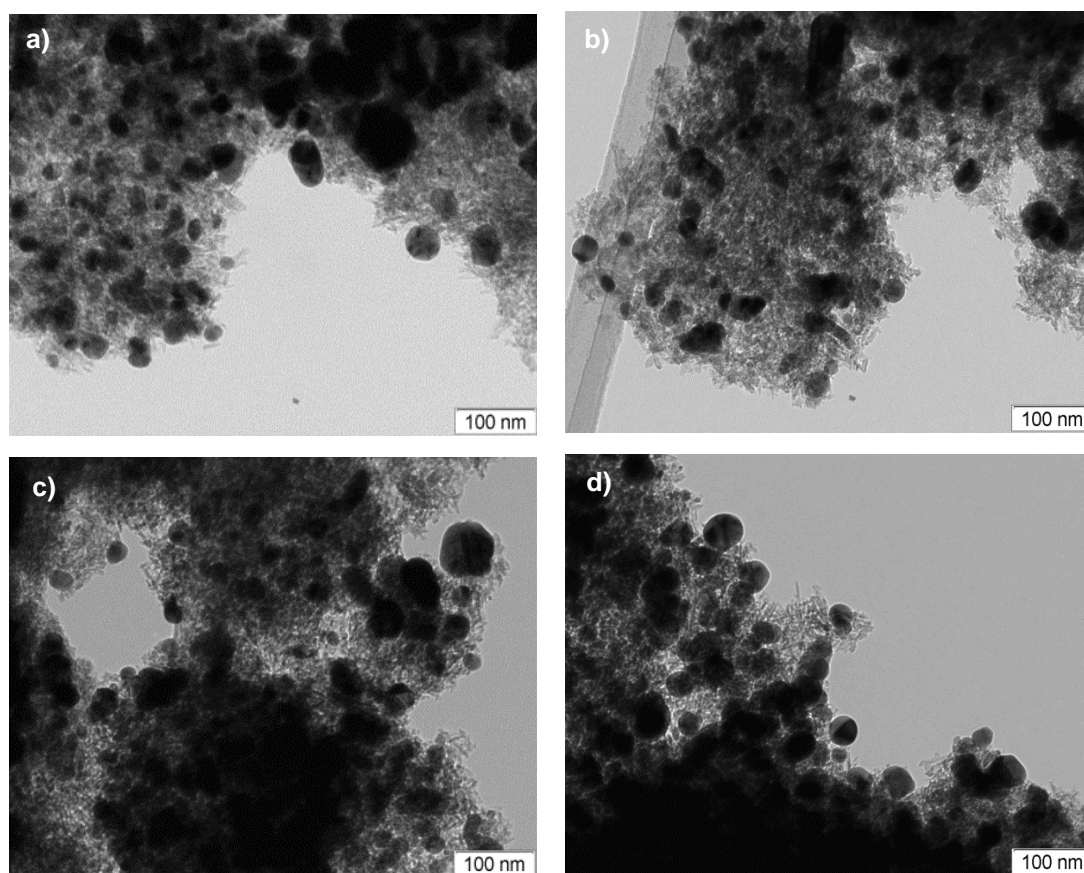


Figure 3.11 - Representative TEM images of the Ag-HTNW sample after the (a) 1st, (b) 2nd, (c) 3rd and (d) 4th photocatalytic degradation cycle.

As can be observed, the Ag nanoparticles size and amount increase with the number of photo-irradiation cycles, which can be due to a combination of two distinct situations. The UV radiation promotes the constant Ag^0 formation, indicating that the Ag-HTNW possesses Ag^+ enough for this continuous reduction reaction. The required silver ions must arise from the Ag^+ located in the TiO_6 interlayers. The slow and gradual release of Ag^+ from HTNW channels has been previously reported [23]. In addition to the radiation, the hydroquinone or catechol, that are two well-known phenol photodegradation by-products [31], can act as reducing agents for the Ag

nanoparticles formation [33]. No modification on the HTNW morphology was detected from the TEM analyzes after each cycle.

These results are interesting, since, during these four cycles a gradual increase in the Ag nanoparticles content was observed without any loss of photocatalytic performance. This is not surprising once it is known that silver nanoparticles when on the surface of a semiconductor it can cause charge separation of photogenerated electron-hole pairs, thus enhancing the overall photocatalytic activity [34]. However, as a direct consequence of this increase in the amount and size of the Ag nanoparticles, the accessibility to the catalytic active HTNW surface should decrease. However, with no changes in the photocatalytic activity of the sample. Considering that silver nanoparticles also exhibit considerable UV light absorption due to the inter-band transition (from the $4d$ electrons to the $5sp$ band), they can act, by themselves, as potential photocatalysts [35].

Based on the experimental results obtained, a mechanism for the main charge-transfer processes between HTNW and Ag nanoparticles, after being activated by the light, is proposed in Figure 3.12. When an aqueous Ag-HTNW suspension is irradiated with energy higher than its bandgap energy, electrons (e^-) and holes (h^+) are generated in the semiconductor's conduction (CB) and valence band (VB), respectively. The photogenerated holes will react with OH^- or H_2O oxidizing them to $\cdot\text{OH}$. The combined action of h^+ and other highly oxidant species, including $\cdot\text{OH}$, will be responsible for phenol degradation. Simultaneously, the continuous reduction of Ag^+ ions to metallic silver consumes electrons, enhancing the separation of electrons and holes, and consequently reducing the photogenerated charge recombination [10]. Since the Fermi level on Ag nanoparticles is lower than the conduction band of HTNW, some photo-excited electrons can be transferred from HTNW CB towards the Ag nanoparticles, forming a Schottky barrier between HTNW and Ag nanoparticles. This promotes the electron-hole separation and consequently reduces the electron-hole recombination probability [36,37].

It has also been reported that photogenerated electrons accumulated on Ag nanoparticles surface could easily transfer to the adsorbed oxygen on the Ag surface and a rapid formation of $\text{O}_2^{\cdot-}$ species may occur [38]. The $\text{O}_2^{\cdot-}$ active species formed, which can participate in the photocatalytic process, are also able to take part in the Ag^+ reduction, leading to the increase of the amount of Ag^0 particles at the surface. This mechanism is in accordance with the XRD and TEM results showing a gradual increase in the number and crystallinity of Ag^0 particles during the four irradiation processes.

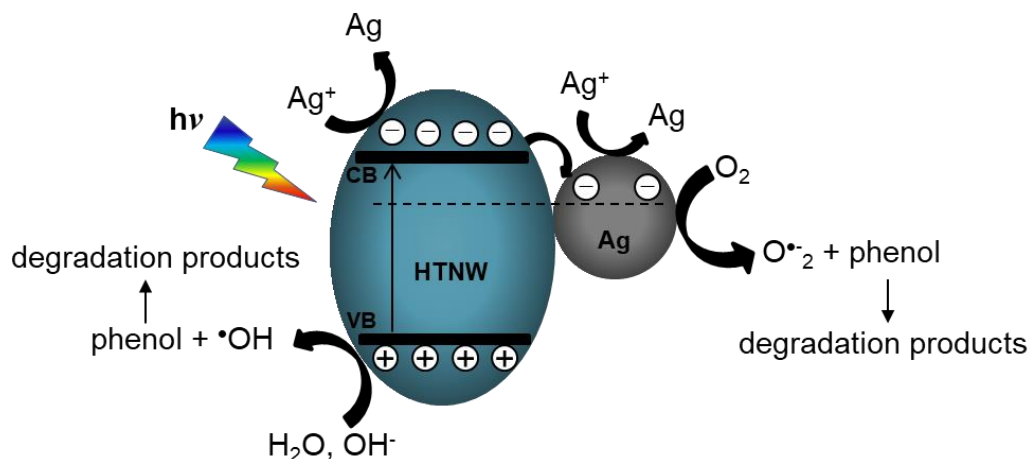


Figure 3.12 - Schematic representation of the energetic structure proposed for the Ag-HTNW nanocomposite particles under irradiation.

3.5 – Conclusions

Crystalline titanate nanostructures were first sensitized with Ag nanoparticles (Ag-HTNW) by photo-irradiation of an Ag^+HTNW sample, previously obtained by an ion-exchange process. The XRD pattern of this sample indicates that the Ag^+ immobilization, in the HTNW, occurs mainly in the TiO_6 interlayers. The formation of metallic Ag nanoparticles in the titanate nanowires surface, through the photo-irradiation, was confirmed by XRD, TEM, and XPS. The photocatalytic properties of the new sensitized materials were evaluated on the terephthalic acid and phenol degradation processes. Compared with pristine HTNW, the sensitized sample demonstrated better photocatalytic performance for both reactions. The results showed that this sensitized catalyst achieved 98.0% photodegradation efficiency of a 20 ppm phenol solution within 20 min under UV–vis radiation (13 mg catalyst / L solution). The Ag-HTNW reusability, as a photocatalyst, was examined in four successive phenol degradation runs and an increase on the Ag content is noticed during these experiments indicating a continuous growth, in size and quantity, of the metallic nanoparticles. This shows that is possible to prepare simultaneously Ag nanoparticles and degrade a phenol aqueous solution, without loss of photocatalytic performance.

The presence of Ag^+ ions in the interlayers and Ag nanoparticles in the HTNW surface, decrease the electron-hole recombination rate. Furthermore, the photogenerated electrons accumulated on the Ag nanoparticles surface can easily be transferred to the adsorbed oxygen on the Ag surface and a rapid formation of $\text{O}_2^{\bullet-}$ species occur. These $\text{O}_2^{\bullet-}$ species which participate directly in the pollutants photodegradation and the Ag^+ reduction reaction, leading to the increase of the Ag^0 particles number in the titanate nanowires surface.

3.6 – References

- 1 - V.C. Ferreira, M.R. Nunes, A.J. Silvestre, O.C. Monteiro, Synthesis and properties of Co-doped titanate nanotubes and their optical sensitization with methylene blue, *Mater. Chem. Phys.* 142 (2013) 355-362.
- 2 - M.A. Garcia, Surface plasmons in metallic nanoparticles: fundamentals and applications, *J. Phys. D Appl. Phys.* 44 (2011) 283001-283020.
- 3 - W. Xie, Y. Li, W. Sun, J. Huang, H. Xie, X. Zhao, Surface modification of ZnO with Ag improves its photocatalytic efficiency and photostability, *J. Photochem. Photobiol. A: Chem.* 216 (2010) 149-155.
- 4 - J. Tian, R. Liu, G. Wang, Y. Xu, X. Wang, H. Yu, Dependence of metallic Ag on the photocatalytic activity and photo-induced stability of Ag/AgCl photocatalyst, *Appl. Surf. Sci.* 319 (2014) 324-331.
- 5 - A.A. Ismail, Facile synthesis of mesoporous Ag-loaded TiO₂ thin film and its photocatalytic properties, *Microporous Mesoporous Mater.* 149 (2012) 69-75.
- 6 - R. Adhikari, G. Gyawali, T. Sekino, S.W. Lee, Microwave assisted hydrothermal synthesis of Ag/AgCl/WO₃ photocatalyst and its photocatalytic activity under simulated solar light, *J. Solid State Chem.* 197 (2013) 560-565.
- 7 - Y. Xu, H. You, TiO₂ modified with Ag nanoparticles synthesized via ultrasonic atomization-UV reduction and the use of kinetic models to determine the acetic acid photocatalytic degradation, *Appl. Surf. Sci.* 321 (2014) 481-487.
- 8 - M. Rycenga, C.M. Cobley, J. Zeng, W. Li, C.H. Moran, Q. Zhang, D. Qin, Y. Xia, Controlling the synthesis and assembly of silver nanostructures for plasmonic applications, *Chem. Rev.* 111 (2011) 3669-3712.
- 9 - L. Du, Q. Xu, M. Huang, L. Xian, J. Feng, Synthesis of small silver nanoparticles under light radiation by fungus *Penicillium oxalicum* and its application for the catalytic reduction of methylene blue, *Mater. Chem. Phys.* 160 (2015) 40-47.

- 10 - N.F. Jaafar, A.A. Jalil, S. Triwahyono, J. Efendi, R.R. Muktif, R. Jusoh, N.W.C. Jusoh, A.H. Karim, N.F.M. Salleh, V. Suendo, Direct in situ activation of Ag⁰ nanoparticles in synthesis of Ag/TiO₂ and its photoactivity, *Appl. Surf. Sci.* 338 (2015) 75-84.
- 11 - S.A. Amin, M. Pazouki, A. Hosseinnia, Synthesis of TiO₂-Ag nanocomposite with sol-gel method and investigation of its antibacterial activity against *E. coli*, *Powder Technol.* 196 (2009) 241-245.
- 12 - M.R. Nunes, O.C. Monteiro, A.L. Castro, D.A. Vasconcelos, A.J. Silvestre, A New Chemical Route to Synthesise TM-Doped (TM = Co, Fe) TiO₂ Nanoparticles, *Eur. J. Inorg. Chem.* 2008 (2008) 961-965.
- 13 - E.K. Ylhäinen, M.R. Nunes, A.J. Silvestre, O.C. Monteiro, Synthesis of titanate nanostructures using amorphous precursor material and their adsorption/photocatalytic properties, *J. Mater. Sci.* 47 (2012) 4305-4312.
- 14 - V. Bem, M.C. Neves, M.R. Nunes, A.J. Silvestre, O.C. Monteiro, Influence of the sodium/proton replacement on the structural, morphological and photocatalytic properties of titanate nanotubes, *J. Photochem. Photobiol. A* 232 (2012) 50-56.
- 15 - P. Umek, A. Gloter, C. Navio, C. Bittencourt, Synthesis and Characterization of Sodium Titanate and TiO₂ Nanostructures Loaded with Silver Nanoparticles, *The 4th Nanoscience and Nanotechnology Symposium (NNS2011) AIP Conf. Proc.* 1415 (2011) 24-27.
- 16 - Z. Wang, Y. Sun, D. Wang, H. Liu, R.I. Boughton, In situ fabrication of silver nanoparticle-filled hydrogen titanate nanotube layer on metallic titanium surface for bacteriostatic and biocompatible implantation, *Int. J. Nanomedicine* 8 (2013) 2903-2916.
- 17 - G. Guo, B. Yu, P. Yu, X. Chen, Synthesis and photocatalytic applications of Ag/TiO₂-nanotubes, *Talanta* 79 (2009) 570-575.
- 18 - P. Finetti, F. Sedona, G.A. Rizzi, U. Mick, F. Sutara, M. Svec, V. Matolin, K. Schierbaum, G. Granozzi, Core and Valence Band Photoemission Spectroscopy of Well-Ordered Ultrathin TiO_x Films on Pt(111), *J. Phys. Chem. C* 111 (2007) 869-876.

- 19 - A.A. Rempel, E.A. Kozlova, T.I. Gorbunova, S.V. Cherepanova, E.Yu. Gerasimov, N.S. Kozhevnikova, A.A. Valeeva, E. Yu. Korovin, V.V. Kaichev, Yu. A. Shchipunov, Synthesis and solar light catalytic properties of titania–cadmium sulfide hybrid nanostructures, *Catal. Commun.* 68 (2015) 61-66.
- 20 - T. Pham, B. Lee, Feasibility of Silver Doped TiO₂/Glass Fiber Photocatalyst under Visible Irradiation as an Indoor Air Germicide, *Int. J. Environ. Res. Public Health* 11 (2014) 3271-3288.
- 21 - X. Chen, S.S. Mao, Titanium Dioxide Nanomaterials: Synthesis, Properties, Modifications, and Applications, *Chem. Rev.* 107 (2007) 2891-2959.
- 22 - N. Liu, X. Chen, J. Zhang, J.W. Schwank, A review on TiO₂-based nanotubes synthesized via hydrothermal method: Formation mechanism, structure modification, and photocatalytic applications, *Catal. Today* 225 (2014) 34-51.
- 23 - J. Paris, Y. Bernhard, J. Boudon, O. Heintz, N. Millot, R. A. Decréau, Phthalocyanine–titanate nanotubes: a promising nanocarrier detectable by optical imaging in the so-called imaging window, *RSC Adv.* 5 (2015) 6315-6322.
- 24 - H.-J. Li, A.-Q. Zhang, Y. Hu, L. Sui, D.-J. Qian, M. Chen, Large-scale synthesis and self-organization of silver nanoparticles with Tween 80 as a reductant and stabilizer, *Nanoscale Res. Lett.* 7 (2012) 612-624.
- 25 - Y. Lai, Huifang Zhuang, K. Xie, D. Gong, Y. Tang, L. Sun, C. Lin, Z. Chen, Fabrication of uniform Ag/TiO₂ nanotube array structures with enhanced photoelectrochemical performance, *New J. Chem.* 34 (2010) 1335-1340.
- 26 - A.M. Ferraria, A.P. Carapeto, A.M. Rego, X-ray photoelectron spectroscopy: Silver salts revisited, *Vacuum* 86 (2012) 1988-1991.
- 27 - P. Pusztai, R. Puskás, E. Varga, A. Erdohelyi, Á. Kukovecz, Z. Kónya, J. Kiss, Influence of gold additives on the stability and phase transformation of titanate nanostructures, *Phys. Chem. Chem. Phys.* 16 (2014) 26786-26797.

- 28 - I. Lopez-Salido, D.C. Lim, Y.D. Kim, Ag nanoparticles on highly ordered pyrolytic graphite (HOPG) surfaces studied using STM and XPS, *Surf. Sci.* 588 (2005) 6-18.
- 29 - G. Kortuem, *Reflectance Spectroscopy: Principles, Methods and Applications*, Springer-Verlag, New York, 1969.
- 30 - S.T. Nishanthi, S. Iyyapushpam, B. Sundarakannan, E. Subramanian, D.P. Padiyan, Plasmonic silver nanoparticles loaded titania nanotube arrays exhibiting enhanced photoelectrochemical and photocatalytic activities, *J. Power Sources* 274 (2015) 885-893.
- 31 - P. Nidheesh, R. Gandhimathi, S. Ramesh, Degradation of dyes from aqueous solution by Fenton processes: a review, *Environ. Sci. Pollut. Res.* 20 (2013) 2099-2132.
- 32 - M.C. Neves, J.M.F. Nogueira, T. Trindade, M.H. Mendonça, M.I. Pereira, O.C. Monteiro, Photosensitization of TiO₂ by Ag₂S and its catalytic activity on phenol photodegradation, *J. Photochem. Photobiol. A* 204 (2009) 168-173.
- 33 - J.A. Jacob, H.S. Mahal, N. Biswas, T. Mukherjee, S. Kapoor, Role of phenol derivatives in the formation of silver nanoparticles, *Langmuir* 24 (2008) 528-533.
- 34 - P.D. Cozzoli, E. Fanizza, R. Comparelli, M.L. Curri, A. Agostiano, Role of metal nanoparticles in TiO₂/Ag nanocomposite-based microheterogeneous photocatalysis, *J. Phys. Chem. B* 108 (2004) 9623-9630.
- 35 - X. Chen, Z. Zheng, X. Ke, E. Jaatinen, T. Xie, D. Wang, C. Guo, J. Zhao, H. Zhu, Supported silver nanoparticles as photocatalysts under ultraviolet and visible light irradiation, *Green Chem.* 12 (2010) 414-419.
- 36 - X. He, Y. Cai, H. Zhang, C. Liang, Photocatalytic degradation of organic pollutants with Ag decorated free-standing TiO₂ nanotube arrays and interface electrochemical response, *J. Mater. Chem.* 21 (2011) 475-480.
- 37 - Q. Wang, X. Yang, D. Liu, J. Zhao, Fabrication, characterization and photocatalytic properties of Ag nanoparticles modified TiO₂ NTs, *J. Alloys Compd.* 527 (2012) 106-111.
- 38 - L. Sun, J. Li, C. Wang, S. Li, Y. Lai, H. Chen, C. Lin, Ultrasound aided photochemical synthesis of Ag loaded TiO₂ nanotube arrays to enhance photocatalytic activity, *J. Hazard. Mater.* 171 (2009) 1045-1050.

Chapter 4
Tailoring titanate nanoparticles photocatalytic properties
by cobalt incorporation

This work was published as:

B. Barrocas, A.J. Silvestre, A.G. Rolo, O.C. Monteiro, The effect of ionic Co presence on the structural, optical and photocatalytic properties of modified cobalt-titanate nanotubes, *Physical Chemistry Chemical Physics* 18 (2016) 18081-18093.

Chapter 4 – Tailoring titanate nanoparticles photocatalytic properties by cobalt incorporation

4.1 - Introduction

In semiconductors, it is well known that doping with transition metal ions can introduce new energetic levels in the forbidden zone, which will act as electron traps, resulting in the production of some defects and, thus, in a decrease of the charge carrier recombination. Therefore, transition metal doping is generally accepted as a swift method to improve TNP' photo-activity under UV-vis radiation [1,2]. Cobalt, a *3d* transition metal, has been described as a dopant element that can significantly narrow the bandgap energy and enhance the optical absorption, extending the semiconductor material light absorption to the visible range [3]. Previous works, reported by Nunes *et al.*, shown that increasing Co doping concentration in TiO₂ nanoparticles, the Co was uniformly incorporated in TiO₂ *anatase* without changing its structure, resulting in a decrease in the bandgap energy (red shift) [4]. This reduction as compared to undoped TiO₂ it was attributed to new electronic states introduced by the *3d* electrons of the Co²⁺ cations. Choudhury *et al.*, reported that the doping of TiO₂ with cobalt shifts the absorption onset to the visible region and reduces the bandgap energy, and this is associated with *d* states of cobalt [5].

The bandgap energy reduction is attributed to either the presence of some mid-band gap states or to the *sp-d* exchange interactions of *sp* electrons of TiO₂ nanomaterials with the *d*-electrons of Co²⁺ dopants [6]. Jiang *et al.*, reported the synthesis of cobalt doped TiO₂ powder using the hydrothermal method. First principle calculation results reveal considerable *3d* impurity states in the forbidden band after substantial cobalt introduction and this contribute to the photocatalytic activity under visible light irradiation [7]. In another recent work, Ali *et al.* showed that cobalt doped TiO₂ was successively used for the photodegradation of amido black dye in water, being its removal mechanism firstly by dye adsorption on the Co/TiO₂ surface and then by degradation under UV radiation [8]. Given the above findings, cobalt is an interesting dopant which can either expand or modify the TiO₂ lattice with an increase or decrease in its lattice volume and change its electronic and optical properties [4,9-11].

Even though many of these photocatalysts are effective for the degradation of organic pollutants, the design of materials that exhibit higher activity under visible light is still a challenge nowadays. Moreover, the stability and efficiency of these materials are still low and need to be improved. Searching for new TNP-based photocatalysts with enhanced photocatalytic activity under visible light irradiation, it was recently reported by our group a

novel chemical route to synthesize homogenous cobalt-doped titanate nanoparticles (Co-TNP) with high adsorption ability for methylene blue [12]. Marques *et al.* [13] reported a modification of titanate nanotubes (TNT) with cerium by the ion-exchange method. The authors showed the intercalation of Ce^{4+} and Ce^{3+} within the TNT layers. The co-modification of titania nanotubes with Cr and N was recently reported by Fan *et al.* [14]. The authors showed the Ti^{4+} substitution by Cr^{3+} ions and conclude that the incorporation of N and Cr dopant into the titania nanotubes resulted in samples with larger specific surface area and lower bandgap energy, which improves the photocatalysis activity when compared with the pristine ones. In this case, nitrogen doping could form a new level located slightly above the valence band, and the overlap of the conduction band could be formed due to Ti^{4+} and Cr^{3+} orbitals. Under light irradiation, electrons can be excited from low to high levels, such as from the N impurity level to the Cr^{3+} impurity level, or from the N impurity level to the CB, or from the VB to the Cr^{3+} impurity level. Meanwhile, the Cr^{3+} dopant was also used as a charge traps, transferring the interfacial electrons to degrade the reactant molecule and therefore lower the e^-/h^+ recombination rate. Consequently, co-doping with nitrogen and Cr^{3+} ion can result in the enhancement of the photoactivity efficiency under solar energy [14].

In this chapter, the synthesis of novel cobalt modified titanate nanowires (TNW), with enhanced optical and photocatalytic properties for emergent pollutants removal, is reported. The synthesis of TNW modified by cobalt doping (CoTNW) and by Na^+/Co ion-exchange (TNW/Co) is described. The influence of the Co content and/or the Co position in the TNW structure on the optical and photocatalytic properties of the materials was studied. The photocatalytic activity of the prepared powders was firstly investigated using the terephthalic acid (TA) as a probe molecule to study the catalytic production of hydroxyl radical ($\cdot OH$). Afterward, the degradation of phenol and naphthol yellow S (NYS) and brilliant green (BG) dyes, used as model pollutants, was evaluated under UV-vis radiation. Anticipating real-world situations, photocatalytic experiments were performed using solutions containing all of these pollutants.

4.2 - Synthesis

A detailed description of the experimental procedure used for titanate nanowires (TNW) synthesis is shown in Chapter 10.

The TNW amorphous precursor was prepared based on a published procedure [4]. A similar procedure was followed to produce the Co-containing precursor, but adding the required molar amount (1% and 5%, nominal molar amount) of metallic cobalt to the titanium trichloride

solution using the published procedure [12,15]. The pristine and Co-modified TNW particles were produced at 160°C for 24 hours using a hydrothermal approach reported procedure [16]. The obtained undoped and Co-doped samples were identified as TNW, Co(1%)TNW and Co(5%)TNW.

The Co ion-exchanged titanate nanowires (TNW/Co) were prepared by adding aqueous cobalt nitrate, with the required Co molar amount of 5%, to the TNW powder previously prepared. The resulting suspension was kept under stirring for 7 hours at room temperature. The obtained Co ion-exchanged sample was identified as TNW/Co(5%).

4.3 – Structural, morphological and optical characterization

The structural characterization of the TNW, Co(1%)TNW, Co(5%)TNW and TNW/Co(5%) prepared samples was analyzed by X-ray powder diffraction (XRD). The obtained XRD patterns are presented in Figure 4.1.

As can be seen, the XRD patterns for TNW, Co(1%)TNW, Co(5%)TNW and TNW/Co(5%) powders, agree with the presence of a crystalline titanate layered structure, type $\text{Na}_{2-x}\text{H}_x\text{Ti}_3\text{O}_7$ ($0 \leq x \leq 2$) [17-19]. No signal of undesirable crystalline phases, *e.g.* cobalt clusters, cobalt oxides or Co-Ti oxide phases, which are known to exist in the bulk Co-Ti-O phase diagram [12,20], were observed in the XRD patterns of all Co-modified TNW samples.

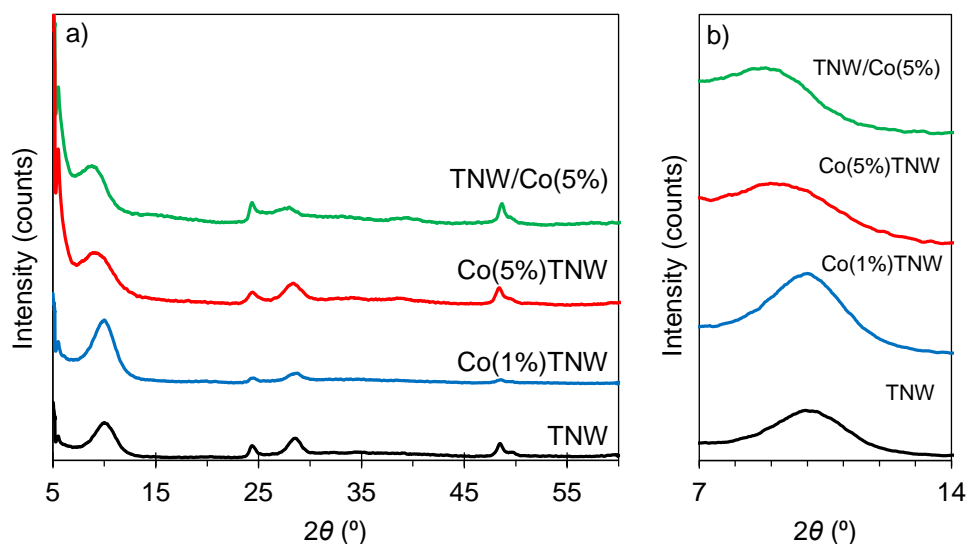


Figure 4.1 – (a) XRD patterns of the TNW, Co(1%)TNW, Co(5%)TNW and TNW/Co(5%) prepared samples; (b) detail of the XRD patterns.

The XRD pattern of the undoped TNW sample shows 2θ peaks centered at 10.22°, 24.34°, 28.40°, and 48.43° corresponding to (100), (102), (111) and (303) crystal planes respectively,

in agreement with a $\text{Na}_2\text{Ti}_3\text{O}_7$ layered titanate structure [21-26], and in good match with $\text{Na}_2\text{Ti}_3\text{O}_7$ JCPDS file no. 72-0148. In particular, the diffraction peak at $2\theta = 10.22^\circ$ is related to the distance between the TiO_6 octahedra sheets that form the layered TNW structure and host the Na^+ ions between them. Shifts in this peak are usually indicative of the Na^+ replacement by other ionic species, *e.g.* H^+ and Ce^{4+} [21,26]. This can be seen in the diffractogram of the Co ion-exchanged TNW/Co(5%) sample, for which the above mentioned peak shifts from $2\theta = 10.22^\circ$ to 8.74° , as a result of the incorporation of cobalt *via* Na/Co ion exchange between the TiO_6 sheets.

It should be noted that the observed decrease of the 2θ position implies an increase of the interlayers distance, which is expected since the ionic radius of Na^+ is smaller than that of hydrated Co^{2+} [27]. In what concerns the XRD pattern of the Co(1%)TNW sample, it is similar to that obtained for the undoped TNW sample, with no shift of the peak related to the TiO_6 interlayers distance. This indicates that no Na/Co replacement took place for this sample, the doping most probably occurring by substitution of Ti^{4+} by Co^{2+} in the TiO_6 octahedra of the TNW crystal structure [12]. Since the effective ionic radius of Co^{2+} is slightly bigger (79.0 pm) than one of the Ti^{4+} (74.5 pm), the replacement of Ti^{4+} by Co^{2+} is likely [28,29].

Regarding the XRD pattern of the doped Co(5%)TNW sample, it shows a clear shift of the aforementioned peak related to the TiO_6 interlayers, although to a less extent of that observed for the ion-exchange TNW/Co(5%) sample. This strongly suggests that some cobalt ions were incorporated between the TiO_6 layers during the Co(5%)TNW sample synthesis process, beyond the expected cobalt doping *via* the $\text{Ti}^{4+}/\text{Co}^{2+}$ replacement in the TiO_6 octahedra.

The effect of ionic Co presence on the structure of TNW was studied by analyzing the lattice parameters and the unit cell volume of the synthesized samples. The lattice parameters of the undoped TNW sample are in good match with that of $\text{Na}_2\text{Ti}_3\text{O}_7$ JCPDS file no. 72-0148 (Annex A – Table A.1), with a unit cell volume deviation of only 3.3% in comparison to the standard value. Concerning the Co(1%)TNW sample, it presents only a slight increase of the unit cell volume concerning the value determined for the undoped TNW sample. However, the V_{cell} values increase significantly for the Co(5%)TNW and TNW/Co(5%) samples, which supports the above-mentioned hypothesis that some cobalt ions were incorporated between the TiO_6 layers during the Co(5%)TNW sample synthesis process, beyond the intended cobalt doping *via* replacing the $\text{Ti}^{4+}/\text{Co}^{2+}$.

The morphology of the pristine and Co-modified TNW samples was evaluated by transmission electron microscopy (TEM). The TEM images for TNW, Co(5%)TNW, Co(1%)TNW and TNW/Co(5%) samples are presented in Figure 4.2.

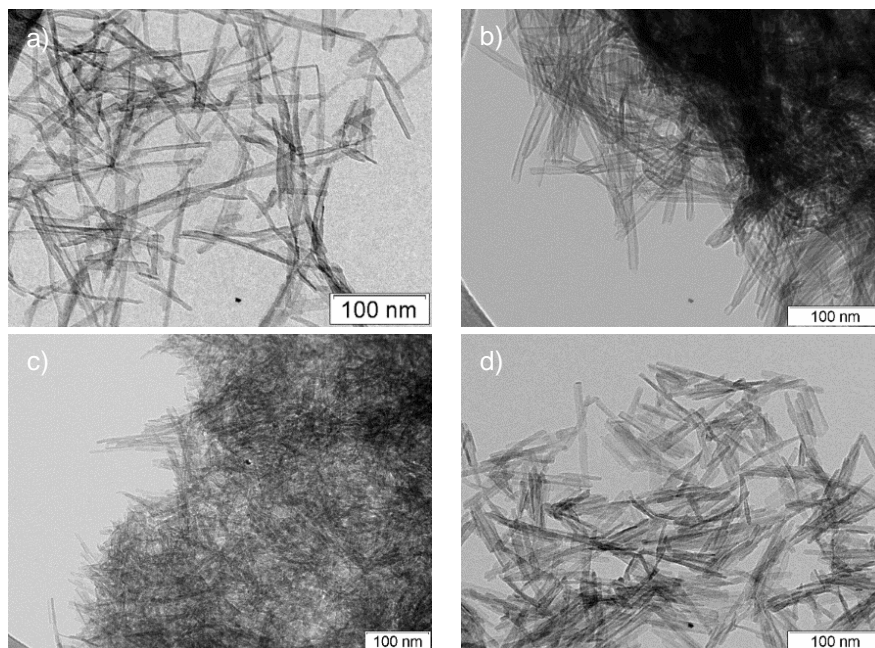


Figure 4.2 - TEM image of the (a) TNW, (b) Co(5%)TNW, (c) Co(1%)TNW and (d) TNW/Co(5%) samples.

As can be seen, all samples present similar morphology, consisting of homogeneous elongated nanowires with a diameter of ~ 7 nm and a high length/diameter aspect ratio. No influence of either the Co doping or the Co ion-exchange step was noticed on the morphology of the samples [12]. For the 5%, cobalt modified samples, *i.e.* Co(5%)TNW and TNW/Co(5%) samples, the presence of the Co in addition to Ti, O and Na elements was confirmed by EDS (not shown). This analysis was not possible for the Co(1%)TNW sample due to equipment limitations.

The specific surface area of the samples was evaluated by the B.E.T. method. The pristine TNW sample shows a value of $288.60 \text{ m}^2 \text{ g}^{-1}$. In comparison, the Co-doped samples present a slight decrease of the specific surface area: $241.59 \text{ m}^2 \text{ g}^{-1}$ and $267.22 \text{ m}^2 \text{ g}^{-1}$ values were obtained for the Co(5%)TNW and Co(1%)TNW samples, respectively. In contrast, the Co ion-exchange TNW/Co(5%) sample presents a specific surface area of $298.88 \text{ m}^2 \text{ g}^{-1}$, higher than that obtained for the pristine powder, this result being also consistent with the substitution of sodium by cobalt in the TNW lamellar structure, as previously shown by Morgado *et al.* [30].

Raman spectroscopy was used to further investigate the structure of the prepared samples. Figure 4.3 shows the Raman spectra of all the prepared samples (TNW, Co(1%)TNW, Co(5%)TNW and TNW/Co(5%)).

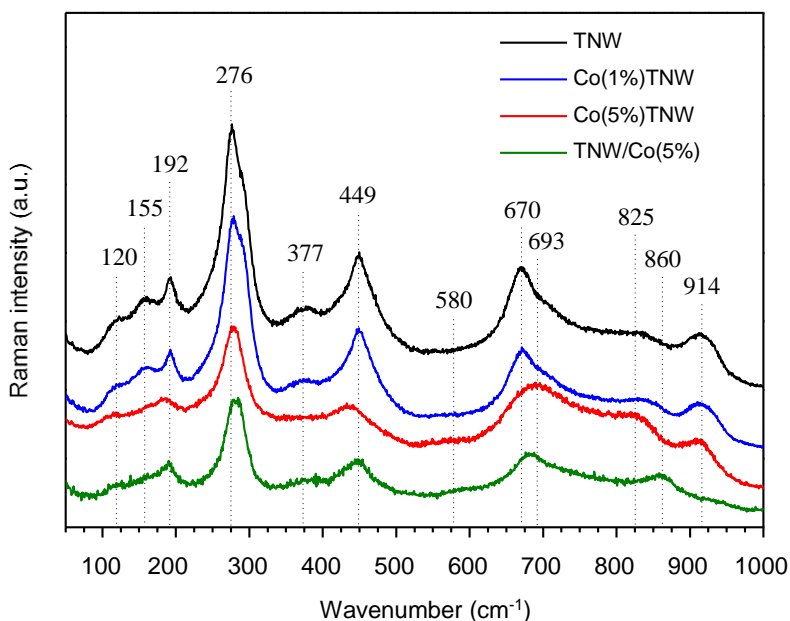


Figure 4.3 - Raman spectra of the TNW, Co(1%)TNW, Co(5%)TNW and TNW/Co(5%) samples.

Raman spectra of TNW show bands near 120, 155, 192, 276, 377, 449, 670, 825, and 914 cm^{-1} . A comparison of the Raman spectra of the synthesized samples with those reported in the literature shows that the set of observed bands agrees with that of $\text{Na}_2\text{Ti}_3\text{O}_7$ [17,26,31,32].

It should also be noted that a direct comparison of the TNW' Raman spectra with that of TiO_2 has strong limitations. It is known that titania exists in three common crystalline structures; *rutile* (tetragonal), *anatase* (tetragonal), and *brookite* (orthorhombic), and belong to space groups D_{4h} ($P4_2/mnm$), D_{4h} ($I4_1/amd$), and D_{2h} ($Pbca$) respectively. However, at room temperature, bulk $\text{Na}_2\text{Ti}_3\text{O}_7$ exhibits a lamellar monoclinic structure within the space group C_{2h}^2 ($P2_1/m$) [31]. Moreover, *rutile* TiO_2 has four Raman active modes ($A_{1g} + B_{1g} + B_{2g} + E_g$) located at 144, 448, 612, and 828 cm^{-1} and *anatase* TiO_2 has six Raman active modes ($A_{1g} + 2B_{1g} + 3E_g$) at 144, 192, 395, 515/519 and 638 cm^{-1} . Therefore, the $\text{Na}_2\text{Ti}_3\text{O}_7$ Raman spectra and the respective structures are different from those of *anatase* and *rutile* phases, although some peaks appeared in the vicinity of the active modes owing to the TiO_2 derived origin. Furthermore, 69 vibrational modes are predicted for $\text{Na}_2\text{Ti}_3\text{O}_7$ bulk structures distributed among the irreducible representations as follows: $24A_g + 11A_u + 12B_g + 22 B_u$ [31]. Additionally, as the nanotubes have a scroll-like structure there is no radial symmetry, therefore it is not appropriate to apply standard factor group analysis.

According to previous studies, Raman peaks at 155 and 192 cm^{-1} correspond to the Na–O–Ti lattice modes, while those located at *ca.* 276, 449, 670 and 693 cm^{-1} can be ascribed to the Ti–O–Ti stretching in edge-shared TiO_6 [17,19,26]. The band at 914 cm^{-1} is attributed to the

stretching vibration of the shorter Ti–O bonds whose oxygen is not shared among the distorted TiO₆ units.

The Raman spectrum of the Co(1%)TNW sample is similar to that obtained for the undoped TNW sample, without any detectable peak shifts within the spectral resolution used. This seems to support the hypothesis that, at this low doping level, only the substitution of Ti⁴⁺ by Co²⁺ in the TiO₆ octahedra occurs. However, the Raman spectra of doped Co(5%)TNW and ion-exchanged TNW/Co(5%) samples display quite different features. The analysis of the obtained spectra indicates a clear influence of the Co doping level and the ion position in the structure of the TNW. The samples' spectra show that both the highest frequency mode (914 cm⁻¹) and the lowest frequency modes (155 and 192 cm⁻¹) have their wavenumbers and intensities affected either by the higher doping level or by the Co ionic position, similarly to that reported by Marques *et al.* for Ce⁴⁺ doping/intercalation within the titanate nanotubes [26]. Besides, the Co(5%)TNW sample shows an increase in the intensity ratio between the modes at 825 cm⁻¹ and 670 cm⁻¹.

The Raman modes at 825 cm⁻¹ and 914 cm⁻¹ are not observed for the ion-exchanged TNW/Co(5%) sample, instead, a new mode appeared at about 860 cm⁻¹. Furthermore, the spectrum of the Co(5%)TNW sample presents a clear broadening and shifting of the wavenumber modes at 449 cm⁻¹ and 670 cm⁻¹ to 435 cm⁻¹ and 693 cm⁻¹, respectively. The fact that these modes correspond to the Ti–O–Ti stretching in edge-shared TiO₆ strengthens the aforementioned hypothesis that some ionic cobalt was incorporated between TiO₆ layers during the Co(5%)TNW sample synthesis process, beyond the expected Co doping *via* the Ti⁴⁺/Co²⁺ substitution into the TiO₆ octahedra. The ion-exchange TNW/Co(5%) sample shows a similar behavior although less pronounced, the peak at 670 cm⁻¹ shifting to 683 cm⁻¹. Additionally, the disappearance of the 914 cm⁻¹ mode and the appearance of a new mode at 860 cm⁻¹, observed for the ion-exchanged TNW/Co(5%) sample, may be seen as a signature of substitution of Na⁺ by ionic hydrated Co into TNW interlayers [31,33,34]. The TNW' interlayer modification can also be pursued in the low wavenumber range, where the lattice Raman mode at 192 cm⁻¹ shifts to 190 cm⁻¹ and the intensity of the mode at 155 cm⁻¹ decreases (or vanishes) with the substitution of Na⁺ by ionic hydrated Co [26]. Thus, the different degrees of structural rearrangement of the prepared samples induced either by Co doping or by Co ion exchange can be attributed to the Raman modes of the samples and are in accordance with the XRD data previously discussed.

The optical characterization of the samples was carried out by measuring their diffuse reflectance, *R*, in the UV-Vis region. *R* is related to the absorption Kubelka–Munk function,

F_{KM} , by the relation $F_{KM}(R) = (1-R)^2/2R$, which is proportional to the absorption coefficient [35]. The samples' absorption spectra are shown in Figure 4.4.

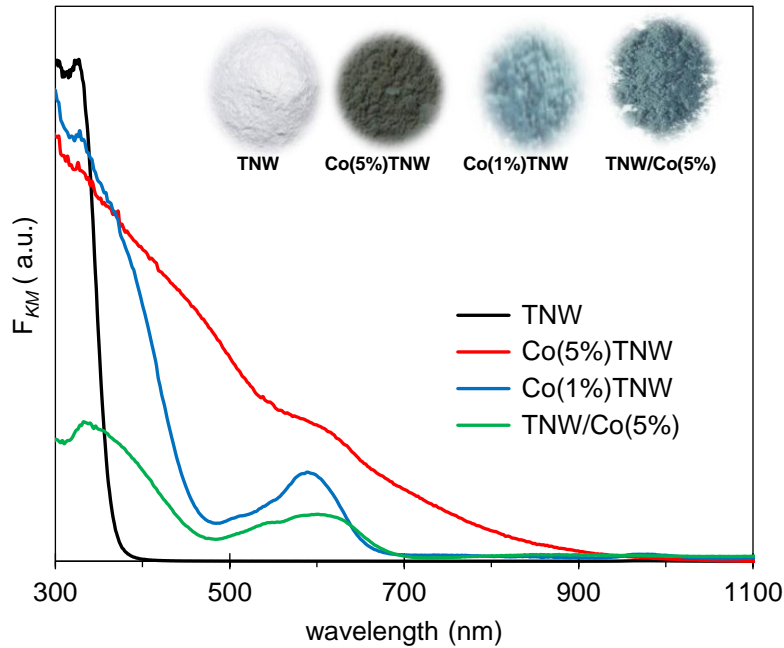


Figure 4.4 – Optical spectra of the TNW, Co(1%)TNW, Co(5%)TNW and TNW/Co(5%) samples.

As can be seen in Figure 4.4, the light absorption edge of the TNW samples is red-shifted after Co modification. The Co-containing samples absorb radiation in the visible region, the Co(5%)TNW sample being the one with higher light absorption capability. The observed optical red shift for the Co-modified samples can be attributed to the insertion of the Co $3d$ orbitals within the forbidden band and subsequent charge-transfer transition between the d -electrons of the dopant and the conduction band of the TNW, besides the defects associated with oxygen vacancies generated for charge balancing when Co^{2+} replaces the Ti^{4+} in the TiO_6 octahedra TNW building blocks [12].

The UV–Vis spectra of Co-doped TNW samples also exhibit an absorption band at around 480–650 nm, a typical feature associated with transition metal doped semiconductors which may arise from charge transfer and d – d transitions of the metal [36]. According to Morgado *et al.* the introduction of Co^{2+} $3d$ states into the trititanate crystal structure results in their splitting, leading to the formation of lower and higher $3d$ energy states [30]. This hypothesis should be experimentally supported by an increase of the d – d transitions with increasing Co content. The analysis of the results obtained for the doped Co(1%)TNW and Co(5%)TNW samples does not allow reaching this conclusion; indeed the Co(5%)TNW absorption band centered at 580 nm is weaker than that of Co(1%)TNW. This result strongly suggests the co-existence of cobalt in the

crystalline lattice and in the interlayers in accordance with the XRD and Raman data. Moreover, this is also supported by some similarities between the optical behavior of the Co(5%)TNW and TNW/Co(5%) samples, especially for wavelengths below 480 nm. Concerning the optical red shift of the ion-exchanged TNW/Co(5%) sample, the intercalated Co ions in the interlayer region may form a one-dimensional Co chain, the overlapped Co-3d orbitals along the channel resulting in a delocalized 1D band below the Fermi level which extends the absorption edge into the visible region, similarly to what happens when Fe is intercalated in TNW based structures [37].

The optical bandgap energy of the samples was calculated using the procedure previously described [38], by plotting the function $f_{KM} = (F_{KM}.hv)^{1/2}$ vs. hv (Tauc plot). The values of 3.27 ± 0.03 eV, 2.43 ± 0.05 eV and 2.27 ± 0.02 eV were obtained for TNW, Co(1%)TNW and TNW/Co(5%) samples respectively. No accurate bandgap energy was possible to infer for the Co(5%)TNW sample since no well-defined band absorption edge was observed due to its near-continuous absorption in the UV-vis region.

To gain a deeper insight into the electronic structure of the synthesized materials, all samples were analyzed by XPS. Figure 4.5(a and b) shows the survey spectra of the pristine TNW and Co(5%)TNW samples. The spectra of Co(1%)TNW and TNW/Co(5%) samples are similar to those obtained for Co(5%)TNW (results not shown). In addition to the Na 1s, Ti 2p, and O 1s photoelectron peaks typical of the TNW (Figure 4.5(a)), the Co(5%)TNW, Co(1%)TNW, and TNW/Co(5%) XPS survey spectra show a Co 2p doublet peak (Figure 4.5(b)).

The high-resolution spectra of Ti 2p and O 1s regions for TNW and Co(5%)TNW samples, and Co 2p regions for all the samples with cobalt (Co(1%)TNW, Co(5%)TNW and TNW/Co(5%)) are presented in Figure 4.5.

The XPS spectrum of the TNW sample shows the Ti 2p_{3/2} and 2p_{1/2} peaks at 458.641 and 464.441 eV, respectively (Figure 4.5(c)). An identical profile was observed for the Co(1%)TNW and TNW/Co(5%) samples (not shown). However, for Co(5%)TNW sample a slight shift of these peaks, to 458.241 and 464.157 eV, respectively, due to the higher Co doping level was observed (Figure 4.5(c)).

For the TNW and Co-modified TNW samples, the doublet splitting energies of the Ti 2p peaks are between 5.7 to 5.9 eV, which also agrees with the presence of titanium only as Ti⁴⁺ in all samples [39,40]. Indeed, no signals are perceptible in the 456.2–457.4 eV range which can be ascribed to Ti³⁺ [41,42].

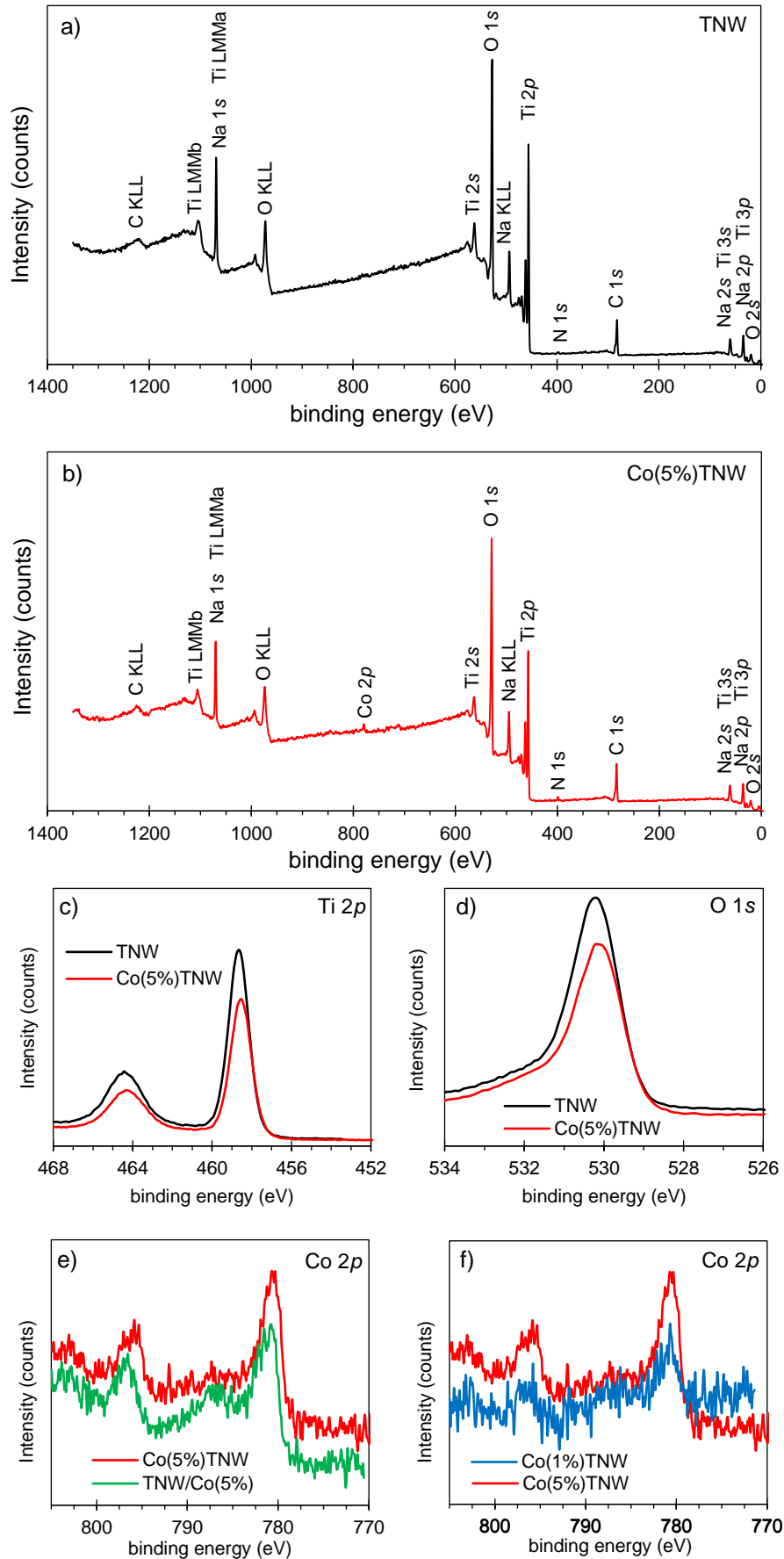


Figure 4.5 – XPS survey spectra of the (a) TNW and (b) Co(5%)TNW samples. XPS high-resolution spectra of the (c) Ti 2p, (d) O 1s and (e and f) Co 2p regions.

The main peak in the O 1s core-spectra at *ca.* 530 eV (Figure 4.5(d)) corresponds to lattice oxygen and it has some contribution of the sodium Auger peak (Na KLL). The high-resolution spectra of the Co 2p region for the TNW/Co(5%) and Co(5%)TNW samples are presented in Figure 4.5(e). Concerning the ion-exchange TNW/Co(5%) sample, the binding energies related to the Co 2p_{1/2} and Co 2p_{3/2} peaks are ~ 780 and ~ 796 eV, respectively. Also, the satellite lines of these two peaks, which are characteristic of the Co(II) oxidation state, are clearly visible for higher energies. A comparative analysis of this spectrum with that of the doped Co(5%)TNW sample shows a shift of the Co 2p_{1/2} and Co 2p_{3/2} peaks towards to higher energies and a decrease of the respective satellite features, which indicate the existence of Co(II) and Co(III) oxidation states [43]. These results are in accordance with those previously reported by Wu *et al.* [44] and seems to support the assumption that during the hydrothermal process the precursor powders were firstly dissolved in NaOH solution before the formation of the TNW sheets [44,45]. Accordingly, some ionic cobalt is dissolved, probably in both Co²⁺ and Co³⁺ oxidation states, remaining afterward in solution and thus leading to Co-doped TNW samples with cobalt in two distinct positions: replacing some Ti⁴⁺ in the TiO₆ octahedra (crystalline network) and between the interlayers.

Once the nanowires thickness is inferior to the XPS radiation penetration, the quantification of the cobalt content in the prepared TNW based samples was also performed. A cobalt content value of 1.7 at%, corresponding to a Co/Ti ratio of 6.38%, was estimated for the ion-exchange TNW/Co(5%) sample. On the other hand, cobalt content values of 0.21 at% (Co/Ti = 0.83%) and 1.41 at% (Co/Ti = 6.26%) were obtained for the Co(1%)TNW and Co(5%)TNW samples, respectively. It is worth noting that the samples' Co content as determined by XPS is close to the samples' nominal Co content. Additionally, the Na⁺ content of the ion-exchange TNW/Co(5%) sample is lower than the content values obtained for the doped samples, in accordance with the expected higher level of Na⁺/Co²⁺ substitution in the TNW interlayer structure of that sample.

4.4 - Photo-induced hydroxyl radical production

Anticipating the use of the prepared materials as photocatalysts, the evaluation of their photocatalytic performances for the hydroxyl radical ([•]OH) production, one of the most oxidative species in advanced oxidative treatments, was studied. Terephthalic acid (TA), was used as a probe molecule and, the generation and quantification of [•]OH were analyzed by fluorescence spectroscopy, as previously discussed in Chapter 1 - Section 1.3. Figure 4.6 shows

the amount of 2-hydroxyterephthalic acid, HTA, produced by TA/catalyst suspensions irradiated for 20 min with UV-vis radiation.

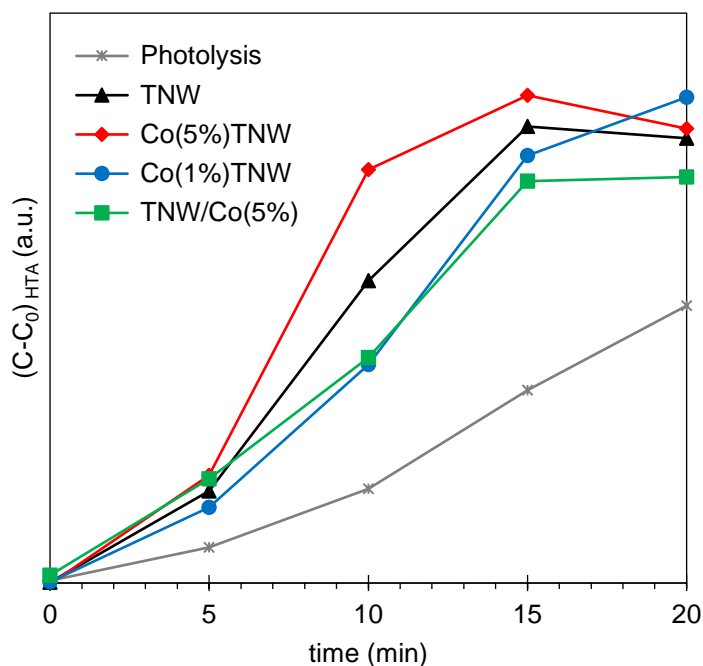


Figure 4.6 – HTA concentration during 20 min of UV-vis irradiation of a TA solution (3 mM, 150 mL) using 10 mg of each photocatalyst.

As can be seen in Figure 4.6, all the prepared samples demonstrated catalytic activity for this reaction, the Co(1%)TNW sample being the best catalyst for the photo-induced hydroxyl radical production after 20 min of irradiation. Taking the TA photolysis performance as a reference, an increase of 75% in the radical production was attained using the Co(1%)TNW sample as a catalyst, while increases of 64% and 61% were attained for Co(5%)TNW and TNW samples, respectively. The slight decrease in the $\cdot\text{OH}$ production observed for these samples after 20 min of irradiation can be explained by the partial photodegradation of HTA [46]. Using the cobalt ion-exchanged TNW/Co(5%) sample, a relative increase of 46% in the reaction yield was observed.

These results allow concluding that the cobalt doping leads to an enhancement of the TNW photocatalytic performance for this reaction. Those results also agree with published works, for which a catalytic activity enhancement is usually attributed to doped samples and is dependent on the metal substitution degree; lower metal substitution levels usually leading to better catalytic performances [47-49].

4.5 - Adsorption and photocatalytic studies

4.5.1 – Phenol, naphthol yellow S and brilliant green adsorption

The photocatalytic ability of the pristine and Co-modified TNW samples for pollutants photodegradation processes was examined by monitoring the degradation of several organic model compounds. To evaluate their photocatalytic flexibility, phenol, a more anionic compound – naphthol yellow S (NYS) – and a more cationic compound – brilliant green (BG) – were chosen as model pollutants. The schematic representation of these three model pollutants is presented in Figure 4.7.

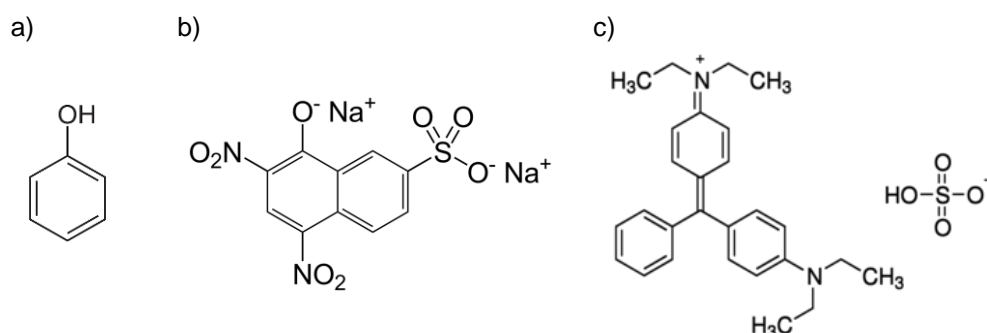


Figure 4.7 – Schematic representation of (a) phenol, (b) naphthol yellow S and (c) brilliant green molecules.

Due to their importance in heterogeneous photocatalytic processes, the adsorption characteristics of each catalyst/pollutant system were evaluated prior to the photocatalytic experiments and the results are summarized in Figure 4.8.

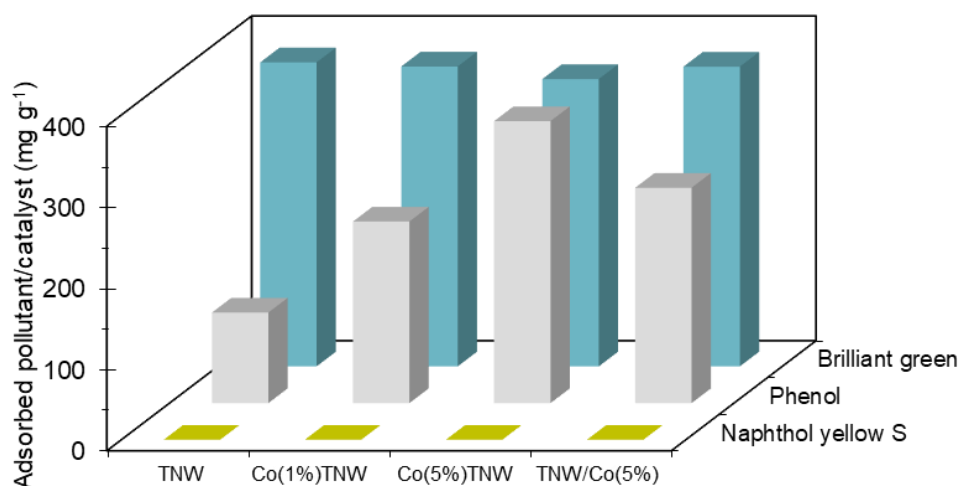


Figure 4.8 - Phenol, BG and NYS adsorption ability using pristine TNW, Co(1%)TNW, Co(5%)TNW and TNW/Co(5%) samples as adsorbents.

Contrarily to phenol and BG, the NYS did not show any affinity for adsorption either on the pristine TNW or on the TNW modified samples. The immobilization of BG seems to be almost

independent of the surface nature. Indeed, values between 374 and 354 mg g^{-1} were obtained for the TNW and Co(5%)TNW samples, respectively. Concerning the phenol adsorption, a value of 111.4 mg g^{-1} was obtained for the pristine TNW sample. Regarding the doped samples, the amount of adsorbed phenol increases from 223.6 to 347.2 mg g^{-1} when the nominal cobalt increases from 1% (Co(1%)TNW sample) to 5% (Co(5%)TNW sample). For the ion-exchanged TNW/Co(5%) value of 265.2 mg g^{-1} was determined.

To decide the most appropriate duration of each pollutant photodegradation experiment, some preliminary photolysis runs were carried out. A period of 90 min was considered adequate for the 20 ppm phenol solution, a period of 45 min for the 20 ppm NYS solution, and also for the 10 ppm BG solution degradation.

4.5.2 – Phenol photocatalytic degradation

The photocatalytic efficiency of the pristine and Co-modified TNW samples, on the degradation of a 20 ppm phenol solution, was studied for 90 min. The results were analyzed by GC-MS and the phenol concentration profiles during irradiation time are depicted in Figure 4.9.

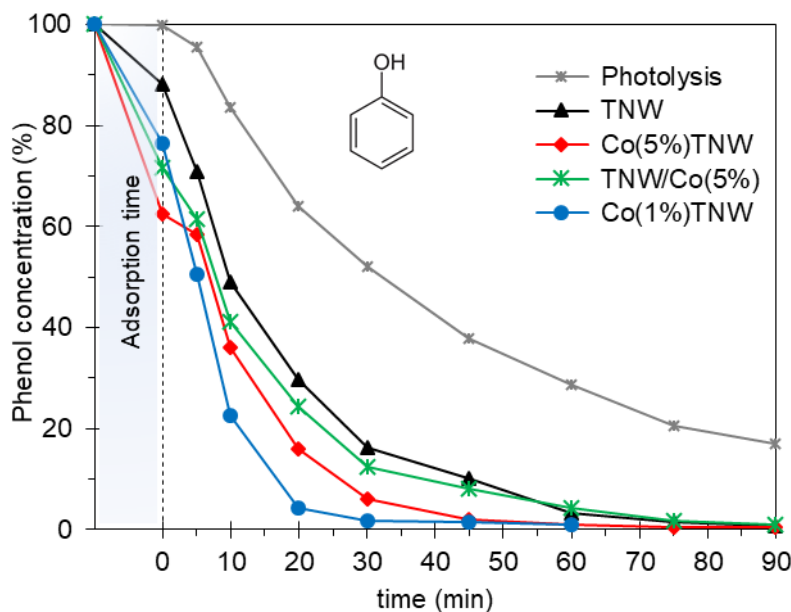


Figure 4.9 – Concentration of phenol during 90 min of irradiation using TNW, Co(1%)TNW, Co(5%)TNW and TNW/Co(5%) samples as photocatalysts.

As can be seen, after a dark period of 60 min, 11.8% of the initial phenol was adsorbed by the TNW surface sample. However, using the Co(1%)TNW and TNW/Co(5%) samples 23.5% and 28.3% of phenol was adsorbed by these samples, respectively. Furthermore, the highest amount

of phenol adsorbed was 37.5% on the Co(5%)TNW surface (the sample with the lower surface area: $241.59 \text{ m}^2 \text{ g}^{-1}$).

Regarding the irradiation period, all the tested samples demonstrated the ability to photodegrade this pollutant. After 30 min of irradiation, the phenol degradation was practically completed (98.3%) using the Co(1%)TNW sample as a photocatalyst, which contrasts with the 83.8% of degradation achieved by the less catalytic sample, the pristine TNW powder. For the same irradiation period, photodegradation of 93.9% and 87.6% were attained using the Co(5%)TNW and TNW/Co(5%) samples, respectively. These results are in agreement with published studies corroborating that metal doping usually enhances the catalytic properties of the pristine material [47-49]. It is interesting to highlight that the best results were accomplished by the sample with the lowest cobalt doping level. Although the Co(5%)TNW and TNW/Co(5%) samples are both catalytic for this degradation process, an additional time of 30 min was required to complete the phenol degradation using Co(5%)TNW sample, and more 30 min were necessary to attain identical degradation level using the TNW/Co(5%) sample.

4.5.3 - Brilliant green (BG) photocatalytic degradation

The photocatalytic efficiency of the TNW and Co-modified TNW samples on 10 ppm BG solution degradation was evaluated during 45 min of irradiation (Figure 4.10). For comparative purposes, the dye photolysis was also evaluated.

Figure 4.10(a) depicts the dye UV-vis spectra during irradiation, in the presence of the Co(1%)TNW sample as a catalyst. As previously discussed, the extensive dye adsorption is easily confirmed by the intensity decrease of the 624 nm peak at $t = 0$ spectrum. As can be seen, during irradiation all the characteristic dye absorption bands decrease gradually with time, which indicates a progressive removal of the dye. Moreover, the disappearance of the lower wavelength absorption bands (typical for aromatic rings), for longer irradiation times, indicates the degradation of the by-products meanwhile formed.

Figure 4.10(b) depicts the BG degradation over the irradiation time, for all the samples tested. As visible in Figure 4.10(b), after 60 min in darkness, 75%, 71%, 74% and 74% of the initial dye were removed from solution by adsorption, using TNW, Co(5%)TNW, Co(1%)TNW and TNW/Co(5%) respectively, as adsorbents.

After turning on the lamp all the samples demonstrated catalytic activity for the dye photodegradation reaction. After 20 min of irradiation, the best sample for the BG removal was the TNW/Co(5%) powder with a 99% decrease in the dye concentration. The second best photocatalyst seems to be the Co(1%)TNW with 97% removal. However, considering that

Co(1%)TNW sample adsorbs more dye than the Co(5%)-TNT sample, the dye degradation at 20 min is better for the latter catalyst (97%). Nevertheless, it should be pointed out that after 45 min, the removal performances of all Co-modified samples were identical and better than that of the pristine TNW sample.

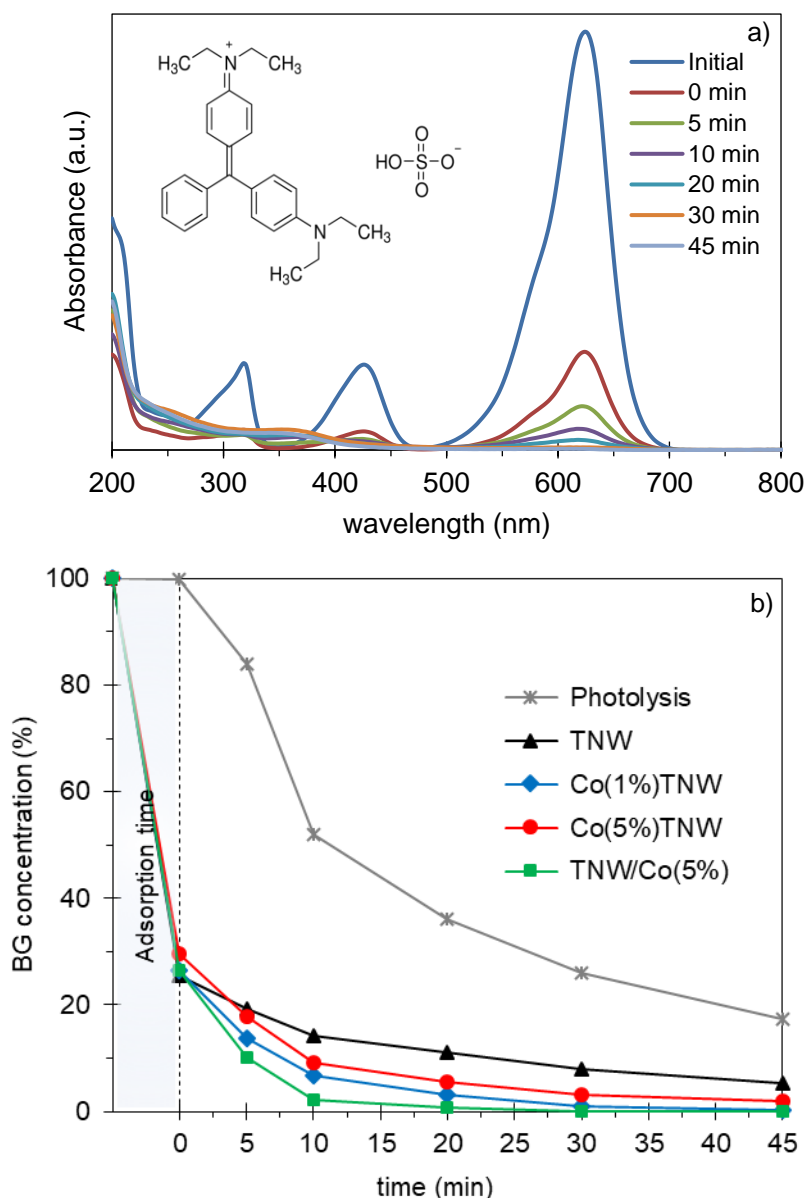


Figure 4.10 – (a) Electronic spectra of a 10 ppm BG solution during 45 min of irradiation using Co(1%)TNW as a photocatalyst and (b) concentration of BG *versus* irradiation time using the prepared samples as catalysts.

4.5.4 - Naphthol yellow S (NYS) photocatalytic degradation

The photocatalytic efficiency of the prepared samples was also tested in the degradation of an NYS dye 20 ppm solution during 45 min of UV-vis irradiation. Figure 4.11(a) shows the electronic NYS spectra during the irradiation period, in the presence of Co(1%)TNW. The reduction of the NYS dye concentration during photoirradiation, using TNW, Co(1%)TNW,

Co(5%)TNW and TNW/Co(5%) as catalysts, is shown in Figure 4.11(b). Since no NYS adsorption occurs prior to irradiation, the adsorption period was not considered in the graphs. As can be seen in Figure 4.11(a), the intensity of all the characteristic absorption bands of the dye decreases with increasing irradiation time, which indicates a gradual removal of this pollutant. However, the unexpected gap between the 10 and 20 min spectral profiles suggests the existence of two distinct stages during this process. This phenomenon was not observed for the photolysis and/or other catalyzed experiments.

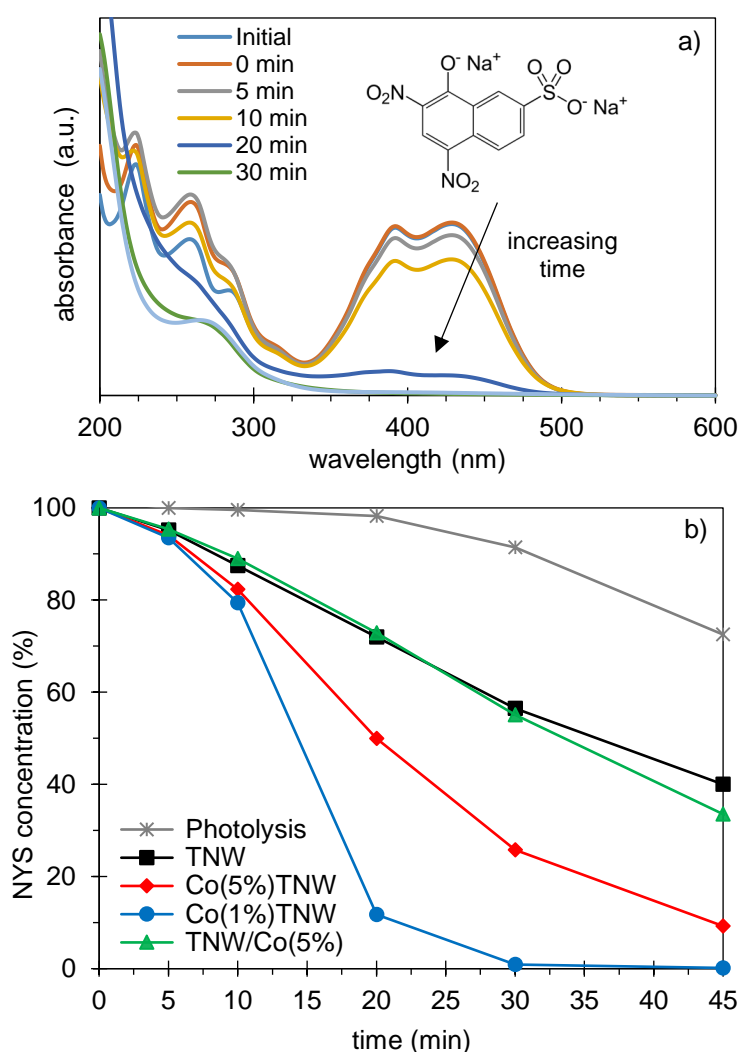


Figure 4.11 – (a) Electronic spectra of a 20 ppm NYS solution during 45 min of irradiation using Co(1%)TNW as photocatalyst and (b) concentration of NYS *versus* irradiation time using the prepared samples as catalysts.

As visible in Figure 4.11(b), after 30 min of irradiation, the dye degradation was complete using Co(1%)TNW as photocatalyst. For the same period, a reduction of 74% of the NYS concentration was achieved using the Co(5%)TNW sample, whereas only a reduction of 45% was attained using either the pristine TNW or the TNW/Co(5%) sample as catalysts. After 45

min of irradiation, the use of the Co(5%)TNW sample enabled achieving a reduction of 91% of the NYS concentration, but only a reduction of 67% and 60% of the dye concentration was observed when using the TNW/Co(5%) and TNW samples, respectively. Therefore, among the prepared samples, the best catalyst for the NYS photodegradation is the Co(1%)TNW sample. Longer irradiation times are required for the other three samples to accomplish the complete dye photodegradation.

The overall analysis of the photodegradation results obtained strongly supports that the existence of Co as a doping element in the TNW crystal structure (replacing the Ti^{4+}) is more advantageous for these oxidative processes when compared with the cobalt located between the TiO_6 interlayers, replacing only the Na^+ .

Taking into account the present results and the reported band structure calculations for Co-doped TiO_2 , [50,51] a mechanism for the light-activated charge-transfer processes in the Co-modified TNW is proposed in Figure 4.12. Accordingly, the valence band (VB) of the Co-modified TNW is derived primarily from O 2p-levels, the conduction band (CB) from the Ti 3d-levels, and the crystal field split Co 3d-levels forming localized bands within the original bandgap energy. For Co-doped TiO_2 , Ha *et al.* [50] estimated that the partially filled Co 3d band is located 2.2 eV below the conduction band. Therefore, when an aqueous Co modified TNW suspension is irradiated with higher energy than TNW' bandgap energy, electrons (e^-) and holes (h^+) are generated in the semiconductor' conduction and valence bands, respectively, and the Co 3d band increasing the availability of the photogenerated charge carriers. The photogenerated electrons could easily transfer to the adsorbed oxygen and a rapid formation of $\text{O}_2^{\bullet-}$ species can occur. The formed $\text{O}_2^{\bullet-}$ active species will participate in the photocatalytic oxidation processes, while the photogenerated holes will react with OH^- or H_2O oxidizing them to $\bullet\text{OH}$ radicals. The combined action of h^+ and the other highly oxidant species, including $\bullet\text{OH}$, will be responsible for the pollutant degradation.

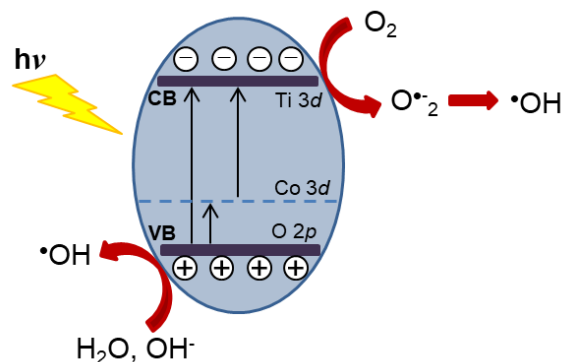


Figure 4.12 – Band structure scheme of Co-modified TNW and the mechanism of photo-induced oxidant radical formation.

4.5.5 - Pollutants mixture photodegradation

Supported by the above-described results and considering that in the real world the simultaneous degradation of several pollutants is required in numerous situations, the degradation of a mixture composed of phenol, naphthol yellow S and brilliant green was carried out. The Co(1%)TNW sample was selected as a catalyst for this study since it demonstrated to have the best catalytic performance. The concentration of each pollutant in the mixture solution was identical to that used in each individual photodegradation study. The period of irradiation was extended to 150 min once the amount of catalyst used was also the same (0.13 g L^{-1}). The obtained results are depicted in Figure 4.13.

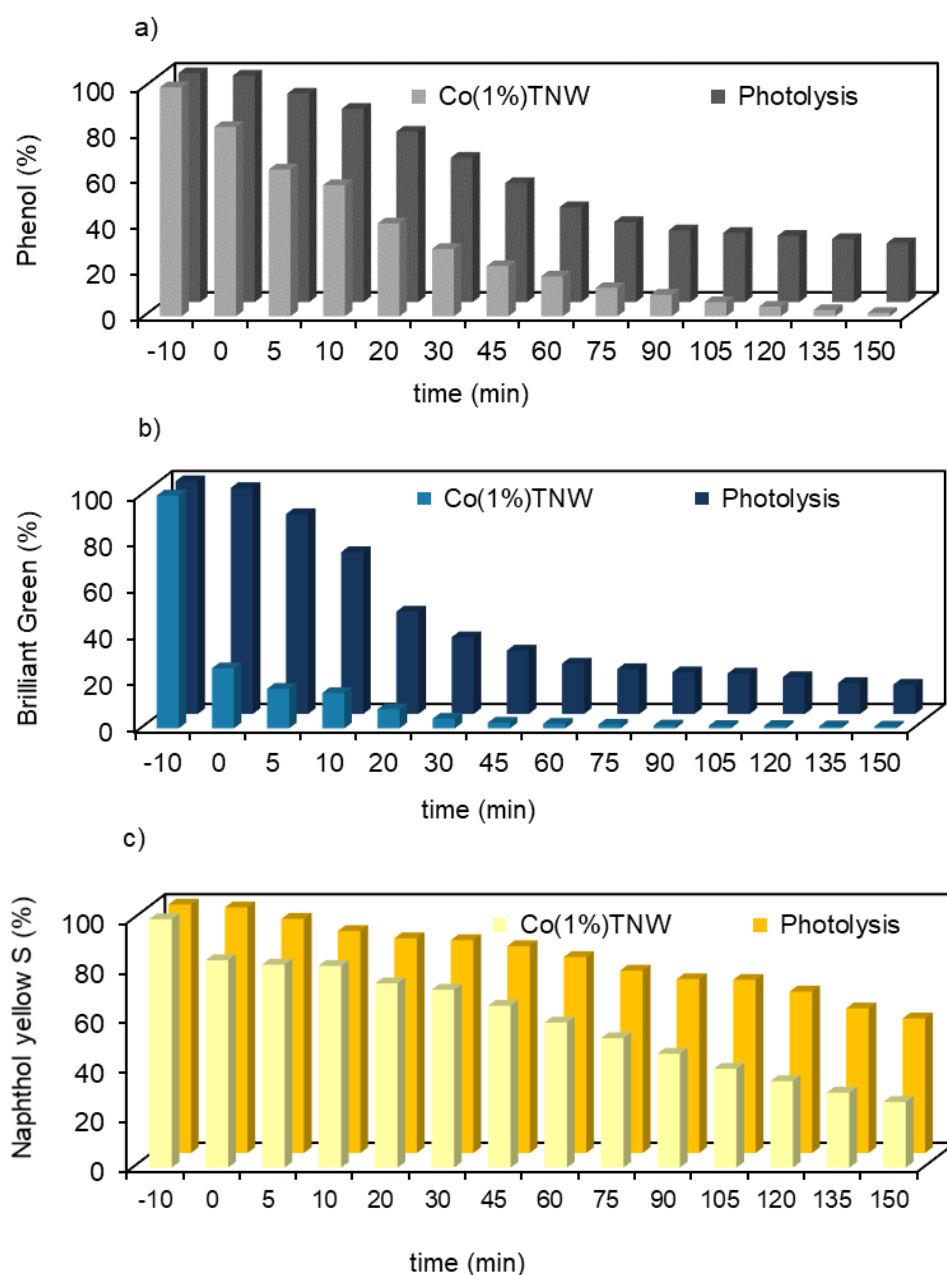


Figure 4.13 – Decrease of the phenol (a), BG (b) and NYS (c) concentration in a pollutant mixture solution, during 150 min of irradiation, using Co(1%)TNW as a catalyst and during photolysis.

Considering first the photolysis experiments, it should be noted that the use of a pollutant mixture solution leads to a slower overall degradation process in comparison to that occurring in single solutions (Figure 4.13). The phenol photodegradation rate was the process most negatively affected by the ‘mixture effect’. Actually, for a period of 90 min, 83.1% of phenol present in the single solution was degraded *via* photolysis while a value of only 68.6% has been achieved for the pollutant mixture solution. Similarly, for 45 min of irradiation, 83% of the BG dye was degraded when in a single solution, whereas only 73% was degraded when taken in the mixture solution. Also, upon 45 min of irradiation, the NYS photolysis leads to a degradation of 28% and 17% of this dye in the single solution and in the pollutant mixture solution, respectively.

Considering now the photocatalytic experiments on the pollutants mixture solution, the Co(1%)TNW sample demonstrated the best catalytic activity as expected. After 150 min of irradiation, less than 1% of phenol, 1% of BG, and 26% of NYS remained in the mixture solution (Figure 4.13(a–c)). During the photodegradation period, the pollutant that was faster removed from the solution was the BG dye (45 min, 98% degraded). To achieve an identical phenol degradation level, an irradiation time of 135 min was required.

It is interesting to notice that, during the adsorption period, the NYS present in the pollutant mixture demonstrated some ability to be adsorbed by the Co(1%)TNW. Indeed, 17% of the dye was adsorbed, contrasting with the absence of NYS adsorption when used individually with the same photocatalyst, as previously described in section 4.5 and shown in Figure 4.8. This fact is more interesting if it is taken into consideration that a relatively smaller amount of solid was available for the simultaneous adsorption of the three pollutants. Preliminary studies, involving the stepwise adsorption of these three pollutants, were performed and the results seem to indicate the occurrence of a multi-layer adsorption process, the NYS adsorption being dependent on the previous adsorption of BG. A systematic investigation of this phenomenon was not the goal of this work. However, the importance of these studies for the correct evaluation of the catalytic performances of materials should be carefully considered.

4.5.6 – Kinetic studies

The pollutant photodegradation data previously discussed allow going further into the kinetics of the several degradation processes studied (Figure 4.14). The photocatalytic degradation rate of most organic pollutants follows the pseudo-first-order kinetics:

$$\ln\left(\frac{C_0}{C}\right) = k_{ap} t \quad (4.1)$$

where C is the pollutant concentration at time t , C_0 is the pollutant concentration at time zero and k_{ap} is the apparent reaction rate constant. Therefore, plotting $\ln C_0/C$ versus t , the experimental data can be fitted by a straight line, whose slope is the apparent first-order rate constant k_{ap} .

Figure 4.14 shows the characteristic plots of the phenol and BG kinetic degradation processes, using either single solutions or a pollutant mixture solution, and for an irradiation period of 30 min. The plots corresponding to the photolysis are shown for comparative purposes.

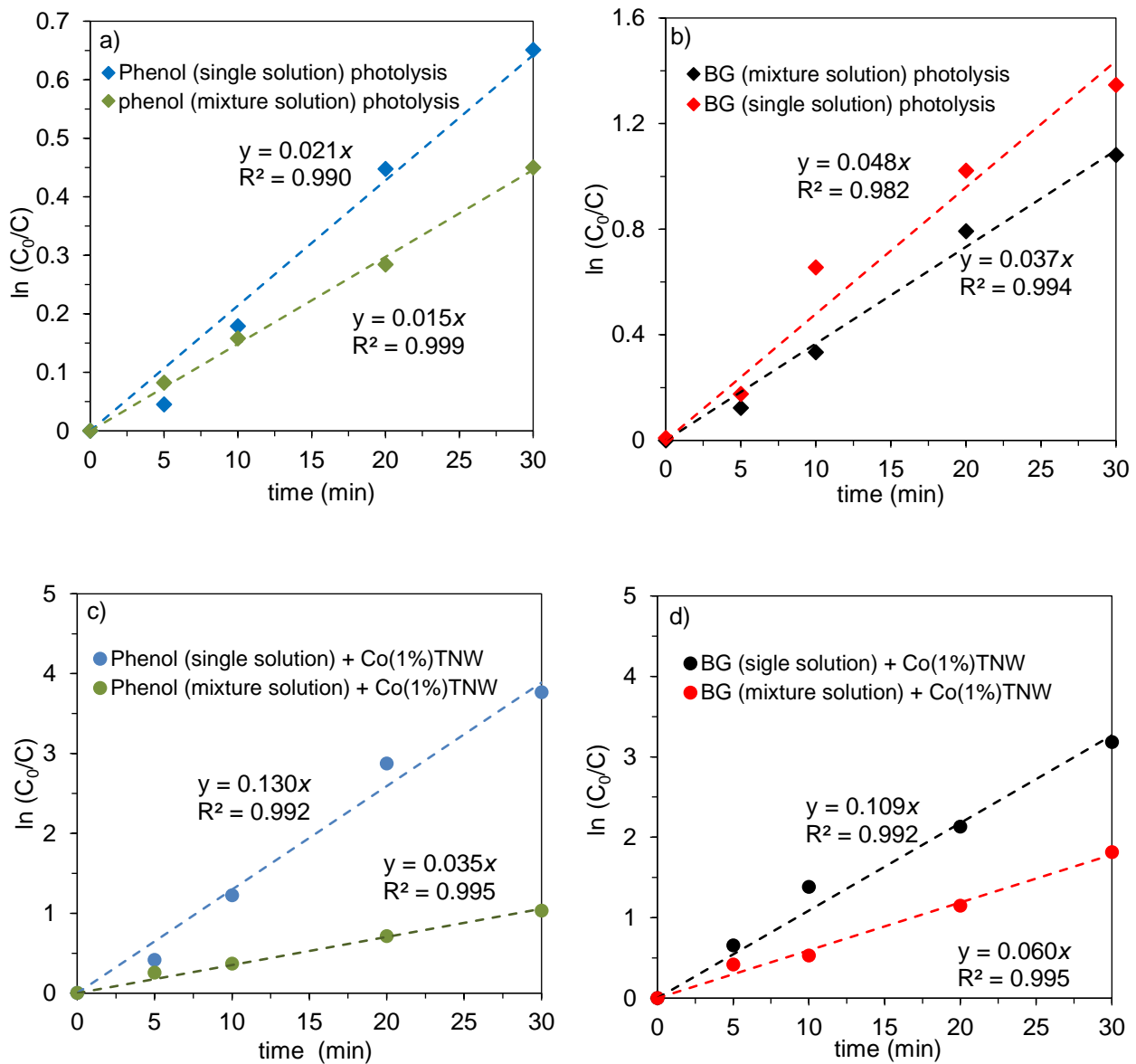


Figure 4.14 – Kinetics of the photodegradation reaction of phenol and of BG, in single solutions and in a pollutant mixture solution (a and b) via photolysis and (c and d) using Co(1%)TNW as a photocatalyst.

It should be noted that no satisfactory fittings were obtained for the NYS dye photodegradation. The apparent first-order rate constants obtained for the photodegradation processes of phenol and BG in single solutions catalyzed by the Co(1%)TNW powders are $k_{ap} = 0.130 \pm 0.005 \text{ s}^{-1}$ and $k_{ap} = 0.109 \pm 0.0043 \text{ s}^{-1}$, respectively, the phenol in a single solution being the faster pollutant to be degraded. The opposite occurs when one considers the pollutant mixture solution, the phenol degradation rate being $k_{ap} = 0.035 \pm 0.001 \text{ s}^{-1}$, lower than that obtained for the degradation of BG, $k_{ap} = 0.060 \pm 0.005 \text{ s}^{-1}$. It is also interesting to note that, when using Co(1%)TNW as a photocatalyst, the differences between the k_{ap} values obtained for the single solutions and that deduced for the pollutant mixture solution are larger than the difference between that values considering photolysis. These results reinforce the importance of the studies with pollutant mixture solutions for the accurate assessment of the photocatalytic performance of materials.

4.6 - Conclusions

Titanate nanowires (TNW) modified by cobalt doping (CoTNW) and by Co ion-exchange (TNW/Co) were successfully prepared by the hydrothermal method.

The influence of the nominal cobalt doping level and the cobalt position in the TNW crystalline structure were studied. XRD, Raman and XPS characterization strongly support that Co doping was accomplished for the doped samples by $\text{Ti}^{4+}/\text{Co}^{2+}$ substitution in the TiO_6 octahedra of the TNW crystalline structure, whereas the incorporation of cobalt between the TiO_6 layers *via* the replacement of Na^+ ions by hydrated Co ions occurred for the ion-exchanged samples.

Beyond the expected doping by $\text{Ti}^{4+}/\text{Co}^{2+}$ substitution, structural analyses of the doped sample with a higher cobalt content (Co(5%)TNW) suggest the co-existence of some cobalt ions between the TiO_6 layers. This particular result seems to agree with the assumption that during the hydrothermal process the precursor powders were firstly dissolved in NaOH solution before the formation of the TNW sheets. Consequently, some ionic cobalt is dissolved, remaining afterward in solution and thus leading to Co-doped TNW samples with cobalt in two distinct positions. Although no perceptible influence of the Co ion position was observed on the morphology of the prepared samples, the optical behavior of the Co-modified TNW samples is clearly dependent on either the cobalt ions substituting the Ti^{4+} ions into the TiO_6 octahedra or replacing the Na^+ ions between the TiO_6 layers. The absorption spectra of the samples showed that all the Co-modified TNW samples absorb radiation in the visible region, Co(5%)TNW being the one with a higher light absorption capability. The optical red shifts shown by the Co-

modified samples may be attributed to the insertion of the Co 3*d* orbitals within the forbidden band and the subsequent charge-transfer transition between the *d*-electrons of the dopant and the conduction band of the TNW. For the Co-doped TNW samples, the UV-vis spectra also exhibit a typical absorption band associated with transition metal doped semiconductors which arise from charge transfer and *d-d* transitions of the metal. A comparative analysis of the optical behavior of the doped and ion-exchanged samples also suggests the co-existence of cobalt in the TiO₆ octahedra and between the TiO₆ sheets in the Co(5%)TNW sample.

The catalytic ability of these materials for pollutants photodegradation was also investigated. First, the catalytic production of the hydroxyl radical was evaluated. Subsequently, phenol, NYS, and BG were used as model pollutants. Anticipating real-world situations, photocatalytic experiments using a mixture solution of these three pollutants were performed. It was shown that the Co modified TNW materials (CoTNW and TNW/Co) are good catalysts, the photocatalytic performance being dependent on the Co/Ti ratio and on the structural Co position. The Co(1%)TNW doped sample showed the best photocatalytic activity for all the degradation processes studied.

4.7 - References

- 1 - J. Choi, H. Park, M.R. Hoffmann, Effects of single metal-ion doping on the visible-light photoreactivity of TiO₂, *J. Phys. Chem. C* 114 (2010) 783-792.
- 2 - S. So, K. Lee, P. Schmuki, Ru-doped TiO₂ nanotubes: improved performance in dye-sensitized solar cells, *Phys. Status Solidi RRL* 6 (2012) 169-171.
- 3 - K. Song, X. Han, G. Shao, electronic properties of rutile TiO₂ doped with 4*d* transition metals: First-principles study, *J. Alloys Compd.* 551 (2013) 118-124.
- 4 - M.R. Nunes, O.C. Monteiro, A.L. Castro, D.A Vasconcelos, A.J. Silvestre, A new chemical route to synthesise TM-doped (TM = Co, Fe) TiO₂ nanoparticles, *Eur. J. Inorg. Chem.* 2008 (2008) 961-965.
- 5 - B. Choudhury, A. Choudhury, Luminescence characteristics of cobalt doped TiO₂ nanoparticles, *J. Lumin.* 132 (2012) 178-184.

- 6 - L.K. Gaur, P. Kumar, D. Kushavah, K.R. Khiangte, M.C. Mathpal, V. Agrahari, S.P. Gairola, M.A.G. Soler, H.C. Swart, A. Agarwal, Laser induced phase transformation influenced by Co doping in TiO₂ nanoparticles, *J. Alloys Compd.* 780 (2019) 25-34.
- 7 - P. Jiang, W. Xiang, J. Kuang, W. Liu, W. Cao, Effect of cobalt doping on the electronic, optical and photocatalytic properties of TiO₂, *Solid State Sci.* 46 (2015) 27-32.
- 8 - I. Ali, O.M.L. Alharbi, Z.A. Alothman, A.Y. Badjah, Kinetics, Thermodynamics, and modeling of amido black dye photodegradation in water using Co/TiO₂ nanoparticles, *Photochem. Photobiol.* 94 (2018) 935-941.
- 9 - J.L. Gole, S.M. Prokes, O.J. Glembocki, J. Wang, X. Qiu, C. Burda, Study of concentration-dependent cobalt ion doping of TiO₂ and TiO_{2-x}N_x at the nanoscale, *Nanoscale* 2 (2010) 1134-1140.
- 10 - S. Mugundan, B. Rajamannan, G. Viruthagiri, N. Shanmugam, R. Gobi, P. Praveen, Synthesis and characterization of undoped and cobalt-doped TiO₂ nanoparticles via sol-gel technique, *Appl Nanosci.* 5 (2015) 449-456.
- 11 - I. Ganesh, A.K. Gupta, P.P. Kumar, P.S. C. Sekhar, K. Radha, G. Padmanabham, G. Sundararajan, Preparation and characterization of Co-doped TiO₂ materials for solar light induced current and photocatalytic applications, *Mater. Chem. Phys.* 135 (2012) 220-234.
- 12 - V.C. Ferreira, M.R. Nunes, A.J. Silvestre, O.C. Monteiro, Synthesis and properties of Co-doped titanate nanotubes and their optical sensitization with methylene blue, *Mater. Chem. Phys.* 142 (2013) 355-362.
- 13 - T.M.F. Marques, O.P. Ferreira, J.A.P. da Costa, Kazunori Fujisawa, M. Terrones, B.C. Viana, Study of the growth of CeO₂ nanoparticles onto titanate nanotubes, *J. Phys. Chem. Solids* 87 (2015) 213-220.
- 14 - J. Fan, Z. Zhao, J. Wang, L. Zhu, Synthesis of Cr,N-codoped titania nanotubes and their visible-light-driven photocatalytic properties, *Appl. Surf. Sci.* 324 (2015) 691-697.

- 15 - B. Barrocas, A.J. Silvestre, A.G. Rolo, O.C. Monteiro, The effect of ionic Co presence on the structural, optical and photocatalytic properties of modified cobalt–titanate nanotubes, *Phys. Chem. Chem. Phys.* 16 (2016) 18081-18093.
- 16 - E.K. Ylhäinen, M.R. Nunes, A.J. Silvestre, O.C. Monteiro, Synthesis of titanate nanostructures using amorphous precursor material and their adsorption/photocatalytic properties, *J. Mater. Sci.* 47 (2012) 4305-4312.
- 17 - D.V. Bavykin, F.C. Walsh, Titanate and titania nanotubes: Synthesis, properties and applications, RSC Nanoscience & Nanotechnology Series, Cambridge, UK, RSC Publishing, 2010.
- 18 - B. Barrocas, M.C. Neves, M. Conceição Oliveira, O.C. Monteiro, Enhanced photocatalytic degradation of psychoactive substances using amine-modified elongated titanate nanostructures, *Environ. Sci. Nano* 5 (2018) 350-361.
- 19 - H. Liu, D. Yang, E.R. Waclawik, X. Ke, Z. Zheng, H. Zhu, R.L. Frost, A Raman spectroscopic study on the active site of sodium cations in the structure of $\text{Na}_2\text{Ti}_3\text{O}_7$ during the adsorption of Sr^{2+} and Ba^{2+} cations, *J. Raman Spectrosc.* 41 (2010) 1792-1796.
- 20 - A. Yankin, O. Vikhreva, V. Balakirev, PeTex diagram of the Co-Ti-O system, *J. Phys. Chem. Sol.* 60 (1999) 139-143.
- 21 - X.D. Li, D.W. Zhang, Z. Sun, Y.W. Chen, S.M. Huang, Metal-free indoline-dye-sensitized TiO_2 nanotube solar cells, *Microelectron. J.* 40 (2009) 108-114.
- 22 - V. Bem, M.C. Neves, M.R. Nunes, A.J. Silvestre, O.C. Monteiro; Influence of the sodium/proton replacement on the structural, morphological and photocatalytic properties of titanate nanotubes, *J. Photochem. Photobiol., A* 232 (2012) 50-56.
- 23 - D. Wu, Y. Chen, J. Liu, X. Zhao, A. Li, N. Ming, Co-doped titanate nanotubes, *Appl. Phys. Lett.* 87 (2005) 112501-112503.
- 24 - F. Dong, W. Zhao, Z. Wu, Characterization and photocatalytic activities of C, N and S co-doped TiO_2 with 1D nanostructure prepared by the nano-confinement effect, *Nanotechnology* 19 (2008) 365607-365617.

- 25 - E. Morgado Jr., M.A.S. Abreu, G.T. Moure, B.A. Marinkovic, P.M. Jardim, A.S. Araujo, Characterization of nanostructured titanates obtained by alkali treatment of TiO₂-anatases with distinct crystal sizes, *Chem. Mater.* 19 (2007) 665-676.
- 26 - T.M.F. Marques, O.P. Ferreira, J.A.P. Costa, K. Fujisawa, M. Terrones, B.C. Viana, Study of the growth of CeO₂ nanoparticles onto titanate nanotubes, *J. Phys. Chem. Solids* 87 (2015) 213-220.
- 27 - J. Kielland, Individual activity coefficients of ions in aqueous solutions, *J. Am. Chem. Soc.* 59 (1937) 1675-1678.
- 28 - N. Drăgan, M. Crișan, M. Răileanu, D. Crișan, A. Ianculescu, P. Oancea, S. Șomăcescu, L. Todan, N. Stănică, B. Vasile, The effect of Co dopant on TiO₂ structure of sol-gel nanopowders used as photocatalysts, *Ceram. Int.* 40 (2014) 12273-12284.
- 29 - R.D. Shannon, Revised effective ionic radii and systematic studies of interatomic distances in halides and chalcogenides, *Acta Crystallogr. A* 32 (1976) 751-767.
- 30 - E. Morgado, B. Marinkovic, P. Jardim, M. Abreu, F. Rizzo, Characterization and thermal stability of cobalt-modified 1-D nanostructured tri titanates, *J. Solid State Chem.* 182 (2009) 172-181.
- 31 - B.C. Viana, O.P. Ferreira, A.G.S. Filho, A.A. Hidalgo, J.M. Filho, O.L. Alves, Alkali metal intercalated titanate nanotubes: a vibrational spectroscopy study, *Vib. Spectrosc.* 55 (2011) 183-187.
- 32 - H. Liu, D. Yang, E.R. Waclawik, X. Ke, Z. Zheng, H. Zhu, R.L. Frost, A Raman spectroscopic study on the active site of sodium cations in the structure of Na₂Ti₃O₇ during the adsorption of Sr²⁺ and Ba²⁺ cations, *J. Raman Spectrosc.* 41 (2010) 1792-1796.
- 33 - X. Sun, Y. Li, Synthesis and characterization of ion-exchangeable titanate nanotubes, *Chem. Eur. J.* 9 (2003) 2229-2238.
- 34 - Z.Y. Wang, W.P. Mao, H.F. Chen, F.A. Zhang, X.P. Fan, G.D. Qian, Copper(II) phthalocyanine tetrasulfonate sensitized nanocrystalline titania photocatalyst: Synthesis in situ and photocatalysis under visible light, *Catal. Commun.* 7 (2006) 518-522.

- 35 - G. Kortuem, *Reflectance spectroscopy: Principles, methods and applications*. Springer-Verlag, New York 1969.
- 36 - P.A. Cox, *Transition metal oxides: An introduction to their electronic structure and properties*, Oxford University Press, New York, 2010.
- 37 - X.G. Xu, X. Ding, Q. Chen, L.-M. Peng, Electronic, optical, and magnetic properties of Fe-intercalated $\text{H}_2\text{Ti}_3\text{O}_7$ nanotubes: First-principles calculations and experiments, *Phys. Rev. B* 73 (2006) 165403(1)-165403(5).
- 38 - T. Entradas, J.F. Cabrita, S. Dalui, M.R. Nunes, O.C. Monteiro, A.J. Silvestre, Synthesis of sub-5 nm Co-doped SnO_2 nanoparticles and their structural, microstructural, optical and photocatalytic properties, *Mater. Chem. Phys.* 147 (2014) 563-571.
- 39 - T. Pham, B. Lee, Feasibility of silver doped TiO_2 /glass fiber photocatalyst under visible irradiation as an indoor air germicide, *Int. J. Environ. Res. Public Health* 11 (2014) 3271-3288.
- 40 - X. Chen, S.S. Mao, *Titanium dioxide nanomaterials: Synthesis, properties, modifications, and applications*, *Chem. Rev.* 107 (2007) 2891-2959.
- 41 - P. Finetti, F. Sedona, G.A. Rizzi, U. Mick, F. Sutara, M. Svec, V. Matolin, K. Schierbaum, G. Granozzi, Core and valence band photoemission spectroscopy of well-ordered ultrathin TiO_x films on Pt (111), *J. Phys. Chem. C* 111 (2007) 869-876.
- 42 - A.A. Rempel, E.A. Kozlova, T.I. Gorbunova, S.V. Cherepanova, E.Yu. Gerasimov, N.S. Kozhevnikova, A.A. Valeeva, E.Yu. Korovin, V.V. Kaichev, Yu.A. Shchipunov, Synthesis and solar light catalytic properties of titania–cadmium sulfide hybrid nanostructures, *Catal. Commun.* 68 (2015) 61-66.
- 43 - M.C. Biesinger, B.P. Payne, A.P. Grosvenor, Leo W.M. Lau, A.R. Gerson, R.C. Smart, Resolving surface chemical states in XPS analysis of first-row transition metals, oxides and hydroxides: Cr, Mn, Fe, Co and Ni, *Appl. Surf. Sci.* 257 (2011) 2717–2730.
- 44 - D. Wu, Y. Chen, J. Liu, X. Zhao, A. Li, N. Ming, Co-doped titanate nanotubes, *Appl. Phys. Lett.* 87 (2005) 112501-112503.

- 45 - D.V. Bavykin, V.N. Parmon, A.A. Lapkin, and F.C. Walsh, The effect of hydrothermal conditions on the mesoporous structure of TiO₂ nanotubes, *J. Mater. Chem.* 14 (2004) 3370-3377.
- 46 - B. Barrocas, T.J. Entradas, C.D. Nunes, O.C. Monteiro, Titanate nanofibers sensitized with ZnS and Ag₂S nanoparticles as novel photocatalysts for phenol removal, *Appl. Catal. B*, 218 (2017) 709-120.
- 47 - W. Choi, A. Termin, M.R. Hoffmann, The role of metal ion dopants in quantum-sized TiO₂: Correlation between photoreactivity and charge carrier recombination dynamics, *J. Phys. Chem.* 98 (1994) 13669-13679.
- 48 - Z.J. Zhang, C. Wang, R. Zakaria, J.Y. Ying, Role of particle size in nanocrystalline TiO₂-based photocatalysts, *Phys. Chem. B* 102 (1998) 10871-10878.
- 49 - J. Zhou, Y. Zhang, X.S. Zhao, A.K. Ray, Photodegradation of benzoic acid over metal-doped TiO₂, *Ind. Eng. Chem. Res.* 45 (2006) 3503-3511.
- 50 - M.G. Ha, E.D. Jeong, M.S. Won, H.G. Kim, H.K. Pak, J.H. Jung, B.H. Shon, S.W. Bae, J.S. Lee, Electronic band structure and photocatalytic activity of M-doped TiO₂ (M = Co and Fe), *J. Korean Phys. Soc.* 49 (2006) S675-S679.
- 51 - M.S. Park, S.K. Kwon, B.I. Min, Electronic structures of doped anatase TiO₂: Ti_{1-x}M_xO₂ (M = Co, Mn, Fe, Ni), *Phys. Rev. B* 65 (2002) 161201-161204.

Chapter 5

Ruthenium modified titanate nanowires for emergent pollutants photocatalytic degradation

This work was subject of the publication:

B.T. Barrocas, M. Conceição Oliveira, H.I.S. Nogueira, S. Fateixa, O.C. Monteiro, Ruthenium-modified titanate nanowires for the photocatalytic oxidative removal of organic pollutants from water, ACS Applied Nano Mat. 2 (2019) 1341-1349.

Chapter 5 – Ruthenium modified titanate nanowires for emergent pollutants photocatalytic degradation

5.1 - Introduction

The modification of the properties of elongated titanate nanoparticles can also occur by metal doping or/and ion-exchange modification. Improvements on the photocatalytic performance of titanate nanostructures were obtained previously, using Co modified titanate nanoparticles, with the dopant localized in two distinct positions: partial substitution of Ti^{4+} and replacement of Na^+ in the interlayers (Chapter 4) [1].

Ruthenium, a $4d$ transition metal, has been described as a dopant element that can significantly promote photogenerated electron-hole pairs separation and it can extend the material light absorption to the visible range, by inducing the creation of intermediate bands (IB) within the forbidden zone. This promotes a redshift in the absorption band edge, with the IB acting not only as intermediate energetic levels, during photo-activation but also as recombination center, extending the lifetime of the charge carriers [2,3]. For a Ru-doped TiO_2 material, with partial substitution of Ti with Ru, the probability of success for both excitation and recombination is conditioned by the bandgap energy and on the IB energetic position [3]. If a forbidden zone is split into 2 sub-gaps regions owing to an IB creation, it is desired that the lower gap will be the narrower one. With this, the probability for driving an electron from the valence band (VB) up to the IB would be higher than the possibility to have an electron, from the conduction band (CB), combining with a hole located at the same IB. Thus, the IB can behave as an efficient step to promote the relay of the electrons into the CB [3].

The Ru oxidation state is critical in the photocatalyst performance. For example, if Ti^{4+} is substituted by Ru^{3+} and/or Ru^{2+} , a new electron donor level is formed, whereas if Ti^{4+} is substituted by Ru^{4+} and/or Ru^{5+} species, an acceptor level in the bandgap is formed, to preserve the total charge balance. Either way, the charge transport, and transfer pathway will be altered. As an outcome, the substitution of Ti^{4+} in TiO_2 based systems by both Ru^{4+} and Ru^{3+} has been proposed [4].

Several methodologies have been described to produce Ru modified TiO_2 based materials, with some of them producing $\text{RuO}_2\text{-TiO}_2$, or TiO_2 combined with Ru metallic nanoparticles. Ru-doped TiO_2 nanofibers have been produced using electrospun Ru- TiO_2 /poly(vinyl acetate) fibers, [5] and monodispersed sea urchin-like Ru-doped *rutile* TiO_2 architectures have been successfully synthesized using an acid-hydrothermal method and low temperatures [2]. $\text{TiO}_2\text{-RuO}_2$ nanocomposites have been described as photoactive for acetone decomposition under

visible light. In this configuration, RuO₂ is essential for composite material bandgap energy decreases [6]. The synthesis of TiO₂ nanotubes combined with metallic Ru nanoparticles, *via* impregnation methods, has also been reported. These nanocomposite particles are catalytic for vinyl acetate and cyclohexene hydroformylation, [7] and they can also be used for the Fischer-Tropsch synthesis [8]. The absorption edge of nanocrystalline TiO₂ can be extended *via* Ru doping, through the formation of new energetic levels in the bandgap, [6] leading to modifications on the electron-hole recombination process. This can be further improved using iron (III) ions as electron acceptors [9].

This research work describes the incorporation of Ru in titanate nanowires (TNW) and the evaluation of their photocatalytic performance on pollutants removal. Due to its environmental impact and resistance to degradation, caffeine was chosen as a model emergent pollutant, for photodegradation under UV-vis and visible irradiation. Caffeine is the most used central nervous system stimulant and it is present, for example, in coffee, tea, soft drinks, chocolate, and pharmaceuticals.

5.2 – Synthesis

Titanate nanowires (TNW) were prepared as previously reported (Chapter 10 for experimental details) [10]. A similar procedure was followed to produce the Ru-containing precursor, by adding the required molar amount (1%, nominal molar amount) of ruthenium (RuCl₃) to the titanium trichloride solution [1]. The pristine and Ru-modified TNW particles were produced using a hydrothermal approach at 160°C for 24 hours [11].

5.3 – Structural, morphological and optical characterization

The prepared samples were analyzed by XRD and the obtained patterns can be visualized in Figure 5.1. The results, for TNW and RuTNW powders, agree with the presence of a crystalline titanate layered structure, type Na_{2-x}H_xTi₃O₇ (0 ≤ x ≤ 2) [12-14].

The XRD pattern of the RuTNW sample does not show any sign of undesirable crystalline phases, mainly those containing ruthenium. Therefore, the segregation of ruthenium, as ruthenium oxide or crystalline metallic (nano)particles, is unlikely during synthesis. Simultaneously, a slight shift to lower values is perceptible, in the 2θ = 10° peak, for the Ru containing a sample. As a result of the excellent ion-exchange ability of these layered materials, the Na⁺ ions, which are localized in the TiO₆ interlayers, are able to be exchanged by H⁺ or other cationic entities, for instance, ionic Ru [15,16]. Therefore, this shift, observed in the

RuTNW sample, suggests that some Ru^{n+} was incorporated during synthesis, between the TiO_6 layers.

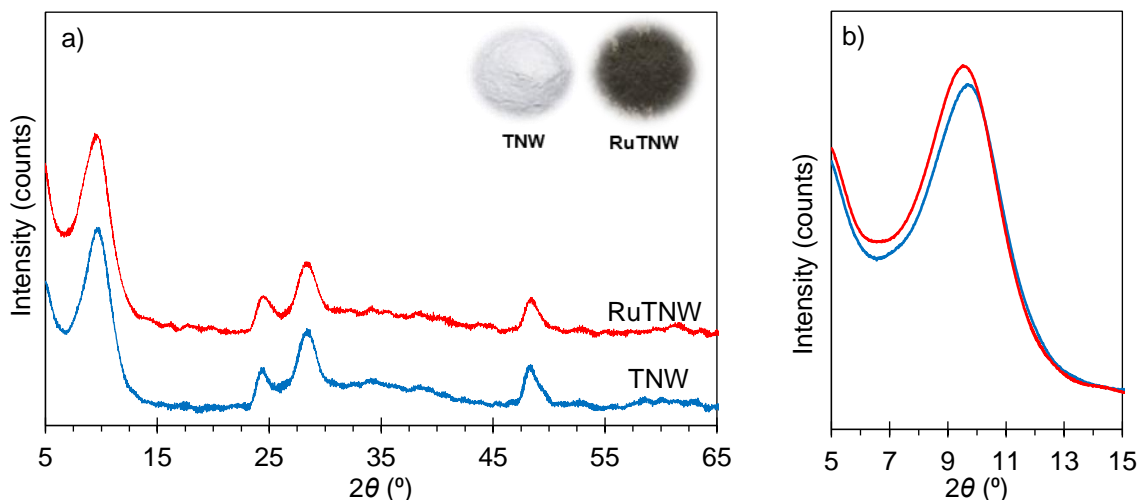


Figure 5.1 – (a) XRD patterns of the TNW and RuTNW prepared samples; (b) detail of the XRD patterns.

Since the effective ionic radius of Ru^{4+} is slightly bigger (76.0 pm) than one of the Ti^{4+} (74.5 pm), the replacement of Ti^{4+} by Ru^{4+} is also likely [2]. Conversely, the Ti^{4+} replacement, by Ru^{3+} ions, is not expected, since its ionic radius is 82.0 pm. Nevertheless, if this specie is present in the crystalline structure, it should be located in interstitial sites [2,17,18].

The Scherrer equation was used to access the crystallite size and, with it, the assessment of the influence of the Ru incorporation on the crystalline structure was possible. The values obtained for RuTNW and TNW crystallites were 24.9 Å and 26.8 Å respectively. This indicates a slight decrease (6.9%) of the crystallite size, due to Ru incorporation.

To study the morphology of the samples, transmission electron microscopy (TEM) was used, and no modifications on the particles' morphology were observed after Ru incorporation.

Figure 5.2 shows a TEM image of the RuTNW sample. The samples are homogeneous and are constituted by very thin and elongated nanowires. No signals of other types of particles were observed. The diameter size of the particles was assessed by direct image measurements and values of 6.5 ± 2.5 nm and 7.3 ± 3.1 nm were obtained for TNW and RuTNW samples, respectively. For the RuTNW sample, the Ru presence was not able to be confirmed by energy-dispersive X-ray spectroscopy (EDS), due to equipment limitations. However, the confirmation was possible by X-ray photoelectron spectroscopy (XPS), as discussed later on. The amount of ruthenium incorporated was measured by micro X-ray fluorescence (μXRF), and a $\text{Ru/Ti} = 3.4\%$ was obtained.

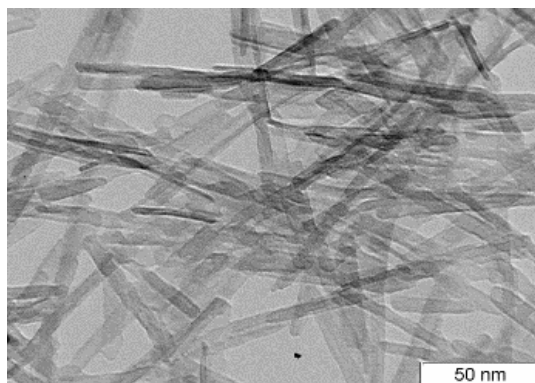


Figure 5.2 - TEM image of the RuTNW sample.

To determine the active surface area, the samples were submitted to N_2 adsorption/desorption at -196°C , using the B.E.T. method. TNW presents a surface area of $238.10\text{ m}^2\text{g}^{-1}$, and a slight decrease (2.5%) to $232.20\text{ m}^2\text{g}^{-1}$ was observed for the RuTNW sample.

The structural characterization of the samples was further investigated by Raman spectroscopy. The Raman spectra of TNW and RuTNW powders (Figure 5.3) are in good agreement with previous works on $\text{Na}_2\text{Ti}_3\text{O}_7$ materials [1,19-21]. The bands at 160 and 196 cm^{-1} are assigned to Na–O–Ti lattice modes. The Ti–O–Ti stretching modes in edge-shared TiO_6 are attributed to the bands at 280, 455 and 676 cm^{-1} . The band at 709 cm^{-1} can be assigned to either Ti–OH or Ti–O–Ti stretching vibrations [28]. The band at *ca.* 915 cm^{-1} is ascribed to the stretching vibration of non-shared Ti–O bonds in distorted TiO_6 units [19,21].

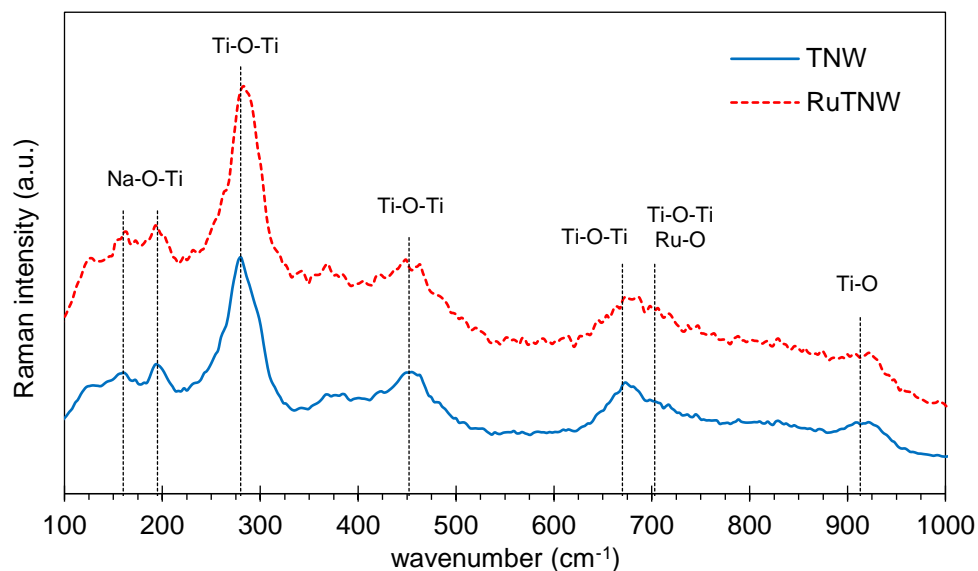


Figure 5.3 - Raman spectra of the TNW and RuTNW samples.

Considering that the Ru–O bond, in monocristalline RuO_2 , has three Raman active modes: E_g , A_{1g} , and B_{2g} at 523, 640, and 708 cm^{-1} respectively, [22,23] the band intensity increase

visualized at 709 cm^{-1} can be due to the Ru existence (B_{2g} mode of Ru-O bond). This attribution agrees with other works, reporting that the wavenumber position and the intensity of the highest frequency mode are both influenced either by the level of doping or the ionic position within the titanate nanostructure [1,14,19].

Raman spectra of both samples are identical; despite this, there is a slight shift in the bands assigned to the Ti-O-Ti stretches. These bands shift from 280 and 676 cm^{-1} to 285 and 678 cm^{-1} for TNW and RuTNW, respectively. This suggests that some $\text{Ru}^{4+}/\text{Ru}^{3+}$ substitution may have occurred, not only in the crystalline structure, replacing the Ti^{4+} and/or in interstitial positions, but also between the TiO_6 layers, replacing the Na^+ , as XRD results suggest.

To better support, this hypothesis, a new sample, labeled TNW/Ru, was prepared by ion-exchange. In this case, only the substitution of Na^+ in the interlayers is possible, with no Ti^{4+} replacement being allowed. The Raman spectrum of this TNW/Ru sample is shown in Figure 5.4. For comparative purposes, the Raman spectrum of the TNW sample used to prepare TNW/Ru is also presented.

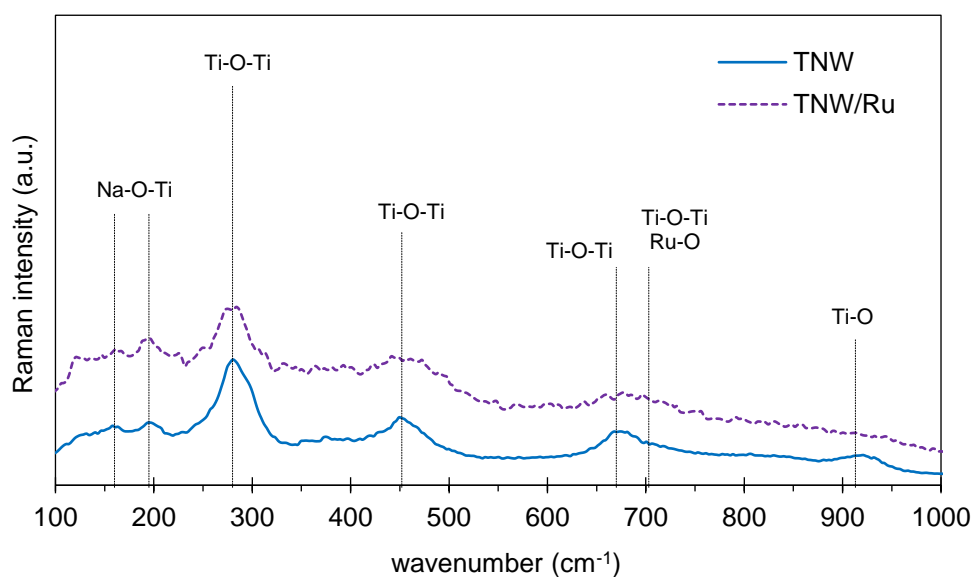


Figure 5.4 - Raman spectra of the TNW and TNW/Ru samples.

The Raman spectrum of the TNW/Ru sample shows broader bands and slight differences in the relative intensities when compared with that of TNW. This is more evident for the Ti-O-Ti stretching bands, at 450 and 712 cm^{-1} . The same effect is visible when the spectra of the RuTNW and TNW samples are compared. These results agree with the hypothesis that, for the RuTNW sample, there might be a $\text{Ru}^{4+}-\text{Ti}^{4+}$ replacement, together with the Na^+ interlayer substitution.

The electronic structure, of the TNW and RuTNW samples, was also analyzed by XPS, and the survey spectra of both samples are very similar. Figure 5.5(a) shows the survey spectra of the RuTNW, where the Na 1s, Ti 2p, and O 1s photoelectron peaks, characteristic of the titanate elongated powders, are visible [1,12] and also the Ru 3d and Ru 3p peaks, confirming the presence of ruthenium in the RuTNW sample.

The high-resolution spectra of Ti 2p, O 1s, and Ru 3p regions for TNW and RuTNW are presented in Figure 5.5(b-d). Typical Ti 2p_{3/2} and Ti 2p_{1/2} binding energies, corresponding to octahedral coordinated Ti⁴⁺ state, were obtained for both samples. The existence of Ti⁴⁺ in both samples was confirmed by the doublet splitting energies of the Ti 2p peaks (5.8 eV) that is typical of the Ti⁴⁺ existence; [17,24-27].

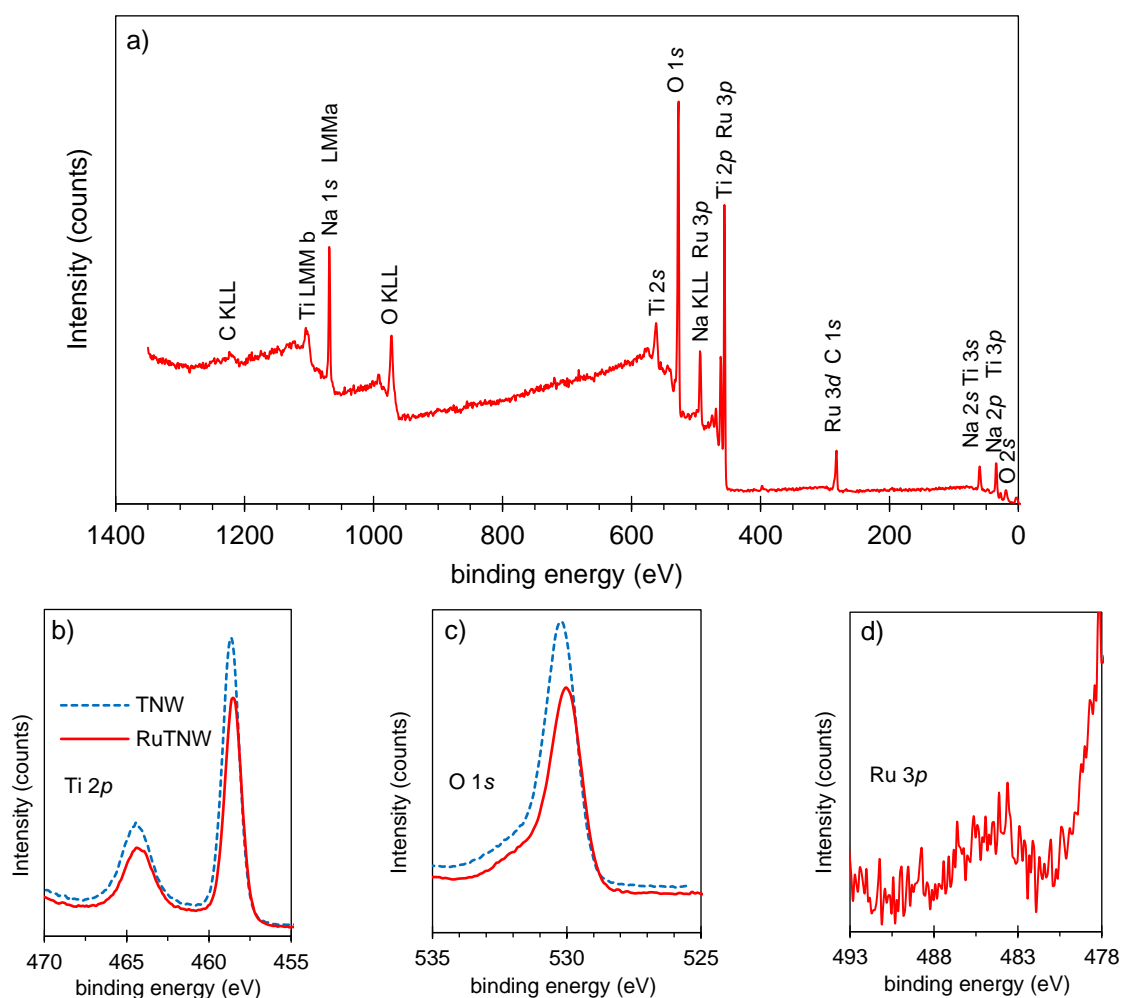


Figure 5.5 – (a) XPS survey spectra of the RuTNW sample and high-resolution spectra of the (b) Ti 2p, (c) O 1s and (d) Ru 3p regions of the TNW and RuTNW samples.

For RuTNW, a shift for lower values, on the Ti 2p_{3/2} and Ti 2p_{1/2} binding energies, was observed, being in accordance with a more negative charge density for the atoms of titanium

and with a non-stoichiometric titanium – oxygen bonding [2]. This agrees with the Ru^{4+} incorporation into the TiO_6 crystalline lattice [2]. In the O 1s core spectrum, the peak at *ca.* 530 eV, (Figure 5.5(c)) is attributed, with some small contribution of the Na Auger peak (Na KLL), to the lattice oxygen [12]. No changes in this peak were observed due to Ru incorporation.

The identification and quantification of ruthenium in the RuTNW sample was not possible using the characteristic Ru $3d_{5/2}$ and $3d_{3/2}$ peaks (at 280-281 eV and 284-286 eV, respectively) due to the partial overlap with the C 1s peak (at \sim 286 eV). The Ru $3p_{1/2}$ (484 eV) was used as an alternative [28], to confirm the metal existence in the RuTNW powder (Figure 5.5(d)). No evidence of Ru-Ru bonding existence (peak at 280 eV) was observed.

Diffuse reflectance spectroscopy (DRS) was used to determine the optical absorption profile of the prepared samples (Figure 5.6).

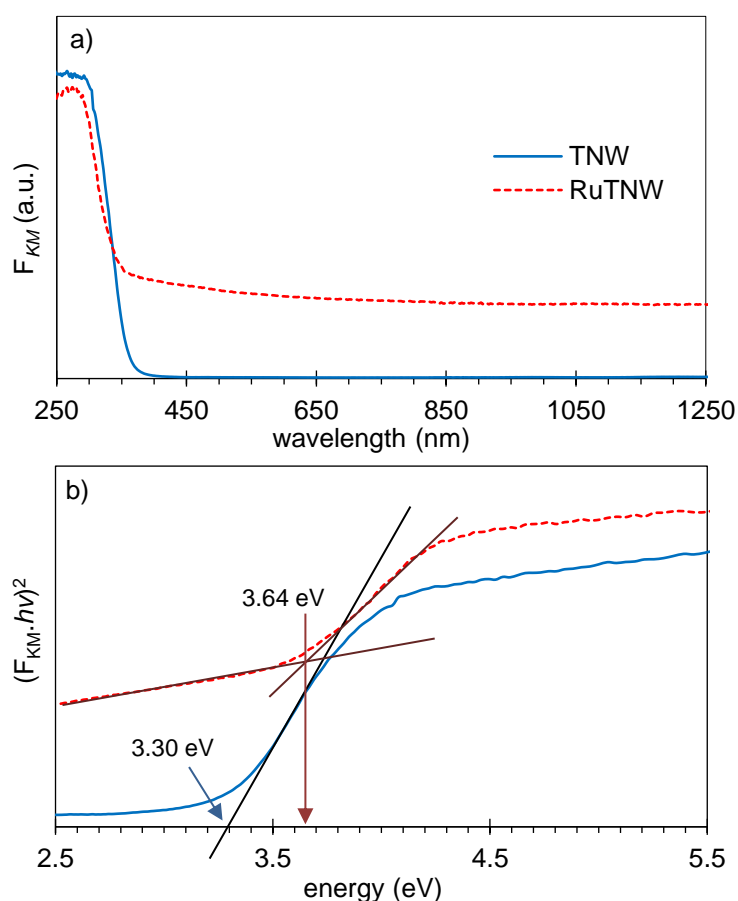


Figure 5.6 – (a) Absorption spectra and (b) representation of the function $(F_{KM} \cdot hv)^2$ versus hv , for the bandgap energy determination of the TNW and RuTNW prepared samples.

The optical spectrum of pristine TNW powder presents an absorption band edge near 400 nm, which is characteristic of titanate elongated nanoparticles (Figure 5.6(a)).

For the Ru-modified sample, a blueshift on this absorption band was observed. The existence of this effect, in semiconductor nanoparticles, is usually attributed to the existence of quantum

size effects. The crystallite size, calculated for the samples, shows a reduction for the Ru-modified sample, as described above.

The existence of internal $d-d$ transitions on the Ru^{4+} ions in the visible range (410 to 620 nm) has been ruled out in this type of materials. Instead, in these cases, the absorption beyond 400 nm, up to the visible and near infrared range, has been ascribed to low-energetic photons and/or thermal excitations of trapped electrons, due to oxygen vacancies [1,2].

The bandgap energy (E_g) of TNW and RuTNW was calculated from their diffuse reflectance spectra [12], as shown in Figure 5.6(b). The obtained values were 3.30 and 3.64 eV for TNW and RuTNW samples respectively.

For elongated titanate materials, the bandgap energy corresponds to the $\text{O } 2p \rightarrow \text{Ti } 3d$ transition. To allow the energetic quantification of this transition, the valence band spectrum (VB-XPS) of each sample was recorded (Figure 5.7(a)). A linear method (extrapolation of the leading edge to the extended baseline of the VB spectra) was used to calculate the position of the valence band [2], as shown in Figure 5.7(a). The corresponding conduction band (CB) energy was calculated using the expression: $E_g = \text{VB} - \text{CB}$.

Figure 5.7(b) shows the scheme of the VB and CB energies for TNW and RuTNW. The energy of VB and CB are distinct for both samples, with RuTNW requiring less energy for photo-activation.

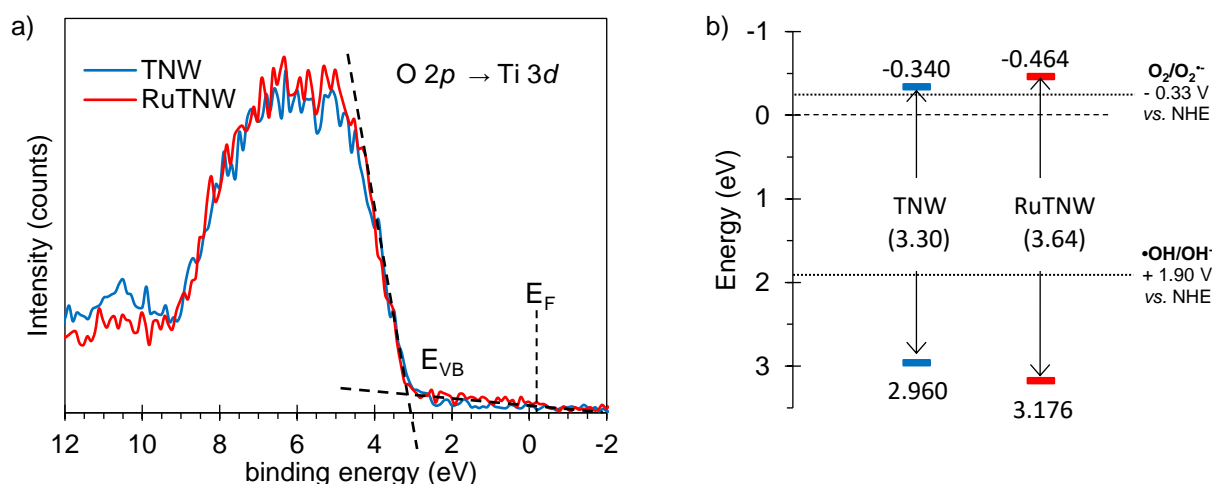


Figure 5.7 - (a) XPS high-resolution spectra of the O $2p$ to Ti $3d$ transition, used for valence band determination; (b) Energy-level diagram with E_g , VB and CB positions, for the prepared samples.

5.4 - Photocatalytic performance

5.4.1 - Photo-induced hydroxyl radical production

To estimate the oxidation capability of the TNW and RuTNW samples, the photo-assisted production of the hydroxyl radical was examined. The $\cdot\text{OH}$ radical production was attained

through the quantification of the 2-hydroxyterephthalic acid (HTA) obtained from the terephthalic acid (TA) photocatalytic degradation [29]. The analysis of the amount of fluorescent HTA obtained after 30 min of light irradiation, shows that both samples are catalytic for this reaction (Figure 5.8), being RuTNW the best photocatalyst.

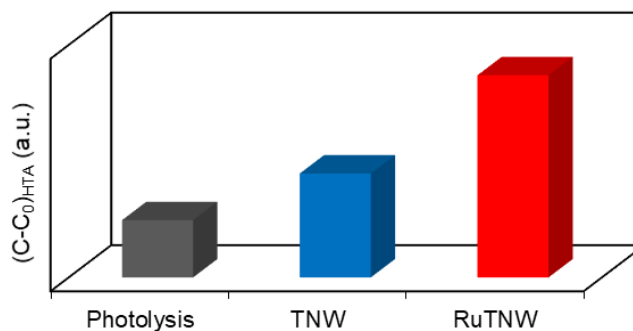


Figure 5.8 - HTA concentration after 30 min of irradiation of a TA solution (3 mM, 150 mL) using 10 mg of each photocatalyst.

Fixing the TA photolysis as a reference, an 18% increase on this radical production was observed, when the pristine TNW sample was used as a catalyst. This result contrasts with an increase of 55% obtained when using the RuTNW sample. These results demonstrate that Ru incorporation leads to an improvement of these materials photocatalytic performance for hydroxyl radical production. This result also agrees with previous reports describing metal doping/incorporation as modification methodologies that conduct enhancement on the materials photocatalytic performances [17,29-31].

5.4.2 - Caffeine photocatalytic degradation

In this work, the catalytic efficiency of the samples in the degradation of caffeine, under UV-vis and visible light was studied. Since in a photocatalytic process, the adsorption characteristics of the pollutant/catalyst system are expected to be important due to photo-oxidation reactions usually occur at the catalyst surface, the ability of the samples to adsorb caffeine was investigated during 60 min, under darkness conditions (Figure 5.9). Adsorption phenomena, and consequent interaction between catalyst surface and pollutant, are usually very relevant in photocatalytic heterogeneous processes and should be carefully evaluated [15,32,33].

Since photocatalysis occurs on the surface of nanoparticles, the performance of the catalyst is highly influenced by the solution pH, as mentioned in Chapter 2. Therefore, the determination of the point of zero charge (p.z.c.) is important to predict the surface charge of nanoparticles. The p.z.c. of the TNW based samples is expected to be about 3.4, a value that has been reported for similar titanate elongated materials [15,16] and the caffeine has a $pK_a = 0.6$. The pH of the

caffeine solution used was measured and a value of 5 was obtained; therefore, no interactions between the catalyst surface and the caffeine molecule were expected. This was experimentally confirmed since no significant caffeine was adsorbed in the RuTNW and TNW surfaces.

Figure 5.9 shows the concentration decrease profile of the 20 ppm caffeine solution, over an irradiation period of 120 min, in the presence of the prepared samples as catalysts. This demonstrates that both powders are catalytic for this degradation process.

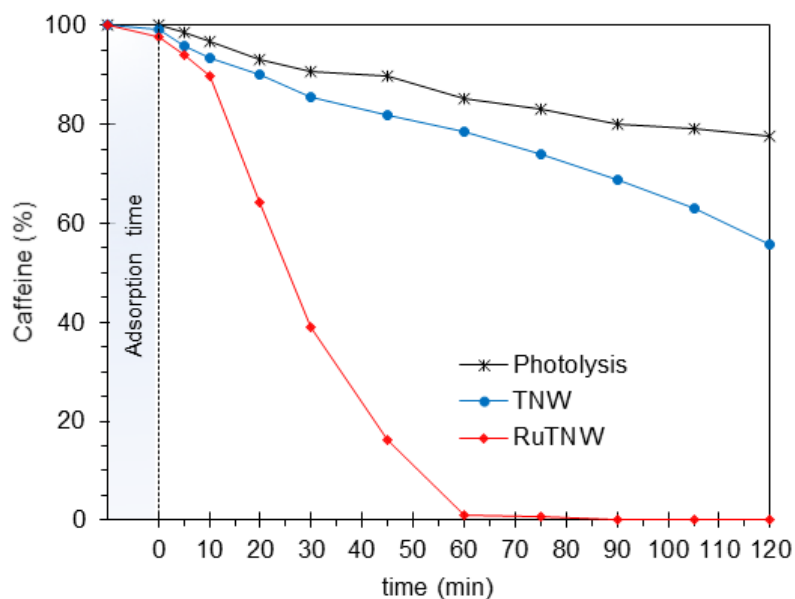
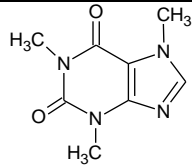
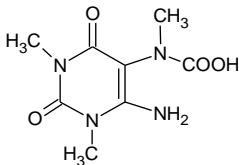
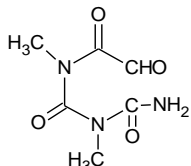
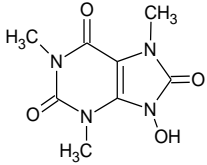
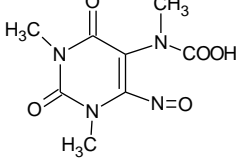
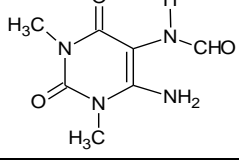


Figure 5.9 - Profiles of the photocatalytic degradation of a 20 ppm caffeine aqueous solution during 120 min of irradiation, with the TNW and RuTNW samples acting as catalysts (0.13 g L^{-1}).

After 60 min of irradiation, the best photocatalyst for this reaction was RuTNW, with the degradation of all the caffeine present in solution. For the same period, only 21.4% of the caffeine was degraded using the pristine nanowires as a catalyst, and 14.7% of the caffeine was degraded using photolysis conditions. Even considering that a RuTNW assisted process removes all caffeine in solution after 60 min, it does not mean that all produced by-products are fully degraded into CO_2 and H_2O .

To further investigate this issue, the identification and quantification of the intermediate products formed during 120 min of caffeine photocatalytic degradation (label as **CAF-1** to **CAF-5**) were performed by LC-HR-ESI/MS. The obtained results (Table 5.1) are in accordance with a mechanism reported in literature (Annex B – Figure B.2) for this pollutant degradation process [34,35].

Table 5.1 - Main fragments and correspondent by-products identified by LC-HR-ESI/MS during the caffeine photodegradation using RuTNW as a catalyst

Compound	Formula	Experimental mass (m/z)	Mol.wt.	Structure
Caffeine	C ₈ H ₁₁ N ₄ O ₂	195.0876	194	
CAF-1	C ₈ H ₁₂ N ₄ O ₄ Na	251.0751	228	
	C ₇ H ₁₀ N ₃ O ₃	184.0713		
	C ₅ H ₇ N ₂ O ₂	127.0499		
CAF-2	C ₆ H ₉ N ₃ O ₄ Na	210.0485	187	
	C ₆ H ₈ N ₃ O ₃	170.0560		
CAF-3	C ₈ H ₁₁ N ₄ O ₄	227.0774	226	
CAF-4	C ₈ H ₁₀ N ₄ O ₅ Na	265.0547	242	
CAF-5	C ₇ H ₁₁ N ₄ O ₃	199.0824	198	
	C ₅ H ₈ N ₃ O ₂	142.0609		

To further analyze this process, the time profile of the by-products was monitored during degradation. Figure 5.10 shows the amount (%) of each intermediate in solution over the irradiation time.

In the first minutes, after starting the irradiation, high amounts of products **CAF-1** (63.8%) and **CAF-2** (36.2%), were detected. The simultaneous high production of **CAF-1** and **CAF-2** intermediates is justified since they are originated from distinct caffeine degradation pathways [35]. When irradiation time increases, the relative concentration of product **CAF-1** also increases, however, the **CAF-2** gradually decreases. After 60–75 min no caffeine was detected, and the relative composition of the solution was drastically altered, *e.g.*, it is notorious a high

decrease of the compound **CAF-1** amount. After 120 min of irradiation, four compounds (**CAF-1** to **CAF-4**) remain in solution, implying that more time is necessary to attain the total degradation of these intermediates.

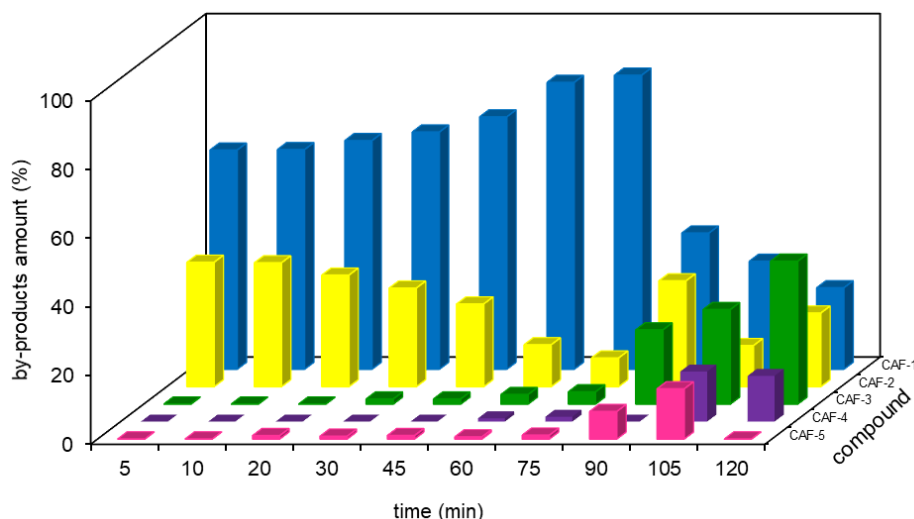


Figure 5.10 – Variation of the intermediate products identified during 120 min of caffeine photodegradation, using RuTNW as a catalyst.

5.5 – Photoactivation mechanism study

Considering that the best photocatalytic results were obtained using the Ru-containing sample. Two distinct experiments were performed to infer if such behavior can be attributed to enhancement on the visible radiation absorption or/and to an electron-hole recombination decrease.

First, the caffeine degradation was performed under visible radiation (Figure 5.11), and afterward, to evaluate the possibility of a charge carrier recombination rate reduction, photoluminescence spectra (PL) of the samples were recorded (Figure 5.12).

As expected, the photodegradation performance of the catalysts under visible radiation was inferior to the one obtained using UV-vis irradiation (Figure 5.11). Under these conditions and after 60 min irradiation, very slight differences were observed for this pollutant degradation, for photolysis and TNW photo-assisted experiments. This indicates that TNW is not catalytic under visible radiation. On the other hand, under visible irradiation, a significant enhancement of the RuTNW catalytic performance was observed, indicating that this material is activated by this type of radiation. These data are in agreement with other reports attesting that Ru doping improves photocatalytic activity under visible light irradiation, with the dopant either reducing the energy gap and/or inducing the creation of an effective intermediate levels within the

forbidden zone. This will promote visible irradiation absorption to support the photo-generated charge carriers' generation [3].

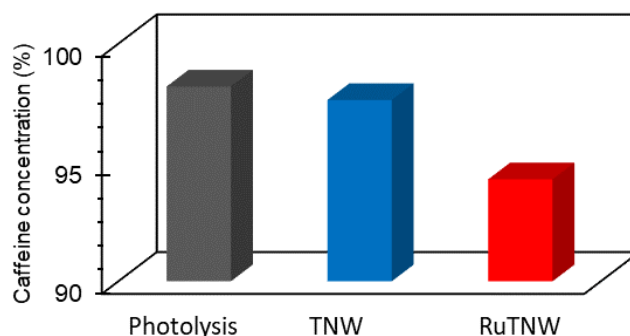


Figure 5.11 - Caffeine concentration, after 60 min of visible light irradiation, using the prepared samples as photocatalysts.

The PL spectra of the TNW and RuTNW samples in Figure 5.12 shows a peak centered at 420 nm, attributed to the bandgap transition (band-to-band transition) [36]. A reduction in this peak intensity, for the RuTNW powder, when compared to TNW response, was observed and suggests a higher and more effective electron-hole separation. This agrees with the possibility of Ru acting as electron trapping.

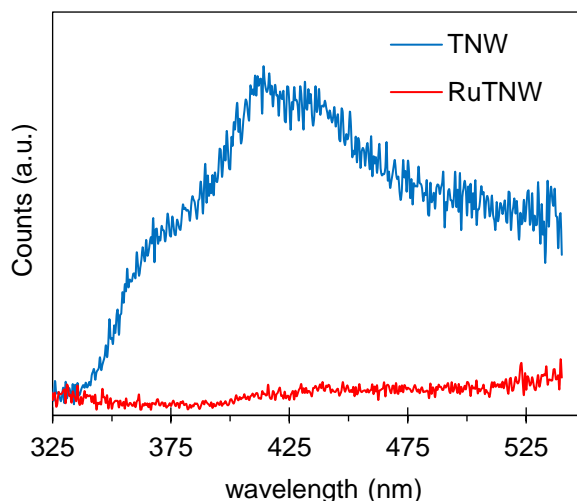


Figure 5.12 - Photoluminescence spectra of the TNW and RuTNW samples.

Supported on the above results and literature [2,4,37,38], a mechanism for the light-activated charge-transfer process in the Ru-modified titanate nanowires sample is proposed in Figure 5.13.

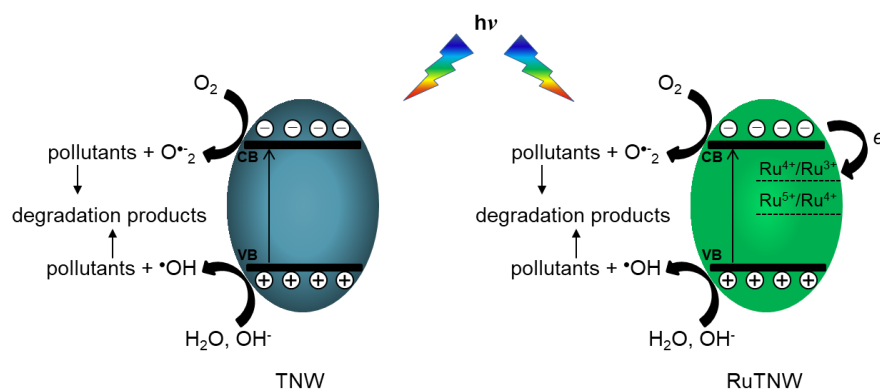


Figure 5.13 - Charge-transfer mechanism proposal for TNW and RuTNW particles, under irradiation.

In TNW, the valence band (VB) is derived from O $2p$ levels and the conduction band (CB) from the Ti $3d$ levels [12]. When an aqueous TNW suspension is submitted to irradiation possessing higher energy than its bandgap energy, electrons (e^-) and holes (h^+) are formed in the CB and VB respectively. These photogenerated electrons could easily be transferred to adsorbed oxygen and, through its reduction, the production of $O_2^{\cdot-}$ can happen. These species can be active in photocatalytic redox processes, while the photogenerated holes will react with adsorbed H_2O or OH^- to produce $\cdot OH$ radicals. Due to the simultaneous action of all the oxidant species present in the system, including h^+ , pollutant degradation is possible. For the Ru-modified titanate nanowires and considering the above results and the redox potential of Ru^{4+}/Ru^{3+} (+ 0.77 V vs. NHE) and Ru^{5+}/Ru^{4+} (+ 1.22 V vs. NHE) [38], the existence of mid-band levels in the forbidden zone, closer to CB, is expected for the RuTNW sample. This will open the possibility of charge transitions of donor type:



or acceptor type:



being the Ru^{4+} to Ru^{3+} acceptor mechanism more likely [38]. The main consequence of the reduction in the recombination rate will be the photocatalytic performance improvement of the Ru-modified materials.

5.6 - Conclusions

In this work, crystalline titanate nanowires modified with Ru (RuTNW) were for the first time prepared by hydrothermal treatment of an amorphous Ru-containing precursor. The amount of incorporated ruthenium (Ru/Ti) was quantified, and a value of 3.4% was obtained.

Characterization results support the conclusion that in the RuTNW sample, Ru^{n+} is in the crystalline structure replacing Ti^{4+} , localized in interstitial sites, and in the interlayers replacing Na^+ . The photocatalytic activity of the obtained powders was tested for the hydroxyl radical production, and RuTNW has presented the best performance. For caffeine degradation, an identical conclusion was possible, when considering the RuTNW photocatalytic performance, under UV–vis and visible irradiation. This photocatalytic behavior was mainly linked with a recombination rate reduction of the photogenerated electron–hole pairs. Considering all the results, a mechanism for the charge-transfer processes on the photoactivated Ru-modified sample was proposed, based on the creation of mid-band levels in the forbidden zone.

5.7 - References

- 1 - B. Barrocas, A.J. Silvestre, A.G. Rolo, O.C. Monteiro, The effect of ionic Co presence on the structural, optical and photocatalytic properties of modified cobalt–titanate nanotubes, *Phys. Chem. Chem. Phys.* 16 (2016) 18081-18093.
- 2 - T.-D. Nguyen-Phan, S. Luo, D. Vovchok, J. Llorca, S. Sallis, S. Kattel, W. Xu, L.F.J. Piper, D.E. Polyansky, S.D. Senanayake, D.J. Stacchiola, J.A. Rodriguez, Three-dimensional ruthenium-doped TiO_2 sea urchins for enhanced visible-light-responsive H_2 production, *Phys. Chem. Chem. Phys.* 18 (2016) 15972-15979.
- 3 - K. Song, X. Han, G. Shao, Electronic properties of rutile TiO_2 doped with 4d transition metals: first-principles study, *J. Alloys Compd.* 551 (2013) 118-124.
- 4 - P. Triggs, Electronic and structural properties of single crystals in the system $\text{TiO}_2\text{-RuO}_2$, *Helv. Phys. Acta* (58) 1985 657-714.
- 5 - D.Y Lee, N.-I. Cho, Y.-J. Oh, J.-Y., Park, Synthesis and characterization of ruthenium doped TiO_2 nanofibers, *J. Sens. Sci. Technol.* 20 (2011) 82-89.
- 6 - V. Houšková, V. Štengl, S. Bakardjieva, N. Murafa, V. Tyrpekl, Efficient gas phase photodecomposition of acetone by Ru-doped titania, *Appl. Catal., B* 89 (2009) 613-619.
- 7 - H. Chuai, X. Liu, Y. Chen, B. Zhu, S. Zhang, W. Huang, Hydroformylation of vinyl acetate and cyclohexene over TiO_2 nanotube supported Rh and Ru nanoparticle catalysts, *RSC Adv* 8 (2018) 12053-12059.

- 8 - X. Yang, W. Wang, L. Wu, X. Li, T. Wang, S. Liao, Effect of confinement of TiO₂ nanotubes over the Ru nanoparticles on Fischer-Tropsch synthesis, *Appl. Catal., A* 526 (2016) 45-52.
- 9 - T. Ohno, F. Tanigawa, K. Fujihara, S. Izumi, M. Matsumura, Photocatalytic oxidation of water by visible light using ruthenium-doped titanium dioxide powder, *J. Photochem. Photobiol. A* 127 (1999) 107-110.
- 10 - M.R. Nunes, O.C. Monteiro, A.L. Castro, D.A. Vasconcelos, A.J. Silvestre, A new chemical route to synthesise TM-doped (TM = Co, Fe) TiO₂ nanoparticles, *Eur. J. Inorg. Chem.* 2008 (2008) 961-965.
- 11 - E.K. Ylhäinen, M.R. Nunes, A.J. Silvestre, O.C. Monteiro, Synthesis of titanate nanostructures using amorphous precursor material and their adsorption/photocatalytic properties, *J. Mater. Sci.* 47 (2012) 4305-4312.
- 12 - D.V. Bavykin, F.C. Walsh, Synthesis, properties and applications, *RSC Nanoscience & Nanotechnology Series*, Cambridge, UK, RSC Publishing, 2010.
- 13 - B. Barrocas, M.C. Neves, M. Conceição Oliveira, O.C. Monteiro, Enhanced photocatalytic degradation of psychoactive substances using amine modified elongated titanate nanostructures, *Environ. Science: Nano* 5 (2018) 350-361.
- 14 - H. Liu, D. Yang, E.R. Waclawik, X. Ke, Z. Zheng, H. Zhu, R.L. Frost, A Raman spectroscopic study on the active site of sodium cations in the structure of Na₂Ti₃O₇ during the adsorption of Sr²⁺ and Ba²⁺ cations, *J. Raman Spectrosc.* 41 (2010) 1792-1796.
- 15 - V.C. Ferreira, O.C. Monteiro, New hybrid titanate elongated nanostructures through organic dye molecules sensitization, *J. Nanopart. Res.* 15 (2013) 1923-1938.
- 16 - V. Bem, M.C. Neves, M.R. Nunes, A.J. Silvestre, O.C. Monteiro, Influence of the sodium/proton replacement on the structural, morphological and photocatalytic properties of titanate nanotubes, *J. Photochem. Photobiol. A* 232 (2012) 50-56.
- 17 - T.M.F. Marques, O.P. Ferreira, J.A.P. Costa, K. Fujisawa, M. Terrones, B.C. Viana, Study of the growth of CeO₂ nanoparticles onto titanate nanotubes, *J. Phys. Chem. Solids* 87 (2015) 213-220.

- 18 - R.D. Shannon, Revised effective ionic radii and systematic studies of interatomic distances in halides and chalcogenides, *Acta Cryst. A* 32 (1976) 751-767.
- 19 - F.L.R. Silva, A.A.A. Filho, M.B. Silva, K. Balzuweit, J.L. Bantignies, E.W.S. Caetano, R.L. Moreira, V.N. Freire, A. Righi, Polarized Raman, FTIR, and DFT study of Na₂Ti₃O₇ microcrystals, *J. Raman Spectrosc.* 49 (2018) 538-548.
- 20 - K.R. Zhu, Y. Yuan, M.S. Zhang, J.M. Hong, Y. Deng, Z. Yin, Structural transformation from NaHTi₃O₇ nanotube to Na₂Ti₆O₁₃ nanorod, *Solid State Commun.* 144 (2007) 450-453.
- 21 - B.C. Viana, O.P. Ferreira, A.G.S. Filho, A.A. Hidalgo, J.M. Filho, O.L. Alves, Alkali metal intercalated titanate nanotubes: A vibrational spectroscopy study, *Vib. Spectrosc.* 55 (2011) 183-187.
- 22 - L.M.M. Tejada, A. Muñoz, M.A. Centeno, J.A. Odriozola, *In-situ* Raman spectroscopy study of Ru/TiO₂ catalyst in the selective methanation of CO, *J. Raman Spectrosc.* 47 (2016) 189-197.
- 23 - R.S. Chen, C.C. Chen, Y.S. Huang, C.T. Chia, H.P. Chen, D.S. Tsai, K.K. Tiong, A comparative study of microstructure of RuO₂ nanorods via Raman scattering and field emission scanning electron microscopy, *Solid State Commun.* 131 (2004) 349-353.
- 24 - T. Pham, B. Lee, Feasibility of silver doped TiO₂/glass fiber photocatalyst under visible irradiation as an indoor air germicide, *Int. J. Environ. Res. Public Health* 11 (2014) 3271-3288.
- 25 - X. Chen, S.S. Mao, Titanium dioxide nanomaterials: synthesis, properties, modifications, and applications, *Chem. Ver.* 107 (2007) 2891-2959.
- 26 - P. Finetti, F. Sedona, G.A. Rizzi, U. Mick, F. Sutara, M. Svec, V. Matolin, K. Schierbaum, G. Granozzi, Core and valence band photoemission spectroscopy of well-ordered ultrathin TiO_x films on Pt(111), *J. Phys. Chem. C* 111 (2007) 869-876.
- 27 - A.A. Rempel, E.A. Kozlova, T.I. Gorbunova, S.V. Cherepanova, E.Yu. Gerasimov, N.S. Kozhevnikova, A.A. Valeeva, E.Yu. Korovin, V.V. Kaichev, Yu.A. Shchipunov, Synthesis and solar light catalytic properties of titania–cadmium sulfide hybrid nanostructures, *Catal. Commun.* 68 (2015) 61-66.

- 28 - D.J. Morgan, Resolving ruthenium: XPS studies of common ruthenium materials, *Surf. Interface Anal.* 47 (2015) 1072-1079.
- 29 - B. Barrocas, T.J. Entradas, C.D. Nunes, O.C. Monteiro, Titanate nanofibers sensitized with ZnS and Ag₂S nanoparticles as novel photocatalysts for phenol removal, *Appl. Catal., B* 218 (2017) 709-120.
- 30 - Z.J. Zhang, C. Wang, R. Zakaria, J.Y. Ying, Role of particle size in nanocrystalline TiO₂-based photocatalysts, *J. Phys. Chem. B* 102 (1998) 10871-10878.
- 31 - J. Zhou, Y. Zhang, X.S. Zhao, A.K. Ray, Photodegradation of benzoic acid over metal-doped TiO₂, *Ind. Eng. Chem. Res.* 45 (2006) 3503-3511.
- 32 - E. Horváth, I. Szilágyi, L. Forró, A. Magrez, Probing titanate nanowire surface acidity through methylene blue adsorption in colloidal suspension and on thin films, *J. Colloid Interface Sci.* 416 (2014) 190-197.
- 33 - S. Muráth, S. Sáringer, Z. Somosi, I. Szilágyi, Effect of ionic compounds of different valences on the stability of titanium oxide colloids, *Colloids Interfaces* 2 (2018) 32-50.
- 34 - R. Rosal, A. Rodríguez, J.A. Perdígón-Melón, A. Petre, E. García-Calvo, M.J. Gómez, A. Agüera, A.R. Fernández-Alba, Degradation of caffeine and identification of the transformation products generated by ozonation, *Chemosphere* 74 (2009) 825-831.
- 35 - F. Qi, W. Chu, B. Xu, Catalytic degradation of caffeine in aqueous solutions by cobalt-MCM 41 activation of peroxydisulfate, *Appl. Catal. B* 134-135 (2013) 324-332.
- 36 - N. Pugazhenthiran, S. Murugesan, S. Anandan, High surface area Ag-TiO₂ nanotubes for solar/visible-light photocatalytic degradation of ceftiofur sodium, *J. Hazard. Mater.* 263 (2013) 541-549.
- 37 - T.M. Inerbaev, J.D. Hoefelmeyer, D.S. Kilin, Photoinduced charge transfer from titania to surface doping site, *J. Phys. Chem. C* 117 (2013) 9673-9692.
- 38 - I. Povar, O. Spinu, Ruthenium redox equilibria, *J. Electrochem. Sci. Eng.* 6 (2016) 145-153.

Chapter 6

Photocatalytic performance of ruthenium modified titanate nanotubes and nanowires: a comparative study

The work presented was subject of the publication:

B. Barrocas, M. Conceição Oliveira, H.I.S. Nogueira, S. Fateixa, O.C. Monteiro, A comparative study on emergent pollutants photo-assisted degradation using ruthenium modified titanate nanotubes and nanowires as catalysts, *Journal of Environmental Sciences* 92 (2020) 38-51.

Chapter 6 – Photocatalytic performance of ruthenium modified titanate nanotubes and nanowires: a comparative study

6.1 - Introduction

Recently, enhancements on the photocatalytic activity of titanate nanowires were reported through the doping with Co and Ru, as shown in Chapters 4 and 5 [1,2]. Both doped particles were produced by hydrothermal treatment of an amorphous metal-containing precursor. It was confirmed the existence of the metal localized in two structural locations: substituting Ti^{4+} and exchanging Na^+ in the interlayers' region.

The elements from the *d*-block of the periodic table are often used as a dopant in photocatalytic semiconductor nanomaterials development. Some of those, like ruthenium, are responsible for the increase of the light absorption in the visible. During photo-irradiation, the redshift usually observed for the doped semiconductor is mainly due to the formation of intermediary bands (IB) in-between the conduction band (CB) and valence band (VB). In the doped semiconductor, these new energetic levels will have a dual function: they will promote photo-activation during excitation, but they also act as recombination platforms for charge carriers [3,4]. In this way, for a Ru doped TiO_2 -based material, the success for either electronic activation or photo-generated charge recombination will be dependent on the IB energy, in comparison to the CB and VB relative energetic positions [4].

Numerous synthesis routes to obtain and manipulate Ru-containing semiconductor photocatalytic nanoparticles have been reported. The effect of Ru incorporation on the optical, electronic and catalytic properties of MoSe_2 nanoflowers has been recently reported [5]. A considerable improvement in the Ru- MoSe_2 catalytic performance towards the hydrogen evolution reaction (HER) was attributed to Ru presence.

Throughout impregnation methods, TiO_2 nanoparticles modified with small Ru crystallites demonstrated enhanced photocatalytic activity for organic compounds degradation [6]. Distinct TiO_2 - RuO_2 nanocomposites, with distinct layouts [7] and Ru- TiO_2 nanoparticles [8] have been described to be catalytic for CO_2 methanation. As shown in the previous chapter, the synthesis and photocatalytic performance of new Ru-doped titanate nanowires (RuTNW) for caffeine removal have been described [2].

Supported on this, in this work a comparative study on the photocatalytic performance of titanate nanowires and titanate nanotubes modified by Ru doping was aimed. Ru-modified titanate nanotubes (RuTNT) and nanowires (RuTNW) materials were produced by hydrothermal treatment of the same amorphous Ru-containing precursor but using distinct

approaches. The two powders were comparatively characterized and evaluated as photocatalysts for sulfamethazine and caffeine removal. Sulfamethazine and caffeine were chosen as model pollutants due to their relevance, as emergent pollutants, in nowadays society. Several differences were observed for the structural, optical and morphological characterization of both Ru-modified samples. RuTNT demonstrated to be better photocatalyst than RuTNW, for caffeine degradation but identical performances were observed for sulfamethazine photo-assisted removal. However, the time profiles of the intermediates formed during irradiation were different, indicating distinct degradation mechanisms for both caffeine and sulfamethazine removal.

6.2 – Synthesis

Titanate nanowires (TNW) and nanotubes (TNT) were prepared using a hydrothermal treatment (160°C, 24 hours) of an amorphous precursor and TiO₂ nanoparticles, respectively, as described in Chapter 10.

An identical synthesis procedure was followed to produce the Ru-containing precursor, by adding the required molar amount (1%, nominal molar amount) of ruthenium to the titanium trichloride solution. In this experiment, a dark grey precursor was obtained. The Ru-containing amorphous precursor was used to obtain the Ru-TiO₂ and RuTNW nanoparticles. The RuTNT nanoparticles were produced using the same hydrothermal approach but using the Ru-TiO₂ crystalline nanoparticles.

6.3 – Structural, morphological and optical characterization

The crystalline structure of the TNT and RuTNT samples was analyzed by XRD (Figure 6.1). Peaks at 10°, 24°, 28° and 48°, corresponding to (100), (201), (003) and (002) lattice planes respectively, were observed in both XRD diffraction patterns. These features are characteristic of crystalline titanate lamellar materials [9,15].

As described in Chapter 5 for RuTNW sample [2], the segregation of ruthenium, as metal oxide or metallic nanoparticles is highly unlikely, since the XRD pattern of RuTNT doesn't show any evidence of other crystalline phase existence.

For this type of lamellar semiconductor, the peak at $2\theta = 10^\circ$ is due to the interlayer distance between the TiO₆ sheets [9,15]. In opposition to what was observed for TNW/RuTNW powders, no shift in the position of this peak was observed for the RuTNT sample [2]. This seems to indicate that for RuTNT, the Ru incorporation occurs

only by substitution of Ti^{4+} by Ru^{n+} in the TiO_6 octahedra and/or in interstitial positions [1,10], and not by Na^+ replacement [11,12].

As discussed in Chapter 5, the substitution of Ti^{4+} by Ru^{4+} in the doped TNT sample is possible since the effective ionic radius of Ru^{4+} and Ti^{4+} are comparable, 76.0 pm and 74.5 pm respectively. The Ti^{4+} replacement by Ru^{3+} ions (ionic radius is 82.0 pm) is not so probable. However, it has been described that this ion can be incorporated in some interstitial locations [3,13].

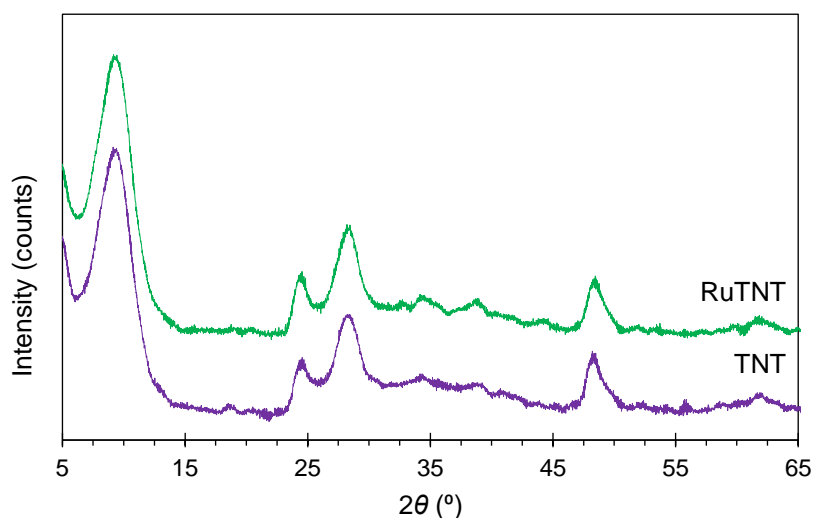


Figure 6.1 - XRD patterns of the TNT and RuTNT prepared samples.

The Ru doping effect in the TNT morphology was evaluated by transmission electronic microscopy (TEM) and no changes were observed for the pristine and Ru-doped titanate powders (Figure 6.2).

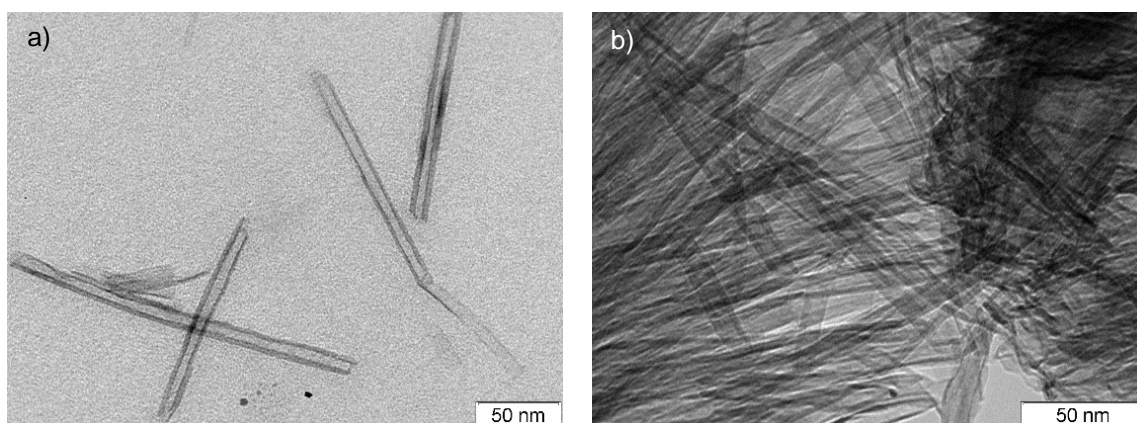


Figure 6.2 - TEM images of the (a) TNT and (b) RuTNT samples.

Both samples are morphologically homogeneous and are constituted by elongated and very thin particles. The cylindrical shape observed for TNT and RuTNT is in accordance with

previous works shown in Chapter 3 [14], and contrasts with the wire type morphology that it was shown for TNW/RuTNW in Chapter 5 [2].

It has been described that during titanate nanomaterials production under alkaline hydrothermal conditions, the precursor, usually TiO_2 (*anatase*, *rutile* or amorphous) is dissolved and intermediate titanate nanosheets are formed. After, and depending on the experimental conditions, mainly temperature and time, they can be converted directly into nanofibres instead of being rolled up to produce nanotubes. This usually occurs at temperatures above 170°C or when KOH is used as a solvent. For lower temperatures, in the $110\text{--}150^\circ\text{C}$ range, and using NaOH solutions, the formation of nanotubes has been reported [15]. Nevertheless, and as discussed in Chapter 2, the production of pristine titanate nanotubes and nanowires using the hydrothermal approach (160°C , 24 h) of the same precursor was obtained [14]. Identical results were obtained in this work, using the same procedure but a Ru-containing precursor. With this, it was possible to demonstrate that doping does not influence the particles' morphology.

The dimension of the nanotubular particles was estimated, by direct measurements, and diameters of 9.6 ± 1.3 nm and 10.8 ± 1.7 nm were found for TNT and RuTNT respectively. The powders were analyzed by EDS but no Ru was detected in the doped RuTNT sample, probably due to the very low amount of the metal in the sample. Despite this limitation, the Ru existence was confirmed by XPS, as discussed below. The absence of any type of impurities was confirmed by EDS analysis (not shown). The metal incorporated in the RuTNT (Ru/Ti) was quantified by μXRF and a value of 2.0% was obtained. It is interesting to verify that this value is considerably inferior if compared to the one reported for a RuTNW sample (3.4%) produced by the direct hydrothermal treatment of the same Ru-amorphous precursor (Chapter 5) [2]. This higher Ru/Ti ratio obtained for a material that was prepared directly from the Ru-containing precursor suggests that some dopant is lost during the Ru-precursor \rightarrow $\text{RuTiO}_2 \rightarrow$ RuTNT process. This additional loss of Ru, during the nanotubular sample synthesis, is in agreement with the dissolution of TiO_2 materials during titanate elongated nanomaterials production that it has been reported [15]. The specific surface areas of $165.10 \text{ m}^2 \text{ g}^{-1}$ and $220.78 \text{ m}^2 \text{ g}^{-1}$ were obtained by the B.E.T. method, for TNT and RuTNT samples, respectively. These values are substantially different from those reported in the previous Chapter, for TNW and RuTNW samples, $238.10 \text{ m}^2 \text{ g}^{-1}$ and $232.20 \text{ m}^2 \text{ g}^{-1}$ respectively [2].

Raman spectroscopy was used to further characterize the structure of the samples. The Raman spectra of TNT and RuTNT powders (Figure 6.3) are in agreement with previous works on $\text{Na}_2\text{Ti}_3\text{O}_7$ nanostructured materials [10,16-18].

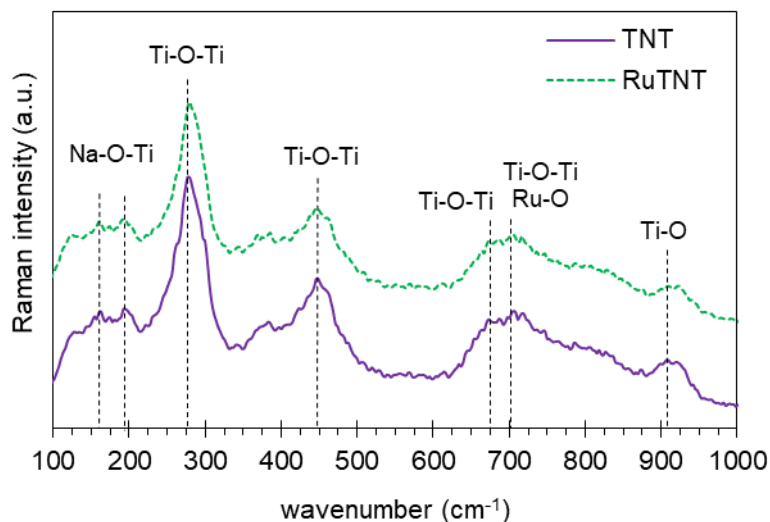


Figure 6.3 - Raman spectra of the TNT and RuTNT prepared samples.

The comparison of the band positions for RuTNT/TNT and RuTNW/TNW sets of samples are shown in Table 6.1. Comparing the characteristic vibration bands on titanate materials, including the Ti-O-Ti and Na-O-Ti, it is notorious some dependence on the particle's morphology. Higher Raman shifts were, in general, obtained for the titanate nanowires samples, TNW and RuTNW.

Type of vibration	TNT	RuTNT	TNW*	RuTNW*
Na-O-Ti lattice mode	161	161	160	160
Na-O-Ti lattice mode	196	196	196	196
Ti-O-Ti stretch	280	280	280	285
Ti-O-Ti stretch	449	449	455	455
Ti-O-Ti stretch	679	679	676	678
Ti-O-Ti and Ru-O stretches	709	709	706	706
Ti-O stretch	916	916	915	915

* from [2] (Chapter 5)

The Raman spectra obtained for TNT and RuTNT samples are similar, without significant shifts in the bands assigned to Ti-O-Ti stretches (at 280, 449 and 679 cm^{-1}) or Na-O-Ti lattice modes (at 161 and 196 cm^{-1}).

The band at 709 cm^{-1} can be assigned to Ti—O—Ti or Ti—OH stretching vibrations [19,20]. A slight increase in the intensity of this band for the RuTNT sample was observed. This intensity increase can be owing to the Ru doping (B_{2g} mode of Ru-O bond), as described in the previous chapter (Chapter 5, Section 5.3).

It has been reported that the highest frequency mode, have its wavenumber position and intensity affected either by the doping level or by the ionic position within the titanate nanostructure [9,16]. The Raman band at 916 cm^{-1} in the RuTNT and TNT spectra, does not show clear changes induced by the Ru addition, but this result is not very meaningful considering that it is a very weak and broadband.

The electronic structure of the prepared samples was investigated by XPS. The survey spectra of TNT and RuTNT powders are similar. Figure 6.4 shows the survey spectra of the RuTNT, where are visible the characteristic photoelectron peaks of titanate elongated materials [14].

The high-resolution spectra of Ti $2p$ and Ru $3p$ regions for TNT and RuTNT samples are also presented in Figure 6.4. Characteristic Ti $2p_{3/2}$ and Ti $2p_{1/2}$ binding energies, at 458.508 and 464.308 eV that corresponds to octahedral coordinated Ti^{4+} were observed for both samples. The doublet splitting energies of the Ti $2p$ peaks (5.8 eV), corroborates the existence of Ti^{4+} [10,21,22].

For the Ru-doped sample a shift on the Ti $2p_{3/2}$ and Ti $2p_{1/2}$ binding energies, for lower values, was observed, by the information previously reported for RuTNW powder (Chapter 5) [2]. This agrees with a higher electron charge density for the Ti atoms and with a non-stoichiometric bonding of titanium atoms to oxygen *via* the incorporation of Ru into the TiO_6 crystalline lattice [3]. No changes in the O $1s$ peak were observed due to Ru doping (not shown).

The presence of ruthenium in the modified sample (Figure 6.4) was confirmed using the Ru $3p_{1/2}$ peak (484 eV) [23], instead, the characteristic Ru $3d_{5/2}$ and $3d_{3/2}$ peaks due to the partial overlap with the C $1s$ peak, as discussed in the previous chapter (Chapter 5, Section 5.3). As mentioned in the previous chapter, no evidence of Ru-Ru bonding was also found for the RuTNT samples.

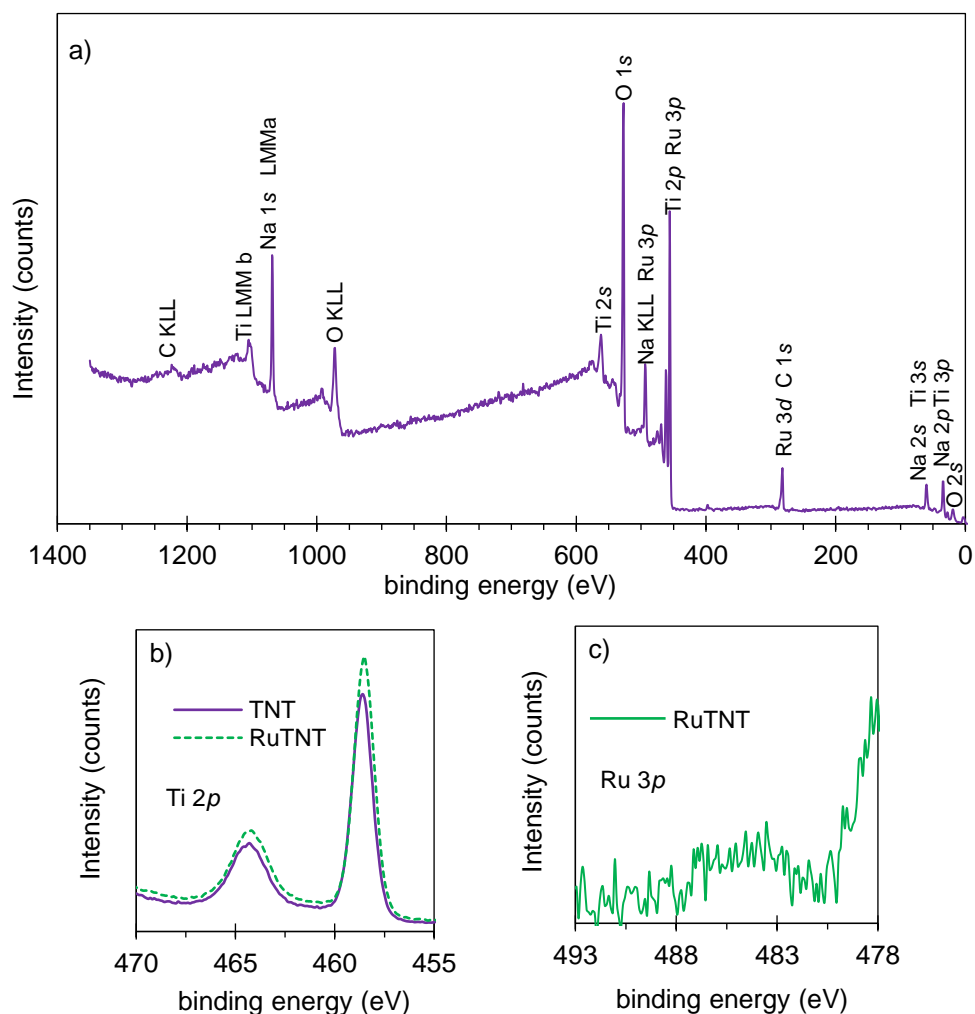


Figure 6.4 - (a) XPS survey spectra of the RuTNT sample and high resolution spectra of the (b) Ti $2p$ and (c) Ru $3p$ regions for the prepared powders.

Diffuse reflectance spectroscopy was used to evaluate the optical absorption profile of the prepared samples (Figure 6.5). The optical spectra of TNT and RuTNT powders are similar, presenting an absorption edge near 400 nm, which is characteristic of titanate elongated nanoparticles [15].

As discussed in previous chapters, this absorption feature is due to the charge transfer from the O $2p$ (valence band) to the Ti $3d$ orbital (conduction band).

An increase in the visible range absorption was observed for the RuTNT powder compared to the pristine TNT. This should be attributed to the Ru presence in the TNT structure and is according to data previously obtained for TNW/RuTNW materials, as analyzed in Chapter 5 [2]. The bandgap energy (E_g) of the samples was evaluated through Kubelka–Munk (KM) data treatment. For TNT and RuTNT samples, the values obtained were 3.38 eV and 3.54 eV respectively. These values are identical to the ones previously obtained (in Chapter 5) for similar titanate nanowires powders, TNW and RuTNW (Figure 6.5 inset) [2].

As mentioned in the previous chapter, the absorption in the visible and near infrared range, it should be endorsed to low-energy photons and/or thermal excitations of trapped electrons due to oxygen vacancies [3].

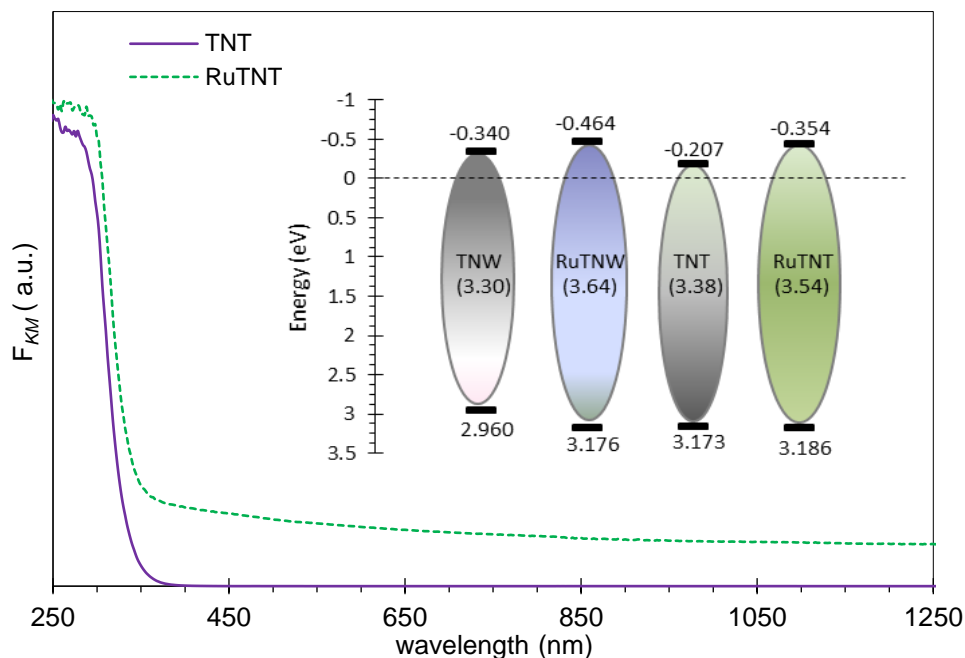


Figure 6.5 – Absorption spectra of the TNT and RuTNT samples. (Inset: energy-level diagram with E_g , VB, and CB positions, for TNT, RuTNT, and TNW, RuTNW [2]).

To better analyze and quantify the photo-induced electronic transitions in these semiconductor materials, the valence band spectrum (VB-XPS) of both samples was recorded (Figure 6.6).

Using a reported linear method, [3] the energetic position of the valence band (VB) was determined directly from the XPS spectra. The conduction band (CB) energetic position was calculated by the expression: $E_g = VB - CB$. Figure 6.5 shows the energetic scheme for the samples analyzed. For comparative purposes, the VB, CB and E_g values from the corresponding nanowires samples (TNW and RuTNW) were also introduced in Figure 6.5.

It is interesting that, despite the identical bandgap energy obtained for TNT and TNW samples, the energetic positions of VB and CB are different for these two powders, with TNT requiring less energy for photo-activation. For the Ru modified samples, the E_g values are similar (3.54 and 3.64 eV for RuTNT and RuTNW, respectively), but the CB and VB energetic positions are distinct, with lower energy requests for the RuTNT sample photo-activation.

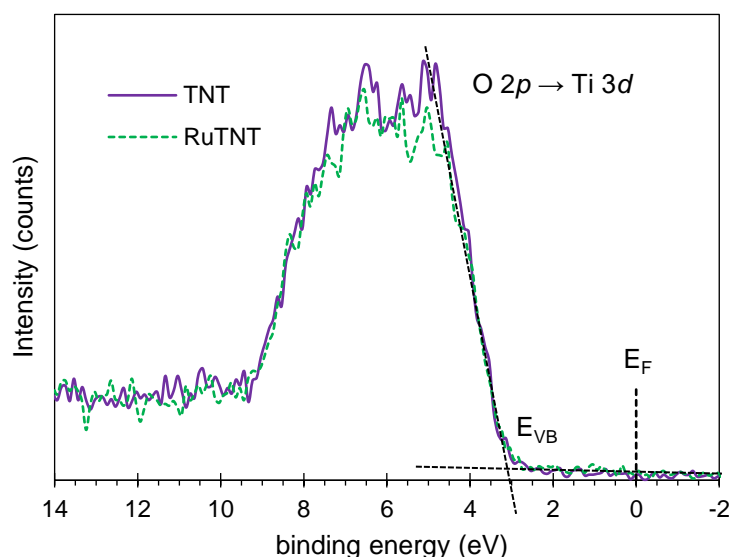


Figure 6.6 – XPS high resolution spectra of the O 2p to Ti 3d transition, used for valence band determination.

To evaluate some alterations in the charge carrier recombination process, due to the Ru incorporation, the photoluminescence spectra were registered. The RuTNT and TNT powders were analyzed by photoluminescence spectroscopy (PL), and the obtained spectra are depicted in Figure 6.7. The obtained results were compared with the ones reported in the previous chapter for RuTNW/TNW [2].

In Figure 6.7, the emission peak around 420 nm is due to the recombination of the charge carriers after semiconductor photo-activation [24]. For the RuTNT powder, a decrease in this peak intensity, in comparison to TNT was observed, being in accordance with the observed for the RuTNW and TNW powders in Chapter 5. This can be justified by a more efficient photo-generated charge carriers' separation, a result of the intermediate bands' creation, within the forbidden zone.

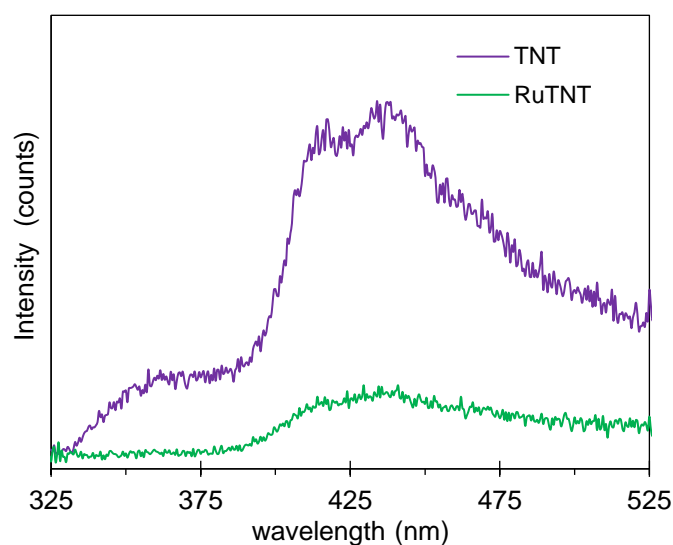


Figure 6.7 – Photoluminescence spectra of RuTNT and TNT prepared powders.

6.4 - Photocatalytic performance evaluation

6.4.1 - Photo-induced hydroxyl radical production

The high ability of a material to photo-catalyze the hydroxyl radical production could be seen as an indicator of its good photocatalytic performance in other photocatalytic processes. Hydroxyl radical ($\cdot\text{OH}$) is a very powerful oxidant agent and has been in charge of numerous oxidation reactions, for instance for emergent pollutants photo-assisted degradation. To evaluate the influence of the Ru doping in the TNT catalytic oxidant ability, the production of this specie was monitored during the terephthalic acid (TA) photodegradation. Figure 6.8 shows the amount of fluorescent 2-hydroxyterephthalic acid (HTA) produced during 30 min of irradiation of a TA/catalyst suspension. For comparative purposes, the results obtained for TNW and RuTNW powders were included in Figure 6.8.

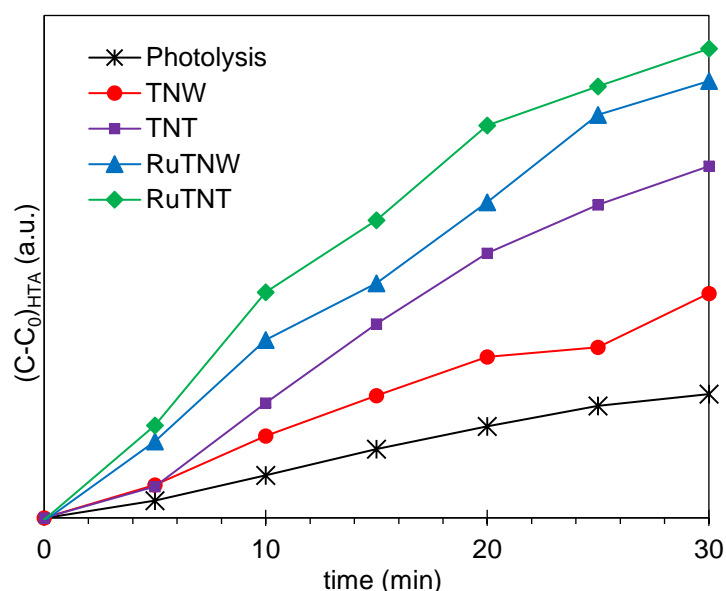


Figure 6.8 – HTA concentration during 30 min of irradiation of a TA solution (3 mM, 150 mL) using 10 mg of each photocatalyst.

As can be observed, all the samples have shown to be catalytic for this process, with RuTNT presenting the best photocatalytic activity. It is interesting that for both sets of samples, TNT/RuTNT and TNW/RuTNW, the best performances were attained by the doped materials. It is also noteworthy that the best results were obtained for the nanotubular samples, TNT and RuTNT, which are the ones possessing the lowest surface areas (165.10 and $220.78 \text{ m}^2 \text{ g}^{-1}$ respectively).

Considering the photolysis as a reference, an improvement of 78% on the $\cdot\text{OH}$ amount was attained using RuTNT as a catalyst. Using RuTNW and TNT as catalysts, this improvement drops to 55% and 40% respectively. The TNW catalyst was responsible for an increase of only

18% on radical production. These results show that the enhancement of these materials for the photocatalytic production of hydroxyl radicals is a direct effect of the Ru doping process.

The highest photocatalytic improvement, in comparison to pristine materials, was observed for RuTNW with an enhancement of 95% contrasting with the 33% observed for the RuTNT. These results are in agreement with others previously reported and show the influence of having nanotubes instead of nanowires for this catalytic purpose [14].

6.4.2 – Caffeine and sulfamethazine photocatalytic degradation

After the promising photocatalytic results obtained with RuTNW/TNW for caffeine degradation (Chapter 5), this molecule was chosen as a model pollutant to compare the efficiency of these materials with the new ones, RuTNT/TNT. Furthermore, sulfamethazine (SMZ) was also chosen as a model pollutant, due to this is an antibiotic of the sulphonamides family and is a drug widely used in medicine and veterinary medicine, being nowadays a relevant emergent pollutant.

• Caffeine photocatalytic degradation

Before irradiation, the ability of the RuTNT/TNT and RuTNW/TNW samples to adsorb caffeine and sulfamethazine was studied in dark conditions for 60 min. As shown in the previous chapter (Chapter 5, Section 5.4.2), no significant caffeine adsorption (less than 5%) was observed in the RuTNW/TNW surfaces [2]. Identical results were obtained for RuTNT/TNT powders.

Figure 6.9 shows the concentration profile of a 20 ppm caffeine solution over 45 min of irradiation, using TNT, RuTNT, TNW and RuTNW powders as photocatalysts. All the powders were catalytic for caffeine degradation. The Ru-doped samples were the best catalytic materials, and RuTNT was the one presenting the best performance. Using this catalyst, only 3.7% of the initial caffeine remains in solution, after 45 min of irradiation. This value increases to 16.2% in the presence of RuTNW. For the same period of irradiation, caffeine degradation values of 43.7% and 18.1% were attained using the pristine nanotubes (TNT) and nanowires (TNW) catalysts respectively. Under the same conditions, but with no catalyst (photolysis) only 10.3% of the initial caffeine was removed from the solution. After an irradiation time of 60 min, the removal of all caffeine was attained using both RuTNW and RuTNT. As discussed for TA, for caffeine degradation, the highest photocatalytic improvement due to Ru doping was observed for TNW with an enhancement of 66% contrasting with the 53% observed for TNT. These results can be explained due to the differences in the VB energy (inset Figure 6.5), for TNW

and RuTNW ($E_{VB} = 2.960$ and 3.176 eV, respectively) the difference between the energy necessary for the activation of the samples is 0.216 eV being higher than the difference for TNT ($E_{VB} = 3.173$ eV) and RuTNT ($E_{VB} = 3.186$ eV) samples, only a 0.013 eV were obtained.

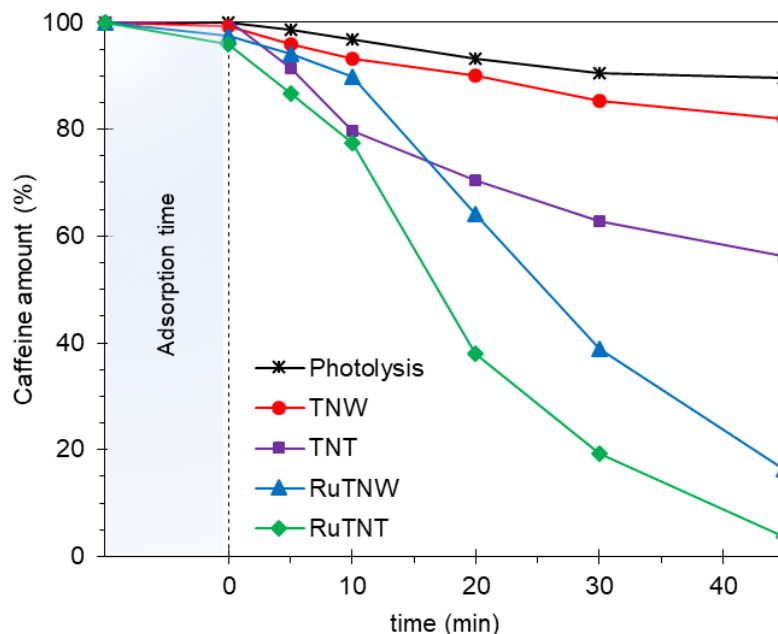
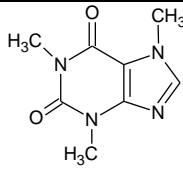
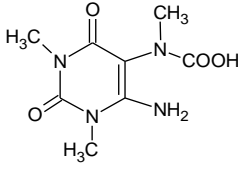
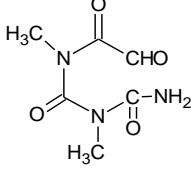
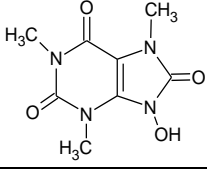
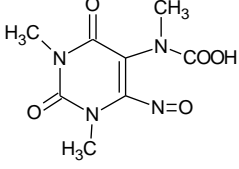
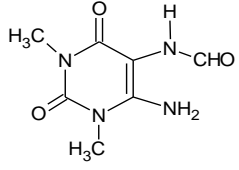
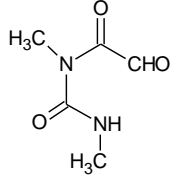


Figure 6.9 – Photocatalytic degradation of a 20 ppm caffeine aqueous solution during 45 min of irradiation using the pristine and modified powders as photocatalysts (0.13 g L^{-1}).

To go further in this study of this photocatalytic degradation process, the production and degradation of intermediates during an irradiation time of 120 min were evaluated. The products formed during RuTNT and RuTNW photo-assisted caffeine degradation were identified and quantified by LC-HR-ESI/MS and the results are shown in Table 6.2. The results obtained are in accordance with a reported degradation mechanism, shown in Annex B – Figure B.2 [25,26]. The time profile of the by-products during degradation was monitored and the results are in Figure 6.10. It is noteworthy that the profiles found for the RuTNT catalyst are distinct from the ones reported in Chapter 5 for the RuTNW photocatalyst [25], especially for compounds **CAF-1** and **CAF-2**. In the first minutes after irradiation, as detected for the RuTNW sample, using RuTNT sample (Figure 6.10(a)), high production of the compounds **CAF-1** and **CAF-2**, was observed. Compounds **CAF-1** and **CAF-2** are the main products in solution during the first 60 min of irradiation. It is notorious for an increase of compound **CAF-2** amount after 75 min of irradiation, contrasting with the decrease observed for compound **CAF-1**. This behavior is completely different from the one observed for RuTNW (Figure 6.10(b)) where a constant and almost linear increase of **CAF-1** and a decrease of **CAF-2** was observed during the first 75 min of irradiation [25].

Table 6.2 – Main fragments and correspondent by-products identified by LC-HR-ESI/MS during caffeine photodegradation using RuTNT and RuTNW samples as catalysts

Compound	Formula	Experimental mass (m/z)	Mol.wt.	Structure
Caffeine	$C_8H_{11}N_4O_2$	195.0876	194	
CAF-1	$C_8H_{12}N_4O_4Na$	251.0751	228	
	$C_7H_{10}N_3O_3$	184.0713		
	$C_5H_7N_2O_2$	127.0499		
CAF-2	$C_6H_9N_3O_4Na$	210.0485	187	
	$C_6H_8N_3O_3$	170.0560		
CAF-3	$C_8H_{11}N_4O_4$	227.0774	226	
CAF-4	$C_8H_{10}N_4O_5Na$	265.0547	242	
CAF-5	$C_7H_{11}N_4O_3$	199.0824	198	
	$C_5H_8N_3O_2$	142.0609		
CAF-6	$C_5H_8N_2O_3Na$	167.0426	144	
	$C_3H_9N_2O$	89.0713		

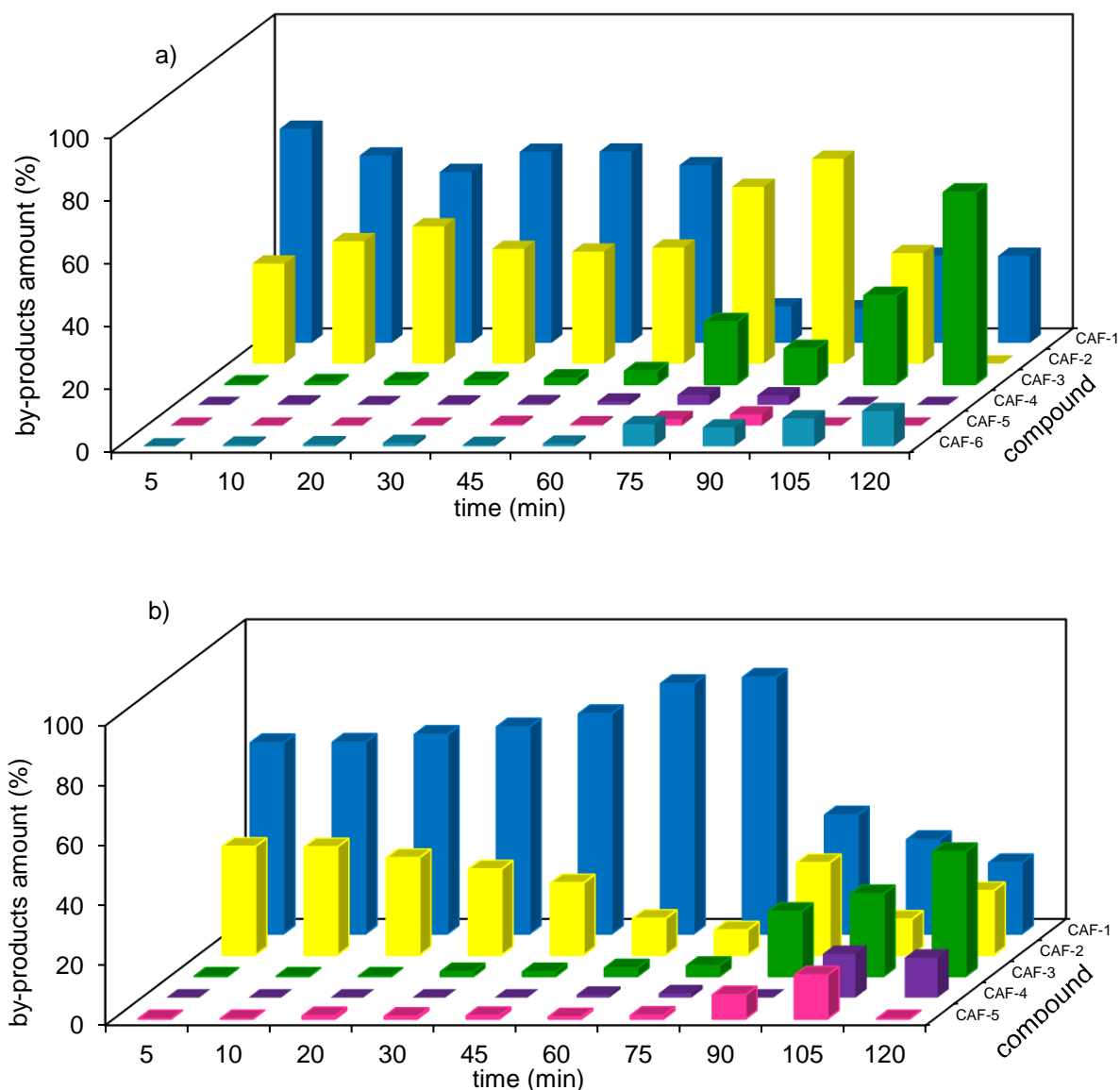


Figure 6.10 – Variation of the intermediate products identified during 120 min of caffeine photocatalytic degradation, using (a) RuTNT and (b) RuTNW as photocatalysts.

After 60 min, using RuTNT (Figure 6.10(a)), no caffeine was detected in solution, but the presence of the compounds **CAF-1** and **CAF-2** were still too high. At 75 min, the compound **CAF-6** amount increases, and after 120 min of irradiation only three compounds (compounds **CAF-1**, **CAF-3**, and **CAF-6**) are still in solution, indicating that more time is required to attain the complete degradation of these products using RuTNT sample as a catalyst.

• **Sulfamethazine photocatalytic degradation**

Sulfamethazine (SMZ) was chosen as a model contaminant to further evaluate the photocatalytic performance of the prepared catalysts. This is an antibiotic of the sulphonamides family and is a drug widely used in medicine and veterinary medicine.

The pristine TNT/TNW and doped RuTNT/RuTNW samples were evaluated as photocatalysts, for the first time, for sulfamethazine removal (Figure 6.11).

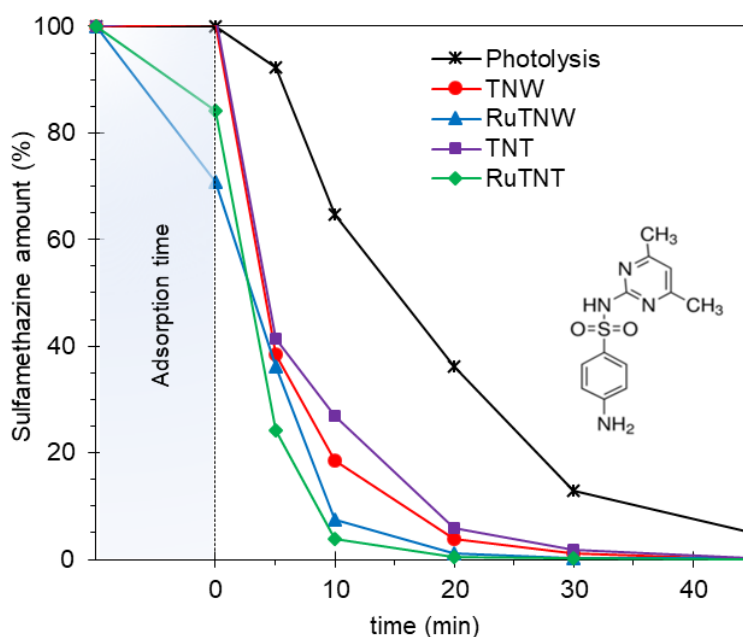


Figure 6.11 - Photocatalytic degradation profile of a 10 ppm sulfamethazine aqueous solution during 45 min of irradiation using the prepared powders as photocatalysts (0.13 g L^{-1}).

As can be seen in Figure 6.11, during the adsorption period, no substantial sulfamethazine adsorption was observed for the pristine TNW/TNT samples. However, 29.1% and 15.8% of the initial sulfamethazine were adsorbed for RuTNW and RuTNT respectively. After 60 min in dark conditions, the photocatalytic efficiency of the pristine and Ru doped samples on the degradation of 10 ppm of sulfamethazine solution was evaluated.

This molecule degrades faster than caffeine and as can be seen in Figure 6.11, all the samples were catalytic for this process. The best photocatalysts were the RuTNT and RuTNW powders with the total pollutant removal after 30 min of irradiation. For sulfamethazine degradation, TNW is a slightly better catalyst than TNT.

The intermediates formed during 90 min of sulfamethazine photodegradation, in the presence of RuTNT and RuTNW, were carried out (Table 6.3). The obtained results are in agreement with a degradation mechanism reported in literature [27-29] and presented in Annex B – Figure B.4.

The profile of such intermediate products degradation/formation with the irradiation time was also studied and the results are in Figure 6.12 where a sequential degradation process can be visualized. It is interesting to verify that distinct time profiles were observed for each intermediate, depending on the morphology of the catalyst, nanotubes or nanowires. As

observed for caffeine, these results indicate that titanate morphology has a strong influence on the sulfamethazine degradation mechanism.

Table 6.3 – Main products identified by LC-HR-ESI/MS during the sulfamethazine photodegradation using RuTNT and RuTNW samples as catalysts

Compound	Formula	Experimental mass (m/z)	Mol. wt.	structure
Sulfamethazine	C ₁₂ H ₁₄ N ₄ O ₂ S	279.0910	278.3	
SMZ-1	C ₁₂ H ₁₄ N ₄ O ₃ S	295.0859	294.4	
SMZ-2	C ₁₂ H ₁₃ N ₃ O	216.1131	215	
SMZ-3	C ₁₂ H ₁₄ N ₄	215.1291	214	
SMZ-4	C ₆ H ₇ NO ₄ S	190.0168	189	
SMZ-5	C ₆ H ₇ NO ₃ S	174.0219	173	
SMZ-6	C ₆ H ₇ N ₃ O ₂	154.0611	153	
SMZ-7	C ₆ H ₈ N ₂ O	125.0709	124	
SMZ-8	C ₆ H ₉ N ₃	124.0869	123	

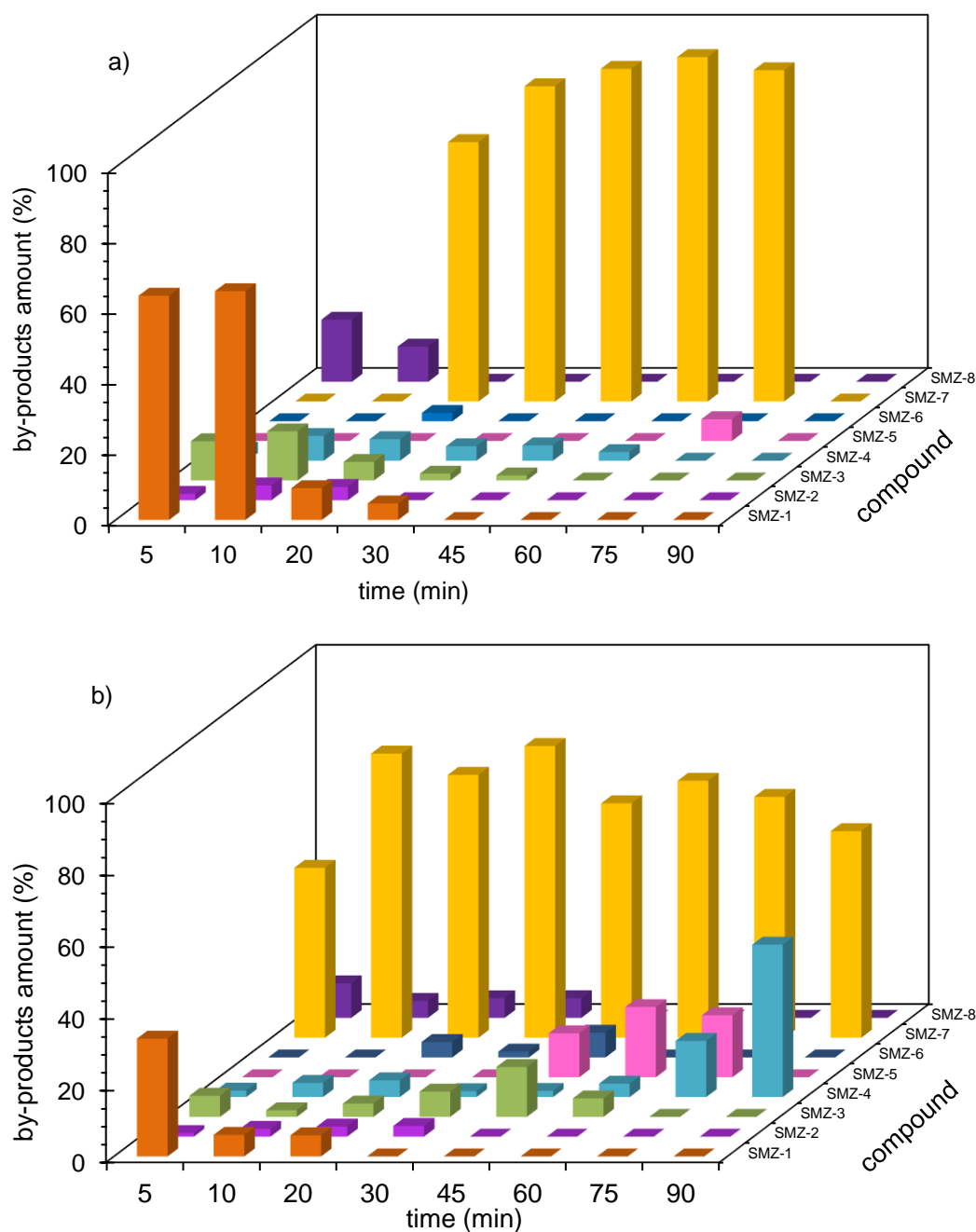


Figure 6.12 – Variation of the by-products identified during 90 min of sulfamethazine photocatalytic degradation, using (a) RuTNT and (b) RuTNW as catalyst.

For RuTNT photocatalyzed process, the sulfamethazine degradation starts with the formation of compounds **SMZ-1**, **SMZ-3**, **SMZ-4**, and **SMZ-8**, and after 5 min the production of compounds **SMZ-1 - SMZ-4** starts. For this time the compound **SMZ-8** starts to be degraded, and after 20 min of irradiation, this compound was completely removed.

Although the fact that after 30 min no sulfamethazine was detected in solution, the presence of small amounts of **SMZ-1**, **SMZ-3**, **SMZ-4** products and a higher amount of **SMZ-7** was observed. After 75 min starts the formation of compound **SMZ-5**, and there is also a large

amount of compound **SMZ-7** in solution. After 90 min of irradiation, no compounds were detected in the solution.

Distinct results were obtained when RuTNW was used as catalyst. First, the formation of compound **SMZ-7** starts immediately with the irradiation. This is the intermediate with the highest expressivity during the 90 min of irradiation. In opposition to what was observed for RuTNT, in this case, the formation and degradation of compounds **SMZ-4** and **SMZ-5** are relevant. After 90 min, the compound **SMZ-7** is still present in solution (57.5%) even if it has been starting to decrease. In opposition, the amount of **SMZ-4** is increasing and represents 42.5% of the composition of the final solution.

The Ru-containing samples were the best catalysts for caffeine and sulfamethazine degradation, and the possibility of such behavior is due to an enlargement on the semiconductor absorption range was carefully evaluated.

For that purpose, caffeine and sulfamethazine degradations were carried out under visible light. Under visible radiation, the catalytic activity of the samples was lower when compared to the experiments performed under UV-vis radiation. The results obtained for sulfamethazine degradation are shown in Figure 6.13.

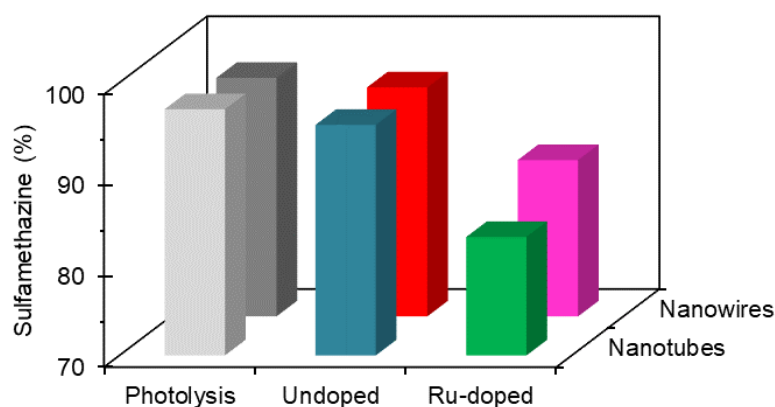


Figure 6.13 – Sulfamethazine concentration after 45 min of irradiation with visible light, using 20 mg of each photocatalyst.

For TNW and TNT assisted experiments, almost no differences in degradation rates were observed if compared to photolysis (less than 1%). This confirms that these materials are not catalytic under visible light. However, a clear improvement in the catalytic activity was observed for the Ru-containing catalysts, RuTNT and RuTNW, in comparison to TNT/TNW, when visible radiation is used.

As for the UV-vis radiation experiments, RuTNT was the best catalyst under visible irradiation. The improvement in the photocatalytic performance under visible light irradiation, due to Ru

doping should be attributed to either a bandgap energy narrowing effect and a decrease on the recombination rate, by the creation of intermediate bands within the prohibited zone.

6.5 - Conclusions

In this work, crystalline Ru modified titanate nanotubes and nanowires were prepared using the same Ru-containing amorphous precursor and identical time and temperature conditions but two distinct procedures. The precursor was used to prepare directly the RuTNW sample and to prepare Ru-TiO₂ nanoparticles, which were afterward used for RuTNT synthesis.

The amount of ruthenium integrated (Ru/Ti) was evaluated for RuTNW and RuTNT samples and values of 3.4% and 2.0% were obtained, respectively. This result agrees with a higher amount of Ru incorporated in the material directly from the Ru-precursor, RuTNW, contrasting with some Ru lost that occurs during the two steps process required for the RuTNT production. Supported on the characterization results it is possible to conclude that in both modified samples, the Ruⁿ⁺ is replacing Ti⁴⁺ and/or in interstitial positions. In opposition to what has been described for RuTNW, for RuTNT no evidence of the metal presence, in the interlayers, was found.

The photocatalytic ability of the prepared samples was studied for the hydroxyl radical production and the results allow to conclude that Ru incorporation leads to an enhancement of both TNT and TNW photocatalytic performances. An identical conclusion can be taken for caffeine and sulfamethazine degradation under UV-vis and visible radiation. The best photocatalytic material, for all the studied processes, was RuTNT.

It was also possible to conclude that for both RuTNT and RuTNW samples, this improvement on the photocatalytic behavior is mainly due to a decrease in the charge carriers' recombination rate rather than to visible light activation. The utmost difference on the photocatalytic performance of having nanotubes or nanowires is mainly related to the pollutants' degradation mechanism and intermediates formation/degradation.

6.6 - References

1 - B. Barrocas, A.J. Silvestre, A.G. Rolo, O.C. Monteiro, The effect of ionic Co presence on the structural, optical and photocatalytic properties of modified cobalt–titanate nanotubes, *Phys. Chem. Chem. Phys.* 18 (2016) 18081-18093.

- 2 - B.T. Barrocas, M. Conceição Oliveira, H.I.S. Nogueira, S. Fateixa, O.C. Monteiro, Ruthenium-modified titanate nanowires for the photocatalytic oxidative removal of organic pollutants from water, *ACS Applied Nano Mat.* 2 (2019) 1341-1349.
- 3 - T.-D. Nguyen-Phan, S. Luo, D. Vovchok, J. Llorca, S. Sallis, S. Kattel, W. Xu, L.F.J. Piper, D.E. Polyansky, S.D. Senanayake, D.J. Stacchiola, J.A. Rodriguez, Three-dimensional ruthenium-doped TiO₂ sea urchins for enhanced visible-light-responsive H₂ production, *Phys. Chem. Chem. Phys.* 18 (2016) 15972-15979.
- 4 - K. Song, X. Han, G. Shao, Electronic properties of rutile TiO₂ doped with 4*d* transition metals: first-principles study, *J. Alloys Compd.* 551 (2013) 118-124.
- 5 - K. Vasu, O.E. Meiron, A.N. Enyashin, R. Bar-Ziv, M. Bar-Sadan, Effect of Ru doping on the properties of MoSe₂ nanoflowers, *J. Phys. Chem. C* 123 (2019) 1987-1994.
- 6 - R.M. Kulkarni, R.S. Malladi, M.S. Hanagadakar, M.R. Doddamani, B. Santhakumari, S.D. Kulkarni, Ru–TiO₂ semiconducting nanoparticles for the photo-catalytic degradation of bromothymol blue, *J. Mater. Sci.: Mater. Electron.* 27 (2016) 13065-13074.
- 7 - A. Kim, D.P. Debecker, F. Devred, V. Dubois, C. Sanchez, C. Sasso, CO₂ methanation on Ru/TiO₂ catalysts: On the effect of mixing anatase and rutile TiO₂ supports, *Appl. Catal. B* 220 (2018) 615-625.
- 8 - A. Petala, P. Panagiotopoulou, Methanation of CO₂ over alkali-promoted Ru/TiO₂ catalysts: I. Effect of alkali additives on catalytic activity and selectivity, *Appl. Catal. B* 224 (2018) 919-927.
- 9 - H. Liu, D. Yang, E.R. Waclawik, X. Ke, Z. Zheng, H. Zhu, R.L. Frost, J. Raman. Spectrosc. 41 (2010) 1792-1796.
- 10 - T.M.F. Marques, O.P. Ferreira, J.A.P. Costa, K. Fujisawa, M. Terrones, B.C. Viana, Study of the growth of CeO₂ nanoparticles onto titanate nanotubes, *J. Phys. Chem. Solids* 87 (2015) 213-220.

11 - V. Bem, M.C. Neves, M.R. Nunes, A.J. Silvestre, O.C. Monteiro, Influence of the sodium/proton replacement on the structural, morphological and photocatalytic properties of titanate nanotubes, *J. Photochem. Photobiol. A* 232 (2012) 50-56.

12 - V.C. Ferreira, M.R. Nunes, A.J. Silvestre, O.C. Monteiro, Synthesis and properties of Co-doped titanate nanotubes and their optical sensitization with methylene blue, *Mat. Chem. Phys.* 142 (2013) 355-362.

13 - R.D. Shannon, Revised effective ionic radii and systematic studies of interatomic distances in halides and chalcogenides, *Acta Cryst. A* 32 (1976) 751-767.

14 - B. Barrocas, M.C. Neves, M. Conceição Oliveira, O.C. Monteiro, Enhanced photocatalytic degradation of psychoactive substances using amine-modified elongated titanate nanostructures, *Environ. Science: Nano* 5 (2018) 350-361.

15 - D.V. Bavykin, F.C. Walsh, Titanate and titania nanotubes: Synthesis, properties and applications, *RSC Nanoscience & Nanotechnology Series*, Cambridge, UK, RSC Publishing, 2010.

16 - F.L.R. Silva, A.A.A. Filho, M.B. Silva, K. Balzuweit, J.L. Bantignies, E.W.S. Caetano, R.L. Moreira, V.N. Freire, A. Righi, Polarized Raman, FTIR, and DFT study of Na₂Ti₃O₇ microcrystals, *J. Raman Spectrosc.* 49 (2018) 538-548.

17 - K.R. Zhu, Y. Yuan, M.S. Zhang, J.M. Hong, Y. Deng, Z. Yin, Structural transformation from NaHTi₃O₇ nanotube to Na₂Ti₆O₁₃ nanorod, *Solid State Commun.* 144 (2007) 450-453.

18 - B.C. Viana, O.P. Ferreira, A.G.S. Filho, A.A. Hidalgo, J.M. Filho, O.L. Alves, Alkali metal intercalated titanate nanotubes: A vibrational spectroscopy study, *Vib. Spectrosc.* 55 (2011) 183-187.

19 - L.M.M. Tejada, A. Muñoz, M.A. Centeno, J.A. Odriozola, *In-situ* Raman spectroscopy study of Ru/TiO₂ catalyst in the selective methanation of CO, *J. Raman Spectrosc.* 47 (2016) 189-197.

- 20 - R.S. Chen, C.C. Chen, Y.S. Huang, C.T. Chia, H.P. Chen, D.S. Tsai, K.K. Tiong, A comparative study of microstructure of RuO₂ nanorods via Raman scattering and field emission scanning electron microscopy, *Solid State Commun.* 131 (2004) 349-353.
- 21 - T. Pham, B. Lee, Feasibility of silver doped TiO₂/glass fiber photocatalyst under visible irradiation as an indoor air germicide, *Int. J. Environ. Res. Public Health* 11 (2014) 3271-3288.
- 22 - X. Chen, S.S. Mao, Titanium dioxide nanomaterials: synthesis, properties, modifications, and applications, *Chem. Ver.* 107 (2007) 2891-2959.
- 23 - D.J. Morgan, Resolving ruthenium: XPS studies of common ruthenium materials, *Surf. Interface Anal.* 47 (2015) 1072-1079.
- 24 - N. Pugazhenthiran, S. Murugesan, S. Anandan, High surface area Ag-TiO₂ nanotubes for solar/visible-light photocatalytic degradation of ceftiofur sodium, *J. Hazard. Mater.* 263 (2013) 541-549.
- 25 - R. Rosal, A. Rodríguez, J.A. Perdigón-Melón, A. Petre, E. García-Calvo, M.J. Gómez, A. Agüera, A. R. Fernández-Alba, Degradation of caffeine and identification of the transformation products generated by ozonation, *Chemosphere* 74 (2009) 825-831.
- 26 - F. Qi, W. Chu, B. Xu, Catalytic degradation of caffeine in aqueous solutions by cobalt-MCM 41 activation of peroxymonosulfate, *Appl. Catal. B* 134-135 (2013) 324-332.
- 27 - Z. Wan, J. Wang, Fenton-like degradation of sulfamethazine using Fe₃O₄/Mn₃O₄ nanocomposite catalyst: kinetics and catalytic mechanism, *Environ. Sci. Pollut. Res.* 24 (2017) 568-577.
- 28 - C. Guo, J. Xu, S. Wang, Y. Zhang, Y. He, X. Li, Photodegradation of sulfamethazine in an aqueous solution by a bismuth molybdate photocatalyst, *Catal. Sci. Technol.* 3 (2013) 1603-1611.
- 29 - R. Nassar, A. Trivella, S. Mokh, M. Al-Iskandarani, H. Budzinski, P. Mazellier, Photodegradation of sulfamethazine, sulfamethoxypyridazine, amitriptyline, and clomipramine drugs in aqueous media, *J. Photoch. Photobio. A* 336 (2017) 176-182.

Chapter 7

Influence of iron and manganese vestigial contamination on the properties of titanate nanowires

This work was subject of the publication:

B. Barrocas, L.D. Chiavassa, M. Conceição Oliveira, O.C. Monteiro, Impact of Fe, Mn co-doping in titanate nanowires photocatalytic performance for emergent organic pollutants removal, *Chemosphere* 250 (2020) 126240(1)-126240(10).

Chapter 7 – Influence of iron and manganese vestigial contamination on the properties of titanate nanowires

7.1 - Introduction

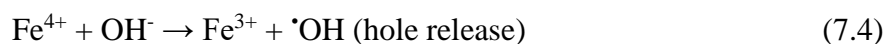
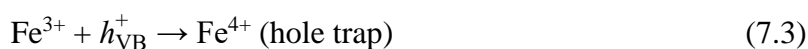
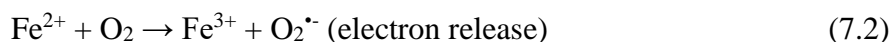
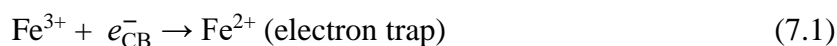
It has been shown, in the previous chapters, that through the modification of TNW with transition metals, for instance, Co or Ru, the catalytic performance of these elongated materials for pollutants removal can be enhanced (Chapters 4 – 6) [1,2]. Usually, this effect can be due to an enlargement to the visible range of the semiconductor optical absorption. However, the major reason for this behavior is often the reduction of the charge recombination rate, due to the creation of intermediate bands in the forbidden zone. It has been reported that the bandgap energy, valence and conduction band positions, Fermi level, and *d*-electron configuration of the electronic structure in TiO₂ and related materials, can be successfully adjusted when transition metal ions, especially the ones possessing *3d* or *4d* electrons, are introduced into semiconductor crystalline structure.

Manganese and iron are transition metal ions, with a *3d* transitions and they widely used as dopant elements to try to extend the material light absorption to the visible range, inducing the creation of intermediate bands (IB) within the forbidden zone. This will promote a redshift in the absorption band edge, with the IB acting not only as intermediate energetic levels, during photo-activation, but also as recombination center under low energy photons illumination, due to the IB can act as stepping stones to relay valence electrons into the conduction band (CB), extending the lifetime of the charge carriers [3,4].

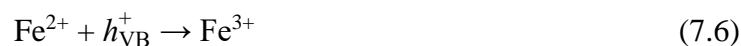
The Fe³⁺ ion attracted a lot of attention due to the remarkable synergistic improvement of the photocatalytic activity of TiO₂ in the visible light range. Recently, it was found that TiO₂ doped with Fe³⁺ ions have higher photoactivation under visible light irradiation [5]. It has been proven that Fe³⁺ ions are an effective doping element in TiO₂ due to their half-filled electronic configuration, and Fe³⁺ modified TiO₂ not only favors the separation of photo-generated electrons and holes but also reduces the TiO₂ bandgap energy [6,7].

Ding *et al.* [8] reported the modification of titanate nanotubes with iron (Fe-TNT), obtained by intercalation of Fe ions in the interlayers. This new Fe-TNT showed an improvement in the optical properties when compared with the pristine TNT, shifting the absorption into the visible range. The authors also modified the TNT with other metals, concluding that the Bi- and Cd-incorporated materials have slightly improved absorption properties, but the transition metals Fe and Ni have a much more significant influence on the optical properties of the titanate nanotubes [8].

Another particularity of the iron, is that Fe^{3+} ions can act as electron and hole trap, resulting in the formation of Fe^{2+} and Fe^{4+} ions, ($E^\circ (\text{Fe}^{3+}/\text{Fe}^{2+}) = 0.771 \text{ V vs. NHE}$ and $E^\circ (\text{Fe}^{4+}/\text{Fe}^{3+}) = 2.07 \text{ V vs. NHE}$), which are less stable as compared to Fe^{3+} ions (due to half filled stable d^5 configuration). So, the trapped charges can be easily released back to form stable Fe^{3+} ions [9]. The redox potential of $\text{Fe}^{3+}/\text{Fe}^{2+}$ is 0.771 V vs. NHE , which is between the VB and CB of the semiconductor materials and can act as a charge carrier trap, as described in the follow equations [10]:

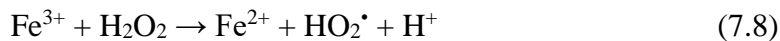
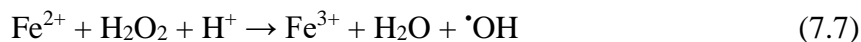


The beneficial effect of Fe^{3+} ions is attributed to electron trapping at the semiconductor surface. The trapping of photoelectrons leaves photogenerated holes available for reaction with hydroxyl ions to form hydroxyl radicals [11]:

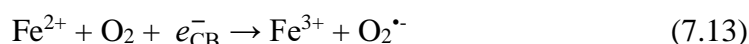
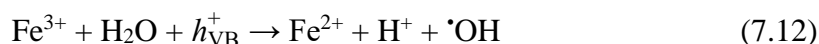
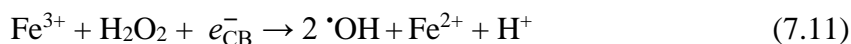
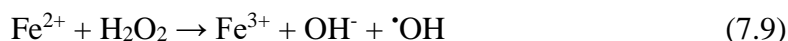


The iron ions (or ferrous ions) are also attractive for the Fenton-based processes. The Fenton oxidation was discovered by H.J.H. Fenton in 1894. The classical Fenton reagents consist of H_2O_2 and iron ions homogeneous solution, both are unstable in chemical properties and easy to lose activity, resulting in a waste of reagents. Also, concentrated H_2O_2 , which is explosive and toxic, is harmful to humans. Therefore, the storage and transportation of concentrated H_2O_2 and homogeneous solutions of iron ions not only increase the costs of organic wastewater treatment but also endanger the health of operators [12-14]. However, nowadays the Fenton-based oxidation process is one of the most effective and suitable methods for organic pollutants' removal. The highly oxidative hydroxyl radical ($\cdot\text{OH}$) formed from the reaction of H_2O_2 with Fe^{2+} under strong acid can quickly and non-selectively degrade most organic pollutants to carbon dioxide and water. The oxidation mechanism for the Fenton process is shown in equation (7.7). Based on this principle, the Fenton process has been widely used in various kinds of organic wastewater treatment.

The Fenton catalytic reactions consist of the oxidation of Fe^{2+} to Fe^{3+} together with the $\cdot\text{OH}$ generation, Eq. (7.7), and the reduction of Fe^{3+} to Fe^{2+} (Eq. (7.8)) [11,13,15].



The photo-Fenton processes are based on the Fenton's reaction in which the hydrogen peroxide is catalyzed, by the ferrous ions, to photo-generate hydroxyl radicals, according the equations:



The generated hydroxyl radicals are strongly oxidizing agents, $E^\circ(\cdot\text{OH}/\text{H}_2\text{O}) = 2.73 \text{ V vs. NHE}$, that can rapidly and non-selectively oxidize organic compounds into carbon dioxide and water and hence can degrade pollutants effectively.

Manganese is an excellent candidate for doping due to it can contribute for a reduction on the bandgap energy, due to Mn doping induces a considerable energetic shift of the valence band maximum, which can contribute to narrow the overall energy gap in the doped materials [16,17]. It can also induce the introduction of intermediate bands (IB) in the forbidden zone, allowing multi-band optical absorption [17].

Recently, TNW modified with Mn, by doping or ion-exchange methodologies were reported [18]. The incorporation of Mn can lead to changes in the crystalline structure of the TNW and on its physical and optical properties [18]. It was concluded that by doping the Mn was incorporated between the TiO_6 interlayers and replacing Ti^{4+} . On the other hand, by an ion-exchange process, the metallic ions were only incorporated in the interlayers' space. It is also interesting to note that the Mn in these samples is present as Mn^{3+} in the doped sample and as $\text{Mn}^{2+}/\text{Mn}^{4+}$ in the intercalated sample. The presence of Mn in both modified samples, promote the absorption in the visible range and a reduction of the charge carriers' recombination rate. The best photocatalytic results reported for the methylparaben removal were obtained using the doped sample [18].

Manganese is also a superoxide ions scavenger, once Mn^{2+} quickly convert the $\text{O}_2^{\cdot-}$ into H_2O_2 [19]. Failli *et al.* reported that Mn(II) complexes with polyamine-polycarboxylate scaffolds were effective $\text{O}_2^{\cdot-}$ scavengers in biological systems and, therefore, may prevent oxidative cell/tissue damage and exert anti-inflammatory therapeutic effects [20].

Recently, was reported that the optical redshift (of 300 nm) in Mn-doped *rutile* is expected to open wide application possibilities for using TiO_2 in a new class of photovoltaic cells, wherein the doped materials will be used as an effective optical absorber for a wide range of solar irradiance from the UV to the near-infrared spectral light [3,16].

This research work describes the Mn and Fe incorporation in titanate nanowires (TNW), due to vestigial contamination, on the initial reagents, and the evaluation of their photocatalytic performance on pollutants removal. The photocatalytic activity of the prepared powders was firstly investigated using the terephthalic acid (TA) to study the catalytic production of hydroxyl radical ($\cdot\text{OH}$). Due to its environmental impact and resistance to degradation, caffeine was chosen as a model emergent pollutant.

Although $\cdot\text{OH}$ radicals have been reported to be the major species responsible for photocatalytic degradation of organic pollutants, many other radicals can participate actively in this process [21]. Therefore, a radical scavengers' detailed study was carried out to define the active oxidant species, involved in the caffeine photocatalytic degradation process. For this, the caffeine photodegradation was carried out with an addition of different scavengers, such as ethanol (EtOH), benzoquinone (BQ) and potassium oxalate (Ox), to trap the $\cdot\text{OH}$, $\text{O}_2^{\cdot-}$ and holes (h^+), respectively. Based on these results, a possible degradation mechanism was proposed.

7.2 – Synthesis

Titanate nanowires were prepared using a hydrothermal treatment of an amorphous precursor in alkaline aqueous media (NaOH, 10 M) at 160°C for 24 hours. The TNW precursor was prepared using a procedure published elsewhere [22]. A detailed description of the experimental procedure is shown in Chapter 10.

During this work two distinct TiCl_3 sources were used, a titanium trichloride (12 wt.% in 20-30 wt.% HCl) from Aldrich and (20 wt.% in 20-30 wt.% HCl) from Acros.

Contrary to what it has been described, a pale pink solid, using the TiCl_3 (12 wt.% in 20-30 wt.% HCl, Aldrich), was obtained. This sample was labeled as 'contaminated precursor'. Anticipating the existence of any kind of contamination in the TiCl_3 commercial solution, the

same procedure was repeated using an identical amount of TiCl_3 but from a distinct source, (20 wt.% in 20–30 wt.% HCl, Acros). In this case, a white solid was obtained.

In fact, through atomic absorption spectroscopy (AAS) analyses of the commercial TiCl_3 solutions, it indicates 8.1 mg L^{-1} of manganese and 4.3 mg L^{-1} of iron in the solution used to prepare the ‘contaminated precursor’, confirming the vestigial contamination with Mn and Fe. With these two distinct TiCl_3 sources, and after hydrothermal treatment of the precursors, two crystalline solids, Fe/Mn-TNW (pink) and TNW (white) were produced.

7.3 – Structural, morphological and optical characterization

The crystalline structure of the samples prepared using the two sources of titanium was analyzed by XRD and the obtained patterns are presented in Figure 7.1.

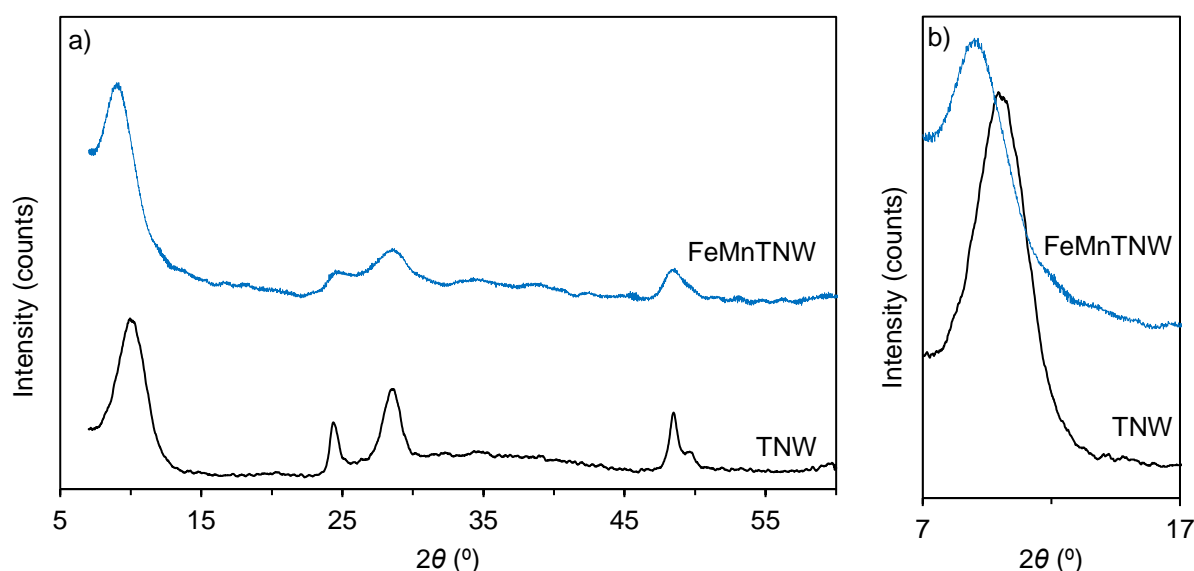


Figure 7.1 – (a) XRD patterns of the TNW and FeMnTNW samples; (b) detail of the XRD patterns.

Figure 7.1 shows that both XRD patterns show peaks typical of a $\text{Na}_2\text{Ti}_3\text{O}_7$ (JCPDS file no. 72-0148) crystalline titanate layered structure [23–28]. No signs of other crystalline phases, *e.g.* metallic clusters, iron or manganese-containing oxides were identified in the diffraction pattern of all the samples, indicating that only crystalline TNW particles were produced.

As previously reported, the diffraction peak at $2\theta \sim 10^\circ$ is correlated to the distance between the TiO_6 octahedra sheets that form the layered structure, usually hosting Na^+ ions.

For the contaminated sample, FeMnTNW, the above-mentioned peak shifts from $2\theta = 9.94^\circ$ for TNW to 9.15° , suggesting the incorporation of some cationic species between the TiO_6 sheets, *via* a Na^+ ion-exchange process. This result is in agreement with other reported works describing the high ability of these titanate layered materials to exchange Na^+ by other cationic

species, *e.g.* H^+ , Ru^{n+} or Co^{2+} [1,2,27,29]. It should be noted that this shift, for the contaminated sample, should be due to an increase of the interlayers' distance since the ionic radius of Na^+ is smaller than that of hydrated ionic Fe and/or Mn [18,30]. The existence of Fe or Mn intercalation presupposes those ions' availability to migrate to the interlayers during TNW synthesis. This result also agrees with the precursor dissolution before titanate sheets formation [1,23,31]. After the loss of some of the Fe/Mn ions from the precursor to the solution, these ions will be available to replace Na^+ in the interlayers, during TNW synthesis.

The modification of a titanate lamellar structure by the incorporation of metal in the interlayers and simultaneously with the metal replacing Ti^{4+} has been described in the literature for several metals [1,2,18]. For a coordination number of 6 and considering that Fe^{3+} and Ti^{4+} have similar ionic radii, 78.5 pm, and 74.5 pm respectively, the substitution of Ti^{4+} by Fe^{3+} in the TiO_6 octahedra is also a possibility. Considering the same structural arrangement, the partial replacement of Ti^{4+} by Mn^{3+} (72.0 pm) or Mn^{2+} (81.0 pm) have also no apparent structural hindrance. The electron configurations of Mn^{2+} and Fe^{3+} are $[Ar] 3d^5$ and $d \rightarrow d$ transitions of those five electrons to a higher level it is possible and would explain the pale pink coloration of the FeMnTNW sample.

To evaluate the possible influence of the Fe/Mn contamination in the TNW morphology, the prepared samples were analyzed by TEM. As can be seen in Figure 7.2, the samples are homogenous and present identical morphology: very thin and elongated particles. However, for the FeMnTNW sample, together with the nanowires, some sheet-type larger particles are also visible.

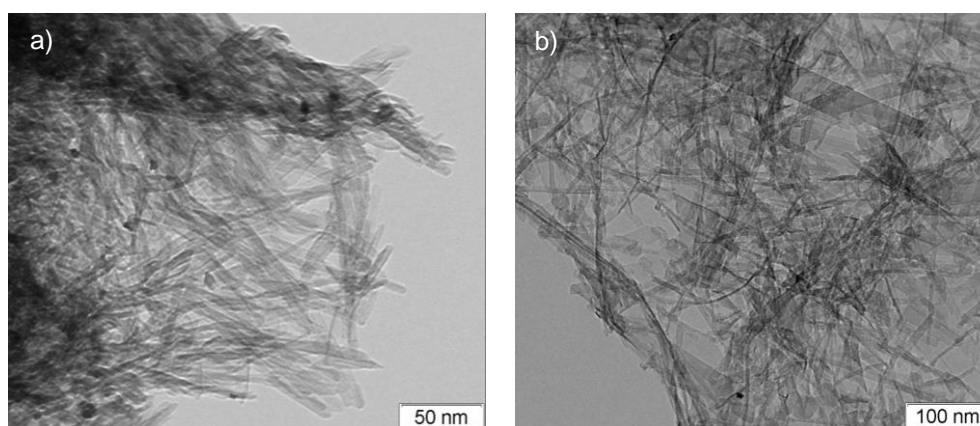


Figure 7.2 - TEM images of the (a) pristine TNW and (b) FeMnTNW prepared samples.

The elemental composition of the prepared samples was tried by energy-dispersive X-ray spectroscopy (EDS) but was not successful due to equipment limitations and the small amount

foreseeing for other elements than Na, Ti and O. Despite this, the quantification of Fe and Mn, in the FeMnTNW sample was possible by μ XRF and posteriorly confirmed by XPS. The Mn amount in the FeMnTNW sample is vestigial ($\text{Mn/Ti} = 0.08\%$), but a higher value 0.14% (Fe/Ti ratio) was obtained for iron. It is noteworthy that the Fe/Mn ratio is 1.75 in the nanowires, contrasting with the value of 0.53 found on the TiCl_3 solution. This seems to be evidence of the superior ability of Fe, when compared to Mn, to be incorporated in the TNW structure.

One of the most attractive properties of elongated nanomaterials, for heterogeneous catalytic applications, is their high specific surface area. Therefore, the specific surface area of the samples was evaluated by the B.E.T. method. Pristine TNW possesses a higher surface area, $238.10 \text{ m}^2 \text{ g}^{-1}$ if compared to the FeMnTNW powder, $124.7 \text{ m}^2 \text{ g}^{-1}$. This fact can be related to the differences observed in the samples' morphology.

The influence of the Fe and Mn incorporation in the TNW structure was further investigated by XPS analysis. Figure 7.3 shows the survey spectra of the pristine TNW and modified FeMnTNW powders, where the titanate typical photoelectron peaks of Na $1s$, Ti $2p$, and O $1s$ are visible. The XPS spectrum of the TNW sample shows the Ti $2p_{3/2}$ and $2p_{1/2}$ peaks at 458.6 and 464.4 eV, respectively (Figure 7.3(a)). Slightly shifts on those peaks, to 458.7 and 464.4 eV were observed for the Fe/Mn containing sample. This agrees with some alterations in the electron density of the Ti^{4+} surrounding structural environment, imposed by the metal/dopant presence [2,32].

No peaks appear at 456.2 – 457.4 eV range indicating that only Ti^{4+} is present in the structure [1,33,34]. This hypothesis is corroborated by the fact the Ti $2p$ peak doublet splitting energy is ~ 5.8 eV, indicating the existence of Ti^{4+} only. The high symmetry of the Ti $2p$ peaks also confirms that no Ti^{4+} reduction had occurred in the samples [1,35,36].

The high-resolution spectra of Ti $2p$, O $1s$, and Fe $2p$ regions are also presented in Figure 7.3. For the FeMnTNW sample, two peaks in the Fe $2p$ region, at 710.2 and 723.4 eV are observed in Figure 7.3(c). These peaks correspond to the $2p_{3/2}$ and $2p_{1/2}$ spin-orbital components, indicating the presence of Fe^{2+} and Fe^{3+} in the sample [37-39]. Due to the extremely small amount of Mn present in the structure and the acquisition conditions, no peaks associated with the presence of this metal were observed.

The Na^+ content in the samples was assessed by XPS and the amount found in the FeMnTNW sample is lower than the one obtained for TNW. This is in accordance with a higher level of Na^+ substitution, by Fe/Mn, in the interlayer space, for the contaminated sample.

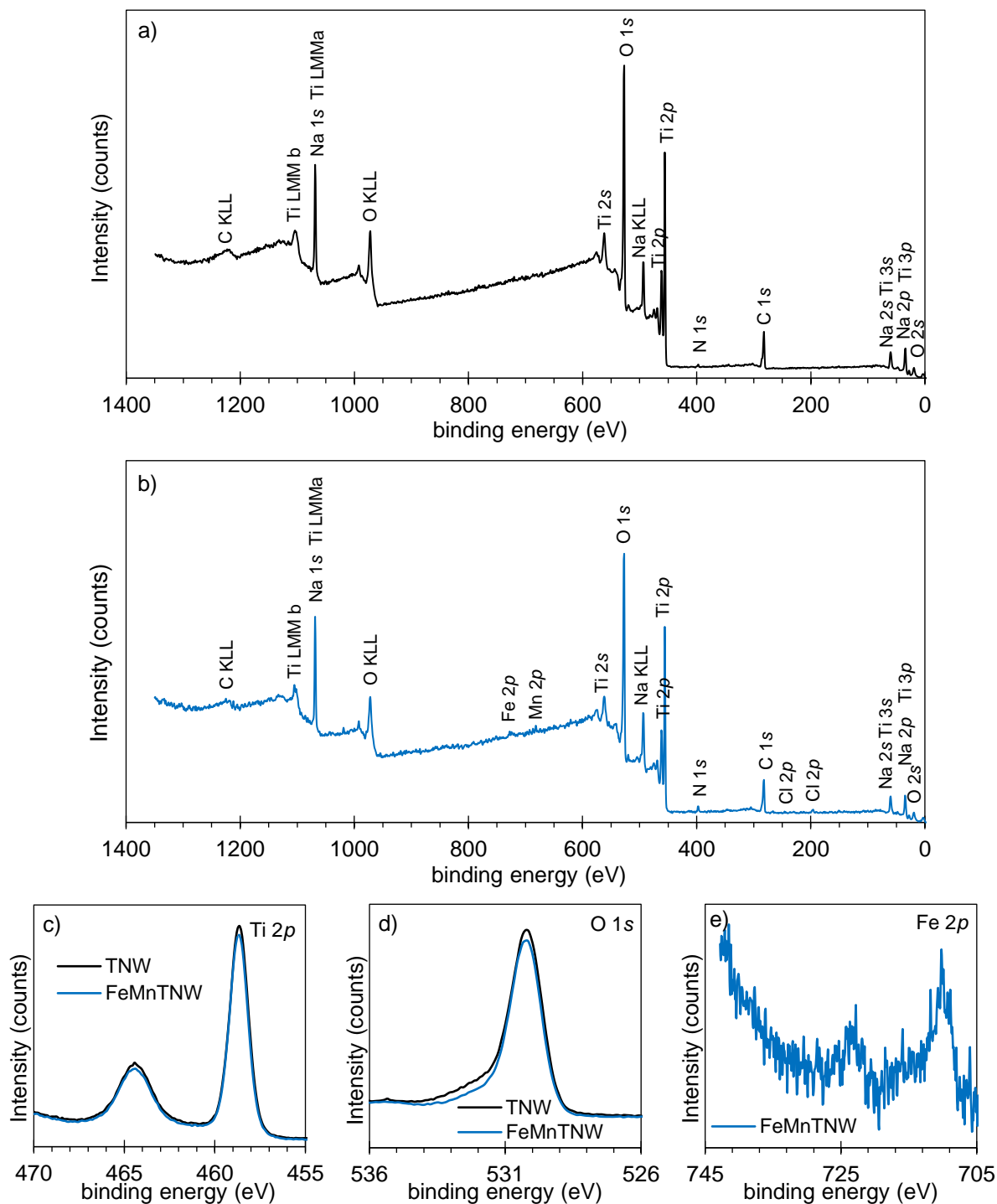


Figure 7.3 - XPS survey spectra of the (a) TNW and (b) FeMnTNW samples. High resolution spectra of the (c) Ti 2p, (d) O 1s and (e) Fe 2p.

The optical characterization of the powders was carried out by recording their diffuse reflectance spectra in the UV-vis-NIR range. Diffuse reflectance, R can be related to the absorption Kubelka–Munk function, F_{KM} [40]. The absorption spectra obtained for the prepared samples are present in Figure 7.4. As can be observed there are some alterations in the optical

behavior of the pristine TNW after Fe/Mn incorporation: a redshift on the absorption edge and a new absorption band centered at 550 nm appear.

From literature, a reduction in the semiconductor bandgap energy and a more efficient photo-generated charge carriers' separation, have been reported for Mn-doped TiO₂ nanotubes [41], and for TiO₂ nanoparticles doped with both Fe and Mn [42]. This has been attributed to the introduction, through metal incorporation, of intermediate energetic levels into the forbidden zone.

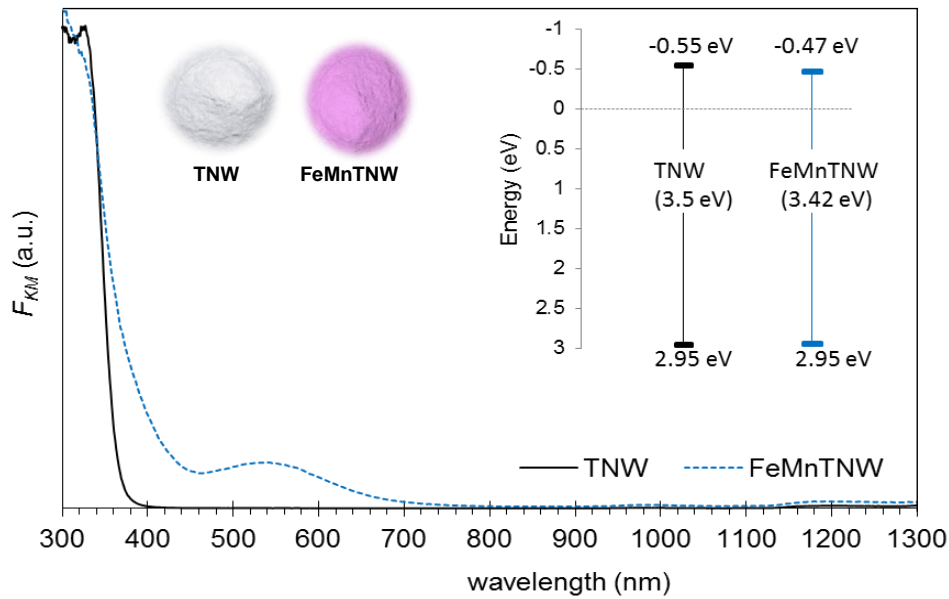


Figure 7.4 - Absorption spectra of the TNW and FeMnTNW samples. (Inset: energetic diagram with E_g , VB, and CB positions, for the prepared samples).

The narrowing effect observed on the absorption edge of the FeMnTNW sample can be attributed to the substitution of Na⁺ by Fe and/or Mn ions in the interlayers of the titanate structure. The absorption band located in the visible region between 440–540 nm, and reported by others [43,44], can be ascribed to $d-d$ transitions of transition metals, like Fe and Mn. As a result, there is an overlapping of the metals 3d orbitals within the forbidden band, thus extending the absorption edge into the visible region [44].

The optical bandgap energy (E_g) of the two samples was calculated using a procedure described [40]. The extrapolation of the linear part of the curve $f_{KM} = (F_{KM} \cdot h\nu)^{1/2}$ vs. $h\nu$ (Tauc plot) where h stands for Planck's constant and ν for the radiation frequency, to zero allows this calculation. E_g values of 3.50 and 3.42 eV were obtained for TNW and FeMnTNW samples respectively. As a consequence of Fe/Mn metals incorporation, a shift on the absorption edge, of about 0.80 eV, towards lower energies was observed. The energetic position of the VB (E_{VB}), for both samples, was determined using the valence band XPS spectra (Figure 7.5). The energy of the

corresponding conduction bands (E_{CB}) was calculated by the expression $E_{CB} = E_{VB} - E_g$ [32]. For more convenient analysis of these data, these values were schematically represented in the diagram shown in Figure 7.4. Although TNW and FeMnTNW have the same E_{VB} (2.95 eV) the two samples possess distinct bandgap energies (3.50 and 3.42 eV respectively) and consequently distinct E_{CB} . FeMnTNW is the sample possessing the relatively less energetic conduction band, -0.47 eV. Nevertheless, for both powders, the CB energy does not limit the O_2 reduction reaction, *via* photogenerated e^- .

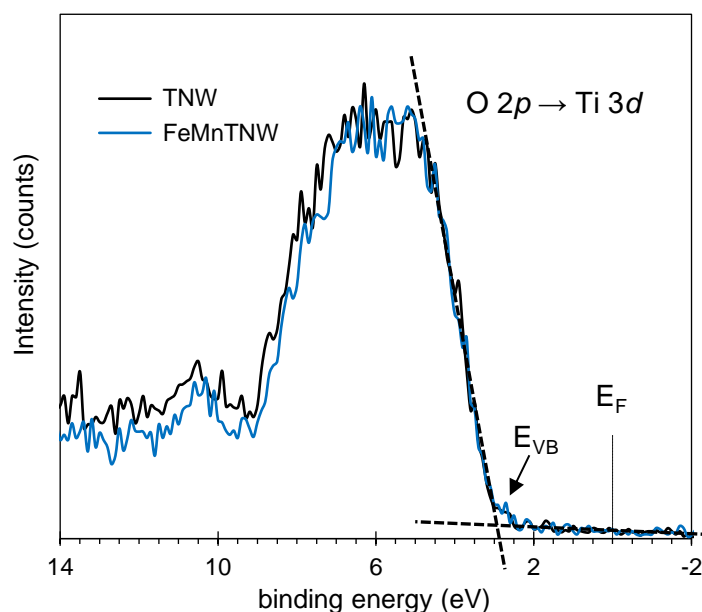


Figure 7.5 – XPS high resolution spectra of the O 2p to Ti 3d transition, used for valence band determination.

7.4 – Photocatalytic performance of the prepared samples

Considering the above promising results, the photocatalytic ability of the pristine and FeMnTNW modified sample for pollutants photocatalytic degradation was studied. A 20 ppm aqueous solution of caffeine was used here as a model pollutant. Previous to the photocatalytic experiments, the adsorption ability of each sample for caffeine was investigated. No significant adsorption was observed (less than 2.5%) for both solid/pollutant combinations.

7.4.1 - Hydroxyl radical production

The hydroxyl radical ($\cdot OH$) possesses one of the highest oxidizing power and it has been the main responsible for several pollutants photodegradation processes. Due to this, and to evaluate the photocatalytic ability of the prepared samples for photo-assisted oxidation processes, the catalytic production of hydroxyl radical ($\cdot OH$) was monitored.

The terephthalic acid (TA) was used as a probe molecule and the production of $\cdot\text{OH}$ was analyzed by fluorescence spectroscopy, *via* the detection of the hydroxylated reaction intermediates formed [31]. Figure 7.6 shows the amount of HTA produced after 20 minutes of TA/catalyst suspensions irradiation. Both TNW samples are catalytic for this process, with the FeMnTNW sample being the best one. Comparing the two catalysts performance, an increase of 39% on the photo-induced hydroxyl radical production was reached using FeMnTNW as a catalyst. Supported by these results, it can be concluded that the Fe/Mn doping leads to enhancement on the TNW photocatalytic performance for the hydroxyl photocatalytic production. These results are in agreement with published works, for which a catalytic activity enhancement is usually attributed to doped samples. However, this improvement is usually dependent on the dopant level; low metal incorporation levels usually leads to better catalytic performances [1,45-49].

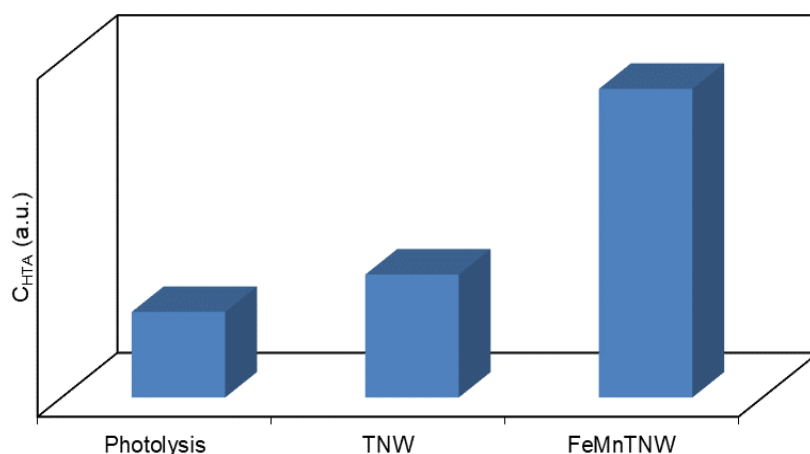


Figure 7.6 - HTA concentration after 20 min of irradiation of a TA solution (3 mM, 150 mL) using 20 mg of each sample as photocatalyst.

7.4.2 - Photoluminescence characterization

The photocatalytic activity of a material is not only related to its ability to absorb photons with energy higher than the bandgap energy but also with the ability to reduce the charge recombination rate. To evaluate the recombination rate of the electron-hole pairs in pristine and FeMn modified samples, the photoluminescence emission spectra were registered after excitation with 315 nm radiation. Figure 7.7 shows the PL spectra of TNW and FeMnTNW samples, within the wavelength range expected for the Ti $3d - \text{O } 2p$ transition. The decrease in the 425 nm peak intensity for the FeMnTNW sample, when compared to TNW, can be attributed to more efficient separation of the electron-hole pairs and consequently to a lower recombination rate [2,31].

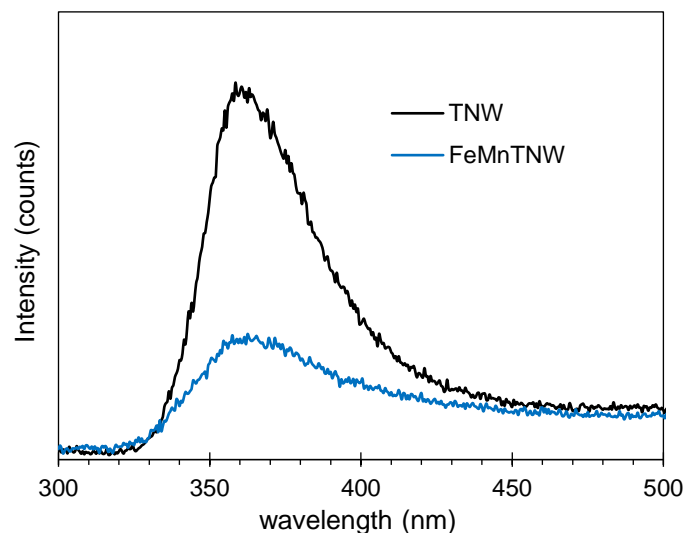


Figure 7.7 - Photoluminescence spectra of the TNW and FeMnTNW prepared samples.

7.4.3 - Caffeine photodegradation

The photocatalytic activity of the TNW and FeMnTNW samples was evaluated for a 20 ppm caffeine solution degradation during 75 min of irradiation (Figure 7.8). For comparative purposes, the pollutant photolysis was also performed.

As can be seen, no significant caffeine was adsorbed during 60 min in the dark and no differences were found using the TNW and FeMnTNW samples. Only ~2.5% of the initial caffeine was removed by adsorption using the two samples.

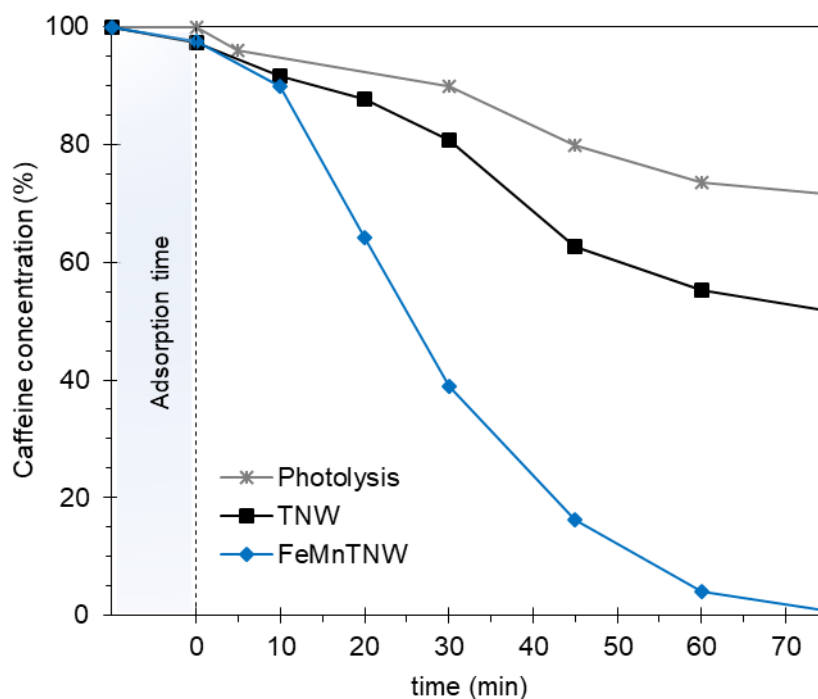


Figure 7.8 - Degradation profile of a 20 ppm caffeine solution during 75 min of irradiation using the prepared samples as photocatalyst.

As can also be seen, during irradiation, all the samples are catalytic for the photodegradation of this pollutant. After 75 min of irradiation, the caffeine degradation is practically complete using FeMnTNW as photocatalyst (99.3%) whereas only a reduction of 48.2% was attained using the pristine TNW.

The success of a catalyst in a pollutant degradation process should be evaluated by the amount and toxicity of the by-products produced and degraded during irradiation time. Often, the period required for the degradation of all the by-products formed is longer than the one required for the removal of the main pollutant. Therefore, the identification and quantification of the intermediates produced during 120 min of irradiation were carried out by LC-HR-ESI/MS and the results are presented in Table 7.1. The intermediates identified during irradiation, in the presence of the FeMnTNW catalyst and by photolysis, are in agreement with a degradation mechanism proposed in literature [50,51], presented in Annex B – Figure B.2. It has been proposed that the caffeine degradation, and independently on the oxidation conditions, starts with the initial attack of (photo) generated hydroxyl radicals on the C4=C5 double bond. This will result in the formation of N,N-dimethylparabanic acid (**CAF-1**) that is further oxidized to other intermediate products [52,53].

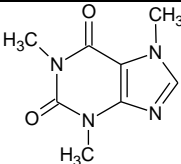
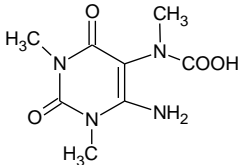
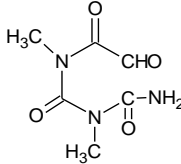
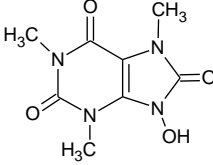
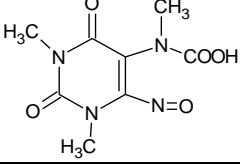
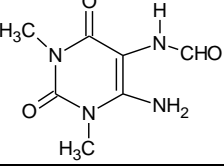
The time profile of the by-products detected is presented in Figure 7.9 where a sequential degradation process can be inferred for photolysis and using the FeMnTNW as a catalyst.

During photolysis (Figure 7.9(a)), and for the first minutes of irradiation, a high formation of compounds **CAF-1** and a reduced amount of **CAF-4**, together with a low amount of **CAF-2**. After 10 min a compound **CAF-3** appears and after 45 min, the compound **CAF-5** was found. After 120 min of irradiation, **CAF-1** compound has the highest concentration and there is a trace of all the other compounds in solution. During the 120 min of irradiation, **CAF-1** is always the by-product of higher concentration in solution. This was also observed when FeMnTNW was used as photocatalyst.

Distinct results were obtained when FeMnTNW as used as a catalyst (Figure 7.9(b)). It is important to emphasize that using this catalyst there was no significant formation of the intermediate compounds **CAF-3** to **CAF-5**. Furthermore, during the 120 min of irradiation, a considerably higher amount of **CAF-2** product was observed. The caffeine degradation starts with the production of the **CAF-1** and **CAF-2** compounds, and then by **CAF-4** compound in small amount, but only after 10 min of irradiation. After 60 min starts the formation of the **CAF-3** compound in a small amount and there is also a large amount of **CAF-1** in solution. After 75 min no more caffeine was detected in solution, but the presence of **CAF-1** and **CAF-2** was detected and the amount of **CAF-1** (74.4%) is still considerable. However, after 120 min

of irradiation, only two compounds are still in solution, **CAF-1**, and **CAF-2**, indicating that more time is required for the complete degradation of these caffeine by-products. It is interesting to note that, during photolysis was found five compounds (**CAF-1** - **CAF-5**) in solution and using the FeMnTNW as a catalyst only two compounds (**CAF-1** and **CAF-2**) still in solution, after 120 min of irradiation, indicating that more time is required for the complete degradation of these caffeine by-products. Supported by these results, it can be concluded that caffeine by-products degradation is more effective using FeMnTNW as catalyst.

Table 7.1 - Main fragments identified by LC-HR-ESI/MS and correspondent by-products formed during the photodegradation of caffeine using FeMnTNW as catalyst

Compound	Formula	Experimental mass (m/z)	Mol.wt.	Structure
Caffeine	$C_8H_{11}N_4O_2$	195.0876	194	
	$C_8H_{12}N_4O_4Na$	251.0751		
CAF-1	$C_7H_{10}N_3O_3$	184.0713	228	
	$C_5H_7N_2O_2$	127.0499		
CAF-2	$C_6H_9N_3O_4Na$	210.0485	187	
	$C_6H_8N_3O_3$	170.0560		
CAF-3	$C_8H_{11}N_4O_4$	227.0774	226	
	$C_8H_{10}N_4O_5Na$	265.0547		
CAF-4	$C_8H_9N_4O_4$	225.0620	242	
	$C_7H_{11}N_4O_3$	199.0824		
CAF-5	$C_5H_8N_3O_2$	142.0609	198	

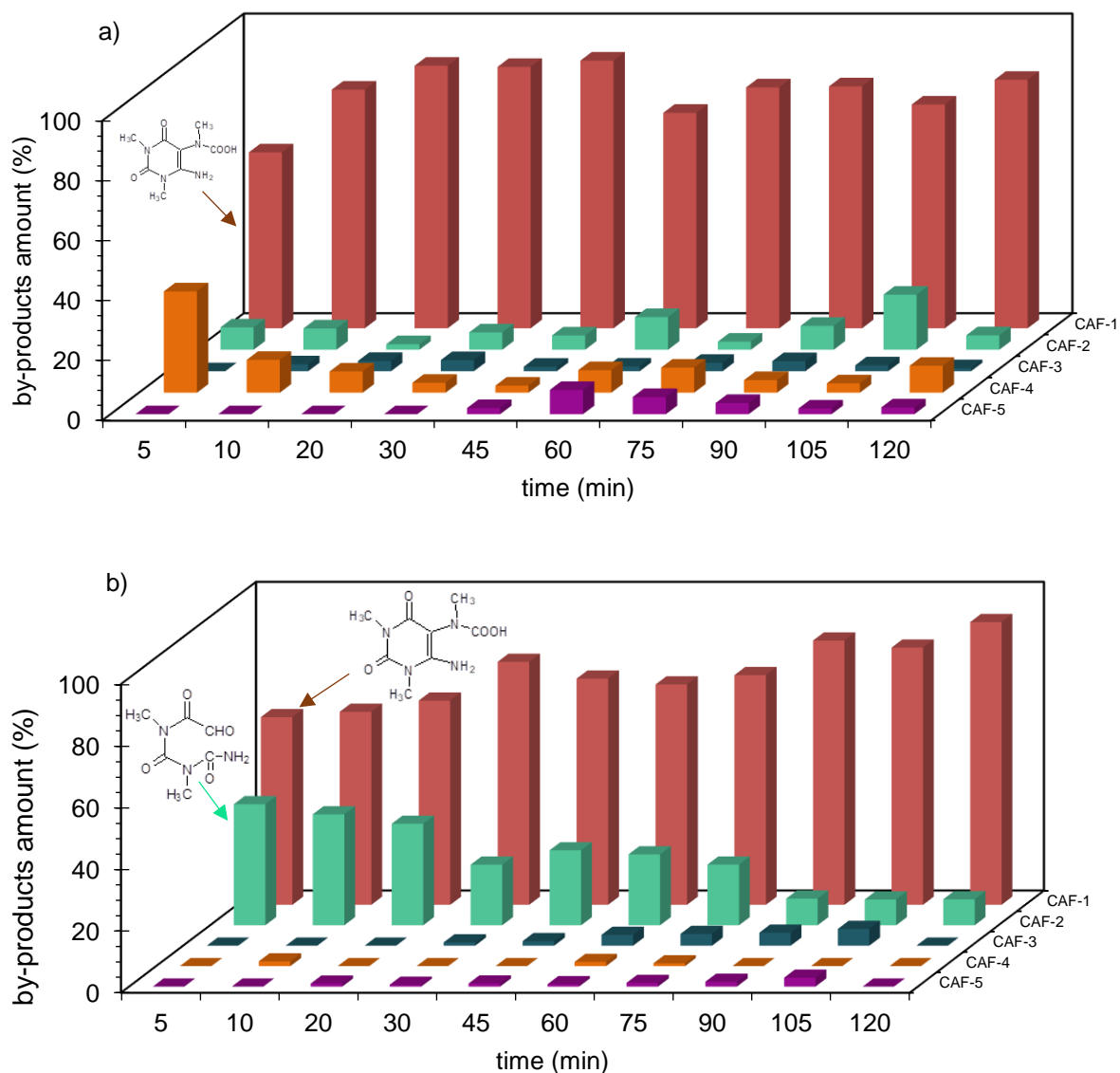


Figure 7.9 – Variation of intermediate products identified during 120 min of caffeine photodegradation, by (a) photolysis and (b) FeMnTNW as catalyst.

7.4.4 - Scavengers study

Aiming to elucidate the combined action of several oxidant radicals during the caffeine degradation process, several photo-assisted experiments were performed in the presence of specific scavengers (Figure 7.10). In distinct photodegradation runs, benzoquinone (BQ), ethanol (EtOH) and potassium oxalate (Ox) were added, as scavengers, to the caffeine solution. During 75 min of irradiation and using the best catalyst, FeMnTNW, the degradation of a 20 ppm caffeine solution containing 0.5 mM of each scavenger (0.1 mM for benzoquinone) was monitored. During this study, and once it is possible to have $\text{Fe}^{3+/2+}/\text{H}_2\text{O}_2$ in the system, special attention was done to the possibility of having a combination of photo and photo-Fenton

processes. Under these conditions, H_2O_2 should be *in situ* generated *via* superoxide radical reduction.

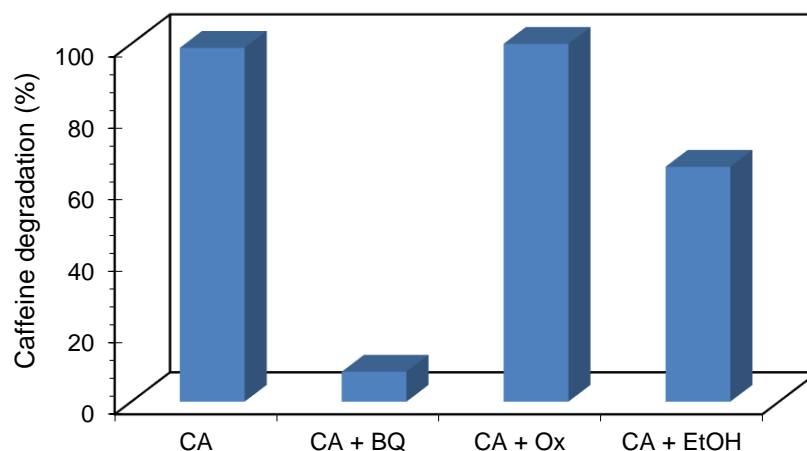


Figure 7.10 - Amount of caffeine degraded after 75 min under UV-vis radiation, in the presence of scavengers, BQ, Ox, and EtOH as radicals' scavengers, and using FeMnTNW as photocatalyst.

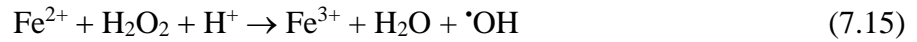
As can be observed in Figure 7.10, the presence of potassium oxalate, a well-known h^+ scavenger, during caffeine photocatalytic degradation it has no relevant effect in the pollutant removal process. This indicates that h^+ does not participate directly in the caffeine photo-oxidation.

On the other hand, the presence of ethanol, a recognized $\cdot\text{OH}$ scavenger, and of benzoquinone, used here as $\text{O}_2^{\cdot-}$ scavenger, demonstrated to influence caffeine photocatalytic degradation. From those, the most pronounced photodegradation suppression was observed when benzoquinone was added to caffeine solution. Supported by these results it is possible to conclude that the degradation of caffeine takes place *via* $\text{O}_2^{\cdot-}$ (or H_2O_2 by photo-Fenton reaction) and $\cdot\text{OH}$ radicals.

7.5 – Photo-activation mechanism proposal

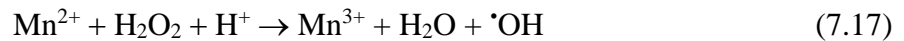
For titanate elongated materials, the valence band (VB) is derived primarily from O $2p$ levels and the conduction band (CB) from the Ti $3d$ levels. From the electronic characterization, it was possible to state that after Mn and Fe incorporation only a slight shift in the E_{CB} was observed. However, due to the energetic position of this band (-0.55 and -0.47 eV, for TNW and FeMnTNW respectively), no significant differences, in the oxidant radicals' photo-assisted production, were expected for both samples. Nevertheless, the existence of Mn and Fe within the TNW structure it should be relevant since they can contribute to the formation of intermediate energetic levels within the forbidden zone. These newly created levels can act as

electron or hole traps and thus they contribute to increasing the lifetime of the charge carriers. Besides, the formation of H_2O_2 during O_2 photo-reduction, combined with the $\text{Fe}^{3+}/\text{Fe}^{2+}$ redox reaction will create the ideal conditions to have a parallel photo-Fenton process, which will contribute for the formation of more $\cdot\text{OH}$ that will be responsible for the pollutant degradation enhancement [48]. In this particular situation, the photo-Fenton can be described as:



Together with the active role in the Fenton reaction, Fe^{3+} can act as both hole and electron traps [49] with a consequent reduction on the electron-hole recombination. In fact, Fe^{3+} can be reduced to Fe^{2+} by direct transfer of photogenerated electrons from CB. However, Fe^{2+} is fairly unstable due to the loss of d^5 electronic configuration and tends to return to the Fe^{3+} more stable configuration. As a consequence, Fe^{2+} could be further oxidized to Fe^{3+} , with the trapped e^- being transferred to the absorbed O_2 on the catalyst surface; and with Fe^{3+} acting as an effective electron trap. In addition, Fe^{3+} can also act as a hole trap due to the $\text{Fe}^{3+}/\text{Fe}^{4+}$ redox potential above the valence band edge (E_{VB}) of the FeMnTNW.

The presence of Mn^{2+} in the structure can also contribute to the improvement of the photo-assisted removal process. It has been reported that in Mn doped oxides, the intermediate levels formed by Mn-3d orbital in the forbidden zone, appears below the CB contributing not only to decrease electron transfer energy but also to suppress the carrier recombination [54]. Mn^{2+} has been described as an efficient superoxide anion scavenger [55]. In addition, and together with Fe^{2+} , Mn^{2+} can also possess a catalytic active role in the photo-Fenton process [56]. The main mechanism of the Mn^{2+} actuation can be described as follows [48]:



Considering the above-discussed results and the literature [57,58], a mechanism proposed for the light-activated charge-transfer process for TNW and FeMnTNW is presented in Figure 7.11.

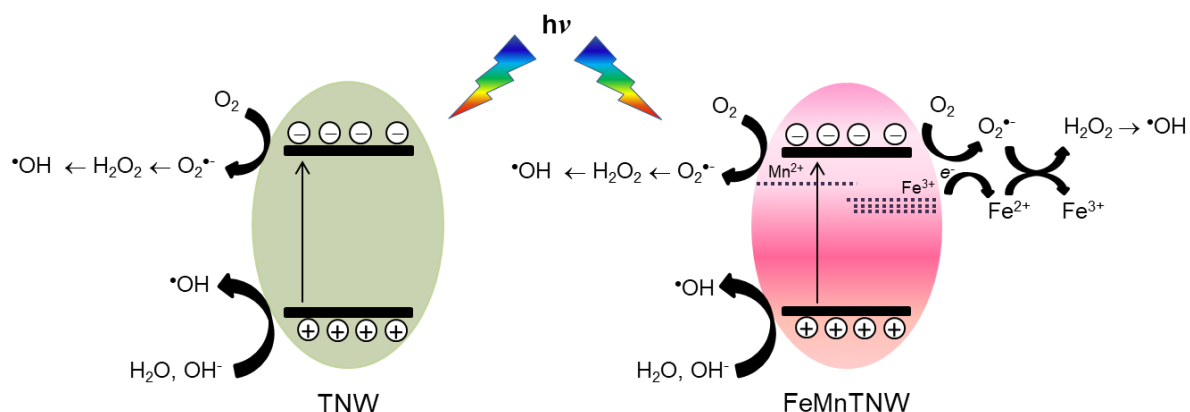


Figure 7.11 - Mechanism proposal for charge-transfer processes for TNW and FeMnTNW samples, when irradiated with UV-vis light.

Through a series of redox reactions described above, several charged species and radicals with high redox potentials are generated. These high oxidant species will further oxidize the organic molecule of caffeine, leading to the formation of intermediates, and finally to their complete mineralization.

7.5.1 - FeMnTNW photocatalytic reusability and stability

To better evaluate the catalytic ability of the FeMnTNW to be used as a photocatalyst, his (photo)chemical stability and recycling possibility were analyzed for four consecutive caffeine degradation runs. The results indicate no loss of photocatalytic performance for caffeine degradation. The final solutions were all of them analyzed by atomic absorption spectroscopy (AAS) and neither Fe nor Mn were detected. To better evaluate the catalyst stability, after the successive photodegradation assays, the solid was collected and analyzed by XRD and no differences were observed (Figure 7.12). These data indicate that the photocatalyst is stable under UV-vis irradiation and it can be used for consecutive runs.

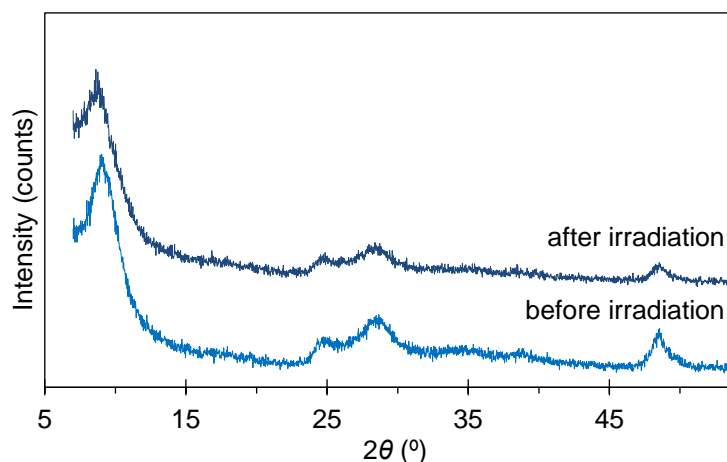


Figure 7.12 - XRD patterns of the FeMnTNW before and after submitted to four consecutive photocatalytic experiments.

7.6 – Conclusions

In this work, distinct titanate nanowires (TNW) materials were obtained when two different commercial titanium sources were used. These two sources of Ti are distinguished due to the existence of vestigial amounts of Mn (8.1 ppm) and Fe (4.3 ppm) in one of them. The incorporation of these metals traces in the TNW structure during synthesis resulted in the production of new co-doped material, FeMnTNW. The pristine and modified samples were structural, morphological and optical characterized. The results indicate that both Mn and Fe were incorporated in the TNW structure by replacement of Na^+ in the interlayers, together with some Ti^{4+} substitution. This result seems to agree with the hypothesis that during the hydrothermal process the precursor is dissolved before the formation of the TNW sheets. Consequently, some ionic manganese and/or iron remain afterward in solution and thus leading to the formation of FeMnTNW sample with Mn and/or Fe in two distinct positions. The potential of these materials to be used as photocatalysts for pollutants photocatalytic degradation was investigated for the photo-assisted hydroxyl radical formation (*via* terephthalic acid degradation) and caffeine degradation. The photocatalytic behavior of the FeMnTNW sample was mainly linked with a recombination rate reduction of the photogenerated electron–hole pairs, due to the introduction of intermediate energetic levels in the forbidden zone, as a result of the presence of ionic Mn and Fe species. Besides, the formation of H_2O_2 during O_2 photo-reduction, combined with the $\text{Fe}^{3+}/\text{Fe}^{2+}$ redox reaction will create the ideal conditions to have a parallel photo-Fenton process, contributing to the pollutant degradation enhancement. The Mn^{2+} together with Fe^{2+} can also possess a catalytic active role in the photo-Fenton process, due to the formation of $\cdot\text{OH}$ radicals. Through a series of redox reactions, several charged species and radicals with high redox potentials are generated. These highly oxidant species will further oxidize the organic molecules of caffeine and leading to the formation of intermediates, and finally to their complete mineralization. Considering all the results, a mechanism for the charge-transfer processes on the photoactivated FeMnTNW sample was proposed, based on the creation of mid-band levels in the forbidden zone.

7.7 - References

1 - B. Barrocas, A.J. Silvestre, A.G. Rolo, O.C. Monteiro, The effect of ionic Co presence on the structural, optical and photocatalytic properties of modified cobalt–titanate nanotubes, *Phys. Chem. Chem. Phys.* 16 (2016) 18081-18093.

- 2 - B.T. Barrocas, M. Conceição Oliveira, H.I.S. Nogueira, S. Fateixa, O.C. Monteiro, Ruthenium-modified titanate nanowires for the photocatalytic oxidative removal of organic pollutants from water, *ACS Applied Nano Mat.* 2 (2019) 1341-1349.
- 3 - K. Song, X. Han, G. Shao, Electronic properties of rutile TiO₂ doped with 4*d* transition metals: first-principles study, *J. Alloys Compd.* 551 (2013) 118-124.
- 4 - Ö. Kerkez-Kuyumcu, E. Kibar, K. Dayıoglu, F. Gedik, A.N. Akın, Ş. Özkara-Aydınoglu, A comparative study for removal of different dyes over M/TiO₂ (M = Cu, Ni, Co, Fe, Mn and Cr) photocatalysts under visible light irradiation, *J. Photochem. Photobio. A* 311 (2015) 176-185.
- 5 - M.Y. Xing, J.L. Zhang, F. Chen, Photocatalytic performance of N-doped TiO₂ adsorbed with Fe³⁺ ions under visible light by a redox treatment, *J. Phys. Chem. C.* 113 (2009) 12848-12853.
- 6 - L. Duan, N. Jiang, N. Lu, K. Shang, J. Lib, Y. Wu, Synergetic effect of TiO₂ and Fe³⁺ as co-catalysts for enhanced phenol degradation in pulsed discharge system, *Appl. Catal. B* 221 (2018) 521-529.
- 7 - M. Liu, X. Qiu, M. Miyauchi, K. Hashimoto, Energy-level matching of Fe(III) ions grafted at surface and doped in bulk for efficient visible-light photocatalysts, *J. Am. Chem. Soc.* 135 (2013) 10064-10072.
- 8 - X. Ding, X.G. Xu, Q. Chen, L.-M. Peng, Preparation and characterization of Fe-incorporated titanate nanotubes, *Nanotechnology* 17 (2006) 5423-5427.
- 9 - S. Sood, A. Umar, S.K. Mehta, S.K. Kansal, Highly effective Fe-doped TiO₂ nanoparticles photocatalysts for visible-light driven photocatalytic degradation of toxic organic compounds, *J. Colloid Interf. Sci.* 450 (2015) 213-223.
- 10 - A. Zaleska-Medynska, *Metal oxide-based photocatalysis: Fundamentals and prospects for application*, Elsevier Publishing, 2018.
- 11 - V. Vamathevan, H. Tse, R. Amal, G. Low, S. McEvoy, Effects of Fe³⁺ and Ag⁺ ions on the photocatalytic degradation of sucrose in water, *Catal. Today* 68 (2001) 201-208.

- 12 - M.A.H.J.H. Fenton, Oxidation of tartaric acid in the presence of iron. *J. Chem. Soc. Trans.* 65 (1894) 899-910.
- 13 - M. Zhang, H. Dong, L. Zhao, D. Wang, D. Meng, A review on Fenton process for organic wastewater treatment based on optimization perspective, *Sci. Total Environ.* 670 (2019) 110-121.
- 14 - S. Giannakis, A review of the concepts, recent advances and niche applications of the (photo) Fenton process, beyond water/wastewater treatment: Surface functionalization, biomass treatment, combatting cancer and other medical uses, *Appl. Catal., B* 248 (2019) 309-319.
- 15 - A.M. Díez, M.A. Sanromán, M. Pazos, Fenton-based processes for the regeneration of catalytic adsorbents, *Catal. Today* 313 (2018) 122-127.
- 16 - L. Wang, X. Zhang, P. Zhang, Z. Cao, J. Hu, Photoelectric conversion performances of Mn doped TiO₂ under > 420 nm visible light irradiation, *J. Saudi Chem. Soc.* 19 (2015) 595-601.
- 17 - L. Wang, J. Fan, Z. Cao, Y. Zheng, Z. Yao, G. Shao, J. Hu, Fabrication of predominantly Mn⁴⁺-doped TiO₂ nanoparticles under equilibrium conditions and their application as visible-light photocatalysts, *Chem. Asian J.* 9 (2014) 1904-1912.
- 18 - S.C.A. Sousa, J.C. Cardoso, O.C. Monteiro, Improved performance of titanate nanostructures for manganese adsorption and posterior pollutants photocatalytic degradation, *J. Photochem. Photobiol. A* 378 (2019) 9-16.
- 19 - Y. Sheng, I.A. Abreu, D.E. Cabelli, M.J. Maroney, A.-F. Miller, M. Teixeira, J.S. Valentine, Superoxide dismutases and superoxide reductases, *Chem. Rev.* 114 (2014) 3854-3918.
- 20 - P. Failli, D. Bani, A. Bencini, M. Cantore, L.D. Cesare Mannelli, C. Ghelardini, C. Giorgi, M. Innocenti, F. Rugi, A. Spepi, R. Udisti, B. Valtancoli, A novel manganese complex effective as superoxide anion scavenger and therapeutic agent against cell and tissue oxidative injury, *J. Med. Chem.* 52 (2009) 7273-7283.

- 21 - Y. Chen, S. Yang, K. Wang, L. Lou, Role of primary active species and TiO₂ surface characteristic in UV-illuminated photodegradation of Acid Orange 7, *J. Photochem. Photobiol. A* 172 (2005) 47-54.
- 22 - M.R. Nunes, O.C. Monteiro, A.L. Castro, D.A. Vasconcelos, A.J. Silvestre, A New Chemical Route to Synthesise TM-Doped (TM = Co, Fe) TiO₂ Nanoparticles, *Eur. J. Inorg. Chem.* 6 (2008) 961-965.
- 23 - D.V. Bavykin, F.C. Walsh, Titanate and titania nanotubes: Synthesis, properties and applications, RSC Publishing, Cambridge, UK, 2010.
- 24 - B. Barrocas, M.C. Neves, M. Conceição Oliveira, O.C. Monteiro, Enhanced photocatalytic degradation of psychoactive substances using amine modified elongated titanate nanostructures, *Environ. Science: Nano* 5 (2018) 350-361.
- 25 - H. Liu, D. Yang, E.R. Waclawik, X. Ke, Z. Zheng, H. Zhu, R.L. Frost, A Raman spectroscopic study on the active site of sodium cations in the structure of Na₂Ti₃O₇ during the adsorption of Sr²⁺ and Ba²⁺ cations, *J. Raman Spectrosc.* 41 (2010) 1792-1796.
- 26 - H.-H. Ou, C.-H. Liao, Y.-H. Liou, J.-H. Hong, S.-L. Lo, Photocatalytic oxidation of aqueous ammonia over microwave-induced titanate nanotubes, *Environ. Sci. Technol.* 42 (2008) 4507-4512.
- 27 - V. Bem, M.C. Neves, M.R. Nunes, A.J. Silvestre, O.C. Monteiro, Influence of the sodium/proton replacement on the structural, morphological and photocatalytic properties of titanate nanotubes, *J. Photochem. Photobiol. A* 232 (2012) 50-56.
- 28 - F. Dong, W. Zhao, Z. Wu, Characterization and photocatalytic activities of C, N and S co-doped TiO₂ with 1D nanostructure prepared by the nano-confinement effect, *Nanotechnology* 19 (2008) 365607-365617.
- 29 - V.C. Ferreira, O.C. Monteiro, New hybrid titanate elongated nanostructures through organic dye molecules sensitization, *J. Nanopart. Res.* 15 (2013) 1923-1938.
- 30 - J. Kielland, Individual activity coefficients of ions in aqueous solutions, *J. Am. Chem. Soc.* 59 (1937) 1675-1678.

- 31 - B. Barrocas, T.J. Entradas, C.D. Nunes, O.C. Monteiro, Titanate nanofibers sensitized with ZnS and Ag₂S nanoparticles as novel photocatalysts for phenol removal, *Appl. Catal. B* 218 (2017) 709-720.
- 32 - T.-D. Nguyen-Phan, S. Luo, D. Vovchok, J. Llorca, S. Sallis, S. Kattel, W. Xu, L.F.J. Piper, D.E. Polyansky, S.D. Senanayake, D.J. Stacchiola, J.A. Rodriguez, Three-dimensional ruthenium-doped TiO₂ sea urchins for enhanced visible-light-responsive H₂ production, *Phys. Chem. Chem. Phys.* 18 (2016) 15972-15979.
- 33 - P. Finetti, F. Sedona, G.A. Rizzi, U. Mick, F. Sutara, M. Svec, V. Matolin, K. Schierbaum, G. Granozzi, Core and valence band photoemission spectroscopy of well-ordered ultrathin TiO_x films on Pt(111), *J. Phys. Chem. C* 111 (2007) 869-876.
- 34 - A.A. Rempel, E.A. Kozlova, T.I. Gorbunova, S.V. Cherepanova, E.Yu. Gerasimov, N.S. Kozhevnikova, A.A. Valeeva, E.Yu. Korovin, V.V. Kaichev, Yu.A. Shchipunov, Synthesis and solar light catalytic properties of titania–cadmium sulfide hybrid nanostructures, *Catal. Commun.* 68 (2015) 61-66.
- 35 - T.-D. Pham, B.-K. Lee, feasibility of silver doped TiO₂/glass fiber photocatalyst under visible irradiation as an indoor air germicide, *Int. J. Environ. Res. Public Health* 11 (2014) 3271-3288.
- 36 - X. Chen, S.S. Mao, Titanium dioxide nanomaterials: Synthesis, properties, modifications, and applications, *Chem. Rev.* 107 (2007) 2891-2959.
- 37 - M. Mullet, V. Khare, C. Ruby, XPS study of Fe(II)-Fe(III) (oxy)hydroxycarbonate green rust compounds, *Surf. Interface Anal.* 40 (2010) 323-328.
- 38 - T. Yamashita, P. Hayes, Analysis of XPS spectra of Fe²⁺ and Fe³⁺ ions in oxide materials, *Appl. Surf. Sci.* 254 (2008) 2441-2449.
- 39 - S. Wang, S. Zheng, Z. Wang, W. Cui, H. Zhang, L. Yang, Y. Zhang, P. Li, Superior lithium adsorption and required magnetic separation behavior of iron-doped lithium ion-sieves, *Chem. Eng. J.* 332 (2018) 160-168.

- 40 - G. Kortuem, Reflectance spectroscopy: Principles, methods and applications. Springer-Verlag, New York 1969.
- 41 - Z. Xu, C. Li, W. Li, N. Fu, G. Zhang, Facile synthesis of Mn-doped TiO₂ nanotubes with enhanced visible light photocatalytic activity, *J. Appl. Electrochem.* 48 (2018) 1197-1203.
- 42 - G. Shao, Red shift in manganese- and iron-doped TiO₂: A DFT+*U* analysis, *J. Phys. Chem. C* 113 (2009) 6800-6808.
- 43 - A. Garg, A. Singh, V.K. Sangal, P.K. Bajpai, N. Garg, Synthesis, characterization and anticancer activities of metal ions Fe and Cu doped and co-doped TiO₂, *New J. Chem.* 41 (2017) 9931-9937.
- 44 - E. Morgado Jr., B.A. Marinkovic, P.M. Jardim, M.A.S. de Abreu, M.G.C. Rocha, P. Bargiela, Studies on Fe-modified nanostructured trititanates, *Mater. Chem. Phys.* 126 (2011) 118-127.
- 45 - W. Choi, A. Termin, M.R. Hoffmann, The role of metal ion dopants in quantum-sized TiO₂: correlation between photoreactivity and charge carrier recombination dynamics, *J. Phys. Chem.* 98 (1994) 13669-13679.
- 46 - Z.J. Zhang, C.-C. Wang, R. Zakaria, J.Y. Ying, Role of particle size in nanocrystalline TiO₂-based photocatalysts, *Phys. Chem. B* 102 (1998) 10871-10878.
- 47 - J. Zhou, Y. Zhang, X.S. Zhao, A.K. Ray, Photodegradation of benzoic acid over metal-doped TiO₂, *Ind. Eng. Chem. Res.* 45 (2006) 3503-3511.
- 48 - N. Wang, T. Zheng, G. Zhang, P. Wang, A review on Fenton-like processes for organic wastewater treatment, *J. Environ. Chem. Eng.* 4 (2016) 762-787.
- 49 - J. Zhu, W. Zheng, Bin He, J. Zhang, M. Anpo, Characterization of Fe-TiO₂ photocatalysts synthesized by hydrothermal method and their photocatalytic reactivity for photodegradation of XRG dye diluted in water, *J. Mol. Catal. A: Chem.* 216 (2004) 35-43.
- 50 - R. Rosal, A. Rodríguez, J.A. Perdigón-Melón, A. Petre, E. García-Calvo, M.J. Gómez, A. Agüera, A.R. Fernández-Alba, Degradation of caffeine and identification of the transformation products generated by ozonation, *Chemosphere* 74 (2009) 825-831.

- 51 - F. Qi, W. Chu, B. Xu, Catalytic degradation of caffeine in aqueous solutions by cobalt-MCM41 activation of peroxymonosulfate, *Appl. Catal. B* 134-135 (2013) 324-332.
- 52 - I. Dalmázio, L.S. Santos, R.P. Lopes, M.N. Eberlin, R. Augusti, Advanced oxidation of caffeine in water: On-line and real-time monitoring by electrospray ionization mass spectrometry, *Environ. Sci. Technol.* 39 (2005) 5982-5988.
- 53 - L.-C. Chuang, C.-H. Luo, S.-W. Huang, Y.-C. Wu, Y.-C. Huang, photocatalytic degradation mechanism and kinetics of caffeine in aqueous suspension of nano-TiO₂, *Adv. Mat. Res.* 214 (2011) 97-102.
- 54 - Y.F. Zhao, C. Li, S. Lu, R.X. Liu, J.Y. Hu, Y.Y. Gong, L.Y. Niu, Electronic, optical and photocatalytic behaviour of Mn, N doped and co-doped TiO₂: Experiment and simulation, *J. Solid State Chem.* 235 (2016) 160-168.
- 55 - K.-L. Fong, P.B. McCay, J.L. Poyer, H.P. Misra, B.B. Keele, Evidence for superoxide-dependent reduction of Fe³⁺ and its role in enzyme-generated hydroxyl radical formation, *Chem. Biol. Interact.* 15 (1976) 77-89.
- 56 - J. Zhao, J.J. Yang, J. Ma, Mn(II)-enhanced oxidation of benzoic acid by Fe(III)/H₂O₂ system, *Chem. Eng. J.* 239 (2014) 171-177.
- 57 - J.O. Carneiro, S. Azevedo, F. Fernandes, E. Freitas, M. Pereira, C.J. Tavares, S. Lanceros-Méndez, V. Teixeira, Synthesis of iron-doped TiO₂ nanoparticles by ball-milling process: the influence of process parameters on the structural, optical, magnetic, and photocatalytic properties, *J. Mater. Sci.* 49 (2014) 7476-7488.
- 58 - J. Li, D. Ren, Z. Wu, C. Huang, H. Yang, Y. Chen, H. Yu, Visible-light-mediated antifungal bamboo based on Fe-doped TiO₂ thin films, *RSC Adv.*, 7 (2017) 55131-55140.

Chapter 8

Immobilization of cobalt and ruthenium modified titanate nanoparticles for photo(electro)catalytic applications

Chapter 8 – Immobilization of cobalt and ruthenium modified titanate nanoparticles for photo(electro)catalytic applications

8.1 - Introduction

Over the past several years, heterogeneous semiconductor photocatalysis has been extensively studied for water and wastewater treatment.

In general, the water treatment photoreactors employ powder-type photocatalysts that have high activity due to low mass transfer limitations between the pollutants and the photocatalyst. However, powder dispersion requires a post-filtration or centrifugation procedures for recovering the photocatalyst from treated water, which complicates the treatment setup [1]. Researchers have tried to develop alternatives to anchor particles onto support materials to avoid the need of a further separation step and to commercialize the process as a full-scale technology [2].

The most common methods used to prepare films of semiconductors include sol-gel process, pulsed laser deposition, anodization using a liquid phase to evaporation, ion beam techniques, chemical vapor deposition and direct current (DC) or a radio frequency (RF) magnetron sputtering [3-9]. The sputtering techniques have the disadvantage that the film deposited onto a substrate is amorphous and it needs a crystallization anneal to become crystalline, increasing the film preparation time. In the sputtering process, the surface of the substrate is critical to the quality of the deposited film. Surface features as small as a fraction of a micron can produce flawed material. In particular, sharp edges such as steps may result in discontinuities or fissures in the film surface [10]. Other disadvantages, for example, it is the poor adherence to the substrates, due to the material detachment from the substrate. Several other techniques can be used to obtain semiconductors thin films, such as spin-coating, drop-casting, chemical deposition, chemical solution deposition (CSD) and chemical vapor deposition (CVD), spray pyrolysis, electrodeposition, and anodization [11-16].

Some strategies involving the semiconductors' immobilization in porous supports such as silica, nanofibers, glass fibers, filters, and polymers, seem like interesting alternatives to be explored to attain a more efficient semiconductors recovery after use [17,18].

Recent research works reported a high efficiency for dyes photodegradation on TiO_2 , TiO_2/WO_3 and WO_3/TiO_2 thin films prepared by DC sputtering, being possible the reuse without loss of catalytic performance [1,19]. Yao *et al.* reported the preparation of titanate nanotubes (TNT) by RF sputtering of Ti on fluorine-doped tin oxide (FTO) substrates, followed by anodization [20]. After posterior modification with MoO_3 by electrodeposition, they have shown that the

coating of TNT with thin layers of MoO_3 offers a viable method for the fabrication of efficient electrochromic devices [20]. Ferreira *et al.* recently reported the successful attachment of semiconducting BiOCl and TiO_2 nanoparticles to cotton fibers by *in situ* approaches [18]. These modified cotton fibers showed catalytic activity in naphthol blue-black photodegradation and were reliable for at least six utilizations [18]. The synthesis of polythionine (PTN)/cobalt-doped titanate nanotubes (CoTNT) hybrid conducting films, using electropolymerization was also reported [21]. The authors show that the electroactivity of the thionine molecules after immobilization in the CoTNT surface is maintained and after electropolymerization, stable and electroactive CoTNT–PTN modified electrodes were obtained. This study allowed to conclude that it is possible to immobilize titanate nanostructures in polymer matrices [21]. Fedorczyk *et al.* reported the immobilization of Au nanoparticles in the poly(1,8-diaminocarbazole) (PDAC) film electrochemically deposited, with improved catalytic activity for 4-nitrophenol reduction [22]. Ferreira *et al.* proposed the attachment of noble metal nanoparticles (NPs) to conducting polymers (such as poly(3,4-ethylenedioxythiophene) (PEDOT)) and showed that PEDOT/Pt-NPs and PEDOT/Au-NPs have catalytic activity in hydrazine reduction reaction [23].

Aiming to expand the practical applicability of the modified titanate nanoparticles (TNP), prepared in the scope of this work, their immobilization/incorporation in electroactive films was studied. To do so, pristine and modified titanate nanostructures were supported on conducting polymers to build new hybrid electrocatalytic-based films. This was carried out by drop-casting method followed by electropolymerization of the monomer 1,8-diaminocarbazole, DAC, (Figure 8.1(a)) [24,25]. The structure of the polymer poly(1,8-diaminocarbazole) (PDAC), proposed by Fedorczyk *et al.* [26], is also depicted in Figure 8.1(b).

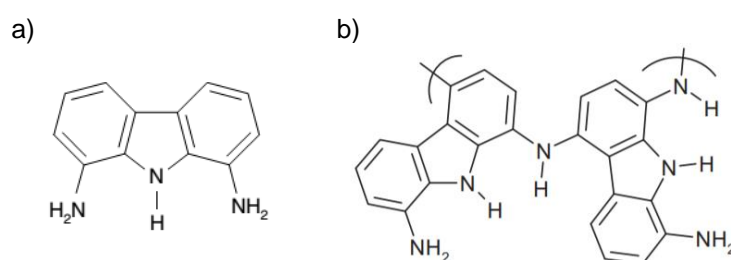


Figure 8.1 - Structural representation of (a) 1,8-diaminocarbazole monomer and (b) poly(1,8-diaminocarbazole).

The photo(electro)catalytic ability of the hybrid system to remove organic pollutants from aqueous media was studied using two model pollutants, methylene blue (MB) and theophylline (Figure 8.2), under UV-vis and visible radiation.

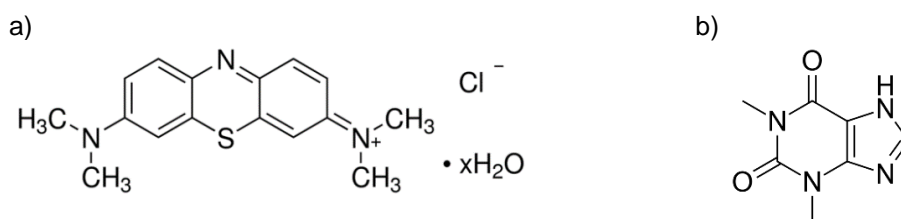


Figure 8.2 - Structural representation of (a) methylene blue and (b) theophylline molecules.

Methylene blue (MB) was chosen since this dye is widely used in different applications. MB is a bright-colored cationic thiazine dye that is extensively used in textile industries, beyond its use in biology and medicine, where it is commonly used in *in vivo* diagnosis, molecular imaging in oncology, and in image-guided surgery [27-29]. Theophylline (1,3-dimethylxanthine) was chosen because it is a pharmaceutical used to prevent and treat wheezing, shortness of breath, and chest tightness caused by asthma, chronic bronchitis, emphysema, and other lung diseases. It has also been described as a more toxic by-product of caffeine photodegradation (one of the most used drugs worldwide) present in coffee, tea, chocolate, soft drinks and pharmaceuticals [30,31].

In this chapter, studies on hybrid films preparation using different immobilization approaches are shown. The best conditions for TNP films preparation were first optimized and then, the most effective films were used for photo(electro)catalytic degradation tests. Here, the cobalt and ruthenium modified TNW and TNT powders were selected for the immobilization of conducting substrates. Then the catalytic performance of the obtained films was analyzed on the MB and theophylline photo(electro)degradation. The degradation experiments were performed under UV-vis and visible irradiation using a 450 W arc Xenon lamp, with and without a 400 nm cut-off filter. For convenience, this radiation was identified as visible_(Xe) and UV-vis_(Xe), respectively.

8.2 – Synthesis

Titanate elongated nanoparticles modified with cobalt and ruthenium were immobilized on conducting substrates (indium tin oxide (ITO)) using different methodologies, such as the drop-casting method and drop-casting followed by electropolymerization of 1,8-diaminocarbazole monomer (DAC). The obtained samples, by drop-casting method, were identified as pristine ITO/TNW and metal modified ITO/MTNW (M = Co and Ru). The conductive polymer, poly(1,8-diaminocarbazole) (PDAC), was deposited by electropolymerization, above the ITO/TNW films. These samples were identified as ITO/TNW/PDAC and ITO/MTNW/PDAC

(M = Co and Ru). The experimental procedure details are shown in Chapter 10 (Methods and experimental).

8.3 – Immobilization of cobalt and ruthenium modified TNW by drop-casting and electropolymerization - hybrid films preparation

Systematic studies were performed, to evaluate the best conditions for TNP immobilization and the highest photo(electro)activity of the ITO/TNP and ITO/TNP/PDAC films for pollutants removal. In this section, the TNW films were prepared by drop-casting (ITO/TNW), drop-casting followed by DAC electropolymerization (ITO/TNW/PDAC) and drop-casting followed by DAC electropolymerization layer-by-layer (ITO/(TNW/PDAC)_n, 1 ≤ n ≤ 4).

8.3.1 – Hybrid films preparation and optimization of the preparation conditions

As mentioned above different strategies were used for TNW immobilization. The drop-casting methodology allowed the immobilization of pristine and Co and Ru modified TNW on the ITO surface. After, the monomer 1,8-diaminocarbazole was electropolymerized into the ITO/TNW surface films. In Figure 8.3 are illustrated the typical voltammograms obtained for the PDAC deposition on the ITO/TNW modified electrodes, with 2 and 20 cycles at 60 mV s⁻¹, between -0.1 and 0.9 V vs. Ag/AgCl/Cl.

As can be seen in Figure 8.3(a) and similarly to that obtained for the growth of PDAC on ITO, the cyclic voltammograms exhibit an oxidation peak (A) at 0.70 V vs. Ag/AgCl/Cl, in the first scan, corresponding to the monomer oxidation, and in the reverse scan, a peak observed at 0.25 V (B') corresponds to the polymer reduction. In the second scan and following cycles, an oxidation peak is observed at 0.76 V (A) which can be assigned to the polymer oxidation and a redox couple (B/B') occurs at 0.37 and 0.24 V, respectively, which increases in intensity over the subsequent polymerization cycles (Figure 8.3(b)). This is characteristic of the doping-undoping of a growing polymeric film [24]. The current density of the PDAC oxidation and reduction peaks increases with the number of cycles, at least 20, indicating the formation of an electroactive and conducting film [24,32]. This result is similar to that observed for PDAC on Pt electrode reported by Skompska *et al.* [24], where it was shown that the presence of two electro-donating amino groups in DAC, it prevents irreversible overoxidation of the polymer film.

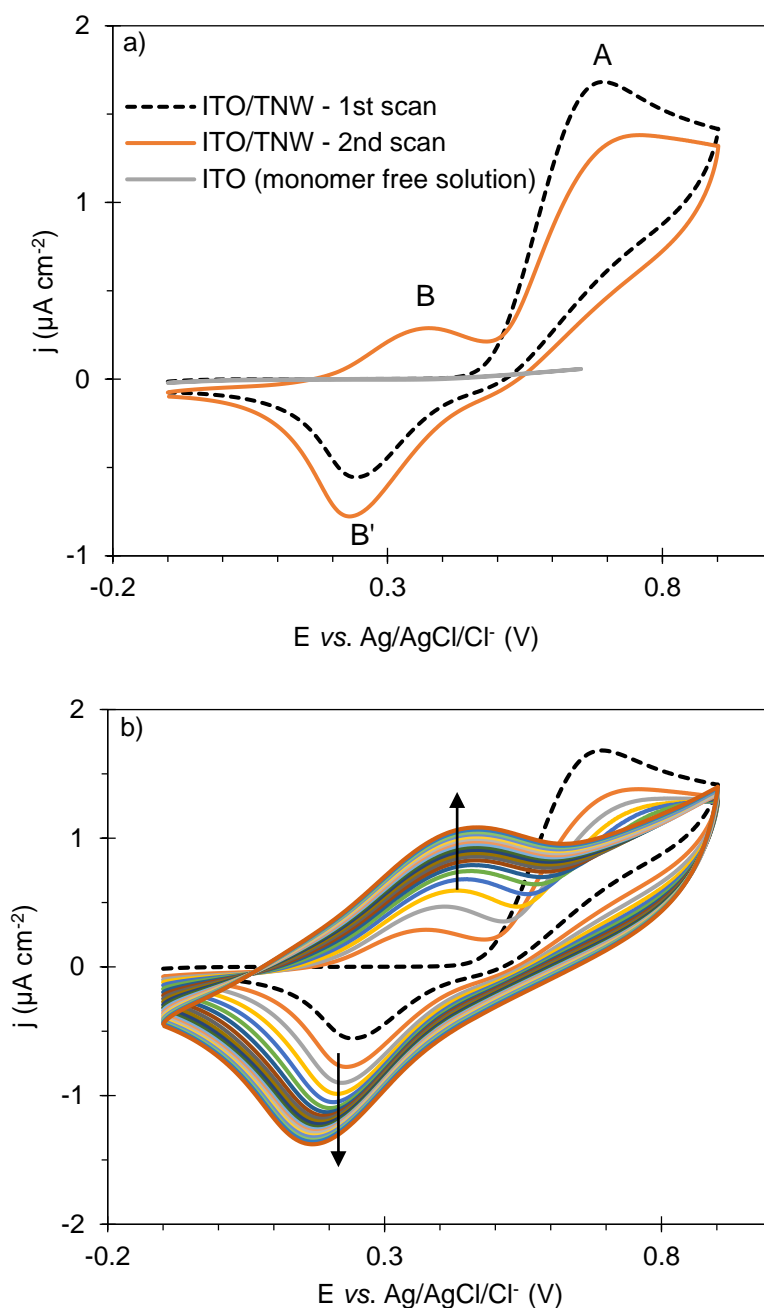


Figure 8.3 - Cyclic voltammograms of DAC electropolymerization on ITO/TNW modified electrode 2 mM DAC in 0.1 M LiClO₄/ACN; (a) cycles 1 and 2, (b) cycles 1 - 20 at 60 mV s⁻¹.

The data obtained during PDAC growth in ITO and ITO/TNW, ITO/CoTNW and ITO/RuTNW modified electrodes, including the current potentials of DAC oxidation peak (A) and redox couple (B/B') for all electrodes, are summarized in Table 8.1.

A positive 40 mV shift was observed for the DAC oxidation peak (A) in the first cycle for the ITO/TNW sample in comparison with the ITO electrode. The separation potential between the oxidation and reduction peaks of the polymer deposited on the TNW is very similar to that for PDAC formed directly on ITO, which means that the layer of TNW does not influence on the

polymer growth. However, for the ITO/CoTNW and ITO/RuTNW modified electrodes a higher separation potential was observed (Table 8.1). This can suggest that the layer of CoTNW and RuTNW influence more the polymer electroactivity, and due to that the shape of the CV obtained is more resistive (*i.e.* the peaks are more separated).

Table 8.1 – Current peak potentials (*vs.* Ag/AgCl/Cl⁻) and respective current densities for the DAC oxidation peak (A) and redox couple (B/B') on ITO, ITO/TNW, ITO/CoTNW, and ITO/RuTNW electrodes, evaluated from the voltammograms

		ITO	ITO/TNW	ITO/CoTNW	ITO/RuTNW
Peak		(V)			
1 st cycle	A	0.66	0.70	0.75	0.81
	B'	0.27	0.25	0.15	0.10
2 nd cycle	A	0.72	0.76	0.77	0.80
	B'	0.25	0.24	0.11	0.07
	B	0.43	0.37	0.50	0.38

After electropolymerization, stable and electroactive ITO/PDAC and nanostructured pristine (ITO/TNW/PDAC) and Co and Ru modified (ITO/CoTNW/PDAC and ITO/RuTNW/PDAC) electrodes were obtained. To illustrate this, in Figure 8.4 are presented the four successive CV obtained for the ITO/TNW/PDAC (selected sample).

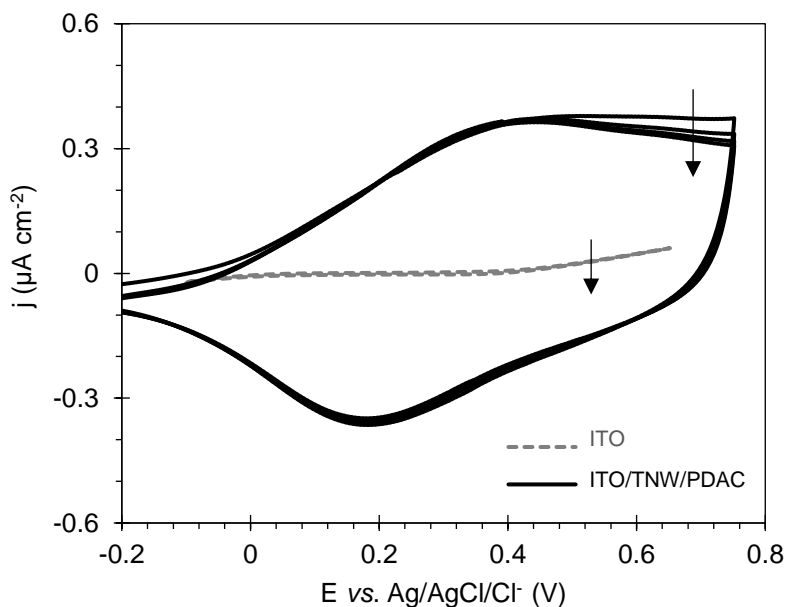


Figure 8.4 - Four successive cyclic voltammograms obtained in the solution of 0.1 M LiClO₄/acetonitrile at 60 mV s⁻¹, for the ITO (grey lines) and ITO/TNW/PDAC (black lines) films.

These results are in accordance with Skompska *et al.* [24] reported work. The symmetrical redox behavior of PDAC and relatively low potential of the oxidation peak, concerning to the monomer oxidation, suggests that the films consist of rather short polymer/oligomer chains. Furthermore, a higher density current intensity was observed for the titanate containing electrodes when compared with ITO/PDAC sample. This reflects the larger active surface area of the electrode when covered with TNW, CoTNW and RuTNW particles.

To study the influence of the number of polymerization scans on the catalytic activity of the films, photodegradation tests using UV-vis(λ_e) light and a 10 ppm MB solution were performed. For this study, samples prepared with 2 and 20 electropolymerization scans were tested. The obtained results are shown in Figure 8.5.

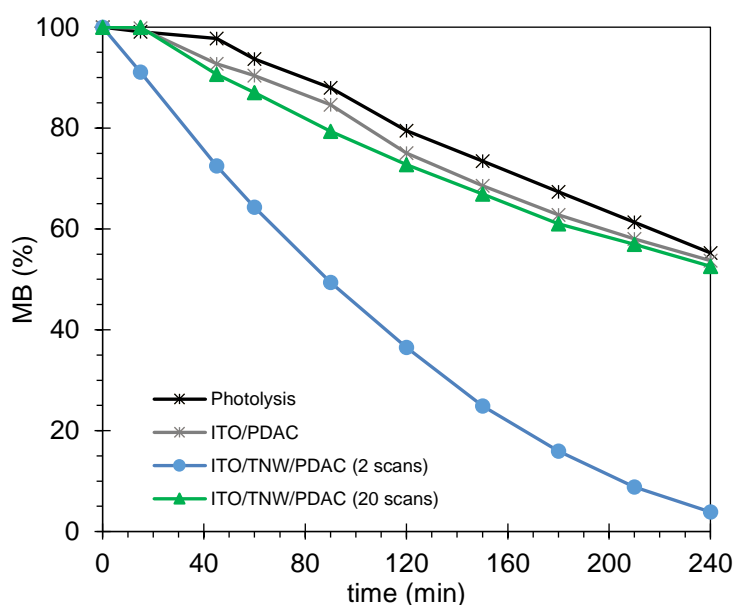


Figure 8.5 - MB degradation percentage evolution using ITO/PDAC, ITO/TNW/PDAC (2 scans) and ITO/TNW/PDAC (20 scans) films as photocatalysts, under UV-vis(λ_e) irradiation.

Both samples demonstrated photocatalytic activity for this process and after 240 min of irradiation, 96% and 47% of the initial MB were degraded, using ITO/TNW/PDAC (2 scans) and ITO/TNW/PDAC (20 scans) respectively. This difference in the degradation performance of both films can be due to the fact that the ITO/TNW/PDAC (20 scans) have a thicker polymer layer that completely covers the TNW particles, once the ITO/PDAC and ITO/TNW/PDAC (20 scans) catalytic performance is very similar. The thicker polymer layer contributes to the reduction of the TNW contact with the pollutant, decreasing the photocatalytic activity of the film. This result is in accordance with previous works with PDAC reported by Aragon *et al.* [33], where the authors showed that the sample with higher amount of polymer is notably less

effective in 4-chlorophenol photodegradation than the obtained after a single polymerization scan.

Therefore, after this analysis, it was concluded that the preparation of the samples only with 2 scans of electropolymerization is more recommended to obtain modified electrodes with higher photocatalytic activity. Therefore, films grown with 2 cycles were used for further studies.

The effect of the number of TNW/PDAC layers on the photocatalytic activity of the modified electrodes was also evaluated. The prepared samples were designated by ITO/(TNW/PDAC)_n ($1 \leq n \leq 4$), where n denotes the number of layers. For this study, PDAC layers were prepared by DAC electropolymerization with 2 scans.

The results obtained for the degradation of MB solution (10 ppm) using UV-vis(λ_{e}) radiation, showed that all ITO/(TNW/PDAC)_n films demonstrated photocatalytic activity for this degradation process. No significant differences were obtained using the ITO/TNW/PDAC samples prepared with a different number of layers. Identical results were obtained with the ITO/(CoTNW/PDAC)_n samples. This suggests that the upper TNW/PDAC layer is probably the only one that is active during the degradation process. Once no significant differences were observed in the photocatalytic activity with the increased number of layers, it was decided to prepare films with only one layer of TNW/PDAC or MTNW/PDAC ($M = \text{Co, Ru}$) prepared with 2 DAC electropolymerization scans.

8.3.2 – Cobalt and ruthenium modified ITO/TNW/PDAC films characterization

In this section is shown the optical, morphological and photo(electro)catalytic characterization of the pristine and metal modified ITO/MTNW and ITO/MTNW/PDAC ($M = \text{Co and Ru}$) films. The optical characterization of the films was performed by DRS. The optical spectra of ITO/PDAC, ITO/TNW, ITO/CoTNW, and ITO/RuTNW samples are shown in Figure 8.6.

In the absorption spectra presented in Figure 8.6(a), a slight blue shift of the absorption edge was observed for the ITO/RuTNW sample when compared with the pristine ITO/TNW sample. In contrast, for the ITO/CoTNW sample, a redshift was observed. These results are following the previous results for these materials presented in Chapters 4 and 5. The presence of Ru in TNW materials shifts the absorption to the blue should be due to the quantum size effects. For this sample, ITO/RuTNW, it is possible to see an absorption increase in the visible range, due to the $d-d$ transitions on the Ru^{4+} ions, as discussed in Chapter 5.

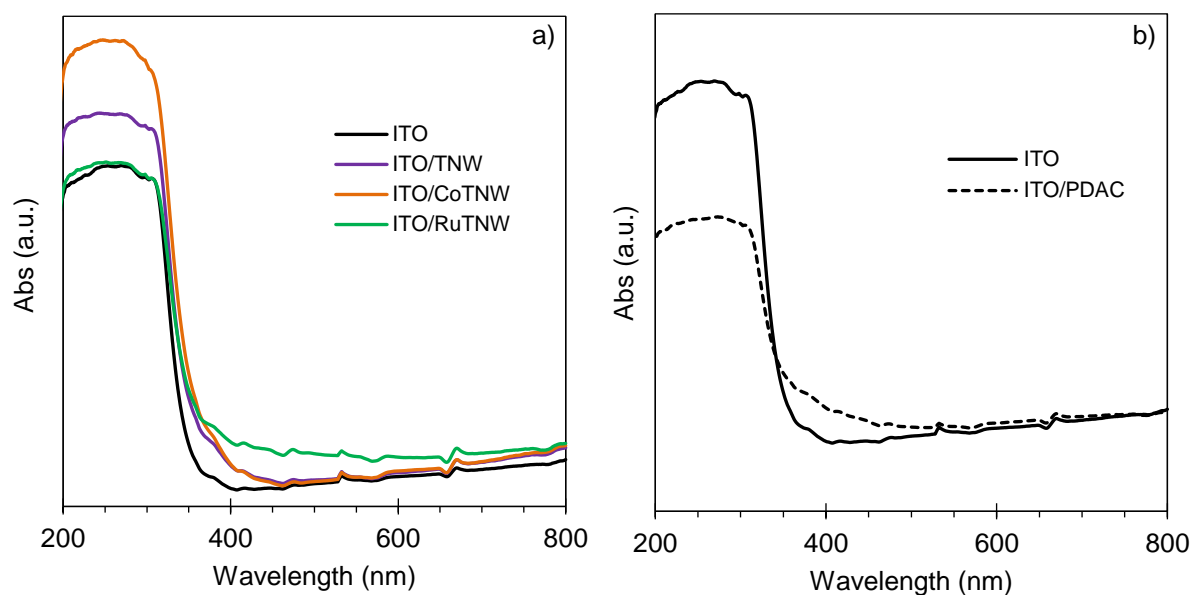


Figure 8.6 - Absorption spectra of the (a) ITO/TNW, ITO/CoTNW and ITO/RuTNW and (b) ITO, ITO/PDAC samples.

Comparing the absorption spectra presented in Figure 8.6(b), for ITO and ITO/PDAC films, a higher absorption after PDAC deposition was observed. ITO is also a semiconductor with absorption in the UV region at wavelength below 350 nm. Upon modification with PDAC its absorption in the visible range increases due to the contribution of the conductive polymer which displays a greyish color. This is in accordance with the reported work by Aragon *et al.* for PDAC films, indicating that this absorption increase in the UV-vis range in the wavelength around 500 nm to 450 nm is due to the electron transition from polaronic level in the oxidized polymer [33].

For the pristine ITO/TNW/PDAC and metal modified ITO/MTNW/PDAC ($M = \text{Co}$ and Ru) samples, an identical behavior was obtained, and no differences in the band edge of the titanates were observed after PDAC deposition. It is important to note that the deposition of the PDAC film on the ITO/TNW, ITO/CoTNW, and ITO/RuTNW surface did not change the absorption band edge of titanate nanowires, this may suggest that the semiconductor photoactivation of these films should not be influenced by the presence of the polymer film.

The morphological characterization of the modified films was performed by scanning electron microscopy (SEM). The obtained images for the selected films with and without PDAC (ITO, ITO/PDAC, ITO/TNW, ITO/TNW/PDAC, ITO/CoTNW, and ITO/CoTNW/PDAC samples) are depicted in Figure 8.7. As can be seen, no significant differences were observed in ITO surface morphology after PDAC deposition, suggesting that the polymer is very thin and smooth. Since pristine and modified TNW have identical morphology, no significant differences were expected in the SEM analysis of ITO/TNW, ITO/CoTNW, and ITO/RuTNW

samples. As observed in Figure 8.7 the morphology of these samples is similar, and no significant differences were found. Only a slight increase in the films' roughness was observed after the polymer growth.

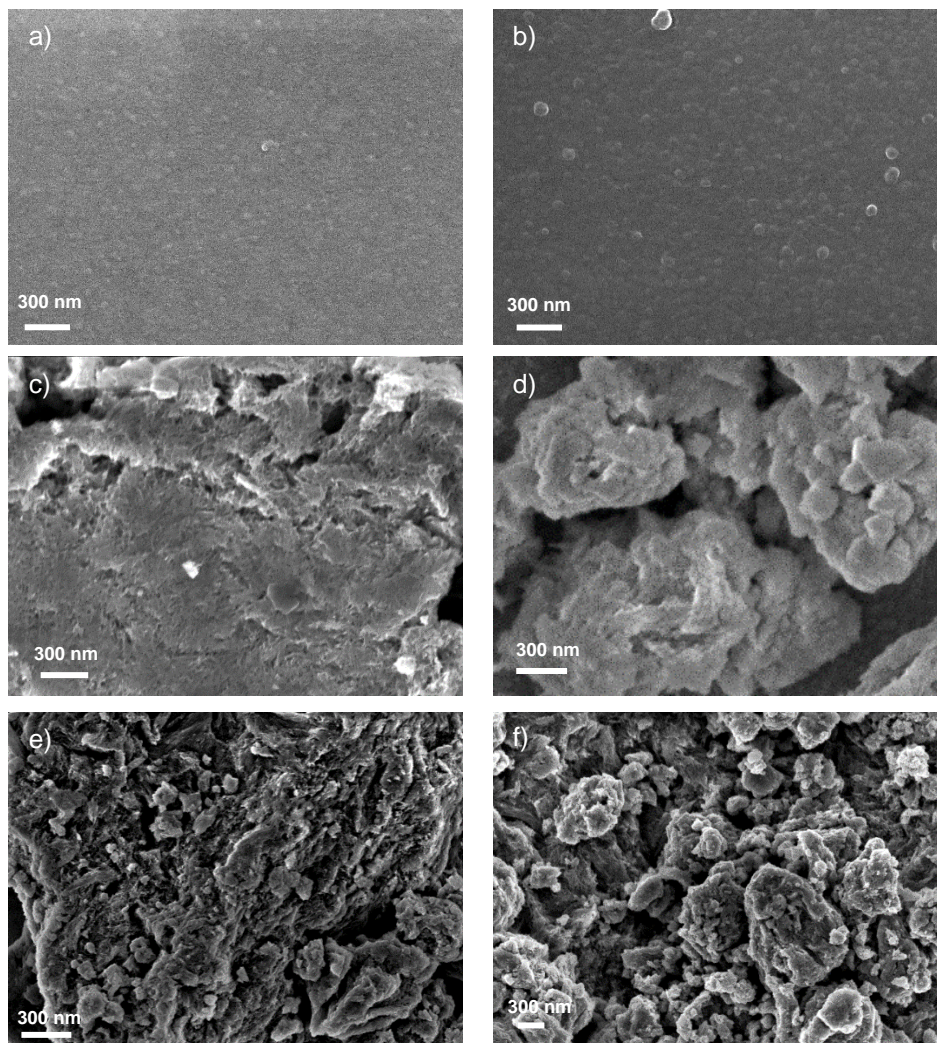


Figure 8.7 - SEM images of the (a) ITO, (b) ITO/PDAC, (c) ITO/TNW, (d) ITO/TNW/PDAC, (e) ITO/CoTNW and (f) ITO/CoTNW/PDAC films.

8.3.3 – Photocatalytic performance evaluation

The photocatalytic activity of the pristine ITO/TNW/PDAC and modified ITO/MTNW/PDAC ($M = \text{Co}, \text{Ru}$) films was evaluated on the degradation of a methylene blue aqueous solution (10 ppm) under UV-vis(Xe) radiation (Figure 8.8). As can be seen, the samples have a high dye adsorption ability. After the dark period of 60 min, 19%, 26% and 30% of the initial dye was removed from solution by adsorption, using ITO/TNW/PDAC, ITO/RuTNW/PDAC, and ITO/CoTNW/PDAC films, respectively. After turned on the light, all the films demonstrated to possess photocatalytic ability for MB degradation, once the adsorption equilibrium was achieved during the dark. ITO/RuTNW/PDAC film was the best catalyst for this degradation

process, with a total MB degradation within 60 min of UV-vis_(Xe) irradiation. More 15 min of irradiation were required to achieve the total MB degradation using the ITO/CoTNW/PDAC film as photocatalyst. It is important to note that after 75 min under UV-vis_(Xe) irradiation only 69% of MB were removed using the ITO/TNW/PDAC film as catalyst. Using the films without TNW particles (ITO/PDAC and ITO) and for the same period, only 43%, 31% of the MB were removed.

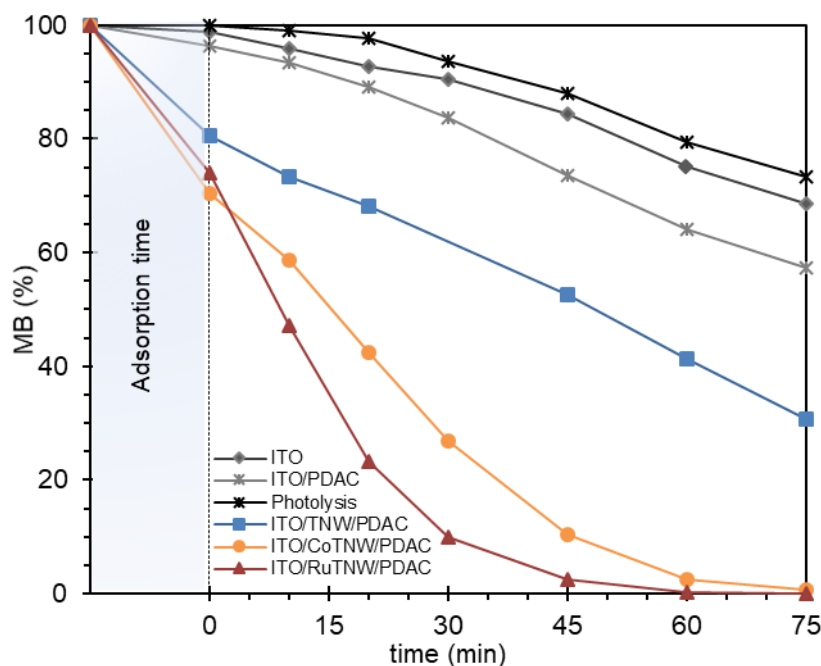


Figure 8.8 - MB photodegradation during 75 min of UV-vis_(Xe) irradiation using ITO/PDAC, ITO/TNW/PDAC, ITO/CoTNW/PDAC and ITO/RuTNW/PDAC films.

The possibility of catalyst recovery and reutilization in photodegradation processes is important since it can contribute significantly to the reduction of operational costs, making photocatalysis an attractive method for wastewater treatment. Furthermore, the catalyst photochemical stability is an important parameter that must be analyzed to better evaluate its catalytic performance with time. In this context, three successive MB photodegradation experiments were performed for the most promising samples, ITO/RuTNW/PDAC and ITO/CoTNW/PDAC, during 75 min of UV-vis_(Xe) irradiation. The obtained results showed that these samples have excellent catalytic performance associated with excellent photochemical stability since only 3% of the initial MB remains in solution after the third cycle. Moreover, this suggests that no catalyst was lost from the film surface. After the reutilization experiments, the films were analyzed by SEM, and no changes in the surface morphology were observed (results not shown).

To go further in this study, to analyze the photocatalytic activity of these hybrid films, the MB photodegradation was also performed under visible_(Xe) light irradiation. The photocatalytic activity of the pristine (ITO/TNW and ITO/TNW/PDAC) and metal modified ITO/MTNW and ITO/MTNW/PDAC (M = Ru, Co) films was tested on the degradation of MB aqueous solutions (10 ppm) during 120 min under visible_(Xe) irradiation (Figure 8.9).

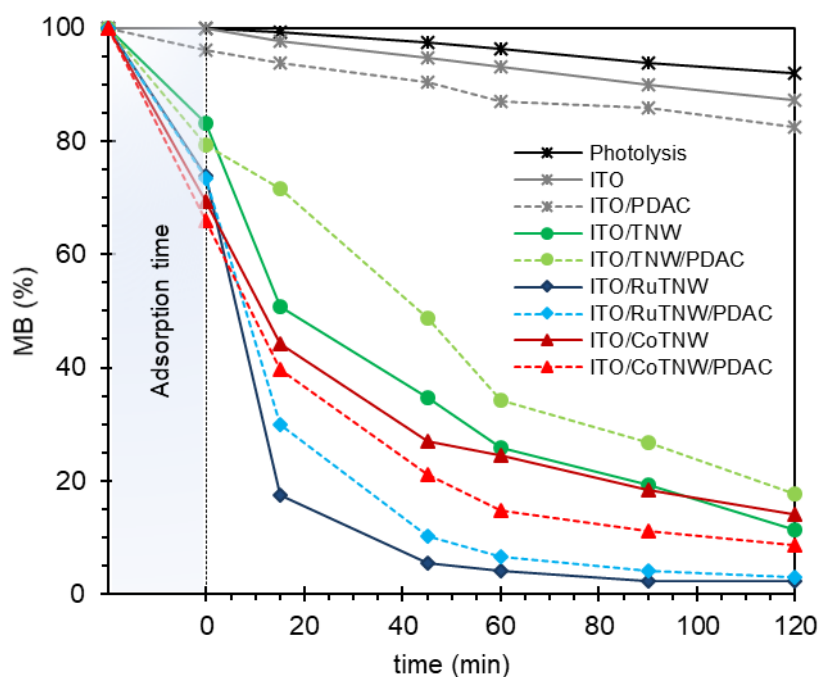


Figure 8.9 - MB photodegradation during 120 min of visible_(Xe) irradiation using ITO/PDAC, ITO/TNW, ITO/CoTNW, ITO/RuTNW, ITO/TNW/PDAC, ITO/CoTNW/PDAC and ITO/RuTNW/PDAC samples.

As can be seen in Figure 8.9, the samples with PDAC have higher adsorption ability for MB, than the films without the polymer layer. This can suggest that the amine groups in the thin layer of PDAC can improve the adsorption effect of the cationic dye. After the dark period (60 min), 17% and 21% of the initial dye were removed from solution by adsorption, using ITO/TNW and ITO/TNW/PDAC, respectively. Using ITO/CoTNW and ITO/CoTNW/PDAC instead, 31% and 34% of MB were adsorbed in the same period. With the ITO/RuTNW and ITO/RuTNW/PDAC films, no significant differences in the absorption were observed, 26% and 27%, respectively.

Concerning the irradiation period, the results showed that all the samples demonstrated catalytic activity for the MB photodegradation process. The samples containing Ru showed the highest catalytic activity, with 97% and 98% of MB removal, within 120 min of irradiation, using ITO/RuTNW/PDAC and ITO/RuTNW films, respectively. Using the ITO/CoTNW/PDAC and ITO/TNW/PDAC samples the dye degradation decreases to 91% and 82%, respectively.

These results are in accordance with previous work, showing that for RuTNW particles the recombination rate is reduced due to the Ru incorporation, by the creation of intermediate levels in the forbidden band. These particles are also active under visible light as described in Chapter 5 [34].

Comparing the samples with and without PDAC, it was possible to conclude by performing recycling experiments with the ITO/RuTNW and ITO/RuTNW/PDAC, that the presence of the polymer allows its reutilization without performance loss for MB photodegradation.

8.4 – Cobalt and ruthenium modified TNT hybrid films - Influence of the metal position

Considering the promising results presented above, in this section, a comparative study about the type and structural metal position is discussed. For this study and considering the results presented in Chapters 4 - 6 the cobalt and ruthenium modified TNT (1% of metal, nominal) samples were selected. These studies were undertaken for the TNT samples, due to their higher photocatalytic activity in comparison with that of TNW materials.

In the doped CoTNT and RuTNT samples, the metal is only replacing the Ti^{4+} in the structure. For comparison, new samples, labeled TNT-Co and TNT-Ru, were prepared by ion-exchange (with the same nominal percentage of Co or Ru, 1%), using the experimental procedure reported elsewhere [34,35]. In this last case, only the substitution of Na^+ in the interlayers is possible, with no Ti^{4+} replacement being allowed. Therefore, it is possible to discuss which metal position is more advantageous for performance improvement in photo(electro)catalytic applications.

8.4.1 – Hybrid films synthesis

The selected cyclic voltammograms during the electropolymerization of DAC directly on ITO and ITO/TNT-Co samples used here as an example are represented in Figure 8.10. The cyclic voltammograms (CV) obtained for ITO/TNW during DAC electropolymerization (see Figure 8.3), and those obtained for ITO/TNT/PDAC, ITO/MTNT/PDAC and ITO/TNT-M/PDAC (M = Co and Ru) samples exhibit similar features. The CV presents an anodic peak (A), in the first scan, corresponding to the monomer oxidation and in the second scan have a redox couple (B/B'), which increases in intensity over the subsequent polymerization cycles [24].

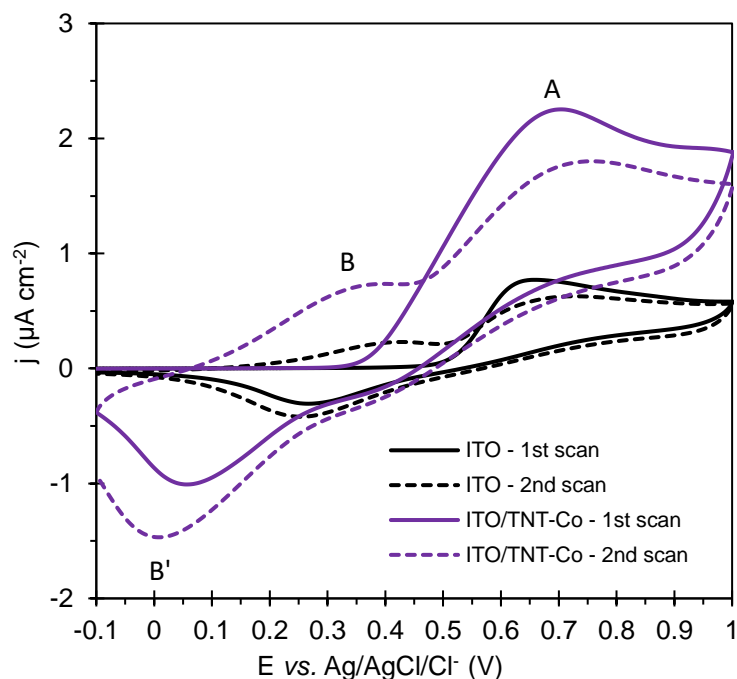


Figure 8.10 - Cyclic voltammograms of DAC (2 mM) electropolymerization on ITO and ITO/TNT-Co films in 0.1 M LiClO₄/ACN; 2 cycles at 60 mV s⁻¹.

The current potentials of DAC oxidation peak (A) in the first cycle and redox couple peaks of the polymer (B/B') for all the modified electrodes are summarized in Table 8.2.

Table 8.2 – Current peak potentials (vs. Ag/AgCl/Cl⁻) and respective current densities for the DAC oxidation peak (A) and redox couple (B/B') on ITO and all prepared electrodes, obtained from the respective cyclic voltammograms

		ITO	ITO/TNT	ITO/CoTNT	ITO/TNT-Co	ITO/RuTNT	ITO/TNT-Ru
Peak		(V)					
1 st cycle	A	0.66	0.73	0.71	0.70	0.89	0.88
	B'	0.27	0.07	0.05	0.06	-0.04	-0.04
2 nd cycle	A	0.72	0.77	1.00	0.75	1.00	0.98
	B'	0.25	0.03	0.02	0.01	-0.08	-0.08
	B	0.43	0.39	0.35	0.39	0.40	0.34

As can be seen, a positive shift was observed for the DAC oxidation peak (A) in the first cycle for all the prepared samples, in comparison with the ITO sample. This shift was considerably higher for the Ru-containing films. The separation potential between the oxidation and reduction peaks of the polymer deposited over the TNT, CoTNT, TNT-Co, RuTNT and TNT-Ru layers is higher than for PDAC formed directly on ITO, which means that the titanate nanotubes influence the polymer electroactivity (Table 8.2), since the shape of the CV obtained is more resistive. This difference is more perceptible for the films containing Ru, ITO/RuTNT and ITO/TNT-Ru, 0.48 V and 0.42 V, respectively. This suggests that the presence of ruthenium

in the TNT materials makes the electrodes more resistive. For the ITO/TNT, ITO/CoTNT and ITO/TNT-Co, differences of 0.36 V, 0.33 V, and 0.38 V, respectively, were observed.

8.4.2 – Optical and morphological characterization

The optical characterization of the films was carried out by diffuse reflectance spectroscopy (DRS) and no significant differences were obtained if compared to the characterization discussed in Chapters 4-6. Contrary to the polymer/oligomers spectrum from literature reported by Aragon *et al.* for PDAC films [33], no shoulder was observed in the wavelength range (700 to 450 nm) related to the electron transition from the polaronic level in the oxidized polymer [33].

The morphology of the modified films was analyzed by SEM. As an example, in Figure 8.11 are depicted the images obtained for ITO/CoTNT and ITO/CoTNT/PDAC films.

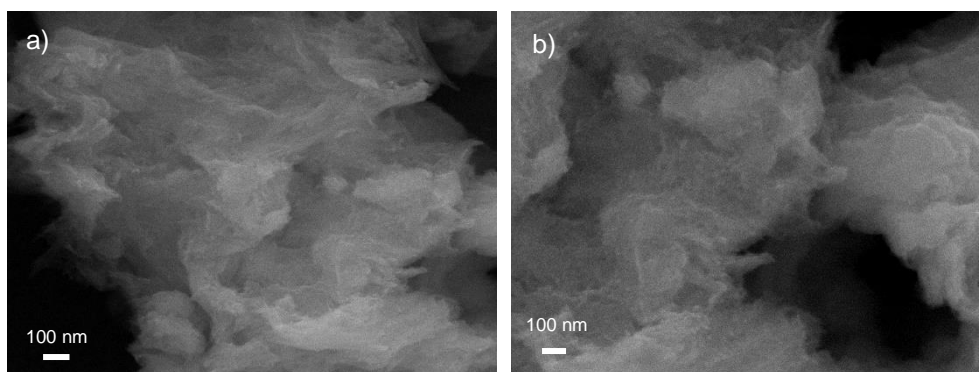


Figure 8.11 - SEM images of the (a) ITO/CoTNT and (b) ITO/CoTNT/PDAC films.

All the Ru- and Co-containing TNT films have an agglomerated morphology, and no differences were observed after PDAC deposition. From the SEM images is not possible to see the presence of the polymer in the samples, probably due to the fact that the polymeric layer is expected to be very thin and smooth. These films have a thin layer of polymer since, for photocatalytic applications, the formation of a thicker polymer film decreases the activity of the samples, as mentioned above in Section 8.3.2.

8.4.3 – Electrochemical characterization

After electropolymerization, pristine ITO/TNT/PDAC and metal modified ITO/MTNT/PDAC and ITO/TNT-M/PDAC (M = Co and Ru) samples were electrochemically characterized by cyclic voltammetry in the monomer-free solution. In Figure 8.12, it is possible to observe that all modified electrodes revealed stable electrochemical behavior, which means that after

electropolymerization, stable and electroactive ITO/TNT/PDAC, ITO/MTNT/PDAC, and ITO/TNT-M/PDAC (M = Co and Ru) electrodes were obtained. No changes or appearance of additional anodic and cathodic peaks, after four successive CVs were observed, for all samples.

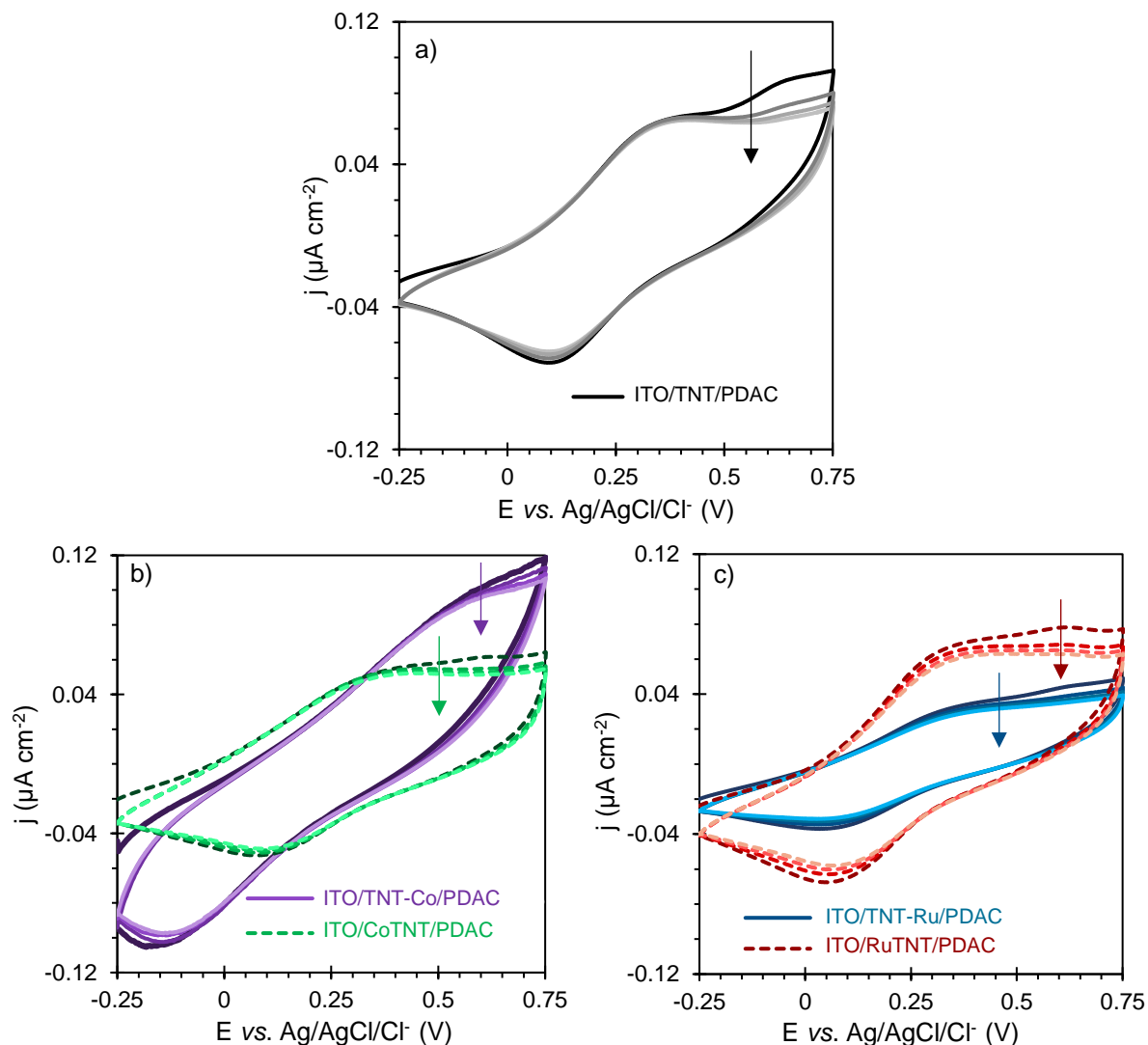


Figure 8.12 - Four successive cyclic voltammograms obtained in the solution of 0.1 M $\text{LiClO}_4/\text{acetonitrile}$, for the (a) ITO/TNT/PDAC, (b) ITO/TNT-Co/PDAC and ITO/CoTNT/PDAC, (c) ITO/TNT-Ru/PDAC and ITO/RuTNT/PDAC samples; 4 cycles at 60 mV s^{-1} .

As can be seen in Figure 8.12(b), the current density for the ITO/TNT-Co/PDAC electrode is higher than the obtained for ITO/CoTNT/PDAC electrode. However, the redox peaks are more separated, for the ITO/TNT-Co/PDAC film which means that this film is more resistive. This result can indicate that the presence of Co^{2+} replacing the Ti^{4+} , into the TiO_6 octahedra, improves the electrochemical behavior of the ITO/CoTNT/PDAC electrode. For the samples containing ruthenium, Figure 8.12(c), the ITO/RuTNT/PDAC electrode has a higher current density than the ITO/TNT-Ru/PDAC electrode. This result showed that Ru position and oxidation state, $\text{Ti}^{4+}/\text{Ru}^{4+}$ and $\text{Na}^+/\text{Ru}^{n+}$ ($n = 3$ and 4) in TNT-Ru and only $\text{Ti}^{4+}/\text{Ru}^{4+}$ replacement

in RuTNT, influences the electrochemical behavior of the modified electrodes. As for Co^{2+} , the presence of the Ru^{4+} only replacing Ti^{4+} improves the electrochemical behavior of the electrode. Comparing the results obtained with both metals modified films, it is possible to see that the ITO/RuTNT/PDAC electrode has a higher current density than the ITO/CoTNT/PDAC electrode. This suggests that the presence of ruthenium in the TNT structure, replacing the Ti^{4+} , rather improves the electrochemical behavior when compared to the Co presence, since the same amount of the photocatalyst was deposited on ITO surface in both cases.

To go further in this study, and in order to analyze the photoelectrochemical behavior of these films, the electrochemical characterization of the cobalt and ruthenium hybrid films was performed first by cyclic voltammetry in the dark and under illumination (using a Xenon lamp (UV-vis_(Xe))). Afterward, the photocurrent transients were recorded under constant potential. For the ITO/CoTNT/PDAC sample, the CVs obtained in dark and under illumination, are depicted in Figure 8.13.

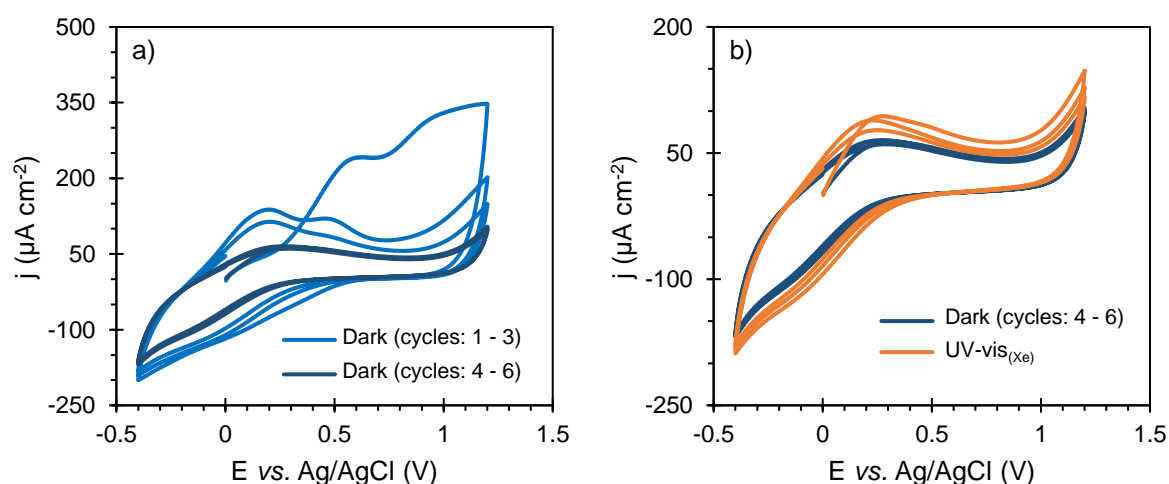


Figure 8.13 - Cyclic voltammograms of the ITO/CoTNT/PDAC sample in 0.1 M Na_2SO_4 aqueous solution in (a) dark during 6 cycles and (b) in dark and under illumination with a xenon lamp (UV-vis_(Xe) radiation).

As observed in Figure 8.13(a), the ITO/CoTNT/PDAC sample stabilization was a very slow process and 6 cycles in the dark were required to obtain it. This should be due to the traces presence of monomer who underwent polymerization during cycling that are visible in the range of positive potentials, but after several cycles in the dark, the current was stabilized. Under illumination, it can be observed an increase of the current density in the range of polymer redox peaks (0.3 V and -0.1 V) suggesting some photoactivity of the PDAC film (see Figure 8.13(b)). In the case of the sample without polymer, ITO/CoTNT (Figure 8.14(a)), a smaller photocurrent is detected in the range of positive potentials (above 0.6 V) when compared with the film with

PDAC. As also can be seen in Figure 8.14(a), the ITO/CoTNT sample stabilization in the dark was faster (only 3 cycles were needed) than the ITO/CoTNT/PDAC sample (Figure 8.13(a)). After the light was switched on, an increase in the current density was observed for the potential range of ~ 0.5 V to 1.0 V.

The CVs obtained for the ITO/CoTNT, ITO/TNT-Co, ITO/RuTNT, and ITO/TNT-Ru electrodes, in dark and under illumination (during 3 cycles each) are depicted in Figure 8.14.

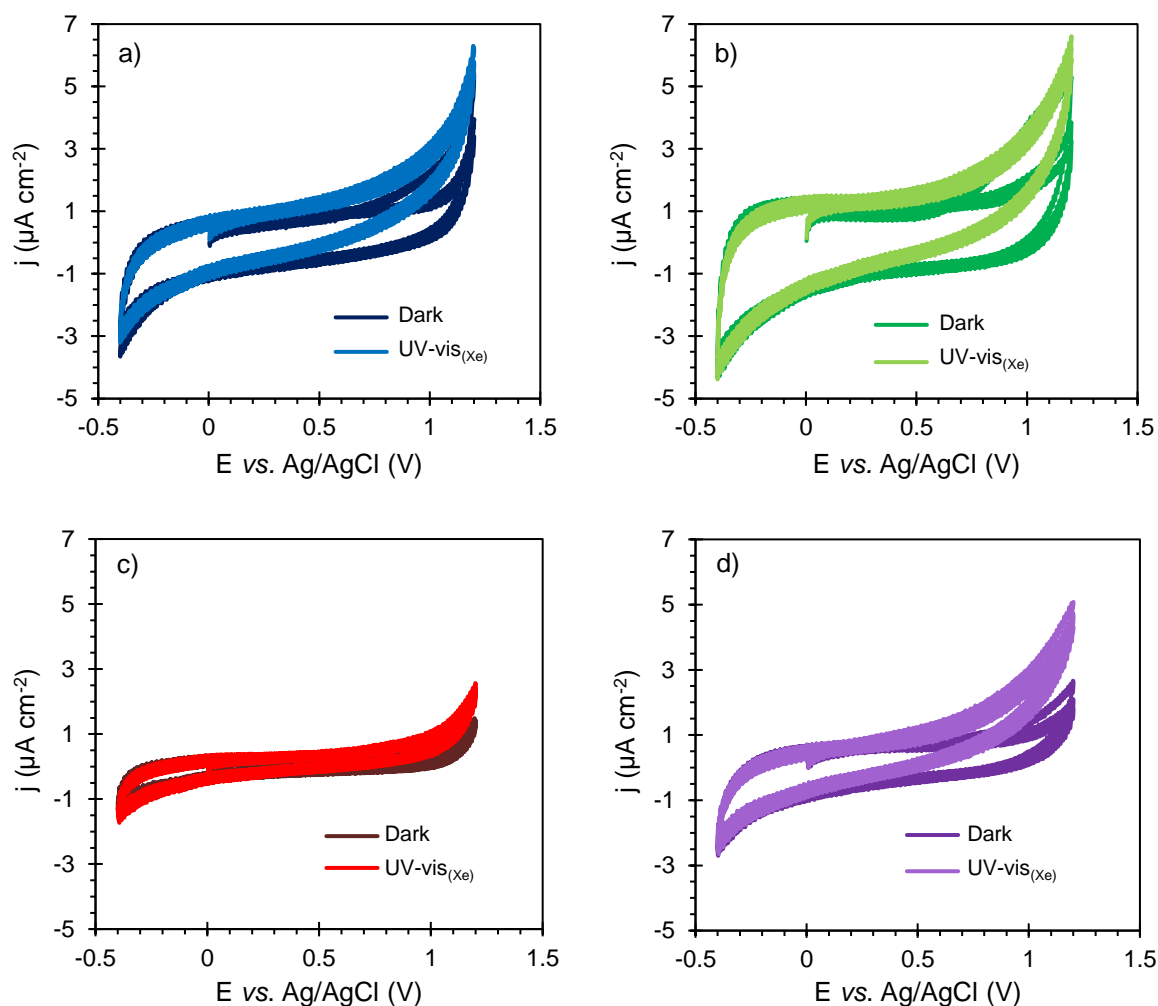


Figure 8.14 - Cyclic voltammograms of the (a) ITO/CoTNT, (b) ITO/TNT-Co, (c) ITO/RuTNT and (d) ITO/TNT-Ru samples in 0.1 M Na_2SO_4 aqueous solution in dark and under illumination with a xenon lamp (UV-vis_(Xe) radiation).

All the samples presented different electrochemical behavior under illumination and in the dark (Figure 8.14), suggesting that these films are photoelectrochemically active, although all of them with low current density (range of -1 to $7 \mu\text{A cm}^{-2}$). The cobalt samples (ITO/CoTNT and ITO/TNT-Co) had higher current density when compared to the ruthenium samples (ITO/RuTNT and ITO/TNT-Ru), being the ITO/TNT-Co electrode the one with higher current density under irradiation, in the range of ~ 0.5 V to 1.0 V. It is also possible to conclude that

ITO/TNT-Ru and ITO/TNT-Co modified electrodes demonstrated higher current density under irradiation than the ITO/RuTNT and ITO/CoTNT, counterparts.

The photocurrent experiments at constant potential were carried out after cyclic voltammetry characterization. Preliminary experiments indicate that ITO/PDAC films were not stable, due to the polymer oxidation. So, it was decided to study only the samples without PDAC. The polarization potential (0.7 V) was selected from the range of photocurrent plateau formed in the cyclic voltammograms (Figure 8.14) recorded in identical conditions. The photocurrent results obtained for ITO/TNT, ITO/CoTNT, ITO/TNT-Co, ITO/RuTNT, and ITO/TNT-Ru samples are presented in Figure 8.15.

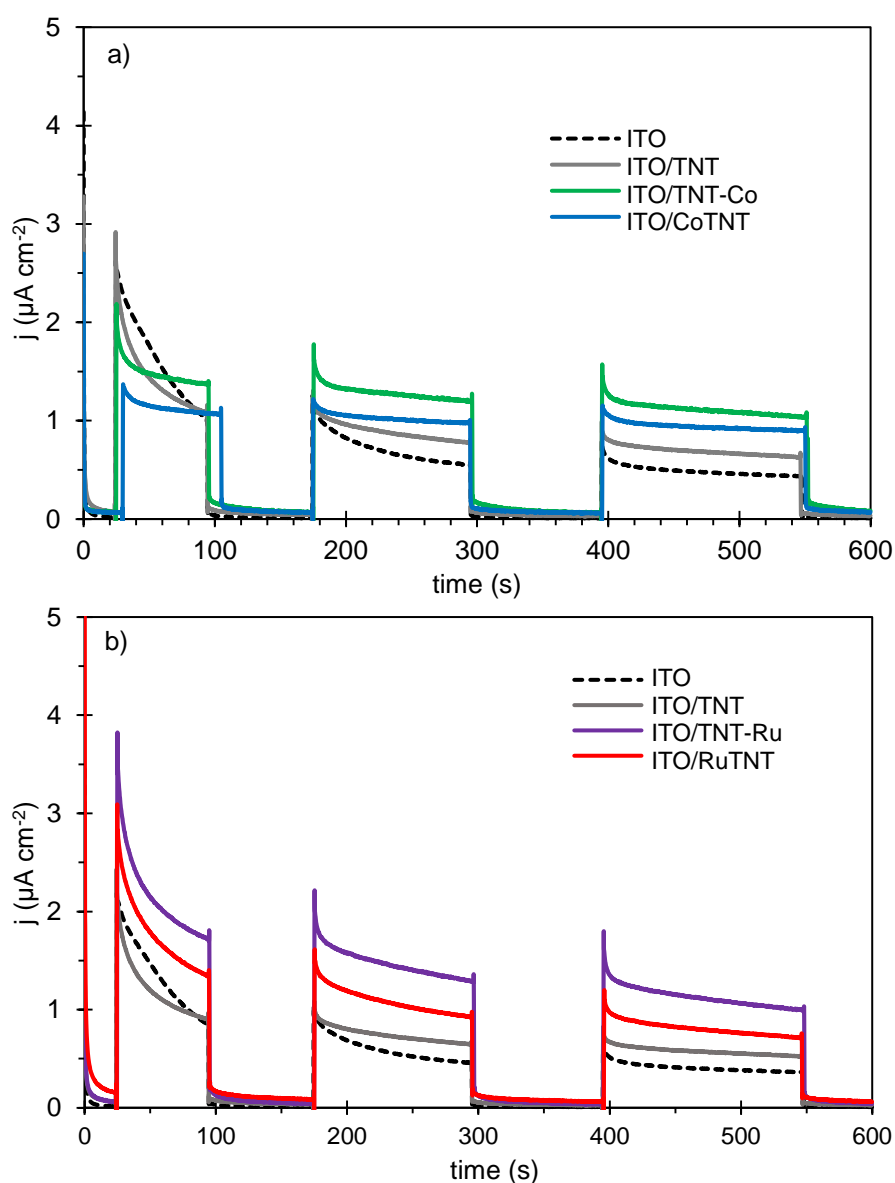


Figure 8.15 - Current transients at constant polarization potential of 0.7 V vs. Ag/AgCl in dark and under illumination with a xenon lamp (UV-vis(xe) radiation) in 0.1 M Na_2SO_4 aqueous solution, for the (a) ITO/TNT-Co and ITO/CoTNT and (b) ITO/TNT-Ru and ITO/RuTNT samples.

The photocurrent response for all the samples is similar, with the current spikes after switching illumination on, followed by an exponential decrease to constant values. It is worth noting that the values of the steady-state photocurrent for both ITO/MTNT and ITO/TNT-M (M = Co, Ru) are higher than those obtained for ITO/TNT electrode. This result can be due to a more efficient electron-hole separation for the M-modified samples. For the ITO/TNT-Co sample, this positive effect (higher photocurrent) is more pronounced. This is in accordance with the results discussed in Chapter 4, showing that the presence of intermediate levels (Co 3d-levels) in the forbidden band reduces the e^-/h^+ recombination. Furthermore, for ITO/RuTNT and ITO/TNT-Ru samples the value of the steady-state photocurrent is higher than that of ITO/CoTNT and ITO/TNT-Co samples. This indicates an even more efficient e^-/h^+ separation for the Ru-modified samples, being in accordance with the results obtained in Chapter 6. For the Ru modified samples, the ITO/TNT-Ru electrode showed the highest photocurrent.

The current spikes formed just after switching the light on are evidence of electron-hole surface recombination, competing with the light-driven electrode reactions at the semiconductor/solution interface [36]. The ratio of the rate constants for the charge transfer across the semiconductor/solution interface (k_{tr}) and electron-hole recombination (k_{rec}), can be determined by the current transients analysis according to the protocol proposed by Peter [36], using the equation:

$$\frac{j_{(\infty)}}{j_{(0)}} = \frac{k_{tr}}{k_{tr}+k_{rec}} \quad (8.1)$$

where j_{∞} is the steady-state current density and j_0 is photocurrent at $t = 0$.

The k_{tr}/k_{rec} ratio obtained for ITO/CoTNT and ITO/TNT-Co samples are 0.364 and 0.490, respectively, and for the ITO/RuTNT and ITO/TNT-Ru samples, the k_{tr}/k_{rec} ratio is 0.442 and 0.818, respectively, being all of them higher than that obtained for ITO/TNT (0.236) and ITO (0.124). This difference in the values of steady-state photocurrent for the pristine and metal modified TNT electrodes is probably a consequence of a higher electron-hole recombination rate in the ITO/TNT sample. These results also allow concluding that ITO/CoTNT, ITO/TNT-Co, ITO/RuTNT, and ITO/TNT-Ru electrodes have lower e^-/h^+ recombination rate than the ITO/TNT and ITO films. Under these conditions, the ITO/TNT-Ru sample was the one presenting the highest photocurrent. This may be ascribed to the generation of a larger amount of charge carriers, once the absorbance for this ruthenium containing samples is higher as it was presented in Figure 8.8 and discussed in Chapters 4-6.

Comparing the obtained results for the ITO/MTNT and ITO/TNT-M (M = Co, Ru) samples, it can be concluded that the presence of Ru in the TNT materials promotes a higher improvement on the photocurrent response than the Co. This can be due to the difference in the energetic position of the valance and conduction bands, once the Ru containing materials requires less energy for photoactivation (as previously discussed in Chapter 6).

To better analyze the influence of Co and Ru modification on the photoelectroactivity of the samples, the photocurrent measurements were also performed at a lower potential, 0.5 V, corresponding to the onset of the current transients for ITO/TNT sample.

The experiments were carried out using a 365 nm diode since these materials are photoactive in this range and a difference between the bang edge of TNT, CoTNT, and RuTNT can be observed. The obtained current transients are presented in Figure 8.16.

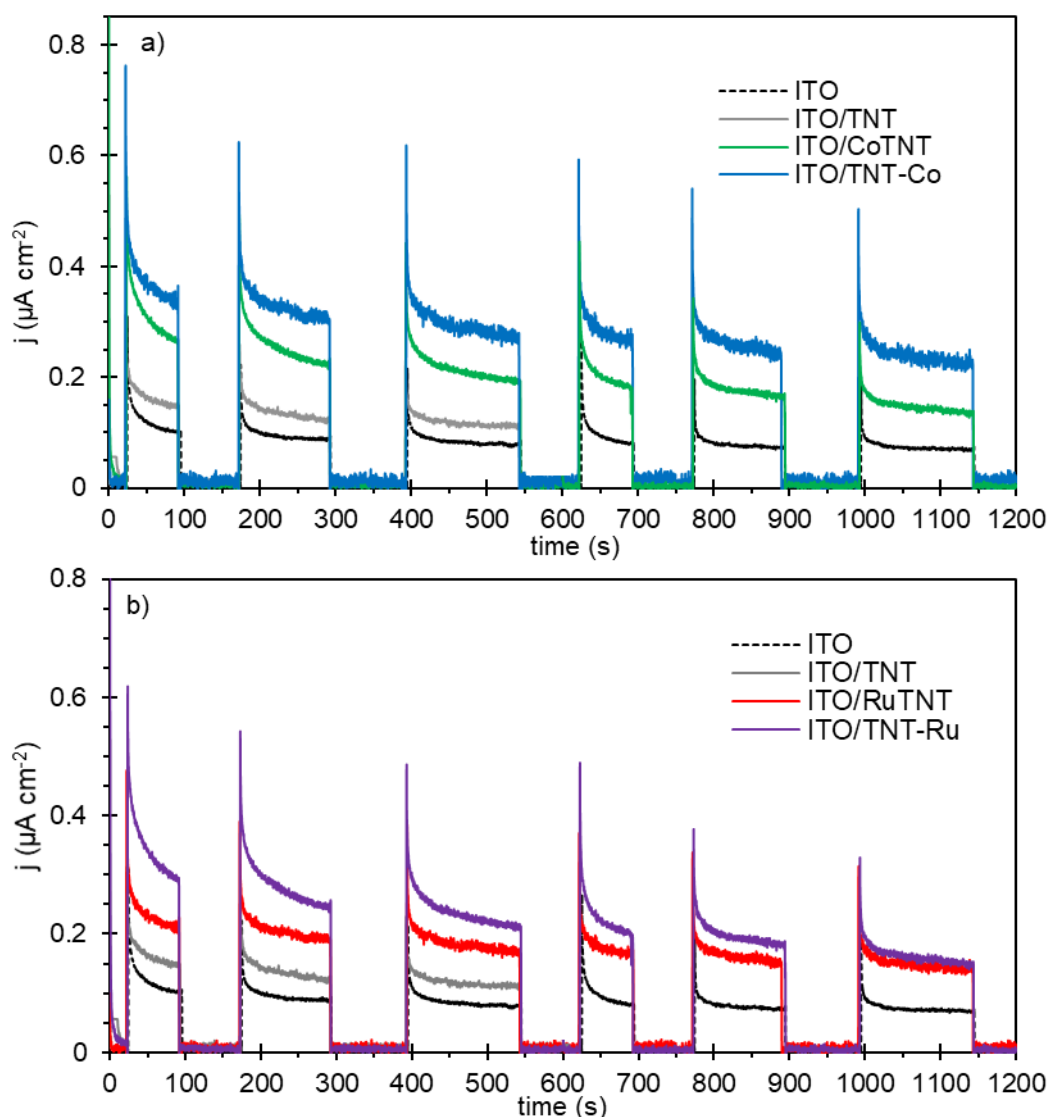


Figure 8.16 - Current transients at constant polarization potential of 0.5 V vs. Ag/AgCl in dark and under illumination with a high-power LED (365 nm), in 0.1 M Na_2SO_4 aqueous solution, for (a) ITO/CoTNT and ITO/TNT-Co and (b) ITO/RuTNT and ITO/TNT-Ru samples.

As can be seen in Figure 8.16, the current transients for ITO and ITO/TNT overlap. Furthermore, the photocurrent for ITO/MTNT and ITO/TNT-M (M = Co, Ru) is higher than for ITO/TNT and ITO electrodes. This agrees with the presence of intermediate levels in the M-containing samples in the forbidden band (as discussed in Chapter 4 for Co and 6 for Ru) [35].

8.4.4 – Photocatalytic and photoelectrocatalytic pollutants degradation experiments

The photo(electro)catalytic ability of the pristine (ITO/TNT/PDAC and ITO/TNT) and metal modified hybrid films, ITO/MTNT/PDAC, ITO/TNT-M/PDAC, ITO/MTNT and ITO/TNT-M (M = Co and Ru) for pollutants degradation was examined. Methylene blue (MB) and theophylline were chosen as model pollutants. MB is a cationic compound ($pK_a = 3.14$) with a strong affinity for adsorption on nanocomposite samples' anionic surfaces. Theophylline ($pK_a = 7.82$) has been described as a toxic intermediate of caffeine degradation and does not reveal strong adsorption ability on the surface of TNT, as shown in Chapter 2.

• Methylene blue (MB) photodegradation

The photocatalytic activity of the films was tested on the degradation of a 10 ppm MB aqueous solutions under visible(x_e) light during 90 min of irradiation. The obtained results are depicted in Figure 8.17.

After a dark period of 60 min, the ITO film does not adsorb MB, while ITO/PDAC removes ~ 8% of the initial MB. In general, it is possible to observe that the films with PDAC showed higher adsorption ability than films without polymer.

For the cobalt-containing films (Figure 8.17(a)) the higher amount of the initial MB (35%) was removed in dark using the ITO/CoTNT/PDAC sample as adsorbent. For the samples containing ruthenium (Figure 8.17(b)), the ITO/RuTNT/PDAC was the best one for the dye removal by adsorption, with a 30% decrease in the MB concentration.

After turning on the light, all the samples demonstrated catalytic activity for the dye photodegradation. Concerning the Co containing films (Figure 8.17(a)), the ITO/CoTNT/PDAC sample was the one with the best catalytic performance, with the total MB removal after 90 min of irradiation. Using the ITO/CoTNT film as catalyst 95% of MB was removed, for the same period. However, for the same irradiation period, the ITO/TNT-Co and ITO/TNT-Co/PDAC films were able to remove only 83% and 87% of the MB, respectively. Under identical conditions, only 11% of MB was removed by photolysis.

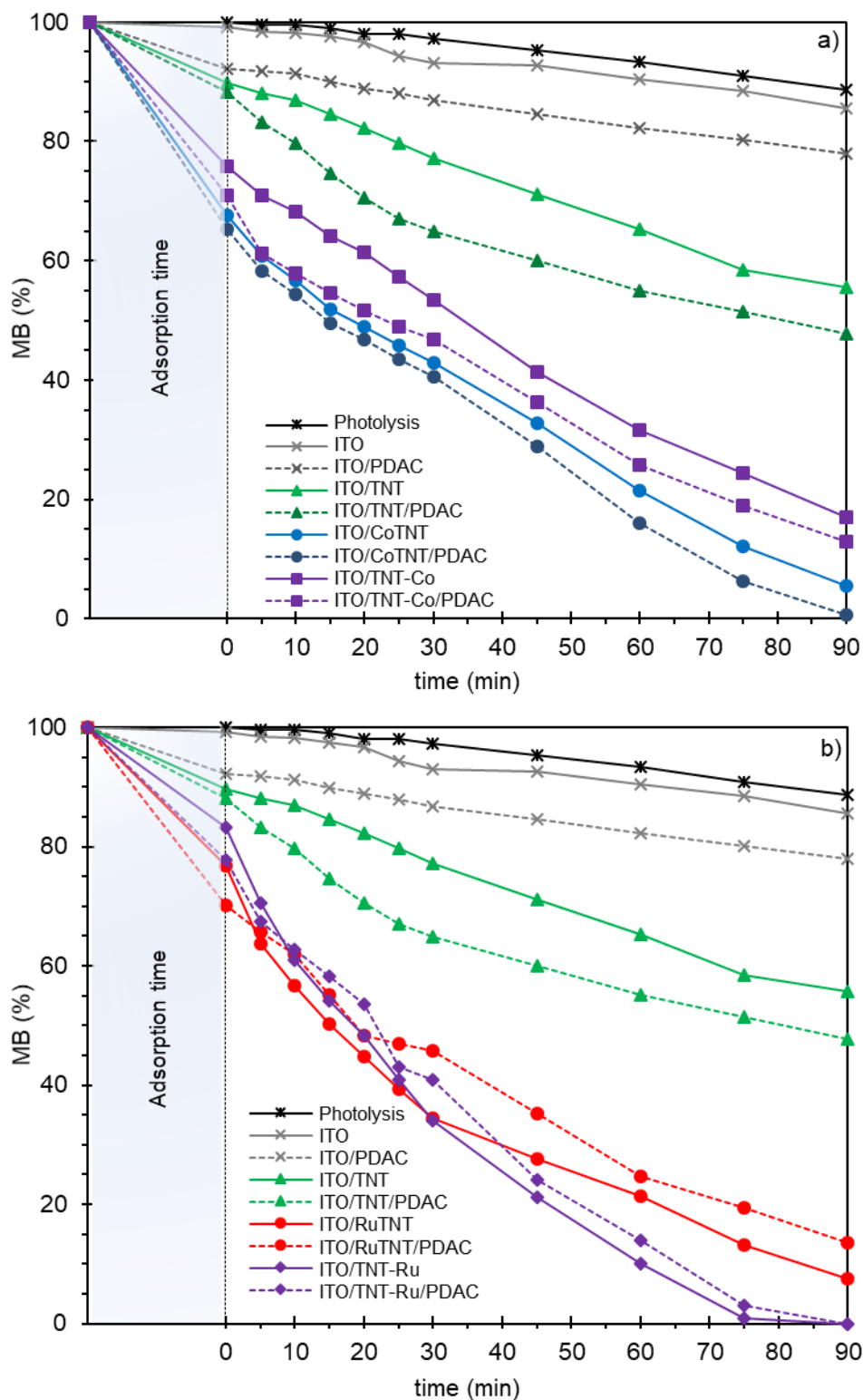


Figure 8.17 - MB photodegradation during 90 min of visible(λ_{vis}) irradiation using (a) the samples containing cobalt and (b) the samples modified with ruthenium.

For the pristine samples, ITO/TNT and ITO/TNT/PDAC, only 44% and 52% of the initial MB was removed for the same period, respectively. These results are in accordance with previous work (Chapter 4), suggesting that the presence of cobalt (1%, nominal) in the structure replacing

the Ti^{4+} (CoTNT sample) induces a higher photocatalytic performance than the TNT-Co sample, with $\text{Na}^+/\text{Co}^{2+}$ replacement. These results also agree with the fact that the presence of cobalt in the titanate nanoparticles reduces the e^-/h^+ recombination rate [35].

Comparing the samples with and without polymer, the presence of PDAC on the TNT and cobalt-containing samples increases the adsorption and the photocatalytic activity of the films. This can be justified by the presence of amino groups (they promote improvement in adsorption and photocatalytic performance) on the surface, as well as the formation of photoinduced charge carriers in the polymer under visible light. Under irradiation, the electrons can be excited from the highest occupied molecular orbital (HOMO) to the lowest unoccupied molecular orbital (LUMO) ($\pi-\pi^*$ transition) of PDAC. Then, the photoinduced electrons can be transferred from LUMO of PDAC to the conduction band of TNP and then involved in the generation of additional superoxide radicals. These latter ones can lead to the formation of hydroxyl radicals, which are active in the pollutant degradation process (Figure 8.18(a)).

About the Ru-containing samples, Figure 8.17(b), the ITO/TNT-Ru and ITO/TNT-Ru/PDAC films were the ones that presented a better performance, with the MB total degradation after 90 min of irradiation. Furthermore, no significant differences were found on the photocatalytic performance of these films. After 75 min of irradiation, there was no more MB still in solution using the ITO/TNT-Ru/PDAC film, and 97% of MB was removed using the ITO/TNT-Ru film as catalyst. These results are following previous work (Chapters 5 and 6) indicating that Ru modified nanostructures are photoactive in visible light and the Ru incorporation on the TNT reduces the e^-/h^+ recombination rate.

Contrary to what was observed for the films with TNT, CoTNT, and TNT-Co, the samples containing ruthenium showed higher photocatalytic activity in the absence of PDAC. This can be explained due to the difference between the conduction band energy of these modified materials (Figure 8.18(b)), as mentioned previously in Chapters 4-6. It is known that the photocatalytic oxidation and reduction abilities of semiconductors are determined by the potentials of their valence and conduction bands, respectively. The conduction band (CB) energy of the Ru-containing samples can reduce the O_2 to $\text{O}_2^{\cdot-}$, due to their CB edge potential is more negative than the superoxide radicals ($\text{O}_2^{\cdot-}$) redox potential (- 0.33 V vs. NHE). Therefore, the probability of the formation of such $\text{O}_2^{\cdot-}$ radicals *via* e^- is high. However, in the case of TNT and Co-containing samples the CB position is more positive than the $E^\circ(\text{O}_2/\text{O}_2^{\cdot-})$, so the formation of $\text{O}_2^{\cdot-}$ radicals in these materials is less likely. For this reason, the presence of PDAC in TNT, TNT-Co and CoTNT films transfer electrons from the LUMO of the polymer

to the CB of these semiconductor materials, promoting the production of $O_2^{\cdot-}$ radicals, and with this improving the photocatalytic degradation results.

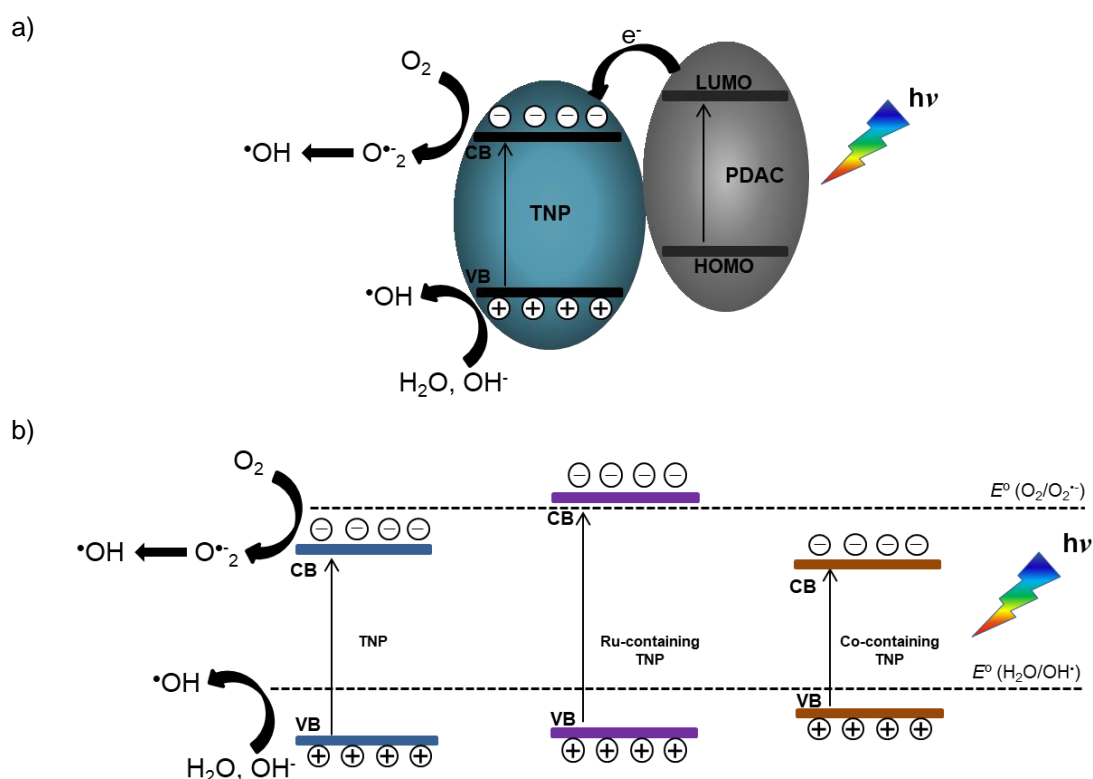


Figure 8.18 - Schematic representation of the charge-transfer mechanism proposal for (a) ITO/TNP/PDAC hybrid films and (b) for the pristine and Co- and Ru-containing TNP samples, under irradiation.

To test the photocatalyst recycling possibility, ITO/CoTNT/PDAC and ITO/TNT-Ru/PDAC samples (the best photocatalysts in this study) were used for 4 successive MB degradation runs (60 min of irradiation each), and the results are presented in Figure 8.19.

In the first degradation trial, 84% and 86% of the initial MB was degraded, using ITO/CoTNT/PDAC and ITO/TNT-Ru/PDAC samples, respectively. After the second and subsequent cycles, no significant differences were observed. These results can indicate that these photocatalysts are stable without significant loss of catalytic activity. No signals of surface poisoning of the ITO/CoTNT/PDAC and the ITO/TNT-Ru/PDAC films during these four successive degradations were observed.

It is important to note that the presence of the polymer over the metal modified TNT layer allowed the film reutilization without loss of performance, once the films without PDAC drop-down (detached from the substrate) after the first MB photodegradation experiment. With these results, it is possible to conclude that the presence of PDAC improves the films stability and it makes possible their use for successive photodegradation experiments. Furthermore, the PDAC

presence also reduces the e^-/h^+ recombination rate as explained above, due to the e^- from the LUMO of PDAC that can be transferred for the TNT conduction band.

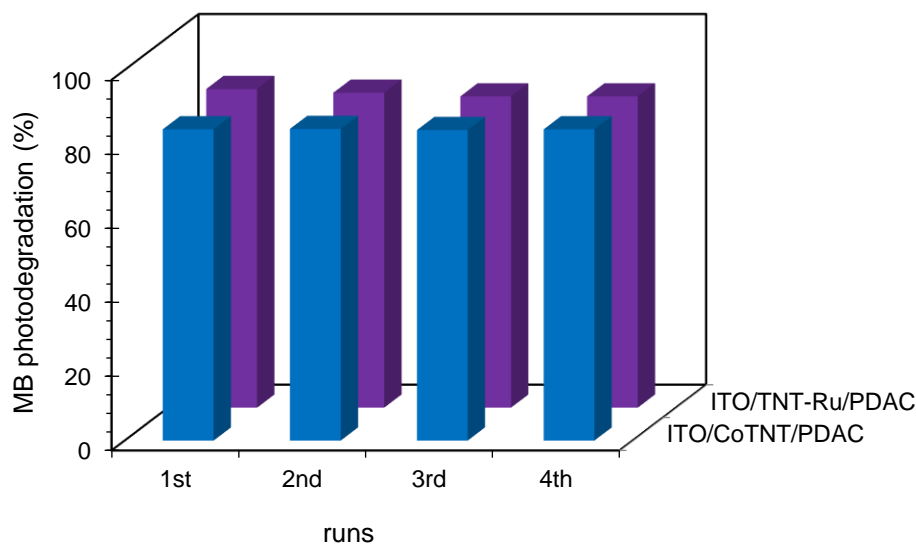


Figure 8.19 - Percentage of a 10 ppm MB solution removal during four consecutive runs, of 60 min each, of photocatalytic degradation, using ITO/CoTNT/PDAC and ITO/TNT-Ru/PDAC samples as catalyst, under visible(λ_e) irradiation.

• Theophylline photodegradation

To extend the applicability of these films, the degradation of a theophylline solution was also evaluated. Once the theophylline degradation under visible(λ_e) irradiation was very slow, it was decided for this study to use UV-vis(λ_e) radiation. Furthermore, only the films containing polymer were used for this study, due to the samples with polymer showed higher stability on the MB degradation experiments. Therefore, the photocatalytic activity of the films was tested on theophylline aqueous solutions (5 ppm) degradation, under UV-vis(λ_e) radiation during 90 min of irradiation. The obtained results are depicted in Figure 8.20, and as can be seen after the dark period (60 min), no significant theophylline was adsorbed on the films' surface. This can be explained due to the fact this pollutant has a $pK_a = 7.82$ and the TNT materials have a p.z.c. around 3.4 [37,38]. The prepared theophylline solution had a pH = 6, therefore, no interactions between the film surface and the theophylline molecule were expected.

After irradiation, it is possible to see that all the samples demonstrated catalytic activity for the theophylline photodegradation reaction. The ITO/TNT-Ru/PDAC and ITO/TNT-Ru samples were the ones with the best performance, with 94% and 95% of theophylline degradation, respectively, after 90 min of irradiation. For this pollutant degradation, no significant differences were observed on the photocatalytic performance for the TNT-Ru samples with and

without polymer (ITO/TNT-Ru and ITO/TNT-Ru/PDAC). These results are in accordance with the ones for the MB removal (Figure 8.17 (b)).

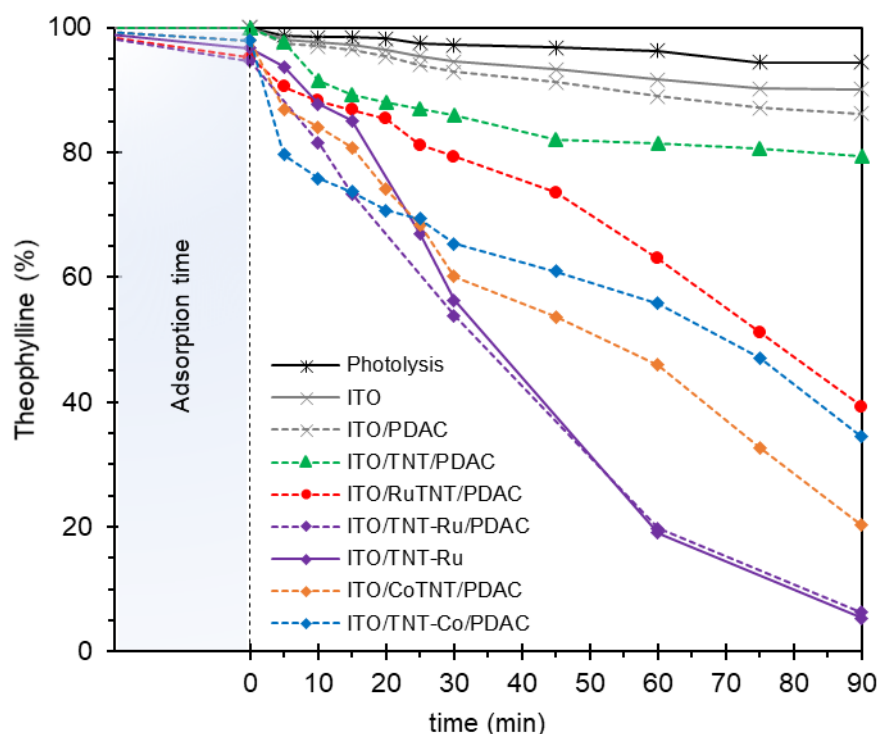


Figure 8.20 - Theophylline photodegradation during 90 min of UV-vis(λ_{exc}) irradiation using ITO/PDAC, ITO/TNT/PDAC, ITO/CoTNT/PDAC, ITO/TNT-Co/PDAC, ITO/TNT-Ru/PDAC, ITO/RuTNT/PDAC, and ITO/TNT-Ru samples.

Since the ITO/TNT-Ru sample showed similar performance of the ITO/TNT-Ru/PDAC sample, and after the theophylline degradation this sample was stable (verified with the naked eye), it was decided to study its reuse in successive degradation runs. In addition and to analyze the photochemical stability of the ITO/CoTNT/PDAC, ITO/TNT-Co/PDAC ITO/TNT-Ru and ITO/TNT-Ru/PDAC samples, four successive theophylline degradation during 90 min each, were performed (Figure 8.21).

As can be seen in Figure 8.21, all the samples presented high catalytic performance and photochemical stability, since no significant differences on the theophylline degradation after four successive degradation runs were observed. These results can suggest no signals of surface poisoning of the films during these four successive degradations. As can also be seen, the film without polymer, sample ITO/TNT-Ru, also presents excellent photochemical stability and catalytic performance. No differences were observed in the four degradation runs. For this process, and in contrary to what was found on the MB degradation, the films with and without polymer allowed the reutilization without loss of catalytic performance. This may suggest that this difference can be due to the type of pollutant used and/or the by-products formed, once the

theophylline molecule is smaller than the MB molecule (Figure 8.2) and also have different functional groups. Furthermore, it can be concluded that for this emergent pollutant degradation the samples without polymer were also stable.

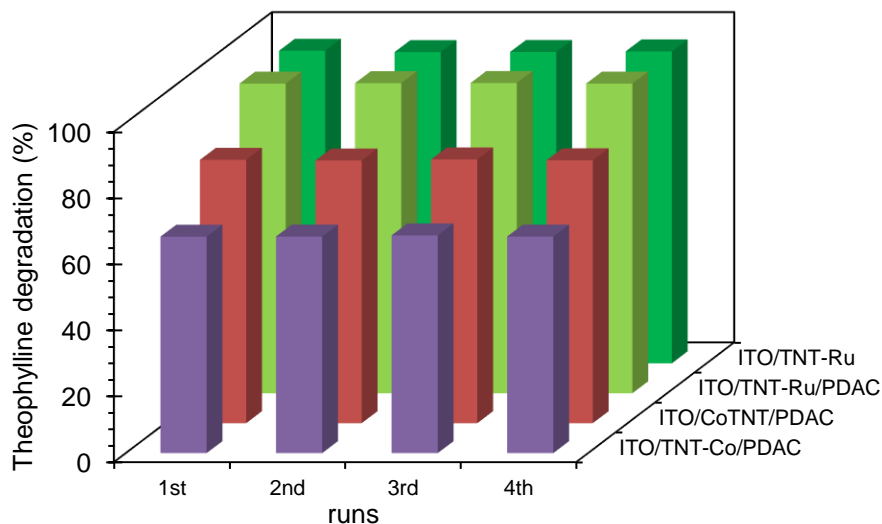


Figure 8.21 - Percentage of a 5 ppm theophylline solution removal during four cycles, of 90 min each, by photocatalytic degradation, using ITO/ CoTNT/PDAC, ITO/TNT-Co/PDAC, ITO/TNT-Ru/PDAC, and ITO/TNT-Ru samples as catalyst.

• Theophylline photo(electro)degradation

From the photoelectrochemical characterization (CV and $j-t$ transients), it was verified that for ITO/MTNT and ITO/TNT-M (M = Co, Ru) samples, the steady-state photocurrent is higher than for ITO/TNT sample. Therefore, it was decided to perform preliminary studies on the theophylline photo(electro)degradation using the ITO/CoTNT, ITO/TNT-Co, ITO/RuTNT, and ITO/TNT-Ru samples, to analyze the influence of the metal position on the photo(electro)catalysis. Since the films without polymer (ITO/TNT, ITO/M-TNT and ITO/TNT-M (M = Co, Ru)) were stable in theophylline degradation, for the theophylline photo(electro)degradation experiments only the samples without PDAC were analyzed.

The conditions used for these experiments were shown in Chapter 10 and the obtained results are depicted in Figure 8.22.

The application of an external potential of 0.5 V to ITO/CoTNT, ITO/TNT-Co, ITO/RuTNT, and ITO/TNT-Ru samples improves the theophylline degradation under UV irradiation (LED 365 nm) once the theophylline degradation was faster in comparison to the experiment without polarization (photocatalysis). These results indicate that the application of a potential enhances the separation of charge and consequently reduces the e^-/h^+ recombination rate.

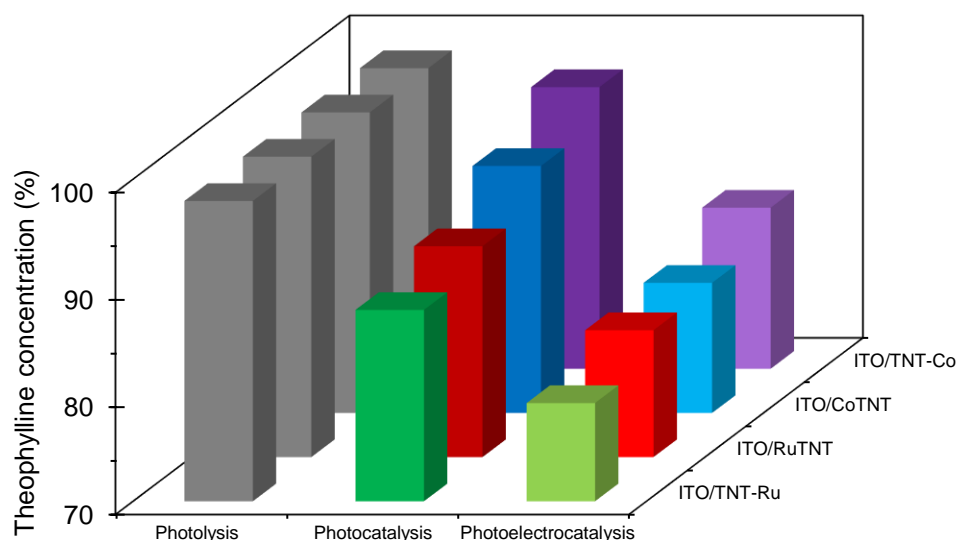


Figure 8.22 - Theophylline concentration after 120 min of UV irradiation (LED 365 nm) during photo and photoelectrodegradation using ITO/CoTNT, ITO/TNT-Co, ITO/RuTNT, and ITO/TNT-Ru samples as catalysts.

8.5 - Conclusions

Nanocrystalline titanate nanoparticles (TNT and TNW) modified with cobalt and ruthenium were successfully immobilized on the ITO substrate by the drop-casting method and by drop-casting followed by the electropolymerization of DAC directly over the TNP thin layer, forming a conductive polymer layer (PDAC) on the surface. These modified materials (ITO/TNP, ITO/MTNP, ITO/TNP-M, ITO/TNP/PDAC, ITO/MTNP/PDAC and ITO/TNP-M/PDAC (M = Co, Ru)) were characterized by SEM, DRS and photoelectrochemical techniques (cyclic voltammetry and chronoamperometric measurements in dark and under illumination). The adsorption and photocatalytic ability of the prepared materials to remove organic pollutants from aqueous media were studied, using methylene blue (MB) and theophylline as models. All the films demonstrated catalytic activity for MB (10 ppm) and theophylline (5 ppm) photodegradation.

For the titanate nanowires, the best MB photocatalytic degradation results were achieved with the ITO/CoTNW/PDAC and ITO/RuTNW/PDAC films, under UV-vis_(Xe) and visible_(Xe) light irradiation. The presence of PDAC on the films allowed their reutilization without performance loss.

Concerning the cobalt and ruthenium modified titanate nanotubes, the highest photocatalytic activity was found for ITO/TNT-Ru/PDAC sample achieving the total degradation of MB and theophylline after 90 min of irradiation. Regarding the ITO/TNT-Ru and ITO/TNT-Ru/PDAC films, similar catalytic activity was obtained for both samples. Moreover, they revealed the

same degradation ability with respect to theophylline even without PDAC deposited on the top of the semiconductor particles.

The reusability of the hybrid films was also evaluated, using fresh MB and theophylline solutions, and a promising photocatalytic performance with a very low variation of the degradation rate after four consecutive degradation tests was observed. The reuse studies showed that for MB degradation, only the samples with PDAC are stable, however, for the theophylline degradation all the samples (with and without polymer) are stable.

Theophylline photo(electro)degradation preliminary results using the Ru- and Co-containing TNT films suggest an improvement in the catalytic performance when a potential was applied. This can be due to a decrease in the e^-/h^+ recombination rate since the application of an external constant potential to the catalysts promotes an enhancement of the charge separation.

8.6 - References

- 1 - B. Barrocas, O.C. Monteiro, M.E. Melo Jorge, S. Sérgio, Photocatalytic activity and reusability study of nanocrystalline TiO₂ films prepared by sputtering technique, *Appl. Surf. Sci.* 264 (2013) 111-116.
- 2 - P. Zeman, S. Takabayashi, Nano-scaled photocatalytic TiO₂ thin films prepared by magnetron sputtering, *Thin Solid Films* 433 (2003) 57-62.
- 3 - D. Papoutsis, P. Lianos, P. Yianoulis, P. Koutsoukos, Sol-gel derived TiO₂ microemulsion gels and coatings, *Langmuir* 10 (1994) 1684-1689.
- 4 - S. Zhang, Y.F. Zhu, E.D. Brodie, Photoconducting TiO₂ prepared by spray pyrolysis using TiCl₄, *Thin Solid Films* 213 (1992) 265-270.
- 5 - M.H. Habibi, N. Talebian, Photocatalytic degradation of an azo dye X6G in water: A comparative study using nanostructured indium tin oxide and titanium oxide thin films, *Dyes Pigments* 73 (2007) 186-194.
- 6 - S. Perathoner, R. Passalacqua, G. Centi, S. Dangshen, S.G. Weinberg, Photoactive titania nanostructured thin films: Synthesis and characteristics of ordered helical nanocoil array, *Catal. Today* 122 (2007) 3-13.

7 - B.S. Liu, X.J. Zhao, L.P. Wen, A simple route to the water-repellent surface based on chemical N modified Ti–O structure films, *Surf. Coat. Tech.* 201 (2006) 3606-3610.

8 - K.L. Siefering, G.L. Griffin, Growth kinetics of CVD TiO₂: Influence of carrier gas, *J. Electrochem. Soc.* 137 (1990) 1206-1208.

9 - A. Ibrahim, J.S. Al-Homoudi, R. Thakur, G.W. NaiK, G. Auner, Newaz, Anatase TiO₂ films based CO gas sensor: film thickness, substrate and temperature effects, *Appl. Surf. Sci.* 253 (2007) 8607-8614.

10 - A.D. Johnson, V. Martynov, V. Gupta, Applications of shape memory alloys: advantages, disadvantages, and limitations, *Micromachining and Microfabrication Process Technology VII, Proc. SPIE* 4557 (2001) 1-11.

11 - M. Biswas, P.-C. Su, Modern technologies for creating the thin-film systems and coatings, Chapter 16 - Chemical solution deposition technique of thin-film ceramic electrolytes for solid oxide fuel cells, IntechOpen publisher, UK, 2017.

12 - M. Eslamian, F. Zabihi, Ultrasonic substrate vibration-assisted drop casting (SVADC) for the fabrication of photovoltaic solar cell arrays and thin-film devices, *Nanoscale Res. Lett.* 10 (2015) 462(1)-462(5).

13 - L. Fu, A. M. Yu, Carbon nanotubes based thin films: Fabrication, characterization and applications, *Rev. Adv. Mater. Sci.* 36 (2014) 40-61.

14 - T.V. Gavrilović, D.J. Jovanović, M.D. Dramićanin, Nanomaterials for green energy, Chapter 2 - Synthesis of multifunctional inorganic materials: From micrometer to nanometer dimensions, Elsevier, Netherlands, 2018.

15 - S. Suehiro, K. Horita, A.D. Pramata, M. Yuasa, Y. Ishiwata, K. Shimano, T. Kida, Efficient solution route to transparent ZnO semiconductor films using colloidal nanocrystals, *J. Asian Ceram. Soc.* 4 (2016) 319-323.

16 - M. Bellardita, A.D. Paola, S. Yurdakal, L. Palmisano, Heterogeneous photocatalysis, Chapter 2 - Preparation of catalysts and photocatalysts used for similar processes, Elsevier, Netherlands, 2019.

- 17 - Kenry, C.T. Lim, Nanofiber technology: current status and emerging developments, *Prog. Polym. Sci.* 70 (2017) 1-17.
- 18 - V.C. Ferreira, A.J. Goddard, O.C. Monteiro, *In situ* synthesis and modification of cotton fibers with bismuthoxychloride and titanium dioxide nanoparticles for photocatalytic applications, *J. Photoch. Photobio. A* 357 (2018) 201-212.
- 19 - L.C. Silva, B. Barrocas, M.E. Melo Jorge, S. Sério, Photocatalytic degradation of rhodamine 6G using TiO₂/WO₃ bilayered films produced by reactive sputtering, The 6th International Conference on Photonics, Optics and Laser Technology (PHOTOPTICS 2018) Special Session in Advanced Optical Materials, Sensors and Devices (AOMatSens) Conf. Proc. 1 (2018) 334-340.
- 20 - D.D. Yao, M.R. Field, A.P. O'Mullane, K. Kalantar-zadeh, J.Z. Ou, Electrochromic properties of TiO₂ nanotubes coated with electrodeposited MoO₃, *Nanoscale* 5 (2013) 10353-10359.
- 21 - V.C. Ferreira, O.C. Monteiro, Synthesis and properties of Polythionine/Co-doped titanatenanotubes hybrid materials, *Electrochim. Acta* 113 (2013) 817-824.
- 22 - A. Fedorczyk, J. Ratajczak, O. Kuzmych, M. Skompska, Kinetic studies of catalytic reduction of 4-nitrophenol with NaBH₄ by means of Au nanoparticles dispersed in a conducting polymer matrix, *J. Solid. State. Electrochem.* 19 (2015) 2849-2858.
- 23 - V.C. Ferreira, A.I. Melato, A.F. Silva, L.M. Abrantes, Attachment of noble metal nanoparticles to conducting polymers containing sulphur – preparation conditions for enhanced electrocatalytic activity, *Electrochim. Acta* 56 (2011) 3567-3574.
- 24 - M. Skompska, M.J. Chmielewski, A. Tarajko, Poly(1,8-diaminocarbazole) – A novel conducting polymer for sensor applications, *Electrochemistry Communications* 9 (2007) 540-544.
- 25 - M. Skompska, A. Tarajko-Wazny, Electrochemical quartz crystal microbalance studies of polymerization and redox process of poly(1,8-diaminocarbazole) in protic and aprotic solutions, *Electrochimica Acta* 56 (2011) 3494-3499.

- 26 - A. Fedorczyk, M. Skompska, Quantitative studies of silver ions removal from aqueous solutions by poly(1,8-diaminocarbazole) films by means of electrochemical quartz crystal microbalance, *Electrochimica Acta* 99 (2013) 62-68.
- 27 - S.B. Mondal, S. Gao, N. Zhu, R. Liang, V. Gruev, S. Achilefu, Chapter Five - Real-Time Fluorescence Image-Guided Oncologic Surgery, *Advances in Cancer Research* 124 (2014) 171-211.
- 28 - Juan Yang, Keqiang Qiu, Preparation of activated carbons from walnut shells via vacuum chemical activation and their application for methylene blue removal, *Chemical Engineering Journal* 165 (2010) 209-217.
- 29 - I.A.W. Tan, B.H. Hameed, A.L. Ahmad, Equilibrium and kinetic studies on basic dye adsorption by oil palm fibre activated carbon, *Chemical Engineering Journal* 127 (2007) 111-119.
- 30 - R.R. Ruddaraju, G. Kiran, A.C. Murugulla, R. Maroju, D.K. Prasad, B.H. Kumar, V. Bakshi, N.S.Reddy, Design, synthesis and biological evaluation of theophylline containing variant acetylene derivatives as α -amylase inhibitors, *Bioorganic Chemistry* 92 (2019) 103120(1)-103120(15).
- 31 - B. Barrocas, M.C. Neves, M. Conceição Oliveira, O.C. Monteiro, Enhanced photocatalytic degradation of psychoactive substances using amine modified elongated titanate nanostructures, *Environ. Science: Nano* 5 (2018) 350-361.
- 32 - A. Tarajko, H. Cybulskia, M.J. Chmielewski, J. Bukowska, M. Skompska, Electrochemical and spectroscopic characterization of poly(1,8-diaminocarbazole): Part I. Electropolymerization and determination of the polymer structure by FTIR studies and DFT calculations, *Electrochimica Acta* 54 (2009) 4743-4750.
- 33 - A.G. Aragon, W. Kierulf-Vieira, T. Łęcki, K. Zarębska, J. Widera-Kalinowska, M. Skompska, Synthesis and application of N-doped TiO₂/CdS/poly(1,8-diaminocarbazole) composite for photocatalytic degradation of 4-chlorophenol under visible light, *Electrochim. Acta* 314 (2019) 73-80.

34 - B.T. Barrocas, M. Conceição Oliveira, H.I.S. Nogueira, S. Fateixa, O.C. Monteiro, Ruthenium-Modified Titanate Nanowires for the Photocatalytic Oxidative Removal of Organic Pollutants from Water, *ACS Applied Nano Mat.* 2 (2019) 1341-1349.

35 - B. Barrocas, A.J. Silvestre, A.G. Rolo, O.C. Monteiro, The effect of ionic Co presence on the structural, optical and photocatalytic properties of modified cobalt–titanate nanotubes, *Phys. Chem. Chem. Phys.* 18 (2016) 18081-18093.

36 - L.M. Peter, Energetics and kinetics of light-driven oxygen evolution at semiconductor electrodes: The example of hematite, *J. Solid State Electrochem.* 17 (2013) 315-326.

37 - V. Bem, M.C. Neves, M.R. Nunes, A.J. Silvestre, O.C. Monteiro, Influence of the sodium/proton replacement on the structural, morphological and photocatalytic properties of titanate nanotubes, *J. Photochem. Photobiol., A* 232 (2012) 50-56.

38 - V.C. Ferreira, O.C. Monteiro, New hybrid titanate elongated nanostructures through organic dye molecules sensitization, *J. Nanopart. Res.* 15 (2013) 1923-1938.

Chapter 9
Final conclusions

Chapter 9 – Final conclusions

Novel functionalized titanate nanowires and nanotubes were synthesized using a hydrothermal method and further used as catalysts in photo(electro)degradation processes for emergent pollutants removal. The photodegradation of different pollutants, including phenol, caffeine, theophylline, sulfamethazine, and dyes, demonstrated that all the modified TNT/TNW samples had a higher photocatalytic ability when compared with the pristine ones.

The work developed in the framework of this dissertation included:

Titanate nanoparticles modified by organic sensitization (Chapter 2):

- For the TNT/TNW sensitized with ethylenediamine, the amine species were on the surface of the samples. The improvement in the photocatalytic activity of the NTNT and NTNW samples occurred due to the increase in the visible light absorption and the lower energetic requirements to activate these catalysts as a result of the lower bandgap energy when compared to the pristine samples. The h^+ , $\cdot\text{OH}$ and the presence of nitrogen oxidant species were the main species involved in the pollutants' degradation processes.

Titanate nanoparticles modified by metallic silver nanoparticles combination (Chapter 3):

- The protonated titanate nanowires, HTNW, were modified by sensitization with Ag nanoparticles. In this case, the Ag^+ immobilization occurred mainly in interlayers, replacing Na^+ and Ag metallic nanoparticles in the HTNW surface. The Ag-HTNW photocatalyst reusability was examined in successive phenol degradation runs, and an increase of the Ag metallic nanoparticles was observed during these experiments, due to the continuous Ag^+ reduction, leading to the formation of Ag^0 nanoparticles on the surface. This result showed that it is possible to simultaneously prepare Ag nanoparticles and degrade a pollutant, without loss of photocatalytic performance. The photodegradation process when the Ag-HTNW was used as catalyst, occurred by h^+ , $\cdot\text{OH}$ radicals and by $\text{O}_2^{\cdot-}$ species formed at the Ag nanoparticles surface.

TNW/TNT modified by transition metals, by ion-exchange and/or doping (Chapters 4-7):

- The modification of TNW by the Co ion-exchange method was, as expected, only by Na^+ replacement on the interlayers. For the samples modified by Co doping (1% and 5%, nominal), a replacement by $\text{Ti}^{4+}/\text{Co}^{2+}$ was obtained. The doped sample with higher cobalt content (5%) showed also a replacement of the Na^+ ions. This happens for high metal content precursors due to the dissolution in NaOH solution during the hydrothermal process. All the Co-modified TNW samples absorbed radiation in the visible region, and the optical redshifts can be assigned to the insertion of the Co 3d orbitals within the forbidden band.

The photocatalytic activity of these Co modified materials was mainly due to the introduction of intermediate levels in the forbidden band, which contribute to the e^-/h^+ recombination rate decrease. Furthermore, a lower doping level (1%) showed to be more efficient for the pollutants' photocatalytic removal. Concluding that the cobalt replacement only in Ti^{4+} improved the catalytic activity of the samples for the photodegradation processes studied.

- The TNT and TNW particles modification by doping with ruthenium (1% of Ru, nominal) showed that a higher amount of Ru was incorporated in the RuTNW sample, contrasting with some Ru loss that occurred during the two steps required for the RuTNT production. In the RuTNW sample, the Ru^{n+} is replacing Ti^{4+} , and Na^+ in the interlayers. However, in the RuTNT sample, the Ru is only replacing the Ti^{4+} . For both Ru-containing samples, the improvement of the photocatalytic behavior was due to a decrease in the e^-/h^+ recombination rate. However, the best photocatalytic activity was obtained with the RuTNT sample, which could be due to the lower Ru content and the substitution only in the Ti^{4+} .
- The co-doping sample, FeMnTNW, was obtained from vestigial metal contamination of an initial reagent during precursor synthesis. The Mn and Fe were incorporated in the TNW structure by replacement of Na^+ in the interlayers, together with some Ti^{4+} substitution. The most active species in caffeine degradation with the FeMnTNW sample were the $\cdot OH$ and $O_2^{\cdot -}$ radicals. The FeMnTNW photocatalytic behavior was mainly associated with the e^-/h^+ recombination rate reduction, due to the introduction of intermediate energetic levels in the forbidden zone, as a result of the presence of ionic Mn and Fe species. Furthermore, the Fe and Mn redox reactions created the ideal conditions for a parallel photo-Fenton process, which contributed to the pollutants' degradation improvement.

Also included in this research was the TNT and TNW immobilization in films to be used as catalysts in pollutants photo(electro)degradation (Chapter 8).

- The TNT/TNW modified with cobalt and ruthenium were successfully immobilized on an ITO substrate by drop-casting method directly and by drop-casting followed by the electropolymerization of 1,8-diaminocarbazole (DAC). All the films had a catalytic activity for the methylene blue and theophylline photodegradation. The best photocatalytic performance was obtained with the ITO/TNT-Ru/PDAC film.

For the Ru-containing films, no differences were found on the photocatalytic activity for the films with and without polymer, making possible the reutilization of both samples. However, for Co-containing films, the presence of the polymer (PDAC) improved the photocatalytic ability for the degradation of the pollutants studied.

Chapter 10
Methods and experimental

Chapter 10 – Methods and experimental

This chapter presents the details related to the development of the experimental work and a brief description of the nanoparticles synthesis conditions and all the characterization techniques used. Examples of the calculations carried out, for the determination of bandgap energy, valence band, crystallite sizes, pollutant degradation rates and kinetic of the degradations are also presented.

10.1 - Reagents

All reagents used during this research were of analytical or chemical-grade (Aldrich, Fluka, Acros or similar) and were used as received. The solutions were prepared with distilled water. However, for the electrochemical and photo(electro)degradation experiments deionized water (Millipore) was used, for the results shown in Chapter 8.

All chemical compounds not used or resulting from the reactions were placed in appropriate containers and/or discarded according to safety procedures.

10.2 – Synthesis

During this research work, all the syntheses start with the preparation of an amorphous precursor. This precursor can be used for the preparation of a titanium dioxide (TiO_2) nanoparticles in an aqueous media (using distillate water), or for the preparation of titanate nanowires (TNW) in alkaline media (using a 10 M sodium hydroxide solution, NaOH). For the preparation of titanate nanotubes (TNT) was used the TiO_2 nanoparticles, previously prepared, in alkaline media.

10.2.1 - TiO_x amorphous precursor synthesis

The amorphous precursor (with a titanium-to-oxygen ration of 0.25:1 [1]) was prepared using a procedure previously reported [1,2]. A titanium trichloride solution (TiCl_3 , 10 or 20 wt.% in 20-30 wt.% HCl) diluted in a ratio of 1:2 in 2 M hydrochloric acid (HCl) solution was used as the titanium source. To this solution, a 4 M ammonia aqueous solution was added dropwise under vigorous stirring, until complete precipitation of a white solid. The resulting suspension was kept overnight at room temperature and then filtered and vigorously rinsed with deionized water in order to remove the remaining ammonia and chloride ions. The white solid obtained (precursor) was afterward stored and used to prepare the titanate nanostructures samples (such as nanotubes, nanowires, nanoparticles) and/or TiO_2 nanoparticles.

10.2.2 - Ru-doped precursor

The ruthenium doped precursor was obtained using a similar procedure using for the undoped precursor (section 10.2.1) by adding the required molar amount (1%, nominal) of ruthenium (III) chloride, RuCl_3 , to the titanium-containing solution. In this case, after ammonia solution precipitation, a dark precursor was obtained.

10.2.3 - Co-doped precursor synthesis

The cobalt doped precursor was obtained using an identical synthesis procedure using for the undoped precursor (section 10.2.1) by adding the required molar amount (nominal percentage of 5% or 1%) of metallic cobalt (Johnson Matthey) to the titanium trichloride solution. The amount 0.1178 g (for Co 5%) and 0.0236 g (for Co 1%) of metallic cobalt powder was carefully dissolved in *ca.* 1 mL of concentrated nitric acid (HNO_3 , 65%). The deep purple solution was heated, to evaporate the solvent, and 2 mL of HCl solution (37%) was added to evaporate the residual nitrates, with the formation of yellow steam. After no yellowish steam was observed, the solution was diluted with 2 M HCl to the 100 mL final volume. This solution was added to 50 mL of TiCl_3 solution. After precipitation with 4 M ammonia solution, the Co-doped precursors were obtained as a bluish-grey solid (1% of Co) and a greenish dark grey solid (5% of Co).

10.2.4 - Titanate nanowires (TNW) synthesis

Sodium titanate nanowires (NaTNW) were synthesized using a hydrothermal approach. This synthesis was performed in an autoclave system using 10 g of precursor in *ca.* 70 mL of a sodium hydroxide (NaOH) 10 M aqueous solution, at 160°C for 24 hours. These conditions were used supported in a previous work [1], described as the ideals to obtain titanate nanowires. After natural cooling until room temperature, the powder was washed several times with water until pH 7 on the filtrate solution to obtain the TNW sample.

10.2.5 – Protonated titanate nanowires (HTNW) synthesis

Protonated titanate nanowires (HTNW) were obtained using the hydrothermal approach described above and a swift and highly controllable post-washing process. This synthesis was performed in an autoclave system (160°C for 24 hours) using 10 g of precursor in *ca.* 70 mL of a NaOH 10 M aqueous solution. After natural cooling until room temperature, the powder was washed several times with water until pH 7 on the filtrate solution to obtain the TNW (or NaTNW) sample. Afterward, this powder was stirred in an HNO_3 0.1 M aqueous solution for 4

hours, to produce the protonated sample (HTNW). The solid was then washed with water until pH 5 in the filtrate.

The elongated titanate nanoparticles ($\text{Na}_{2-x}\text{H}_x\text{Ti}_3\text{O}_7$ ($0 \leq x \leq 2$)) structure have layers of two-dimensional TiO_6 octahedral sheets intercalated by Na^+ ions, which can be exchanged with other ions, including H^+ . After acid treatment, all the Na^+ present in the interlayers can be replaced by H^+ and the structure changes to $\text{H}_2\text{Ti}_3\text{O}_7$.

10.2.6 – Titanium dioxide (TiO_2) nanoparticles synthesis

The TiO_2 samples were synthesized in an autoclave using ~ 10 g of the precursor in *ca.* 60 mL of distillate water. Based on previous works [2], the crystallization of the precursor to obtaining TiO_2 nanoparticles was performed at 200°C for 6 hours. After cooling and being washed several times with deionized water, the TiO_2 nanoparticles were dried and stored.

10.2.7 – Titanate nanotubes (TNT) synthesis

TNT particles were synthesized using the hydrothermal approach described in section 10.2.4, but using TiO_2 nanoparticles instead of the precursor. The synthesis was performed in an autoclave system (160°C, 24 hours) using 10 g of the previously prepared TiO_2 sample in *ca.* 70 mL of a 10 M NaOH aqueous solution. After cooling until room temperature, the powder was washed several times with water until the pH of the filtrate solution was 7, and afterward dried at 60°C.

10.2.8 – Ag-HTNW synthesis

HTNW modified with Ag nanoparticles were produced by a photo-reduction method. First, the HTNW particles (prepared as described in section 10.2.5) were treated with a 0.5 M silver nitrate (AgNO_3) aqueous solution during 24 hours, under vigorous stirring. After, the white solid was washed several times with distillate water to remove un-adsorbed Ag^+ ions. The formation of metallic silver was attained by irradiating the white solid aqueous suspension with a mercury lamp for 60 min.

Experimentally, the Ag^+ photo-reduction to metallic Ag was conducted using a 250 mL refrigerated photo-reactor [3]. A 450 W Hanovia medium-pressure mercury-vapor lamp was used as a radiation source; the total irradiated energy is 40-48% in the ultraviolet range and 40-43% in the visible region. The suspensions were prepared by adding 2 g of the powder to 150 mL of distilled water. After irradiation, the dark grey-brown suspensions were centrifuged, washed and dried at room temperature.

10.2.9 – TNT and TNW modification with amines - ethylenediamine (EDAmine)

The TNW and TNT samples were sensitized with EDAmine adding 2.5 mL of the amine to 50 mL of an acetone suspension containing 0.250 g of TNW or TNT. The suspensions were stirred at reflux temperature for 4 hours. After cooling to room temperature, NTNW and NTNT (crème solids) were isolated by centrifugation, washed with acetone and dried at room temperature over silica gel.

10.2.10 – Synthesis of ruthenium modified nanoparticles

• Ru-TiO₂ synthesis

The Ru-TiO₂ nanoparticles were produced using the Ru-doped precursor (section 10.2.2) in the same conditions used for TiO₂ nanoparticles synthesis, 200°C and 6 hours, (section 10.2.6). After being washed, the Ru-TiO₂ nanoparticles (dark solid) were dried and stored.

• RuTNW and RuTNT synthesis

The Ru-modified TNW and TNT particles were produced using 160°C and 24 hours of reaction. The two powders obtained through the hydrothermal treatment of the Ru-containing precursor and Ru-TiO₂ nanoparticles were labeled as RuTNW and RuTNT (dark brown solids), respectively.

10.2.11 – Synthesis of cobalt modified nanoparticles

• Co-TiO₂ synthesis

The Co-TiO₂ nanoparticles were produced using the Co-doped precursor (section 10.2.3) in the same conditions used for TiO₂ nanoparticles synthesis, 200°C and 6 hours, (section 10.2.6). After being washed, the Co-TiO₂ nanoparticles (bluish solid) were dried and stored.

• CoTNT and CoTNW synthesis

The CoTNW and CoTNT samples were synthesized in an autoclave using 10 g of Co-doped precursor and Co-TiO₂ nanoparticles, respectively, in *ca.* 70 mL of NaOH 10 M aqueous solution. The samples were prepared at 160°C for 24 hours. After cooling to room temperature, the suspensions were filtered, and the powders were washed several times with deionized water until a filtrate with pH = 7 was attained. The obtained Co-doped samples were identified as Co(1%)-TNW and Co(5%)TNW, and Co(1%)TNT and Co(5%)TNT.

These Co-doped TNT or TNW were obtained as a bluish solid (1% of Co) and a greenish dark grey solid (5% of Co).

• **TNW/Co and TNT/Co synthesis**

The Co ion-exchanged titanate nanostructures were synthesized using 10 g of TNT or TNW previously prepared in 60 mL of cobalt nitrate ($\text{Co}(\text{NO}_3)_2 \cdot 6\text{H}_2\text{O}$) aqueous solution, by adding the required Co molar amount of 1% and 5% related with Ti. The resulting suspensions were kept for 7 hours under stirring at room temperature. Afterward, the suspensions were vigorously rinsed with deionized water in order to remove the remaining cobalt ions. The obtained Co ion-exchanged samples were identified as TNT/Co($x\%$) and TNW/Co($x\%$) with $x = 1$ and 5. Afterward, these bluish solids were dried and stored.

10.3 – Nanoparticles characterization

10.3.1 – X-ray powder diffraction (XRD)

The samples identification and structural characterization were performed by XRD using a Philips Analytical X-ray diffractometer (PW 3050/60) with automatic data acquisition (X' Pert Data Collector (v2.0b) software), employing Cu $K\alpha$ radiation ($\lambda = 0.15406$ nm) working at 40 kV/30 mA. The diffraction patterns were collected in the 2θ range $5^\circ - 60^\circ$ with a 0.02° step size and an acquisition time of 200 s/step. For crystallite size calculations, the acquisitions were done in the $5^\circ - 15^\circ$ 2θ range, using an acquisition time of 600 s/step.

To be possible the XRD characterization, samples were prepared by placing the TNP powder on a silicon support.

The $K\alpha_2$ contribution was removed before the XRD pattern analyses. The 2θ angular position of the diffraction peaks and their full-width at half maximum, β , were calculated by fitting the experimental diffraction lines with a Pseudo-Voigt function. The β values were corrected taking into account the instrumental broadening.

• **Crystallite size determination:**

The crystallite size determination is possible using the Scherrer equation [4,5]:

$$D = \frac{K\lambda}{\beta \cos\theta} \quad (10.1)$$

D is the average crystallite size, K a constant that depends on the crystallite shape ($K = 0.89$ for spherical crystallites), λ the incident radiation wavelength, θ the Bragg diffraction angle of the

peak of highest intensity, β is the width at half-height of the highest intensity peak defined by $\beta^2 = \beta_m^2 - \beta_s^2$ where β_m and β_s are the half-height widths of the sample and pattern diffraction peaks, respectively. The standard is a highly crystalline compound, such as polycrystalline silicon, which allows correcting peak widening due to instrumental factors [4].

10.3.2 - Transmission electron microscopy (TEM)

The TEM images and high-resolution transmission electron microscopy (HRTEM) images were obtained using a JEOL 200CX microscope operating at 300 kV. Perforated copper grids with a formvar film were used to support the samples containing elongated particles.

10.3.3 - Energy-dispersive X-ray spectroscopy (EDS)

The samples elemental composition was evaluated by energy-dispersive X-ray spectroscopy (EDS) using a ThermoNoran model SystemSix spectroscope coupled to the TEM equipment.

10.3.4 – Specific surface area determination (B.E.T. method)

Specific surface areas were obtained by the B.E.T. method, from nitrogen (AirLiquide, 99.999%) adsorption data at -196°C , using a volumetric apparatus from Quantachrome mod NOVA 2200e. The samples, weighing approximately 55 mg, were previously degassed for 2.5 hours at 300°C at a pressure lower than 0.133 Pa.

10.3.5 – Micro X-ray fluorescence (μXRF)

The quantification of the metal immobilized in the titanate nanostructures (silver and ruthenium) was attained by micro X-ray fluorescence (μXRF). The XRF equipment was an M4 Tornado from Bruker comprising an Oxford Instruments Eclipse IV X-ray source with an anode of Rh and a 250 μm thick Be window (50 kV, 300 μA , 150 s) with a poly-capillary lens, offering a spot size down to a 25 μm at a working distance of 10 mm, coupled to an XFlash[®] silicon drift detector (SDD) technology, with a 30 mm^2 sensitive area and an energy resolution < 145 eV. Several spot analyses were carried out and the elemental quantification was performed using ESPRIT software.

10.3.6 - Diffuse reflectance spectroscopy (DRS)

The optical characterization of the prepared samples was obtained on a UV–vis spectrometer Shimadzu UV-2600PC equipped with an ISR 2600 plus integrating sphere, in the wavelength range of 200-1400 nm, and using barium sulfate (BaSO_4) as reference.

The bandgap energy (E_g) of the samples was calculated from their diffuse reflectance (R) spectra, using the Kubelka–Munk (KM) spectra (after conversion of diffuse-reflectance to KM). Through the relation $F_{KM}(R) = (1 - R)^2/2R$, and by plotting the function $f_{KM} = (F_{KM}.hv)^2$ versus hv , where h stands for Planck's constant and ν for the radiation frequency, E_g is obtained by extrapolating the linear portion of the curve to zero absorption [6], as explained in the following example:

• **Bandgap energy determination:**

In semiconductors, the function that relates energy to the absorption coefficient $\alpha(h\nu)$ can be expressed as follows:

$$\alpha = \frac{\alpha_0(h\nu - E_g)^n}{h\nu} \quad (10.2)$$

for direct and indirect transitions. For direct transitions $n = 1/2$ and for indirect transitions $n = 2$. For titanate nanoparticles and high values of α , nearby to the bandgap, a direct transition ($n = 1/2$) is expected to occur:

$$(\alpha h\nu)^2 = \alpha_0(h\nu) - \alpha_0 E_g \quad (10.3)$$

Plotting the graph $(\alpha.h\nu)^2$ versus $(h\nu)$ it is possible to determine the bandgap energy, as shown in the example:

- 1) Considering the following optical spectrum, from a TNW sample:

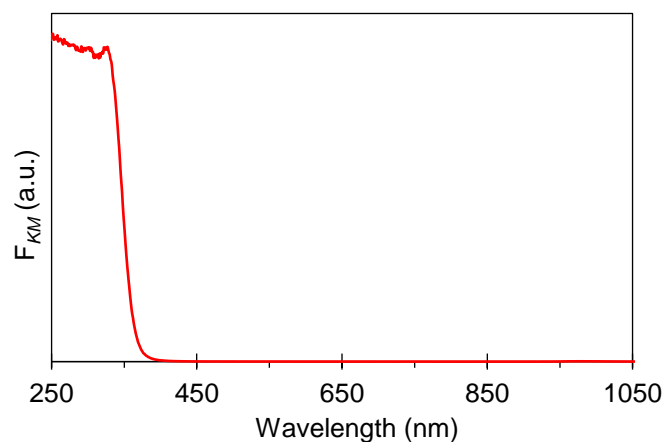


Figure 10.1 – Absorption spectra of a TNW sample.

- 2) considering that 1 nm corresponds to 1239.84 eV it is possible to convert λ in $(h\nu)$;

- 3) as the absorbance of a sample is directly proportional to the absorption coefficient (assuming that the optical path does not change) then $(\alpha \cdot hv)^2$ corresponds to $k \cdot (KM \cdot hv)^2$ where k is a constant;
- 4) the representation of $(KM \cdot hv)^2$ as a function of (hv) , where h stands for Planck's constant and ν for the radiation frequency, as illustrated in Figure 10.2:
- 5)

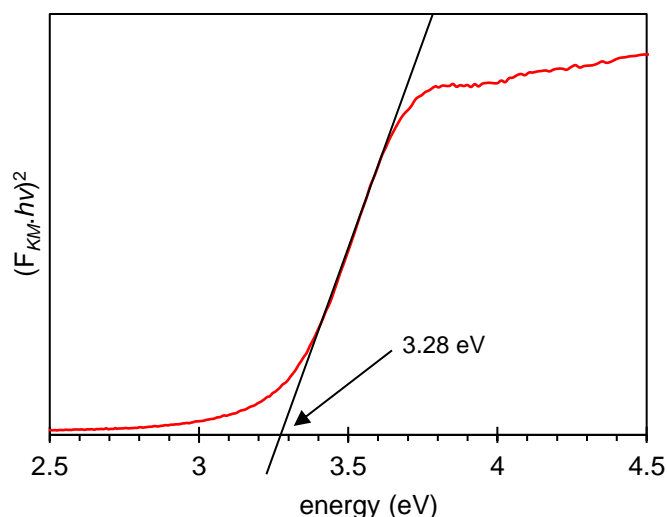


Figure 10.2 – Representation of the function $(F_{KM} \cdot hv)^2$ versus hv , for the bandgap energy (of a TNW sample) determination.

- 6) in the region nearby to the absorption band, the graph corresponds to a line whose intercept with the xx axis corresponds to the value of the bandgap energy (3.28 eV, in this case). E_g is obtained by extrapolating the linear portion of the curve to zero absorption.

10.3.7 – Photoluminescence spectroscopy (PL)

The photoluminescence spectra were measured on a SpexFluorolog 3-22/Tau 3, using 20 mg of samples. The excitation was performed at 280 nm, and the emission acquisition on the wavelength range of 350 to 610 nm.

10.3.8 – X-ray photoelectron spectroscopy (XPS)

The XPS analyses were performed at CEMUP - Centro de Materiais da Universidade do Porto, using a Kratos AXIS Ultra HSA, with VISION software for data acquisition and CASAXPS software for data analysis. The analyses were performed with a monochromatic Al $K\alpha$ X-ray source (1486.7 eV), operating at 15kV (90 W), in FAT mode (Fixed Analyser Transmission), with a pass energy of 40 eV for regions ROI and 80 eV for the survey.

Data acquisition was performed with a pressure lower than $1.E^{-6}$ Pa, and it was used a charge neutralization system. The effect of the electric charge was corrected by the reference of the carbon peak (285 eV). The deconvolution of spectra may be carried out using the XPSPEAK41 or CasaXPS programs, in which a peak fitting is performed using Gaussian-Lorentzian peak shape and Shirley (or Linear) type background subtraction.

The valence band energy (VB) of the samples was determinate from the XPS high-resolution spectra of the O $2p \rightarrow$ Ti $3d$ transition, as explained in the example:

• **Valence band (VB) determination:**

The bandgap energy of a semiconductor corresponds to the difference between the energy of the higher level of the valence band and the lower level of the conduction band. For elongated titanate materials, this energy corresponds to the O $2p \rightarrow$ Ti $3d$ transition. To allow the energetic quantification of this transition, the valence band spectrum (VB-XPS) of each sample was recorded (Figure 10.3 shown an example for a TNW sample). A linear method (extrapolation of the leading edge to the extended baseline of the VB spectra) was used to calculate the position of the valence band [7], as shown in Figure 10.3. The corresponding conduction band (CB) energy was posteriorly calculated using the expression: $E_g = VB - CB$.

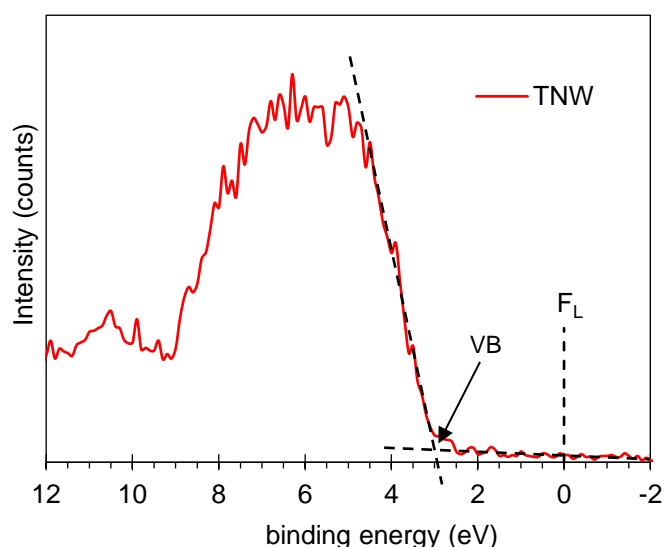


Figure 10.3 – XPS high-resolution spectra of the O $2p$ to Ti $3d$ transition, used for valence band determination (of a TNW sample).

10.3.9 – Raman spectroscopy

For the titanate nanoparticles modified with ethylenediamine (Chapter 3) the analysis by Raman spectroscopy was carried out at CICECO - Centro de Investigação em Materiais Cerâmicos e

Compósitos da Universidade de Aveiro, using an FT Raman Bruker RFS 100/S spectrometer and spectra acquisition were obtained after 300 scans and a resolution of 4 cm^{-1} .

In Chapter 5, for the characterization of cobalt modified nanoparticles, a room temperature micro-Raman spectra were measured using a Jobin–Yvon T64000 spectrometer equipped with liquid nitrogen cooled CCD detector using the 514.5 nm excitation line of an Ar^+ laser, with an incident power of 0.4 mW or 4 mW on the sample surface in approximately 1 mm spot, a $20\times$ objective lens with a spectral resolution of 1 cm^{-1} and backscattering geometry. Several spectra were recorded in different places of each sample using two incident powers of 0.4 mW and 4 mW , with no significant differences being detected. These analyses were carried out at Centro de Física da Universidade do Minho.

Raman spectra of all the ruthenium modified and pristine TNT/TNW materials (Chapters 5 and 6) were obtained, at CICECO - Centro de Investigação em Materiais Cerâmicos e Compósitos da Universidade de Aveiro, using a combined Raman-AFM-SNOM confocal microscope WITec alpha300 RAS+ (WITec, Ulm, Germany). An Nd: YAG laser operating at 532 nm was used as the excitation source with the power set at 1 mW . Raman spectra were collected with a $100\times$ objective lens with an acquisition time of 2 s and 10 acquisitions. Raman imaging experiments were performed by raster-scanning the laser beam over the samples and accumulating a full Raman spectrum at each pixel. Raman images were constructed by integrating over specific Raman bands using WITec software for data evaluation and processing.

10.3.10 – Point of zero charge (p.z.c.)

The zeta potential analyses were performed in CICECO - Centro de Investigação em Materiais Cerâmicos e Compósitos da Universidade de Aveiro, using a Malvern NanoZS Zetasizer working at 148 V . The samples were suspended in aqueous media and NaOH or HCl aqueous solutions were used to adjust the suspension pH between 2 and 6.

10.4 – Photocatalytic experiments

The photodegradation experiments were conducted using a 250 mL refrigerated photo-reactor (Figure 10.4). A 450 W Hanovia medium-pressure mercury-vapor lamp was used as a radiation source; the total irradiated light is $40\text{-}48\%$ in the ultraviolet range and $40\text{-}43\%$ in the visible region of the electromagnetic spectrum. For the visible light experiments, a Pyrex filter was used.

The catalytic photodegradation experiments were performed by adding 20 mg of catalyst to 150 mL of pollutant aqueous solutions. Prior to irradiation, suspensions were stirred in darkness for 60 min to ensure adsorption equilibrium. For convenience, during this work, the adsorption time (1 hour) is marked in the graphics before $t = 0$. During irradiation, suspensions were sampled at regular intervals, centrifuged and analyzed by gas chromatography-mass spectrometry (GC-MS), UV-vis spectrophotometry or liquid chromatography high-resolution with electrospray ionization coupled to mass spectrometry (LC-HR-ESI/MS) depending on the organic compound (see below).

To study the reusability of the catalysts, all the experimental parameters were kept constant and the photodegradation measurements were repeated for four trials using the same catalyst and fresh pollutant solutions. After each photodegradation experiment, the catalyst was centrifugated and washed/cleaned with distilled water to remove any organic contamination from the previous run. During this process, the stability of the photocatalysts was studied by XRD, TEM, Raman, and DRS.

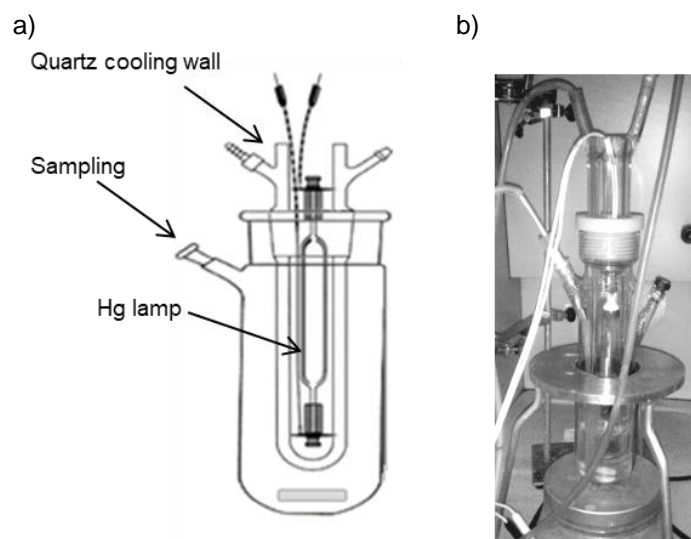


Figure 10.4 – (a) Representation and (b) photograph of the photo-reactor used in the photocatalytic experiments.

10.4.1 - Fluorescence spectroscopy

Fluorescence spectra of 2-hydroxyterephthalic acid (HTA) were measured on a SpexFluorolog 3-22/Tau 3, with excitation and emission wavelengths 315 and 425 nm, respectively. The emission acquisition was performed in the wavelength range 320 – 575 nm, using a quartz cell with four sides cleaned (*i.e.* all transparent walls).

• Production of hydroxyl radical ($\cdot\text{OH}$)

The photocatalytic degradation of terephthalic acid (TA) was performed to evaluate the production of the hydroxyl radical. This probe molecule is a natural $\cdot\text{OH}$ scavenger and the production of the oxidant can be followed through the formation/detection, during catalyst irradiation, of the fluorescent 2-hydroxyterephthalic acid (HTA). The TA photocatalytic experiments were carried out using a fresh 3 mM TA solution (prepared in 0.01 M NaOH aqueous solution) and 10 mg of each sample and the conditions described in section 10.4. During irradiation, the suspensions were sampled at regular intervals, centrifuged and analyzed by fluorescence spectroscopy. For some samples, the TA degradation experiment was also performed in the absence of O_2 (during the reaction the suspension was purged with high-purity (99.999%) N_2 by Air Liquide) to be able to analyze a possible mechanism of charge-transfer during samples irradiation.

10.4.2 – UV-vis spectrophotometry

A UV-vis spectrophotometer Shimadzu UV-2600PC was used for monitoring the absorption of dyes, such as brilliant green (BG) and naphthol yellow S (NYS) solutions.

• Photocatalytic degradation efficiency determination:

The photocatalytic degradation efficiency could be calculated as follows:

$$\eta = \frac{C_0 - C}{C_0} \times 100 \quad (10.4)$$

where C_0 is the initial concentration of pollutant before photocatalytic reaction (mg L^{-1}) and C is the real-time concentration of pollutant after light irradiation (mg L^{-1}).

10.4.3 – Gas chromatography-mass spectrometry (GC-MS)

A GC-MS was used to evaluate the phenol degradation and their by-products identification. The conversion of products was monitored by taking samples, at different times of irradiation, and analyzing them using a Shimadzu QP2100-Plus GC/MS system with a capillary column Tecknokroma TRB-5MS.

10.4.4 – Liquid chromatography high-resolution with electrospray ionization coupled to mass spectrometry (LC-HR-ESI/MS)

The identification and quantification of caffeine, theophylline, sulfamethazine, diclofenac and carbamazepine, and their by-products were performed by LC-HR-ESI/MS, on a QqTOF Impact II™ mass spectrometer equipped with an ESI source (Bruker Daltonics, Germany) and interfaced with a Dionex UltiMate® 3000 RSLCnano (Thermo Fisher Scientific Inc., USA). The LCnano system was composed of an RSLCnano HPG pump, an NCS-3500RS column compartment, and a thermostatted WPS-3000TPL autosampler. The separation was carried out with a Hypersil Gold C18 column 150 x 2.1 mm, 1.9 μm (Thermo Fisher Scientific Inc., USA) at 35°C constant temperature. The mass spectrometer was operated in the ESI positive ion mode operating in the high-resolution mode. The optimized parameters were: ion spray voltage, 4.5 kV; endplate offset, -500 V, nebulizer gas (N₂), 2.8 bars; dry gas (N₂), 8 L min⁻¹; dry heater, 200°C. The mass spectra were acquired on the bbCID mode over a mass range of 50-1000 *m/z*, and a spectra rate of 1 Hz. The calibration of the TOF analyzer was performed with a 10 mM sodium formate calibrant solution. Data was processing using Data Analysis 4.1 software (Bruker Daltonics, Germany)

10.5 – Nanocomposite films preparation, characterization and application in pollutants photo(electro)degradation

10.5.1 – Films preparation

Different methods were used to immobilize the titanate nanostructures, such as drop-casting method, drop-casting followed by electropolymerization of 1,8-diaminocarbazole monomer (DAC) (Figure 10.5).

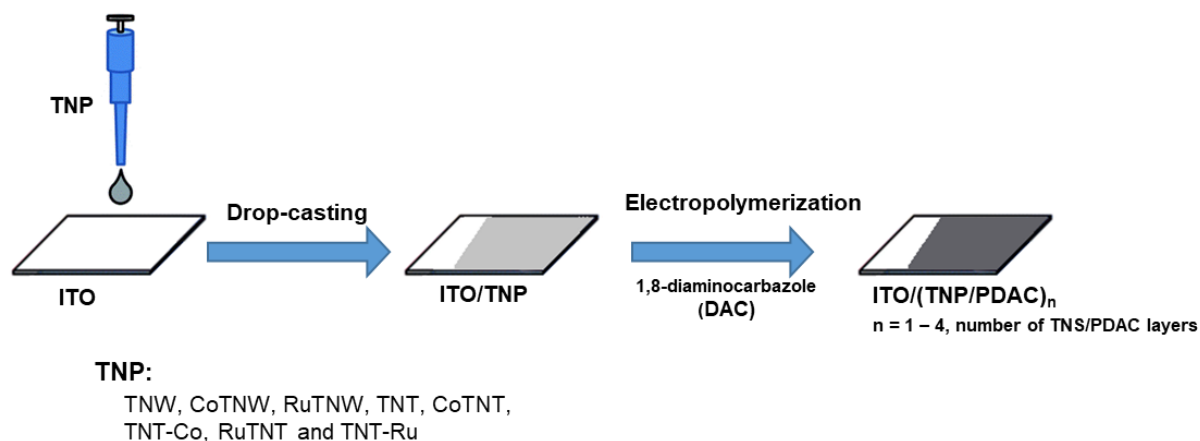


Figure 10.5 – Schematic representation of TNP deposition methods used.

• Drop-casting films preparation

The immobilization of the nanostructures and metal-modified TNW or TNT (*e.g.* cobalt and ruthenium) was carried out on indium tin oxide (ITO) coated quartz glass substrates (1 cm x 2 cm) by a drop-cast methodology, using 15 μL of a 1 mg mL^{-1} suspension in Millipore distillate water. In order to obtain a better contact with the ITO and the nanostructures, before the preparation of the samples, the ITO surface was activated in a NaOH 0.1 M solution followed by an H_2SO_4 0.1 M solution, and then washed with Millipore water.

The obtained samples were identified as pristine and metal modified ITO/MTNW, ITO/TNW-M, ITO/MTNT and ITO/TNT-M (M = Co or Ru).

• DAC Electropolymerization

The electropolymerization of 1,8-diaminocarbazole (DAC) [8] was carried out, obtaining the poly(1,8-diaminocarbazole) (PDAC). This conductive polymer, PDAC, was deposited by electropolymerization, above the pristine and modified ITO/TNT and ITO/TNW samples.

Electrochemical synthesis of PDAC was carried out in a single-compartment cell (as illustrated in Figure 10.6) with a platinum wire counter electrode and a silver wire reference electrode (in 0.1 M LiClO_4).

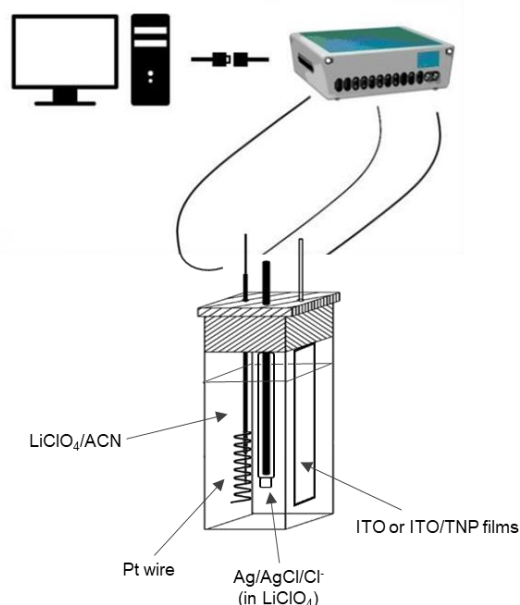


Figure 10.6 - Representation of the cell used for electropolymerization and electrochemical characterization.

The working electrode was an ITO substrate (surface area of 1.2 cm^2). PDAC was obtained by cyclic voltammetry using a PGSTAT 30N (Metrohm, Autolab, The Netherlands) in the -0.1 to 1.0 V potential range and a scan rate of 60 mV s^{-1} . A 2 mM 1,8-diaminocarbazole solution

in acetonitrile containing 0.1 M LiClO₄ as supporting electrolyte was used. Films with different polymer thickness were obtained using 2 or 20 cycles.

These obtained films were labeled as pristine and metal modified ITO/MTNW/PDAC, ITO/MTNT/PDAC and ITO/TNT-M/PDAC (M = Co or Ru).

10.5.2 – Modified electrodes characterization

• Cyclic voltammetry

After electrodes modification, a four successive cyclic voltammograms (CV) characterization was performed using the same apparatus (Figure 10.6, in monomer free solution) used for electropolymerization (section 10.5.1), in the potential range from -0.25 to 0.75 V using as electrolyte a 0.1 M LiClO₄ in acetonitrile solution.

• Optical characterization

The optical absorption properties of the modified electrodes, within the range of 200–800 nm, were analyzed using a Shimadzu UV-3600 spectrometer equipped with an integrating sphere and BaSO₄ as reference.

• Morphology characterization

The morphology of the films was analyzed by scanning electron microscopy (SEM) in a field emission gun – scanning electron microscope JEOL-7001F (FEG-SEM), operating at 5 kV.

During the development of the work during the stay in Warsaw, Poland, a field-emission scanning electron microscope FE-SEM (Merlin, Carl Zeiss) operating at 3 kV was also used to examine the morphology of some of the films.

• Photoelectrochemical characterization

Photoelectrochemical measurements were performed with the potentiostat AUTOLAB PGSTAT 302N Metrohm Autolab (The Netherlands). In a cell with three electrode compartments, ITO/TNT/PDAC or ITO/TNT were used as working electrodes (approx. 1 cm² geometrical working surface area), Ag/AgCl/Cl⁻ (3 M KCl) as a reference electrode, and Pt wire as a counter electrode. The experiments were carried out in an aqueous solution of 0.1 M Na₂SO₄. The working electrode was illuminated with arc 450 W Xenon lamp (OPTEL, Poland) at a power density of 100 mW cm⁻², and also with a device based on high-power LED (365 nm) described elsewhere [9] at the continuous magnetic stirring of the solution. The power density

of illumination in the place of the sample, measured with IL1700 International Light (USA) radiometer was 100 mW cm^{-2} .

For the photocurrent measurements, the electrodes were polarized at a constant potential of 0.7 V in 0.1 M Na_2SO_4 aqueous solution in dark and under illumination with a xenon lamp.

Photocurrent measurements were also performed using identical conditions with the electrodes polarized at 0.5 V constant potential and using a high-power LED (365 nm). This potential was chosen since it is located at the beginning of the photocurrent plateau formed in the CV recorded in the same conditions. Figure 10.7 shown the cell used for the photoelectrochemical characterization under illumination with a Xe lamp and a LED (365 nm) device.

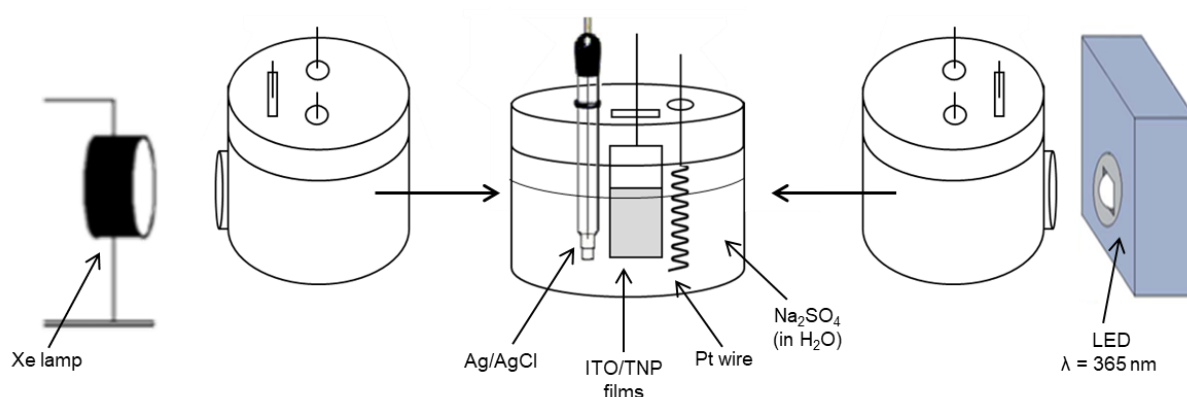


Figure 10.7 - Representation of the cell used in the photoelectrochemical characterization using a Xe lamp and a LED (365 nm).

The current spikes formed just after switching the light on are evidence of electron-hole surface recombination, competing with the light-driven electrode reactions at the semiconductor/solution interface [10]. The ratio of the rate constants for the charge transfer across the semiconductor/solution interface (k_{tr}) and electron-hole recombination (k_{rec}), by analysis of the current transients according to the protocol proposed by Peter [10], using the equation:

$$\frac{j(\infty)}{j(0)} = \frac{k_{tr}}{k_{tr} + k_{rec}} \quad (10.5)$$

where j_{∞} is the steady-state current density and j_0 is photocurrent in $t = 0$.

For example, the k_{tr}/k_{rec} ratio obtained for the ITO/PDAC is 0.176, being higher than that for ITO (0.124). This difference can be associated with the lower rate of the electron-hole recombination in the ITO sample.

10.5.3 – Photodegradation experiments

Photocatalytic experiments were performed in a standard quartz cuvette with a width of 2 cm and an optical path length of 1 cm (4 transparent walls), as illustrated in Figure 10.8.

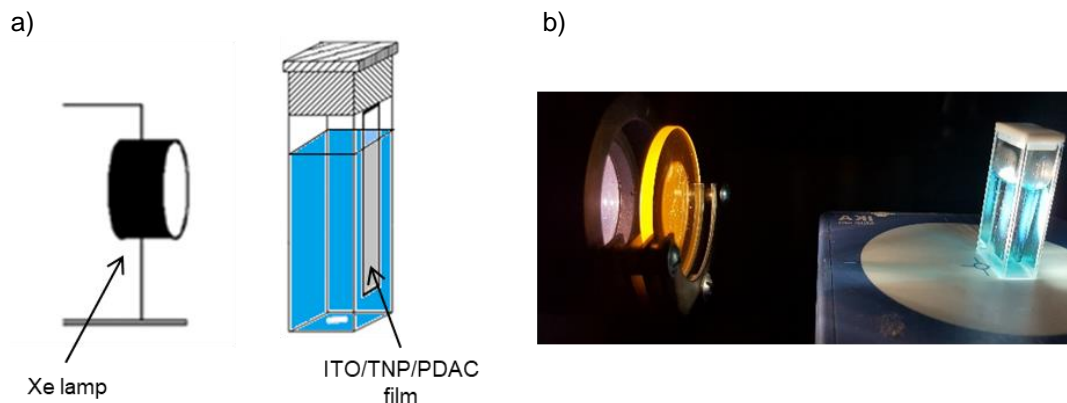


Figure 10.8 - (a) Schematic representation and (b) photography of the reactor used in the photocatalytic experiments.

The ITO/TNP/PDAC composites, deposited only on one side of the ITO substrate, was placed on the sidewall of the cuvette (Figure 10.8(a)).

A 450 W arc xenon lamp (OPTTEL) with a power density of 100 mW cm^{-2} , was used as the irradiation source. For the experiments with visible light, a UV filter cutting off the radiation below 400 nm was used.

The catalytic photodegradation experiments were performed using the ITO/TNP/PDAC films with an identical geometric area (1.2 cm^2) and 5 mL of 10 ppm methylene blue or 5 ppm of theophylline aqueous solutions. The films were immersed in the pollutant solution and prior to irradiation, the solutions were kept in darkness for 1 hour to ensure the adsorption equilibrium. During irradiation, the solutions were directly analyzed by UV–vis spectroscopy (in a spectrophotometer Shimadzu UV-3600 in the wavelength range from 800 to 500 nm) at regular intervals. In such an experimental arrangement there was no need to remove the catalyst from the pollutant solution, and the measurements were recorded using the cuvette with this film/solution.

The spectra of the solution were recorded in 5-, 15- or 30- min time intervals. For comparison reasons, the photodegradation experiments were also performed using the samples in powder (not supported). For these experiments, the same amount of TNP used in the preparation of films was used to be able to the comparison.

10.5.4 – Photo(electro)degradation experiments

The photo(electro)degradation experiments were performed using an AUTOLAB PGSTAT 302N Metrohm Autolab (The Netherlands) potentiostat. Figure 10.9 shown the representation and the photography of the cell used for the photo(electro)degradation experiments.

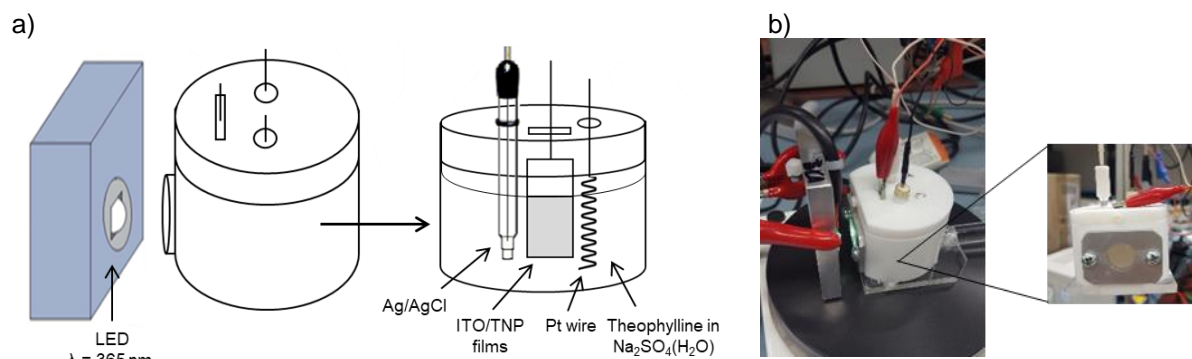


Figure 10.9 - (a) Schematic representation and (b) photography of the cell used in the photo(electro)catalytic experiments.

A cell with three compartments was used. ITO/TNT samples were used as working electrodes (approx. 1 cm^2 geometrical working surface area), Ag/AgCl/Cl⁻ (3 M KCl) as a reference electrode, and Pt wire as a counter electrode. The experiments were carried out with a 5 ppm theophylline solution prepared in 0.1 M Na₂SO₄ aqueous solution. The UV-vis spectra were collected at each 30 min periods, until a total time of 2 hours. During irradiation, with a high-power LED (365 nm), the solution was continuous stirring, using the same conditions used on the photoelectrochemical characterization of the samples (section 10.5.2).

10.6 – References

- 1 - E.K. Ylhäinen, M.R. Nunes, A.J. Silvestre, O.C. Monteiro, Synthesis of titanate nanostructures using amorphous precursor material and their adsorption/photocatalytic properties, *J. Mater. Sci.* 47 (2012) 4305-4312.
- 2 - M.R. Nunes, O.C. Monteiro, A.L. Castro, D.A. Vasconcelos, A.J. Silvestre, A new chemical route to synthesise TM-doped (TM = Co, Fe) TiO₂ nanoparticles, *Eur. J. Inorg. Chem.* 2008 (2008) 961-965.

- 3 - A. Franco, M.C. Neves, M.M.L. Ribeiro Carrott, M.H. Mendonça, M.I. Pereira, O.C. Monteiro, Photocatalytic decolorization of methylene blue in the presence of TiO₂/ZnS nanocomposites, *J. Hazard. Mater.* 161 (2009) 545-550.
- 4 - M.T. Weller, *Inorganic materials chemistry*, Oxford Science Publications, 1994, New York.
- 5 - V. Uvarov, I. Popov, Metrological characterization of X-ray diffraction methods for determination of crystallite size in nano-scale materials, *Materials Characterization* 58 (2007) 883-891.
- 6 - B. Barrocas, M.C. Neves, M. Conceição Oliveira, O.C. Monteiro, Enhanced photocatalytic degradation of psychoactive substances using amine-modified elongated titanate nanostructures, *Environ. Sci.: Nano* 5 (2018) 350-361.
- 7 - T.-D. Nguyen-Phan, S. Luo, D. Vovchok, J. Llorca, S. Sallis, S. Kattel, W. Xu, L.F.J. Piper, D.E. Polyansky, S.D. Senanayake, D.J. Stacchiola, J.A. Rodriguez, Three-dimensional ruthenium-doped TiO₂ sea urchins for enhanced visible-light-responsive H₂ production, *Phys. Chem. Chem. Phys.* 18 (2016) 15972-15979.
- 8 - M. Skompska, M.J. Chmielewski, A. Tarajko, Poly(1,8-diaminocarbazole) – A novel conducting polymer for sensor applications, *Electrochem. Commun.* 9 (2007) 540-544.
- 9 - M. Kwiatkowski, I. Bezverkhy, M. Skompska, ZnO nanorods covered with a TiO₂ layer: simple sol-gel preparation, and optical, photocatalytic and photoelectrochemical properties, *J. Mater. Chem. A* 3 (2015) 12748-12760.
- 10 - L.M. Peter, Energetics and kinetics of light-driven oxygen evolution at semiconductor electrodes: The example of hematite, *J. Solid State Electrochem.* 17 (2013) 315-326.

Annexes

Annexes

Annex A - ICDD-JCPDS files

Table A.1 – ICDD-JCPDS file no. 72-0148 ($\text{Na}_2\text{Ti}_3\text{O}_7$).

2θ (°)	I	h	k	l
9.875	29	0	0	1
10.527	999	1	0	0
12.919	47	-1	0	1
15.842	280	1	0	1
19.825	52	0	0	2
20.517	1	-1	0	2
21.144	8	2	0	0
21.483	47	-2	0	1
24.324	6	1	0	2
25.151	2	2	0	1
25.689	323	1	1	0
26.006	23	-2	0	2
26.789	4	-1	1	1
28.357	117	1	1	1
29.678	45	-1	0	3
29.929	130	0	0	3
30.827	64	0	1	2
31.289	70	-1	1	2
31.716	69	2	1	0
31.943	99	2	0	2
31.943	99	-2	1	1
33.141	36	-2	0	3
33.818	53	1	0	3
33.981	76	1	1	2
34.182	132	-3	0	2
34.596	74	2	1	1
35.241	46	-2	1	2
35.443	67	3	0	1
38.112	21	-1	1	3
38.313	51	0	1	3
39.450	9	-3	0	3
39.584	7	-3	1	1
39.999	4	3	1	0
39.999	4	2	1	2
40.277	6	0	0	4
40.420	3	2	0	3
40.947	1	-2	1	3

Table A.1 – (Continued)

2θ (°)	l	h	k	l
41.302	2	3	0	2
41.513	5	1	1	3
41.820	16	-3	1	2
42.888	14	3	1	1
43.055	20	4	0	0
43.771	208	-4	0	2
43.883	312	1	0	4
46.327	41	4	0	1
46.327	41	-3	0	4
47.085	9	-3	0	4
47.085	11	0	1	4
47.211	11	2	1	3
47.782	204	0	2	0
48.841	6	3	0	3
49.071	19	1	2	0
49.557	4	4	1	0
49.711	4	-1	2	1
49.840	13	-1	0	5
49.840	13	2	0	4
50.201	61	-4	1	2
50.302	44	1	1	4
50.656	14	1	2	1
50.981	1	0	0	5
51.274	5	-2	0	5
51.629	14	4	0	2
52.216	4	0	2	2
52.517	3	4	1	1
52.517	3	-1	2	2
52.739	8	-3	1	4
52.739	8	2	2	0
52.952	6	-2	2	1
53.411	5	-5	0	1
53.747	1	-4	1	3
54.325	2	-5	0	2
54.325	2	1	2	2
54.474	7	1	0	5
54.604	4	5	0	0
54.821	4	3	1	3
55.033	10	-3	0	5
55.201	8	-2	2	2

Table A.1 – (Continued)

2θ (°)	I	h	k	l
55.742	35	-1	1	5
55.742	35	2	1	4
56.800	3	0	1	5
57.072	12	-2	1	5
57.263	15	-1	2	3
57.263	15	-5	0	3
57.411	31	0	2	3
57.411	31	4	1	2
57.627	16	3	0	4
57.810	5	5	0	1
58.355	1	-3	2	1
58.666	4	3	2	0
58.666	4	2	2	2
59.065	27	-5	1	1
59.384	12	-2	2	3
59.817	15	1	2	3
59.915	19	-5	1	2
60.052	39	-3	2	2
60.052	39	2	0	5
60.185	20	5	1	0
60.587	3	-3	1	5
60.879	26	-4	0	5
60.879	26	3	2	1
61.623	13	-2	0	6
62.041	4	-5	0	4
62.187	7	0	0	6
62.686	6	-5	1	3
62.832	24	5	0	2
63.037	31	3	1	4
63.210	17	5	1	1
63.632	3	-1	2	4
63.632	3	-3	2	3
63.940	2	4	1	3
64.222	2	0	2	4
64.588	37	-3	0	6
65.338	6	2	1	5
65.338	6	-6	0	1

Na₂Ti₃O₇ (72-0148)

Monoclinic

Lattice parameters: $a = 8.571 \text{ \AA}$, $b = 3.804 \text{ \AA}$, $c = 9.135 \text{ \AA}$

Radiation: CuK α_1 ($\lambda = 1.54056 \text{ \AA}$)

Table A.2 - ICDD-JCPDS file no. 41-0192 (H₂Ti₃O₇).

2θ (°)	I	h	k	l
9.919	6	0	0	1
11.306	100	2	0	0
13.487	3	2	0	-1
16.494	40	2	0	1
19.801	6	0	0	2
24.503	28	1	1	0
26.579	3	4	0	1
27.048	2	4	0	-2
29.356	10	3	1	0
29.777	32	0	0	3
32.137	7	3	1	1
33.758	3	6	0	-1
34.116	5	2	0	3
36.161	16	6	0	-2
37.637	2	3	1	2
38.000	4	1	1	-3
40.097	4	0	0	4
41.089	3	6	0	-3
44.029	20	2	0	4
46.662	6	7	1	-1
48.679	11	0	2	0
49.498	2	8	0	1

H₂Ti₃O₇ (41-0192)Radiation: CuKα₁ (λ = 1.54056 Å)

First ref.: V. Nalbandyan, I. Trubnikov, Russ. J. Inorg. Chem. (Engl. Transl.) 32 (1987) 639.

Table A.3 - ICDD-JCPDS file no. 04-0783.

2θ (°)	I	h	k	l
38.3182	100	1	1	1
44.4975	52	2	0	0
64.6119	32	2	2	0
77.5385	36	3	1	1
81.6839	12	2	2	2

Silver (04-0783)

Lattice parameter: a = 4.0862 Å

Symmetry: cubic

Radiation: CuKα₁ (λ = 1.54056 Å)

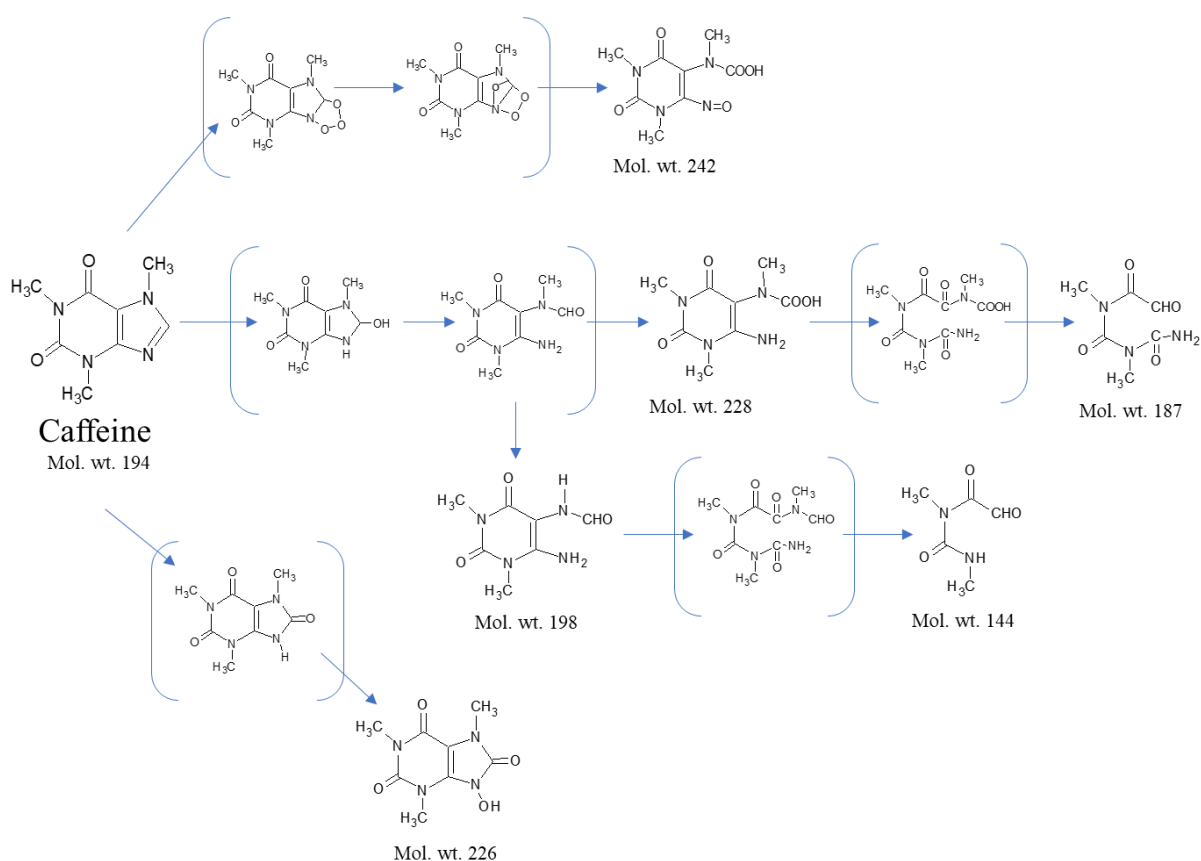


Figure B.2 – Degradation mechanism used for the intermediate products identification during caffeine removal. (Adapted from [2])

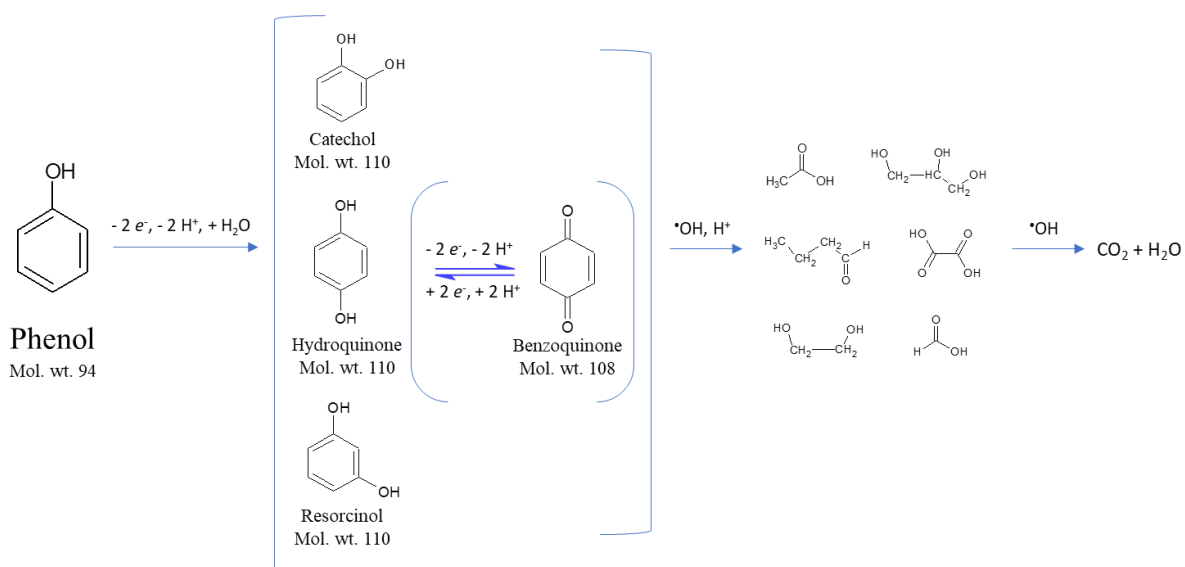


Figure B.3 – Degradation mechanism used for the intermediate products identification during phenol removal. (Adapted from [3])

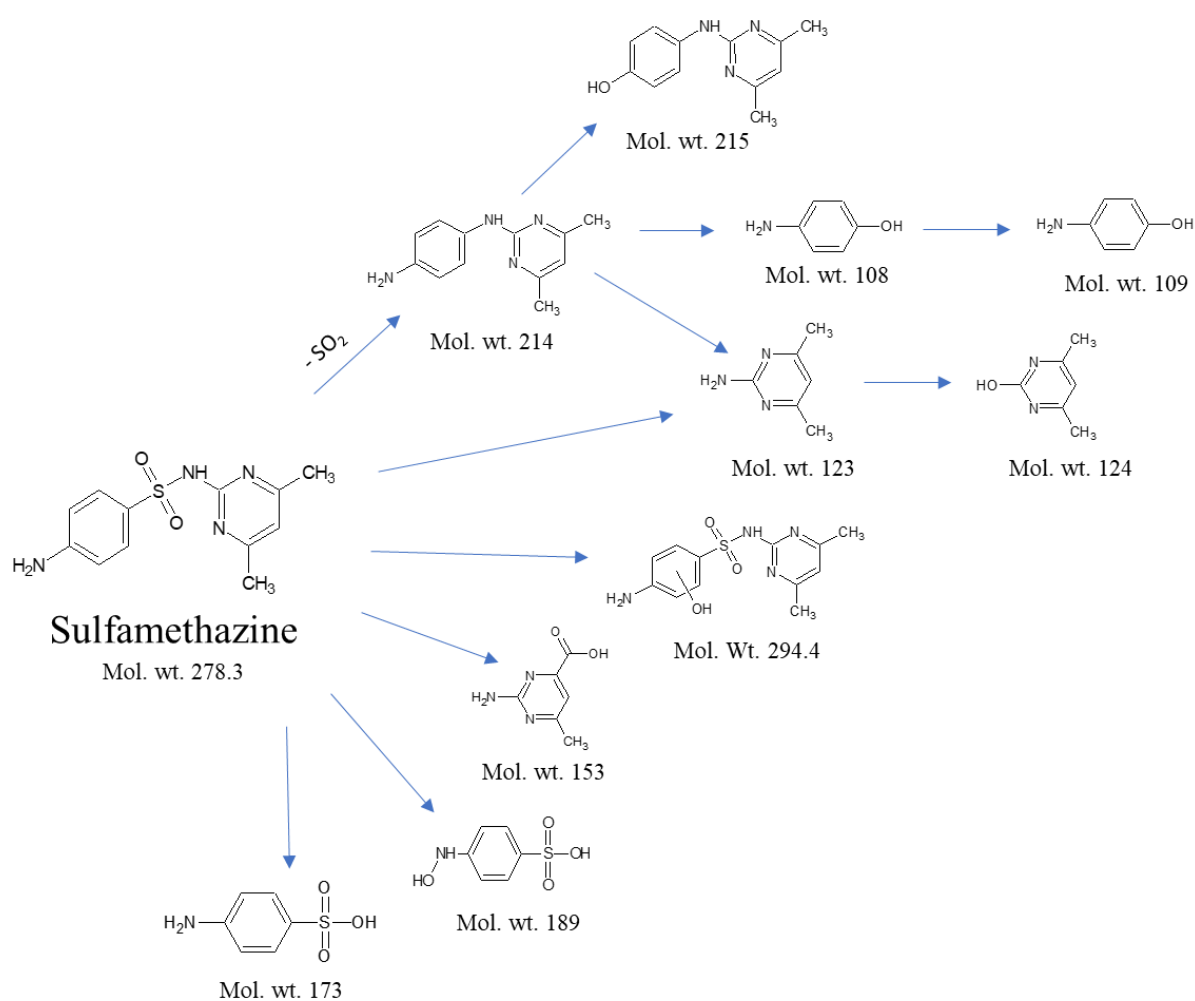


Figure B.4 – Degradation mechanism used for the intermediate products identification during sulfamethazine removal. (Adapted from [4-6])

References

- 1 - M.M. Sunil Paul, U.K. Aravind, G. Pramod, A. Saha, C.T. Aravindakumar, Hydroxyl radical induced oxidation of theophylline in water: a kinetic and mechanistic study, *Org. Biomol. Chem.* 12 (2014) 5611-5620.
- 2 - R. Rosal, A. Rodríguez, J.A. Perdigón-Melón, A. Petre, E. García-Calvo, M.J. Gómez, A. Agüera, A.R. Fernández-Alba, Degradation of caffeine and identification of the transformation products generated by ozonation, *Chemosphere* 74 (2009) 825-831.

- 3 - T.T.T. Dang, S.T.T. Le, D. Channei, W. Khanitchaidecha, A. Nakaruk, Photodegradation mechanisms of phenol in the photocatalytic process, *Res. Chem. Intermediat.* 42 (2016) 5961-5974.
- 4 - Z. Wan, J. Wang, Fenton-like degradation of sulfamethazine using $\text{Fe}_3\text{O}_4/\text{Mn}_3\text{O}_4$ nanocomposite catalyst: kinetics and catalytic mechanism, *Environ. Sci. Pollut. Res.* 24 (2017) 568-577.
- 5 - C. Guo, J. Xu, S. Wang, Y. Zhang, Y. He, X. Li, Photodegradation of sulfamethazine in an aqueous solution by a bismuth molybdate photocatalyst, *Catal. Sci. Technol.* 3 (2013) 1603-1611.
- 6 - R. Nassar, A. Trivella, S. Mokh, M. Al-Iskandarani, H. Budzinski, P. Mazellier, Photodegradation of sulfamethazine, sulfamethoxypyridazine, amitriptyline, and clomipramine drugs in aqueous media, *J. Photoch. Photobio. A* 336 (2017) 176-182.

